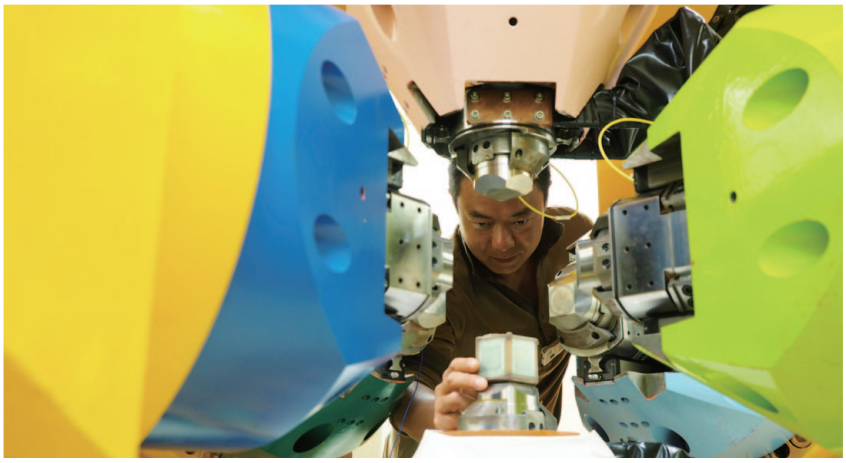

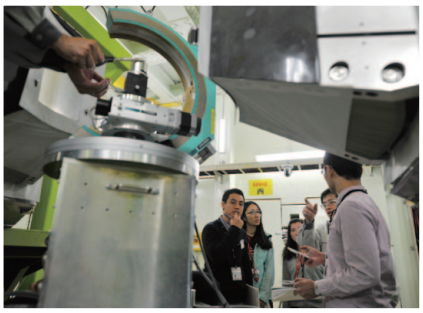

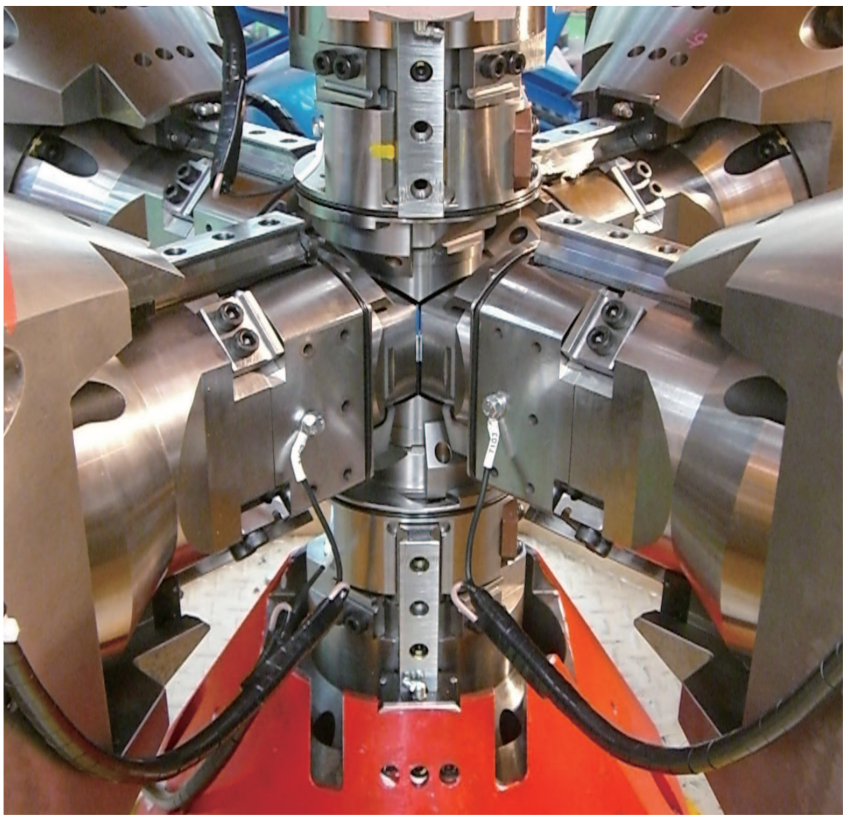

J-PARC

ANNUAL REPORT 2017

Vol.2: Materials and Life Science Experimental Facility

MLF ANNUAL REPORT

J-PARC MLF
Materials and Life Science Division
J-PARC Center
http://j-parc.jp/MatLife/en/

J-PARC was jointly constructed and is now operated by the High Energy Accelerator Research Organization (KEK) and the Japan Atomic Energy Agency (JAEA).

Comprehensive Research Organization for Science and Society
http://www.cross-tokai.jp/

J-PARC 18-04

Preface

Toshiji Kanaya
Division Head of Materials and Life Science Division, MLF

In fiscal year 2017, the operation of the Material and Life Science Experimental Facility (MLF) started with the neutron production mercury target (#2), which had an older design without helium bubbling system. The power was limited to 150 kW, although the operation was very stable. In the summer maintenance period, we replaced the target with a new one (#8) with helium bubbling system. On October 24, after the summer maintenance period, the operation started with power of 300 kW , which was increased to 400 kW in the beginning of 2018 to continue the stable operation to the end of fiscal year 2017. The beam availability to the scheduled beam time in fiscal year 2017 was 92%. The operation of the muon production target, replaced with a rotating design target in 2014, continued without major problems. The great efforts of J-PARC MLF staffs ensured the stable operations of the neutron and muon targets. The scientific results from the delivered beam of neutrons and muons, as well as the status report of the beamlines, spectrometers and the research environment, are provided in this Annual Report. In the coming years, we will make efforts to achieve beam power of 1 MW, while keeping the operations stable.

Many activities were held in MLF in 2017. One of the most important international meetings was the 2nd collaboration workshop between the European Spallation Source (ESS) and J-PARC, held at ESS in Lund on January 18 and 19, 2018. The meeting was carried out under the Memorandum of Collaboration (MoC) in the field of spallation neutron-related development between ESS and J-PARC. The extension signing ceremony of the MoC was held in Stockholm on July 7, 2017 in the presence of Sweden's Prime Minister Stefan Löfven and the Japanese Prime Minister Shinzō Abe. Ten delegates from the J-PARC Center participated in the workshop to exchange information about management of the organization, radiation and general safety issues, accelerator technology, neutron source, and neutron instruments and data management. An important domestic meeting was the Quantum Beam Science Festa, which is a conference for users of J-PARC MLF, also, the Institute of Materials Structure Science (IMSS) of High Energy Accelerator Research Organization (KEK) was held in Mito, Ibaraki Prefecture, on March 2, 3 and 4, with 524 participants, to discuss the MLF facility status, scientific results and developments, and the future plans for MLF. The details of the meetings are presented in the Annual Report.

Education of a new generation and invitation of new users are crucial for the sustainable development and research activities of the facility in the future. The 2nd Neutron and Muon School was jointly organized with the 9th AONSA neutron school from November 16 to 20. The participants in the school included 49 young researchers and graduate students from 13 countries: Korea, India, Australia, Thailand, China, Indonesia, Malaysia, Nepal, New Zealand, Russia, Taiwan, Vietnam and Japan. They enjoyed neutron and muon lectures, a site tour to J-PARC and JRR-3, and hands-experiments with neutron and muon instruments at MLF.

I would like to introduce the reader to the research highlights and status reports of MLF in the fiscal year 2017 in this annual report. For the development of neutron and muon science and technology in J-PARC MLF we will do our best in the future.

Materials and Life Science Division, Japan Proton Accelerator Research Complex
http://j-parc.jp/MatLife/en/

Preface

Hideaki Yokomizo
Director, CROSS

CROSS has served as a Registered Institution of specific neutron beam Facilities of J-PARC appointed by the Government since 2011. We have been supporting the appropriate user program operation of the Public Beamlines at Materials and Life Science Experimental Facility (MLF). We have also been engaged in facility promotion activities, such as operating a fair and open proposal selection system for the MLF Public Beamlines, providing high-quality user support and promoting facility utilization for both academic and industrial researchers. In 2017, the number of science coordinators at CROSS increased to four in order to encourage the industrial use and to help the management of the Industrial Users Society for Neutron Application.

CROSS supported the user programs at seven fully-operational Public Beamlines: BL01 *4SEASONS*, BL02 *DNA*, BL11 *PLANET*, BL15 *TAIKAN*, BL17 *SHARAKU,* BL18 *SENJU and* BL22 *RADEN*. In 2017, we had to start with beam power of 150 kW using a spare target vessel, which had no protection from the pitting damage on the beam window. The beam power was increased to 300–400 kW after the summer shutdown when a new target vessel equipped with pitting protection system was installed. We accomplished a stable and highly reliable machine operation, which reached over 90% of the planned users' time.

The special program for New User Promotion (NUP) started in 2016 to provide sufficient guidance and assistance for scientists who are new to the neutron research. NUP has a preferential beam time allocation to first-time or novice users in order to learn how to use the neutron facility. NUP is expected to cultivate new scientific field by conducting their first experiments successfully with sufficient and generous support by our staffs. Another special program, the Elementary Strategy Initiative, was completed successfully this year. In the 2017B proposal round, a new program called Long-Term Proposal was started to select and approve the experimental plans that will be carried out in a period of three years. Complementary Use is a program that encourages and facilitates the complementary and collaborative use of pulsed neutrons (J-PARC MLF), synchrotron radiation (SPring-8), and supercomputer (K computer).

I hope this Annual Report would serve as a useful information source for anyone wishing to know more about the current status of MLF, its recent scientific achievements, the technical R&D projects that support the science program, and the operational details of our facility.

On behalf of the team at the Neutron Science and Technology Center, CROSS, I extend a warm welcome to all researchers who wish to use the Public Beamlines at J-PARC MLF.

Neutron Science and Technology Center, Comprehensive Research Organization for Science and Society
www.cross-tokai.jp/en

Contents

Neutron Science

Muon Science

MLF Safety

MLF Operations in 2017

Organization Chart

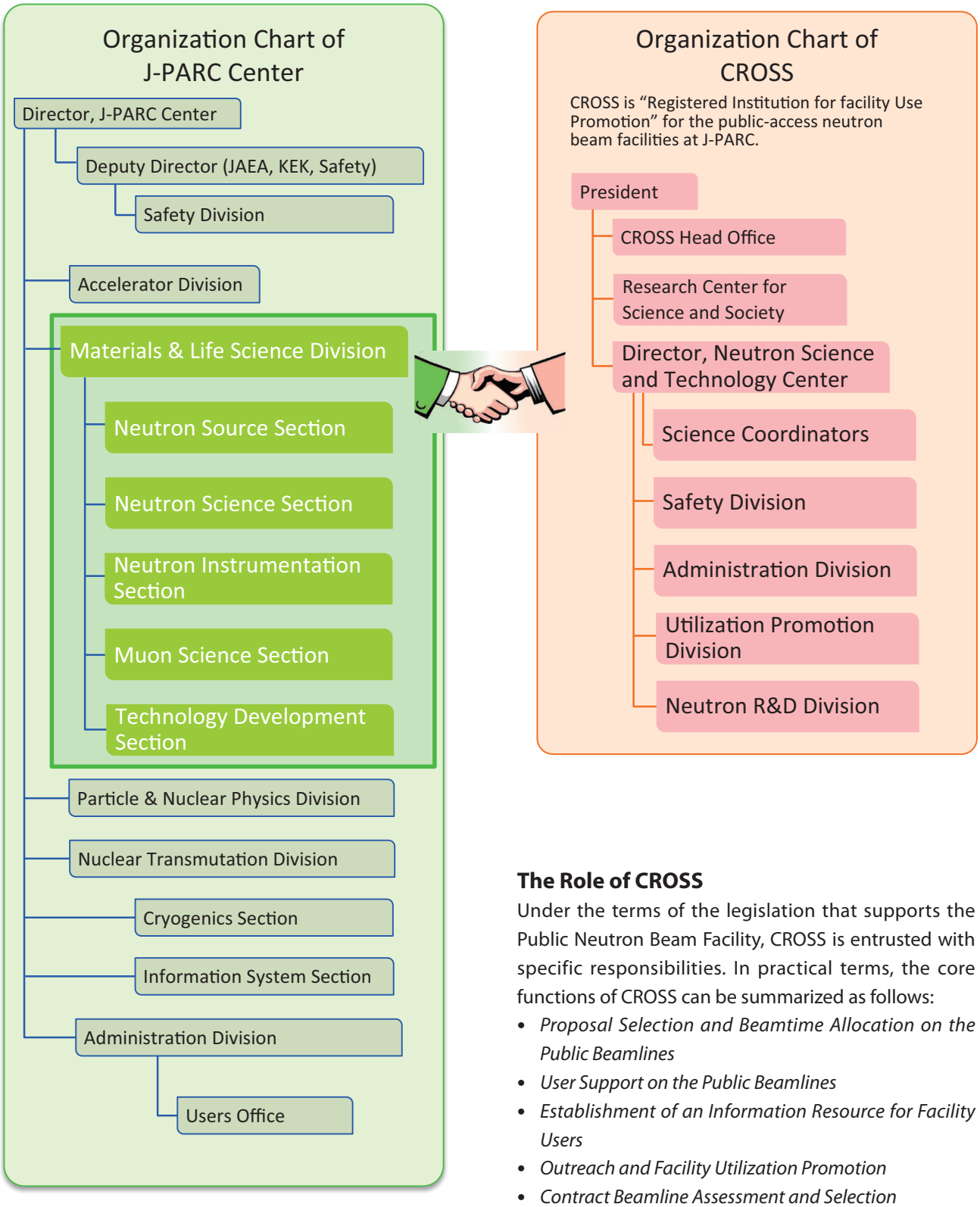

The Role of CROSS

Under the terms of the legislation that supports the Public Neutron Beam Facility, CROSS is entrusted with specific responsibilities. In practical terms, the core functions of CROSS can be summarized as follows:

- *Proposal Selection and Beamtime Allocation on the Public Beamlines*
- *User Support on the Public Beamlines*
- *Establishment of an Information Resource for Facility Users*
- *Outreach and Facility Utilization Promotion*
- *Contract Beamline Assessment and Selection*

J-PARC Map

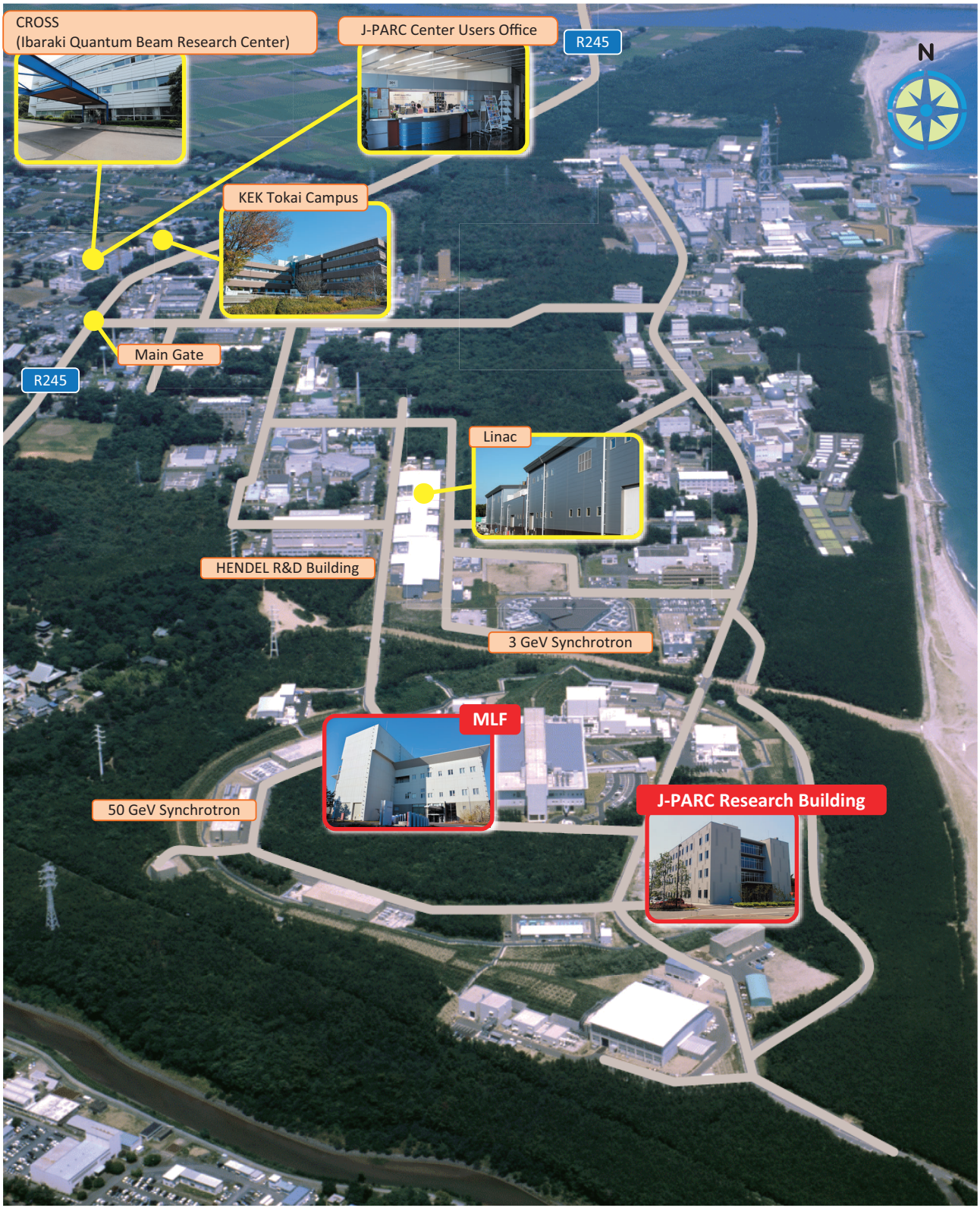
CROSS
(Ibaraki Quantum Beam Research Center)
J-PARC Center Users Office
R245
N
KEK Tokai Campus
Main Gate
R245
Linac
HENDEL R&D Building
3 GeV Synchrotron
MLF
50 GeV Synchrotron
J-PARC Research Building

Muon and Neutron Instruments

Muon Source

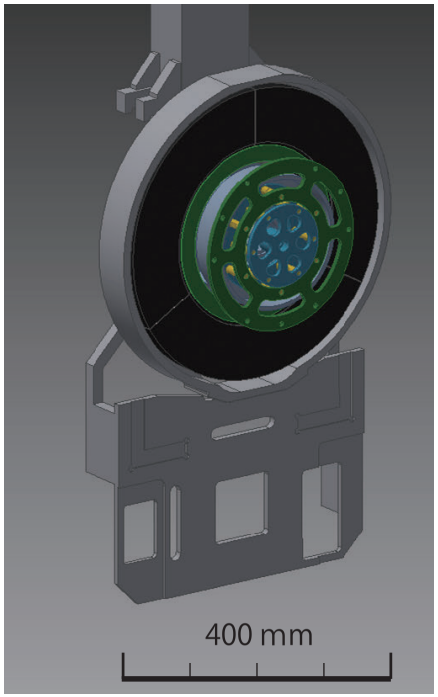

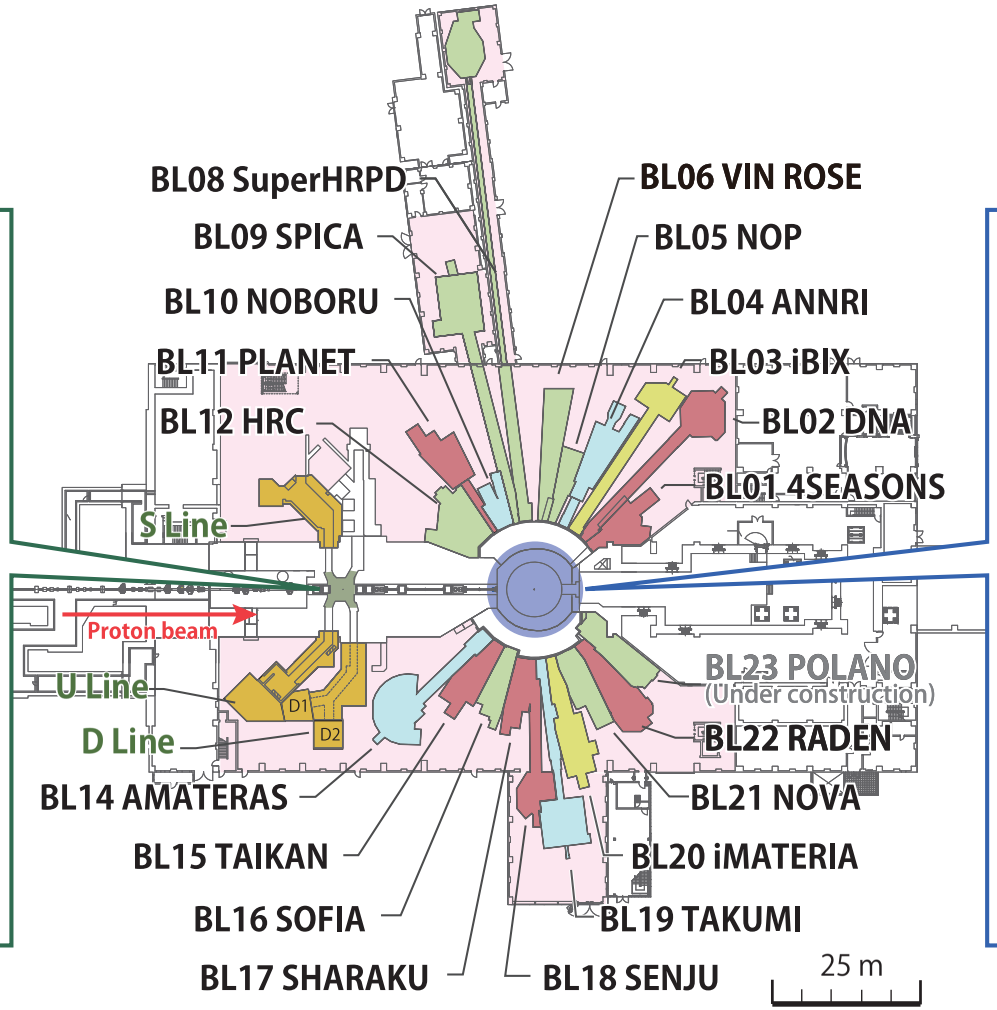

Neutron Source

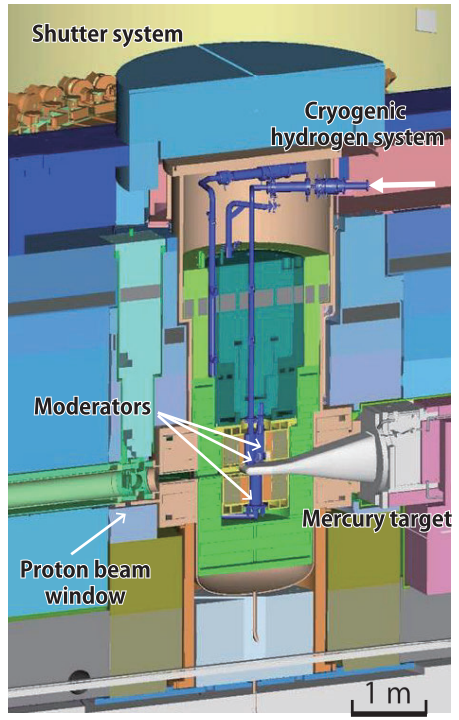

Muon Instruments

Neutron Instruments

JAEA

KEK

Public beam lines

Ibaraki Pref.

As of March 2018

Research and Development Highlights

Crystal Structure of B-Site Defected 12L-Perovskites $Ba_2La_2MW_2O_{12}$ (M = Mn, Co, Ni, Zn)

1. Introduction

Low-dimensional magnetic materials have attracted a great deal of interest because of their anomalous magnetic properties at low temperatures. In particular, the antiferromagnetism on the two-dimensional triangular lattice has been extensively studied from the aspects of geometrical frustration and quantum spin liquid. In order to find further interesting magnetic behaviors, it is absolutely essential to explore new compounds with a triangular arrangement of magnetic ions.

Recently, we have focused on the $Ba_2La_2MW_2O_{12}$ (M = Co, Mn, Ni, Zn). They have a B-site defected 12L-perovskite structure (Fig. 1(a)), in which the M ions form a two-dimensional triangular lattice in *ab* plane. This structural feature is very similar to that of the 6L-perovskites $Ba_2MSb_2O_9$ whose low-dimensional magnetic properties are attracting significant attention [1-3]; thus, the $Ba_2La_2MW_2O_{12}$ could be a new series of compounds showing further interesting physical properties.

For the crystal structure of $Ba_2La_2MW_2O_{12}$ and isostructural compounds, some structural models have been proposed [4-7], but have not yet been clearly determined. Therefore, we have carried out the powder neutron diffraction measurements.

2. Experiments

The $Ba_2La_2MW_2O_{12}$ (M = Co, Mn, Ni, Zn) were prepared as polycrystalline samples by the solid-state reaction. $BaCO_3$, BaO, La_2O_3, CoO, MnO, NiO, ZnO and WO_3 were used as starting materials. The mixture was pressed into pellets, and heated at 900°C for 12 h, 1100°C for 12 h, and 1200°C for 12 h × 2-3 in air (M = Co, Ni, Zn) or at 1200°C for 3 h in an evacuated silica ampoule and quenched by liquid nitrogen (M = Mn).

The powder x-ray diffraction (XRD) measurements were performed at room temperature in the range 10° ≤ 2θ ≤ 120° using a 2θ step size of 0.02° with Cu-Kα radiation on a Rigaku MultiFlex diffractometer.

The powder neutron diffraction (ND) profiles were collected at room temperature. For M = Ni, the ND measurement (the neutron wavelength λ = 1.84843 Å) was performed by HERMES [8], installed at the JRR-3M reactor in Japan Atomic Energy Agency (JAEA), Tokai. For M = Zn, the time-of flight neutron diffraction (TOF-ND) by Super HRPD (BL08), installed at the Material and Life Science Experimental Facility (MLF) of the Japan Proton Accelerator Research Complex (J-PARC). The data were analyzed by the Rietveld technique by using the program RIETAN-FP [9] for both XRD and ND, and the Z-code program package [10,11] for the TOF-ND. The crystal structures were drawn by the VESTA program [12].

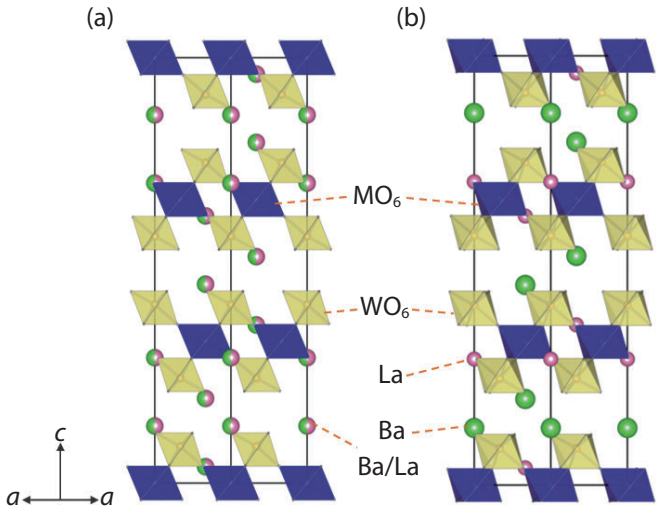

Figure 1. Schematic crystal structures of $Ba_2La_2MW_2O_{12}$ and comparison between the two structural models: (a) space group *R*–3*m* with a disordered one in earlier reports and (b) *R*–3 with an ordered A-site arrangement in this study.

3. Results and discussion

The title compounds $Ba_2La_2MW_2O_{12}$ (M = Mn, Co, Ni, and Zn) were prepared as polycrystalline samples. Their XRD data were well indexed by a rhombohedral unit cell (a ~ 5.7 Å, c ~ 27.4 Å). The Rietveld analysis was carried out using the R-3m model proposed for $Ba_2La_2MW_2O_{12}$ and isostructural compounds [4-8] and this model was a good fit for the data; however, we have found a better model based on the results of neutron diffraction measurements which will be described below.

We have performed the neutron diffraction measurements for $Ba_2La_2MW_2O_{12}$ (M = Ni and Zn). Figure 2(a) shows the TOF-ND profile for $Ba_2La_2ZnW_2O_{12}$ and the calculated profile obtained from the above R-3m model. It was found that this structural model was obviously not suitable for the observed data. The reason for the discrepancy was that the model was not suitable, i.e., there are differences that cannot be well distinguished in the XRD measurements, such as the space group, ordered/disordered arrangement of Ba/La ions, possibility of oxygen ion defects, and so on. Therefore, we tried to analyze the ND data by using many structural models, and finally found that a model with the space group R-3 was adequate. The calculated profile is plotted in Fig. 2(b), which shows a good agreement with the observed one. This model also gives good results for the ND data for $Ba_2La_2NiW_2O_{12}$ and XRD data for all compounds.

The structural parameters for $Ba_2La_2ZnW_2O_{12}$ were determined by using the R-3 model, and the crystal structures for both R-3m (old) and R-3 (new) models are illustrated in Fig. 1. Both structures have the same unit cell dimension but reflecting the loss of mirror plane from R-3m to R-3, the crystallographic sites of oxygen ions (O1 and O2) are different, which brings about the tilting of connection of MO_6 and WO_6 octahedra. In addition, two kinds of A-site cations, Ba^{2+} and La^{3+}, adopt a fully ordered arrangement unlike some earlier reports [4-7], and there are no oxygen defects within the standard deviation. The BVS values calculated from the structural parameters suggest that the valence states of cations are represented as $Ba^{2+}{}_2La^{3+}{}_2M^{2+}W^{6+}{}_2O_{12}$. In this crystal structure, the magnetic M^{2+} ions form a triangular lattice in ab plane, and each plane is magnetically separated (~9 Å) by nonmagnetic layers consisting of Ba^{2+}, La^{3+}, and W^{6+} ions. Therefore, in the view of the magnetism, the B-site defected 12L-perovskites $Ba_2La_2MW_2O_{12}$ can be regarded as ideal candidates for the two-dimensional magnetically frustrated system.

Afterwards, the magnetic, thermal, and optical properties were measured for the title compounds, and the DFT calculations based on above structural data were carried out. The details have been published in another paper [13].

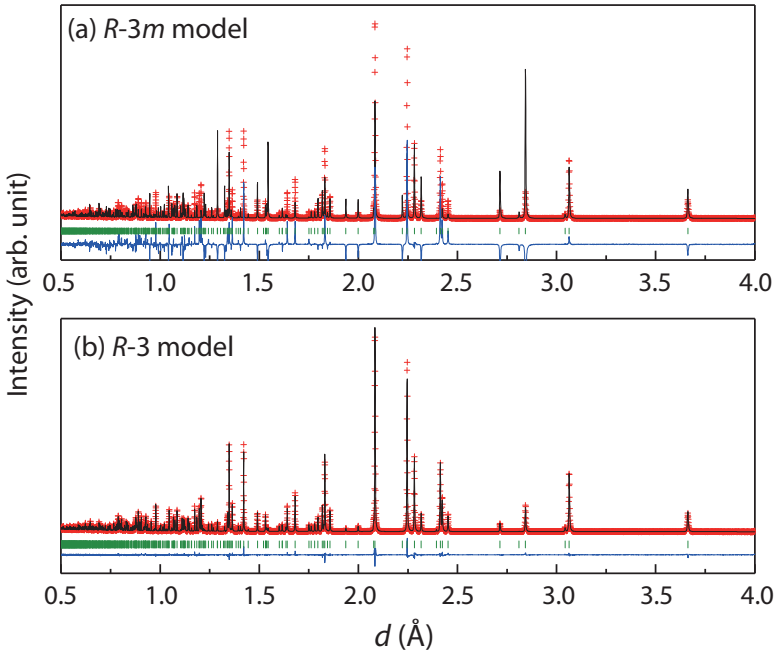

Figure 2. Time-of-flight powder neutron diffraction profiles for $Ba_2La_2ZnW_2O_{12}$, calculated by using (a) R–3m and (b) R–3 models. The blue line indicates the difference between the observed and calculated profiles.

4. Conclusion

The neutron diffraction measurements were performed for the B-site defected 12L-perovskites $Ba_2La_2MW_2O_{12}$ (M = Ni and Zn), and it was found that they adopt not the *R*-3*m* structure proposed in earlier works but the *R*-3 one. Their detailed structural parameters were determined, and these results indicated that the magnetic M^{2+} ions form an ideal two-dimensional triangular lattice.

References

[1] Y. Doi, Y. Hinatsu, and K. Ohoyama, J. Phys.: Condens. Matter, **16**, 8923–8935 (2004).

[2] H.D. Zhou, E.S. Choi, G. Li, L. Balicas, C.R. Wiebe, Y. Qiu, J.R.D. Copley, and J.S. Gardner, Phys. Rev. Lett., **106**, 147204 1–4 (2011).

[3] J.G. Cheng, G. Li, L. Balicas, J.S. Zhou, J.B. Goodenough, C. Xu and H.D. Zhou, Phys. Rev. Lett., **106**, 197204 1–4 (2011).

[4] S. Kemmler-Sack, Z. Anorg. Allg. Chem., **461**, 142–145 (1980).

[5] H.J. Rother, A. Fadini, and S. Kemmler-Sack, Z. Anorg. Allg. Chem., **463**, 137–143 (1980).

[6] R. Yu, M. Li, N. Xie, T. Wang, N. Xue, J. Am. Ceram. Soc., **98**, 3849–3855 (2015).

[7] R. Rawl, M. Lee, E.S. Choi, G. Li, K.W. Chen, R. Baumbach, C.R. dela Cruz, J. Ma, and H.D. Zhou, Phys. Rev. B, **95**, 174438 1–9 (2017).

[9] K. Ohoyama, T. Kanouchi, K. Nemoto, M. Ohashi, T. Kajitani, Y. Yamaguchi, Jpn. J. Appl. Phys., **37,** 3319–3326 (1998).

[10] R. Oishi, M. Yonemura, Y. Nishimaki, S. Torii, A. Hoshikawa, T. Ishigaki, T. Morishima, K. Mori, T. Kamiyama, Nucl. Instrum. Methods Phys. Res. A, **600**, 94–96 (2009).

[11] R. Oishi-Tomiyasu, M. Yonemura, T. Morishima, A. Hoshikawa, S. Torii, T. Ishigaki, T. Kamiyama, J. Appl. Crystallogr., **45**, 299–308 (2012).

[12] K. Momma and F. Izumi, J. Appl. Crystallogr., **41**, 653–658 (2008).

[13] Y. Doi, M. Wakeshima, K. Tezuka, Y.J. Shan, K. Ohoyama, S. Lee, S. Torii, T. Kamiyama, and Y. Hinatsu, J. Phys.: Condens. Matter, 29, 365802 1–11 (2017).

Y. Doi[1], M. Wakeshima[1], K. Ohoyama[2], S. Lee[3], S. Torii[3], T. Kamiyama[3], and Y. Hinatsu[1]

[1]*Department of Chemistry, Faculty of Science, Hokkaido University;* [2]*Graduate School of Science and Engineering, Ibaraki University;* [3]*Neutron Science Section, Materials and Life Science Division, J-PARC Center, Institute of Materials Structure Science, KEK*

Mechanical Synthesis and Structural Properties of the Fast Fluoride-Ion Conductor $PbSnF_4$

1. Introduction

The all-solid-state rechargeable battery is a key technology for large-scale applications such as electric vehicles, plug-in hybrid vehicles, and electrical energy-storage systems in future smart grids. The use of solid electrolytes is critical for improving the battery performance parameters: energy density, power capacity, lifespan, and reliability. In the last decade, fluoride-ion batteries (FIBs) have attracted much attention as alternative candidates for lithium-ion batteries, nickel-metal hydride batteries, sodium-ion batteries, and so on [1-4]. The fluoride anion (F^-) is considerably stable as a charge transfer ion in FIBs because it exhibits the highest electronegativity (3.98) of all elements. The chemical reaction of the fluoride anion with metals leads to the formation of metal fluorides, which can release several electrons per metal atom. This masks the possibility that the theoretical energy densities of FIBs outperform those of lithium-ion batteries. All-solid-state FIBs based on the "metal (anode)/metal fluoride (cathode)" pair have been assembled experimentally and characterized using fluoride-ion conductors, for example, $La_{1-x}Ba_xF_{3-x}$ (as a solid electrolyte) [6]. The ionic conductivity of $La_{0.9}Ba_{0.1}F_{2.9}$ (2.8×10^{-4} S/cm at 433 K) is sufficiently high, but not sufficiently high enough at room temperature (RT). Therefore, all-solid-state FIBs based on a metal/metal fluoride pair can work only at elevated temperatures. For the realization of all-solid-state FIBs at RT, it is very important to explore new fast fluoride-ion conductors.

$PbSnF_4$ exhibits the highest ionic conductivity ($\approx 10^{-3}$ S/cm at RT) among the proposed fluoride-ion conductors [7-9]. In spite of its narrow electrochemical stability window, the superior ionic conductivity is also fascinating from the practical point of view. It has been reported that $PbSnF_4$ can be synthesized by mechanical milling (MM) of the two starting materials: SnF_2 and α-PbF_2 [12-14]. The ionic conductivity of $PbSnF_4$ obtained by MM is $\approx 10^{-3}$ S/cm at RT, which is comparable to that obtained by the two conventional methods. In the XRD measurements, several allotropic forms such as β-$PbSnF_4$ (tetragonal system, space group = *P*4 / *nmm*) and γ-$PbSnF_4$ (fluorite-type structure, space group: $Fm\bar{3}m$) have been observed. However, the detailed crystal structure and the fluoride-ion conduction mechanism are still unclear.

In the present work, γ-$PbSnF_4$ was synthesized by MM at RT, and β-$PbSnF_4$ was obtained by aging it at 473 K. We discuss the fluoride-ion conduction mechanism in γ- and β-$PbSnF_4$ from structural point of view.

2. Crystal structures of γ- and β-$PbSnF_4$

Crystal structure analysis for γ- and β-$PbSnF_4$ was performed using neutron diffraction data. The neutron diffraction data were collected at BL09 (SPICA) in MLF. The Rietveld refinement patterns for γ-$PbSnF_4$ are shown in Fig. 1. First, the structure parameters were refined on the basis of the fluorite-type structure (space group: $Fm\bar{3}m$) with a single Sn/Pb site and a single F site (henceforth termed "$F^{\gamma}(1)$ normal site"). Note that the Sn/Pb atomic ratio is 1:1. As shown in Fig. 1(a), the fluoride ions were located at the four-fold coordinated sites (i.e., $F^{\gamma}(1)[Sn/Pb]_4$ tetrahedral units) only. While a fairly good agreement was obtained between the observed and calculated intensities, this was insufficient to refine several Bragg reflections, such as (200) and (311). Next, we employed an additional F site in the general position (henceforth termed "$F^{\gamma}(2)$ interstitial site"), being consistent with the interstitial sites of PbF_2 [15]. The change of the structure model achieved a meaningful improvement (see, Fig. 1(b)). In the figure, fluoride ions were located at the six-fold coordinated sites with off-center displacement (i.e., $F^{\gamma}(2)[Sn/Pb]_6$ octahedral units) in addition to the four-fold coordinated sites (i.e., $F^{\gamma}(1)[Sn/Pb]_4$ tetrahedral units). The occupancies (*g*) at the $F^{\gamma}(1)$ and $F^{\gamma}(2)$ sites were less than 1, meaning that vacancies exist at both sites. The ratio of the number of fluoride ions at $F^{\gamma}(1)$ to those at $F^{\gamma}(2)$ was approximately 5:3. This indicates that the fluoride ions have a preference for the $F^{\gamma}(1)$ normal site over the $F^{\gamma}(2)$ interstitial site.

Figure 2 shows the Rietveld refinement patterns of β-$PbSnF_4$. The crystal structure of β-$PbSnF_4$ was refined on the basis of the tetragonal system (space group: *P*4 / *nmm*). The model assumed a single Sn site, a single Pb site, and three F sites: $F^{\beta}(1)$, $F^{\beta}(2)$, and $F^{\beta}(3)$. The $F^{\beta}(1)$ and $F^{\beta}(3)$ sites correspond to the F sites between Sn and Pb layers (i.e., –SnPb–), and the $F^{\beta}(2)$ site corresponds to the F site between the Pb layers (i.e., –PbPb–). The F site between Sn layers (i.e., –SnSn–) was omitted in our refinement due to the Sn^{2+} lone pair [10, 11]. In fact, the *g* value was close to zero when we assumed the F site between Sn layers together with the $F^{\beta}(1)$, $F^{\beta}(2)$,

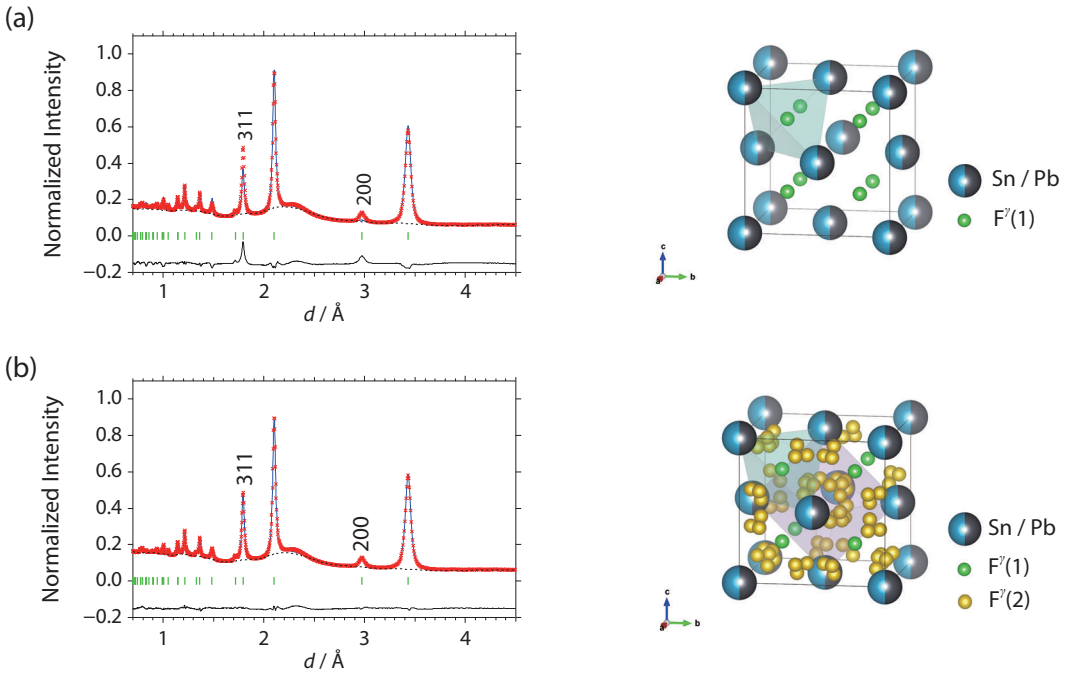

Figure 1. The crystal structure refinement for γ-$PbSnF_4$ using neutron diffraction data

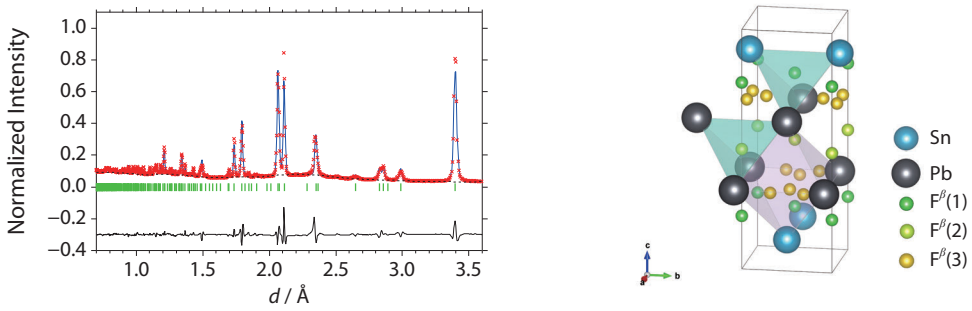

Figure 2. The crystal structure refinement of β-$PbSnF_4$ using neutron diffraction data.

and $F^{\beta}(3)$ sites in the preliminary refinements. The $F^{\beta}(1)$ and $F^{\beta}(3)$ sites were found to be deficient, whereas the $F^{\beta}(2)$ site was fully occupied, so that the g of the $F^{\beta}(2)$ site was fixed at unity in further refinements. The crystal structure of β-$PbSnF_4$ is illustrated in Fig. 2. The $F^{\beta}(1)$ and $F^{\beta}(3)$ sites had $g < 1$, while the $F^{\beta}(2)$ site exhibited $g = 1$. The ratio of the number of fluoride ions at $F^{\beta}(1)$, $F^{\beta}(2)$, and $F^{\beta}(3)$ was approximately 5:4:7. Thus, we concluded that fluoride ions prefer the $F^{\beta}(3)$ site (henceforth termed "$F^{\beta}(3)$ interstitial site"), followed by the $F^{\beta}(1)$ site (henceforth termed "$F^{\beta}(1)$ normal site"), and the $F^{\beta}(2)$ site (henceforth termed "$F^{\beta}(2)$ normal site"). It is worth noting that the $F^{\beta}(1)$ and $F^{\beta}(2)$ normal sites are the four-fold coordinated sites and the $F^{\beta}(3)$ interstitial site is a six-fold coordinated site with off-center displacement (Fig. 2).

3. Fluoride ion pathway

Figure 3 presents the crystal structures of γ- and β-$PbSnF_4$, viewed down the $a + b$ diagonal direction and the a-axis, respectively. The relation between the lattice parameters of γ- and β-$PbSnF_4$ is as follows: $a_{\beta} \approx (\sqrt{2}/2)a_{\gamma}$ and $c_{\beta} \approx 2a_{\gamma}$. In the figure, the atomic arrangement of γ-$PbSnF_4$ is similar to that of β-$PbSnF_4$, although the $F^{\gamma}(1)$ normal site occurs as two sites: the $F^{\beta}(1)$ and $F^{\beta}(2)$ normal sites, and the $F^{\gamma}(2)$ interstitial site becomes the $F^{\beta}(3)$ interstitial site. In particular, the number of fluoride ions at the F interstitial site appreciably increased by the γ-to-β phase transition: 38.1% at $F^{\gamma}(2)$ to 43.9% at $F^{\beta}(3)$, from the g values for each F site.

In β-$PbSnF_4$, the $F^{\beta}(2)$ normal site is fully occupied, whereas the $F^{\beta}(1)$ normal site and the $F^{\beta}(3)$ interstitial site are partially occupied, when we assume the absence of fluoride ions between the Sn layers due to

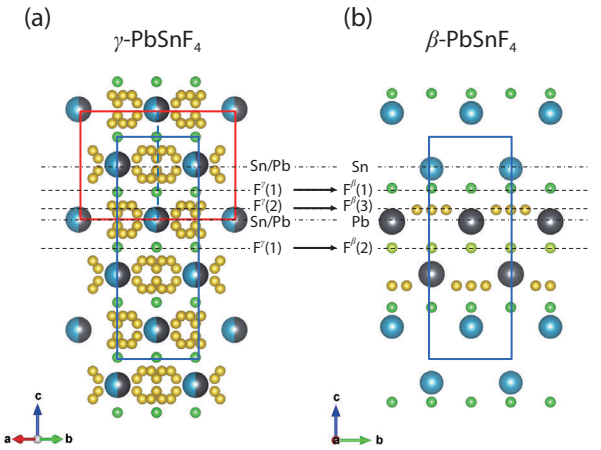

Figure 3. Crystal structures of (a) γ-$PbSnF_4$ and (b) β-$PbSnF_4$, viewed down the $a + b$ diagonal direction and the a-axis. The $F^{\gamma}(1)$ normal site is divided into two sites: the $F^{\beta}(1)$ and $F^{\beta}(2)$ normal sites; and the $F^{\gamma}(2)$ interstitial site becomes the $F^{\beta}(3)$ interstitial site.

the Sn^{2+} lone pair. According to the vacancy diffusion mechanism, it is sufficient to say that the "–$F^{\beta}(1)$–$F^{\beta}(3)$–$F^{\beta}(3)$–$F^{\beta}(1)$–" zigzag network with fluoride ions and vacancies on the *ab*-plane facilitates the two-dimensional fast fluoride-ion conduction and there is no space available for migrating fluoride ions via the $F^{\beta}(2)$ normal sites along the *c*-axis.

The electrical conductivity of β-$PbSnF_4$ (1.6×10^{-3} S/cm at 298 K) is relatively higher than that of γ-$PbSnF_4$ (3.4×10^{-4} S/cm at 298 K). In the vacancy diffusion mechanism, σ can be represented by the following equation: $\sigma = (Ze)n\mu$, where Ze is the valence of the ion carrier ($Z = 1$ for Li^+), n is the effective carrier concentration, and μ is the mobility of ions. It is worth noting that the "–$F^{\beta}(1)$–$F^{\beta}(3)$–$F^{\beta}(3)$–$F^{\beta}(1)$–" network is formed between the single Sn and the single Pb layers, whereas the "–$F^{\gamma}(1)$–$F^{\gamma}(2)$–$F^{\gamma}(2)$–$F^{\gamma}(1)$–" network occurs between the mixed Sn/Pb layers (see, Fig. 3). It seems that the ordered framework of the single Sn and Pb layers in β-$PbSnF_4$ plays an important role in improving μ (or σ). Furthermore, n depends directly on the number of fluoride ions at the F interstitial site: 38.1% at $F^{\gamma}(2)$ to 43.9% at $F^{\beta}(3)$. It is most likely that n in the "–$F^{\beta}(1)$–$F^{\beta}(3)$–$F^{\beta}(3)$–$F^{\beta}(1)$–" network is optimized, compared with that in the "–$F^{\gamma}(1)$–$F^{\gamma}(2)$–$F^{\gamma}(2)$–$F^{\gamma}(1)$–" network. More details are provided in paper [16].

4. Acknowledgement

TOF-ND experiments were approved by the Neutron Scattering Program Advisory Committee of IMSS, KEK (Proposal No. 2014S10). This work was predominantly supported by the Research and Development Initiative for Scientific Innovation of New General Batteries 2 (RISING 2) project, No. P16001, from the New Energy and Industrial Technology Development Organization (NEDO), Japan. This work was partially supported by a Grant-in-Aid for Science Research (C), No. 15K06483, from the Japan Society for the Promotion of Science (JSPS).

References

[1] G.G. Amatucci, N. Pereira, J. Fluorine Chem. 128 (2007) 243.
[2] N.I. Sorokin, B.P. Sobolev, Crystallogr. Rep. 52 (2007) 870.
[3] L.N. Patro, K. Hariharan, Solid State Ionics 239 (2013) 41.
[4] C. Rongeat, M.A. Reddy, et al., ACS Appl. Mater. Interfaces 6 (2014) 2103.
[5] F. Gschwind, G. Rodriguez-Garcia, et al., J. Fluorine Chem. 182 (2016) 76.
[6] M.A. Reddy, M. Fichtner, J. Mater. Chem. 21 (2011) 17059.
[7] J.M. Réau, C. Lucat, et al., Mat. Res. Bull. 13 (1978) 877.
[8] S. Vilminot, G. Perez, et al., Solid State Ionics 2 (1981) 87.
[9] R. Kanno, S. Nakamura, et al., Mat. Res. Bull. 26 (1991) 1111.
[10] G. Denes, Y.H. Yu, et al., Solid State Ionics 104 (1993) 239.
[11] M. Castiglione, P.A. Madden, et al., J. Phys. Condens. Matter 17 (2005) 845.
[12] A. Collin, G. Dénès, D.L. Roux, et al., Int. J. Inorg. Mater. 1 (1999) 289.
[13] S. Suda, T. Eguchi, J. Kuwano, Key Eng. Mater. 181–182 (2000) 203.
[14] M. Uno, M. Onitsuka, et al., Solid State Ionics 176 (2005) 2493.
[15] K. Koto, H. Schulz, R.A. Huggins, Solid State Ionics 1 (1980) 355.
[16] F. Fujisaki, K. Mori, et al., J. Solid State Chem., 253(2017)287.

F. Fujisaki[1], K. Mori[2], M. Yonemura[3,4], Y. Ishikawa[3,4], T. Kamiyama[3,4], T. Otomo[3,4], E. Matsubara[1], T. Fukunaga[1] J. Suzuki[1,2], Y. Inamura[3], T. Ito[4], and T. Nakatani[3]

[1]*Office of Society-Academia Collaboration for Innovation, Kyoto University;* [2]*Institute for Integrated Radiation and Nuclear Science, Kyoto University;* [3]*Neutron Science Section, Materials and Life Science Division, J-PARC Center;* [4]*Institute of Materials Structure Science, KEK*

Inverse Pole Figure Mapping of Crystalline Grains by Bragg-dip Neutron Transmission Imaging

1. Introduction

Mapping of crystalline grains and their crystal orientations by using SEM-EBSD or X-ray diffraction imaging is a powerful methodology for materials characterization. In general, neutrons have higher material penetration ability than electrons and X-rays. Therefore, analyses of bulk-averaged crystallographic information in a centimeter-sized polycrystalline material such as steel are being performed by neutron diffraction and Bragg-edge neutron transmission imaging [1]. Furthermore, recently, development projects of neutron diffraction imaging were launched using both continuous [2] and pulsed [3] sources for the grain orientation analysis.

On the other hand, as described in this article, we are developing a grain orientation mapping method based on pulsed neutron Bragg-dip transmission imaging [4]. This is because neutron transmission imaging setup can achieve an imaging of large field-of-view with high spatial resolution around a few hundred micrometers. In addition, it is expected that Bragg-dip neutron transmission measurement for single crystal [5] is convenient since the crystal-lattice direction along the neutron transmission direction can be deduced from the neutron wavelengths of Bragg-dips without sample rotation [4]. This feature is efficient for imaging of grain orientation, even in the case of two-dimensional imaging. However, the orientation determination of each grain in a grain-overlapping material is quite difficult for the least-squares fitting/refinement of a whole Bragg-dip pattern without a rough initial guess of crystallographic parameters of each single-crystal included in the neutron transmission path. We developed a method to solve this difficulty.

In the present paper, we describe a new Bragg-dip pattern analysis method, which can rapidly determine the number of grains and their crystal-lattice directions along the neutron transmission path. A demonstration experiment applying this method was performed by using a large-grained Si-steel plate at J-PARC MLF BL10 "NOBORU".

2. Experimental condition

Figure 1 shows a specimen photograph of 3.4wt% Si-steel plate (BCC crystal structure, 5 mm thickness). Grain boundaries can be observed on the surface with a naked eye. The grains have sizes ranging approximately from a millimeter to several centimeters. The observed grain shapes were slightly different between the surface and the reverse face. This means that there are regions, where two or more stacked grains exist along the normal direction of the plate.

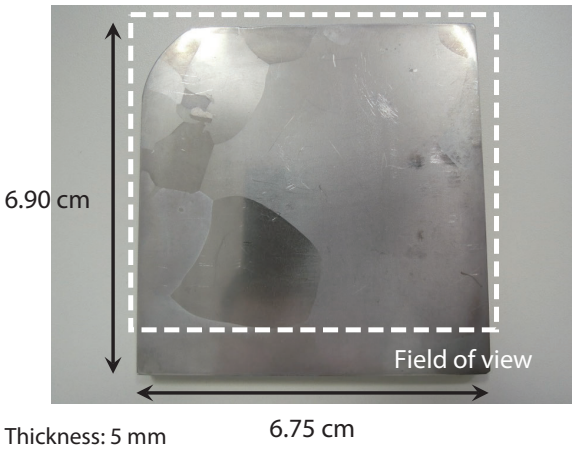

Figure 1. Photograph of the Si-steel specimen [1, 4].

During the experiment performed at NOBORU, the proton beam powers were 400 kW or 500 kW. The collimator ratio L/D was set at about 2400, and the neutron flight path length was 14.26 m. In this experiment, a GEM (gas electron multiplier) detector [6] was used for measurements of position-dependent Bragg-dip neutron transmission time-of-flight spectra of the sample, with an 800 μm pixel size. The distance between the sample and the detector was 4 cm. The measurement time was about 7.2 hours for an open beam measurement and about 14.5 hours for a sample measurement, respectively. Such a long time was required due to the limitation in the counting rate of the detector.

3. Test of a new Bragg-dip pattern analysis method

Figure 2 shows an example of Bragg-dip neutron transmission spectrum and an indexing result obtained by the developed Bragg-dip pattern analysis method, namely, the database matching method. An important feature of the developed analysis method is its speed for determining the number of grains and their crystal-lattice directions along the neutron transmission path. This method uses a database containing Bragg-dip wavelength patterns about various crystal-lattice directions. Through the matching between wavelength

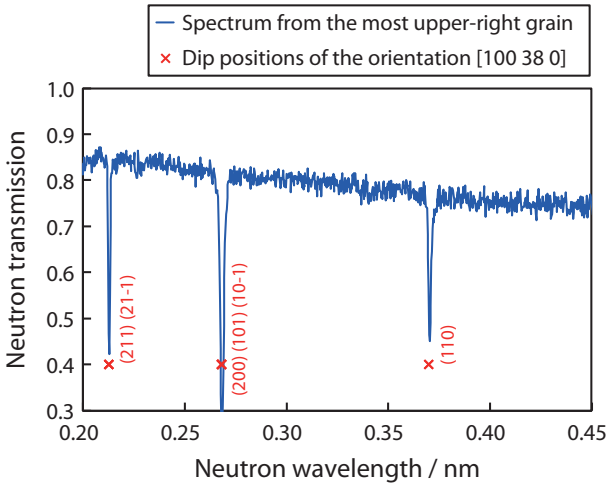

Figure 2. Bragg-dip neutron transmission spectrum [4].

patterns of experimental Bragg-dips and the database, the most probable crystal-lattice direction along the neutron transmission direction is uniquely identified for each grain.

The indexing result in Fig. 2 shows that the database matching method can reasonably determine the crystal-lattice direction. This Bragg-dip transmission spectrum is that of crystalline grain of the most upper right, and two integrated Bragg-dips are observed at 0.213 nm and 0.268 nm. The former dip consists of double dips of (211) and (21-1) according to the database matching and deepens in the experiment. The latter dip consists of triple dips of (200) and (101) and (10-1) according to the database matching and becomes deeper in the experiment. Thus, there was no contradiction between the experimental result and the analysis result in terms of dip depth, although the dip depth was not evaluated in the data analysis at all. It seems that the crystal-lattice direction estimated by the proposed method is correct.

4. Crystalline grain orientation imaging

Figure 3 shows inverse pole figure (IPF) maps of the crystalline grains included in the specimen. The crystal-lattice directions indicated by IPF correspond to the normal direction of the plate (the neutron transmission direction). In Fig. 3 (a), "black" regions, except for the most upper left, indicate the region, where two grains are stacked along the neutron transmission path. The crystal-lattice directions of such stacked grains are also shown by Fig. 3 (b) and (c), respectively. In addition, note that these images can show the crystal-lattice directions of grains in the bulk or at the opposite surface, which cannot be detected by SEM-EBSD and X-ray diffraction imaging.

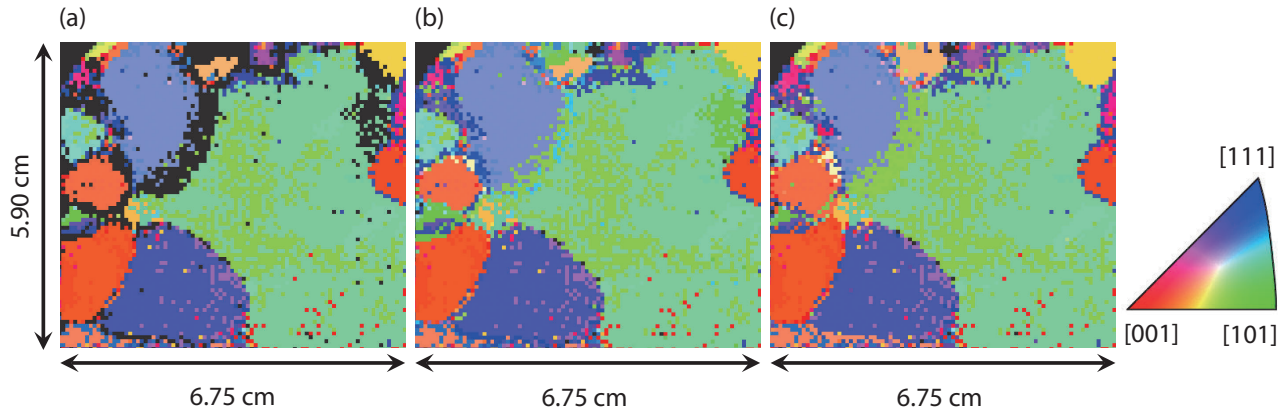

Figure 3. Inverse pole figure maps of bulk crystalline grains obtained by Bragg-dip neutron transmission imaging [4].

5. Conclusion and future works

We successfully demonstrated the IPF imaging of bulk crystalline grains by combining the pulsed neutron Bragg-dip transmission measurements and the new data analysis method, which can rapidly and uniquely identify the crystal-lattice directions of each grain along the neutron transmission path. This method will provide new opportunities for the characterization of coarse grain-sized engineering materials, e.g. electromagnetic steels and turbine blades.

There are two issues for future research. One is crystal-lattice direction analysis along not only the normal direction but also the perpendicular direction (full crystal orientation analysis). The other is real-space imaging of grain structure with crystal orientation information in three dimensions.

References

[1] H. Sato, J. Imaging 4 (2018) 7.

[2] S. Peetermans, A. King, W. Ludwig, P. Reischig and E. H. Lehmann, Analyst 139 (2014) 5765-5771.

[3] A. Cereser, M. Strobl, S. A. Hall, A. Steuwer, R. Kiyanagi et al., Sci. Rep. 7 (2017) 9561.

[4] H. Sato, Y. Shiota, S. Morooka, Y. Todaka, N. Adachi et al., J. Appl. Cryst. 50 (2017) 1601-1610.

[5] F. Malamud and J. R. Santisteban, J. Appl. Cryst. 49 (2016) 348-365.

[6] S. Uno, T. Uchida, M. Sekimoto, T. Murakami, K. Miyama et al., Phys. Procedia 26 (2012) 142-152.

H. Sato[1], Y. Shiota[2], S. Morooka[3], Y. Todaka[4], N. Adachi[4], S. Sadamatsu[5], K. Oikawa[6], M. Harada[7], S.Y. Zhang[8], Y.H. Su[9], T. Kamiyama[1], M. Ohnuma[1], M. Furusaka[1], T. Shinohara[6], and Y. Kiyanagi[2]

[1]Faculty of Engineering, Hokkaido University; [2]Graduate School of Engineering, Nagoya University; [3]Materials Sciences Research Center, JAEA; [4]Department of Mechanical Engineering, Toyohashi University of Technology; [5]Graduate School of Science and Engineering, Kagoshima University; [6]Neutron Science Section, Materials and Life Science Division, J-PARC Center; [7]Neutron Source Section, Materials and Life Science Division, J-PARC Center; [8]Neutron Science and Technology Center, CROSS; [9]Technology Development Section, Materials and Life Science Division, J-PARC Center

Stress Partitioning Behavior in Pearlitic Steels

1. Introduction

Pearlitic steels constitute a significant class of carbon steel because of their industrial applications, besides, their combined structure induces interesting mechanical properties. *In situ* neutron diffraction measurements during deformation have revealed the superposition of various kinds of internal stresses for pearlitic steels. Phase stress is accompanied by misfit plastic strains between the ferrite and cementite phases both for ferrite-cementite lamellar [1] or cementite-spheroidized specimens [2]. Furthermore, plastic flow in the individual ferrite grain depends on the crystallographic orientation, *hkl* plane, with regard to the tensile direction, as a result of the Schmid factor for the slip-system and strong elastic anisotropy of the BCC crystal. This is generally known as "intergranular stress" and should be referred to as "block stress" in pearlite. Therefore, phase and block stresses are superimposed in a plastically deformed ferrite matrix, and potentially in cementite. Recently, a neutron diffraction peak profile reveals a heterogeneous deformation induced peak asymmetry [3-5]. It is argued that the asymmetry is caused by stress partitioning among colonies.

2. Experimental procedures

The steel used in this study was created by induction heat melting in a vacuum, and the chemical compositions were 0.801C-0.01Mn-0.01Si-0.01P-0.01S (mass pct). The steels were austenitized at 1103 K for 3.6 ks in a vacuum and then isothermally held at 673 K or 748 K for 3.6 ks, in order to obtain full pearlite structures with different lamellar spacings. Dog-bone-shaped specimens, with a diameter of 3 mm and a gauge length of 30 mm, were prepared.

The *in situ* neutron diffraction measurements were performed using a high-intensity, high-resolution time-of-flight (TOF) neutron diffractometer, TAKUMI (BL19), at the Materials and Life Science Facility of the Japan Proton Accelerator Research Complex, J-PARC. A 20 kN tensile tester was mounted on the diffractometer in such a way that the loading axis was at a 45° angle to the incident beam. Therefore, the diffraction profiles for two scattering vectors in terms of the axial (tensile) and transverse directions were measured simultaneously by two detector banks set at ±90° against the incident beam. The specimens were deformed in tension at room temperature step-by-step in the elastic deformation region, and subsequently in a continuous manner in the elasto-plastic region, using a strain rate of 10^{-5} s^{-1}. The strain was measured and controlled using a strain gauge that was glued onto the specimen surface. The diffraction data were collected continuously using event-recording mode during tensile deformation and time-sliced with 0.9 ks intervals for analyses following measurement.

3. Results and discussion

As typical examples, ferrite 200 axial and transverse diffraction peaks are illustrated in Fig. 1(a). The diffraction peak profiles in the axial direction, obtained prior to deformation and subsequently deformed by 4.7% with an external tensile load, are compared in Fig. 1(a). We particularly focus on the evolution of the peak asymmetry.

In order to compare the profile shape more clearly, these two profiles are normalized to be of identical heights (see inserted figure). It shows that the broadening on the right-hand side is larger than that on the left in the deformed case, which indicates asymmetry. On the contrary, the diffraction profile of the deformed specimen in the transverse direction exhibits slightly larger broadening on the left-hand side; that is, the larger broadening side is opposite in the tensile and transverse directions. Such asymmetry becomes more obvious with increasing plastic deformation. It is argued that the peak asymmetry is caused by a distribution of lattice strain in different colonies. Therefore, the diffraction profiles were fitted according to double peaks with different lattice spacings. The results for the axial and transverse directions are presented in Fig. 1(b). The hard colony (HC) peak (blue curve) shifts towards wider lattice spacing, while the soft colony (SC) peak (green curve) is narrower, and the magnitude of SC is lower than that of HC in the axial direction. The strains of SC and HC (ε_{SC} and ε_{HC}) were determined using the following equations:

$$\varepsilon_{SC} = (d^{S}_{hkl} - d^{0}_{hkl}) / d^{0}_{hkl}$$

$$\varepsilon_{HC} = (d^{H}_{hkl} - d^{0}_{hkl}) / d^{0}_{hkl}$$

where d^{S}_{hkl}, d^{H}_{hkl}, and d^{0}_{hkl} refer to the *hkl* plane spacing for SC, HC, and stress-free, respectively. Here, ferrite 110, 200, and 211 diffraction peaks were employed for double peak fitting.

Figure 2(a) compares the SC and HC results for the coarse pearlite. Firstly, the strains increase linearly with an increase in macroscopic strain near the yielding point. Beyond yielding, colony strain of HC increases

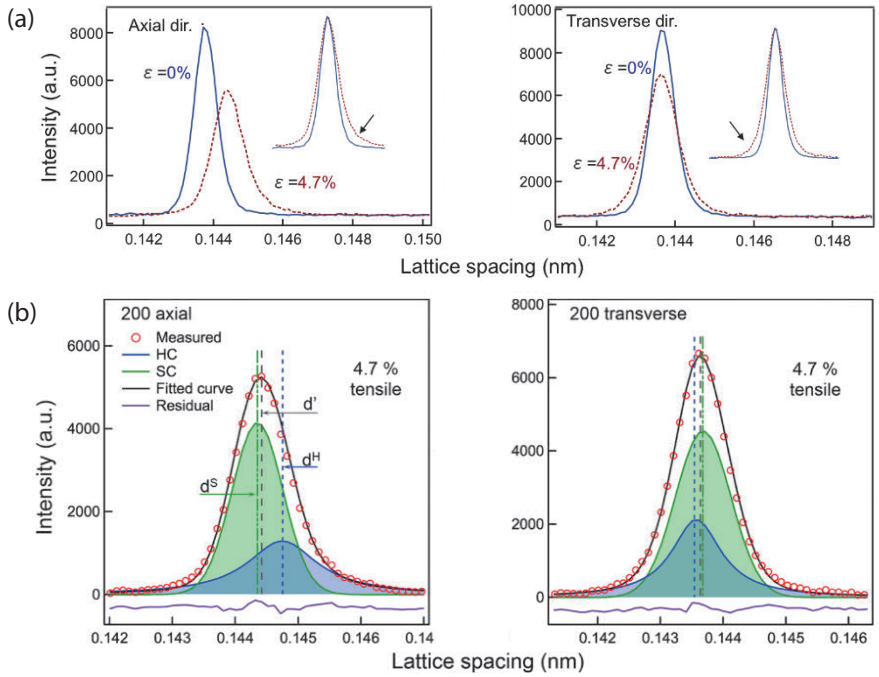

Figure 1. Examples of ferrite 200 diffraction peaks before and after deformation in axial and transverse directions (a). The double peaks corresponding to the SC and HC in the axial and transverse directions (b).

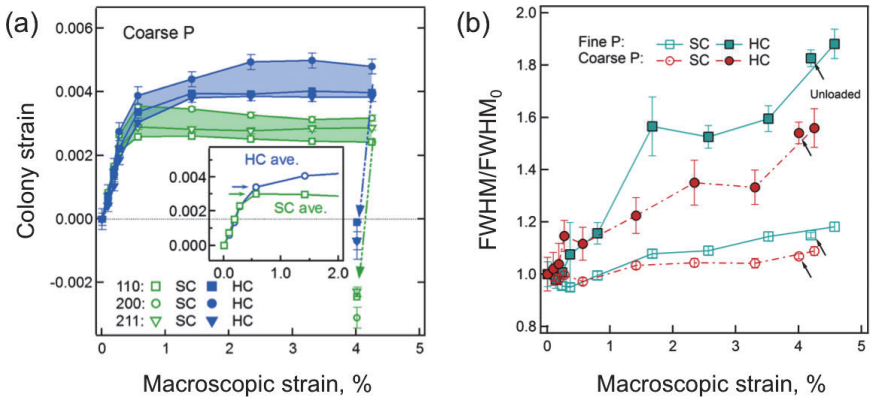

Figure 2. Stress partitioning between hard and soft colonies (a) and change of relative FWHM with tensile deformation (b). The embedded figure shows the average of the colony strain for 110, 200 and 211 reflections.

rapidly, but ceases to increase for the SC one, retaining *hkl* dependence. Hence, in addition to the stress partitioning of phase and intergranular stresses, colony stress is overlapped.

The relative full width at half maximum (FWHM) value, computed as the average of the FWHMs for 110, 200, and 211 reflections, is shown in Fig. 2(b). It can be seen that FWHM apparently increases in HC, but not in SC, after yielding. In this case, FWHM is believed to depend mainly on dislocation density. It is speculated that the pile-up of dislocations at the ferrite/cementite interface is affected by lamellar alignment: in the case of 45° in terms of the tensile direction (SC), the free path for dislocation movement is large, and hence work hardening must be low, due to poor accumulation and easy dislocation annihilation. Furthermore, the increment of dislocation density is larger in fine pearlite of HC constituent.

4. Conclusions

Colonies with different lamellar orientation exhibit different work hardening capability, which is determined by the asymmetry of the diffraction peaks and the lamellar spacing affects the stress partitioning of colony-unit deformation.

Acknowledgements

Neutron experiments were performed under proposal No. 2012P0102.

References

[1] Y. Tomota, P. Lukáš, D. Heov, S. Harjo, Y.R. Abe, Acta Mater., 51, 805-817 (2003).

[2] C. Zheng, L. Li, Y. Wang, W. Yang, Z. Sun, Mater. Sci. Eng. A, 631, 181-188 (2015).

[3] T. Ungár, S. Harjo, T. Kawasaki, Y. Tomota, G. Ribárik, Z. Shi, Metall. Mater. Trans. A, 48, 159-167 (2017).

[4] S. Harjo, T. Kawasaki, Y. Tomota, W. Gong, K. Aizawa, G. Tichy, T. Ungár, Metall. Mater. Trans. A, 48, 4080-4092 (2017).

[5] Y. Wang, T. Ohnuki, Y. Tomota, S. Harjo, T. Ohmura, Scripta Mater., 140, 45-49 (2017).

Y. Wang[1], T. Ohnuki[2], Y. Tomota[1], S. Harjo[3], and T. Ohmura[1]

[1]Research Center for Structure Material, National Institute for Materials Science; [2]Tokyo Metropolitan College of Industrial Technology; [3]Neutron Science Section, Materials and Life Science Division, J-PARC Center

Behavior of Hydrogen in the Early Stage of Earth's Evolution

1. Introduction

The current Earth's core consists mainly of iron alloy, and seismological observations have reported that the density of the outer core is ~10% lower than that of pure iron. This density deficit is explained by the dissolution of light elements, such as sulfur, silicone, oxygen, carbon, and hydrogen into the core, and experimental and simulation studies have clarified the chemical species and amounts of these light element(s). In particular, hydrogen, the most abundant element in the universe, is expected to significantly affect density deficit. However, there have been few studies focusing on hydrogen due to several experimental problems. First, the dissolution of hydrogen into iron is quite limited (ppm order) at ambient condition and it only occurs under high pressure above 3.5 GPa [1]. In conventional quench-experiments, it has been impossible to detect hydrogen, although the trace of included hydrogen was observed as many bubbles in the recovered sample [2]. Second, *in-situ* synchrotron X-ray diffraction observations [3-6] cannot detect the lightest element and several assumptions were needed for estimating the amount of dissolved hydrogen. In this study, we have conducted high-pressure and high-temperature *in-situ* neutron diffraction experiments using a multi-anvil apparatus with six independently acting 500-ton rams (ATSUHIME 6-axis press) [7] installed at "PLANET" beamline (BL11) [8], MLF, J-PARC.

2. Neutron diffraction observation using a newly developed anvil assembly

To reproduce the early stage of the Earth's formation, the experiments were conducted for the iron-hydrous mineral system. As a starting material, Fe rod (2.35 mmϕ × 2 mmh) and an equimolar powder mixture of SiO_2, $Mg(OD)_2$ (or MgO) were placed in a graphite capsule (3 mmϕ × 4.5 mmh) in the molar ratio of 2:1. This initial composition is a simple representation of the primordial materials of the Earth with/without water. We used a multi-anvil 6-6 type (MA6-6) assembly [9] newly developed for the neutron experiments to achieve large sample volume, stable pressure(*P*)-temperature(*T*) generation and intense diffraction signals. In all three experimental runs, the pressures were initially increased up to ~5 GPa, and then the temperatures were changed as shown in Fig. 1. Diffraction data were collected for ~10 hours in the *PT* region at ~4 GPa and ~700°C. The incident beam was truncated into almost the same size as iron for obtaining the diffraction patterns of iron alone. All the quenched samples were analyzed by X-ray diffraction (XRD) and scanning electron microscopy-energy dispersive X-ray spectroscopy (SEM-EDS).

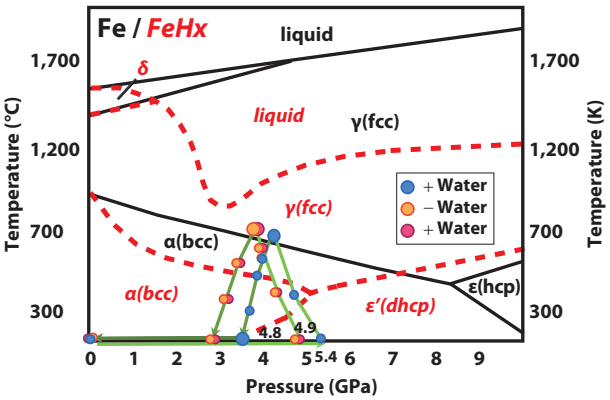

Figure 1. Phase diagrams of pure Fe (black, solid line) and FeH_x (red, dotted line) with the *PT* paths in the three experiments (with/without water). Phase boundaries are referred by [3-6]. The large and small circles represent the *PT* conditions at which quick and long measurements (~10 h) were made, respectively.

3. Results

Figure 2 shows the temperature dependence of diffraction patterns. In the sample including water, most of the peaks in the initial pattern were attributed to iron, while a few peaks of sample surrounding materials were observed due to the divergence of the incident beam. With increasing temperature, water was supplied to iron by dehydration of $Mg(OD)_2$ and the iron *bcc-fcc* phase transition was observed subsequently. On cooling after the long exposure at 725°C, the *bcc* iron appeared again. On the other hand, in the experimental run using MgO instead of $Mg(OD)_2$, the phase transition of pure iron was observed together with disappearance of MgO and appearance of olivine phases.

When comparing the time dependence of the unit cell volume of *fcc* iron between the experiments with and without water, a significant difference was observed (Fig. 3). The volume increased only in the sample including water, suggesting the dissolution of deuterium into iron. Here, we could not observe the shrinkage of the cell volume due to the formation of super abundant vacancy (SAV), which had been reported by Fukai et al. [4].

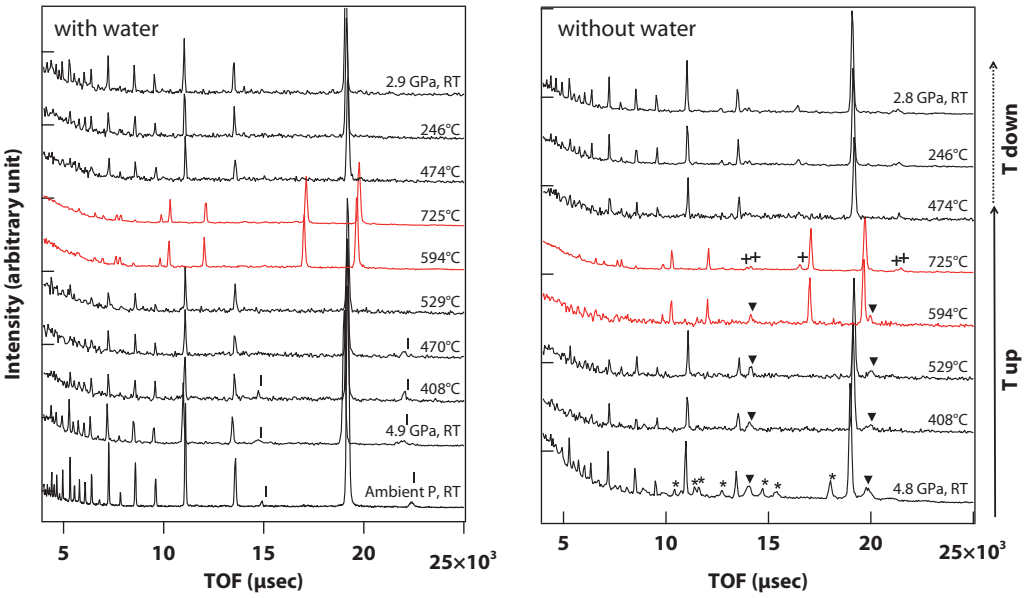

Figure 2. Temperature dependence of the diffraction profiles at ~4 GPa in the experiments with and without water. In both runs, iron *bcc* (black) -*fcc* (red) phase transformation occurred at ~600°C. In the run including water, $Mg(OD)_2$ (marked with vertical bars) disappeared due to dehydration at ~500°C. On the other hand, in the run without water, peaks of MgO (triangle) disappeared and then olivine (cross) appeared instead. A bottom profile in the run without water was obtained using a larger beam size to determine the lattice parameters of NaCl used as a pressure marker (asterisk).

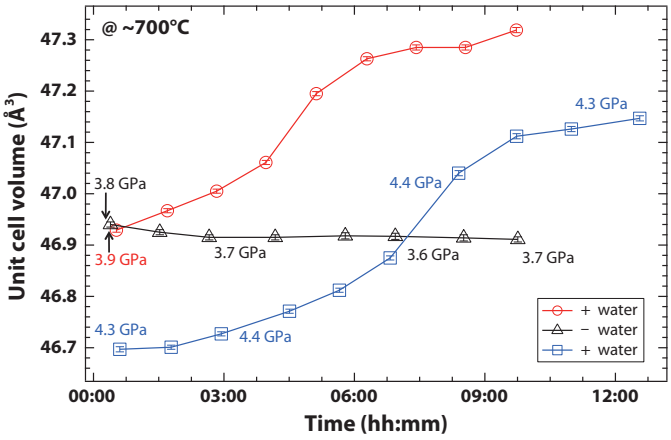

Figure 3. Time changes of unit cell volume of *fcc* iron while keeping at ~700°C in three runs. Each data plot was calculated using the data obtained every hour. Uncertainty of the volume was estimated from standard deviation of the lattice parameter refined by Rietveld analysis. Pressure variation was less than 0.05 GPa.

For the iron including hydrogen, the deuterium content *x* was determined to be 0.19 (~0.7 wt.%) by Rietveld refinement using an initial structure model of *fcc* iron hydride (FeD_x) with deuterium atoms occupying both tetrahedral and octahedral sites [10]. This value was small compared to previous neutron (2.24 wt.% at 6.3 GPa, 715°C for Fe-D_2 system [10]) and XRD studies (*x*~1). It might be due to the differences in the experimental conditions, such as lower-*PT*, sample capsule, starting materials, and the reaction speed related to the different formation process of FeD_x in the current iron-silicate-D_2O system. SEM analyses of the recovered samples supported this view (Fig. 4). In the recovered sample containing water, a thin FeO layer was observed on the surface of the iron rod, as well as many small vacant holes within it, probably due to the degassed hydrogen on the release of pressure. Besides, Fe-rich $(Fe, Mg)_2SiO_4$ olivines existed around the iron rod, whereas Fe-poor $(Fe, Mg)SiO_3$ pyroxene was located far from it. These results suggest that the reaction speed of hydrogenation of the iron rod is decreased by the existence of the FeO layer, which was formed in the redox reaction:

$$2Fe + H_2O \rightarrow FeO + FeH_x + (1-x/2)H_2\uparrow.$$

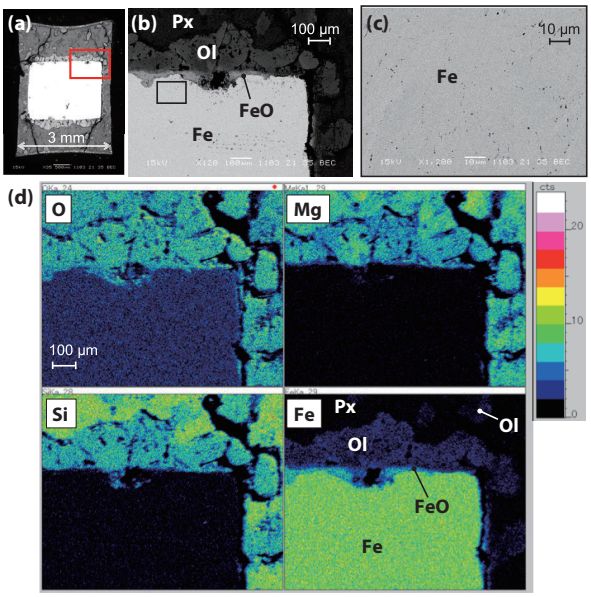

Figure 4. Results of SEM analysis of the recovered sample including water. (a-c) Electron images with different magnification, and (d) elemental maps on O, Mg, Si and Fe. The iron contained many small vacant holes as the evidence of degassed hydrogen on the release of pressure. The surface of an iron rod was covered with a thin layer of FeO. Two silicates of olivine (Ol) and pyroxene (Px) containing iron were found in the area initially occupied by the mixture of $Mg(OD)_2$ and SiO_2. Olivine with large Fe contents is preferentially located close to the iron rod.

4. Implication for Earth's evolution process

The results of our study indicate that hydrogen supplied from the hydrous minerals can dissolve into the solid iron at much lower temperatures than its melting point. This suggests that hydrogenation of iron could have inevitably occurred in the very early stage of the Earth's history before the primordial materials were molten with a magmatic ocean. Thus, other light elements might have been incorporated in the later process because they can dissolve only in the molten iron at much higher temperatures. In the end, it is likely that silicates (olivine and pyroxene) remained in the mantle, and iron including light elements sank and formed the core. To reveal the detailed process, further studies on the partitioning of the multi-light elements between silicates and iron hydride (not pure iron) are required. This study suggests the importance of the effects of hydrogen on the Earth's mantle-core formation. Our continuous research of the iron hydride-silicate-light elements system is now in progress.

References

[1] Y. Fukai, Nature 308, 174 (1984).
[2] T. Okuchi, Science 278, 1781–1784 (1997).
[3] V. E. Antonov, I. T. Belash, E. G. Ponyatovsky, Scr. Metal. 16, 203–208 (1982).
[4] Y. Fukai, K. Mori, H. Shinomiya, J. Alloys Compd. 348, 105–109 (2003).
[5] K. Sakamaki, E. Takahashi, Y. Nakajima, Y. Nishihara, K. Funakoshi, T. Suzuki, Y. Fukai, Phys. Earth Planet. Int. 174, 192 (2009).
[6] T. Yagi, T. Hishinuma, Geophys. Res. Lett. 22, 1933–1936 (1995).
[7] A. Sano-Furukawa, T. Hattori, H. Arima, A. Yamada, S. Tabata, M. Kondo, A. Nakamura, H. Kagi, T. Yagi, Rev. Sci. Instrum. 85, 113905 (2014).
[8] T. Hattori, A. Sano-Furukawa, H. Arima, K. Komatsu, A. Yamada, Y. Inamura, T. Nakatani, Y. Seto, T. Nagai, W. Utsumi, T. Iitaka, H. Kagi, Y. Katayama, T. Inoue, T. Otomo, K. Suzuya, T. Kamiyama, M. Arai, T. Yagi, Nucl. Instrum. Methods Phys. Res. A 780, 55–67 (2015).
[9] R. Iizuka-Oku, T. Yagi, H. Gotou, T. Okuchi, T. Hattori, A. Sano-Furukawa, Nature Commun. 8, 14096 (2017).
[10] A. Machida, H. Saitoh, H. Sugimoto, T. Hattori, A. Sano-Furukawa, N. Endo, Y. Katayama, R. Iizuka, T. Sato, M. Matsuo, S. Orimo, K. Aoki, Nature Commun. 5, 5063 (2014).

R. Iizuka-Oku[1], T. Yagi[1], H. Gotou[2], T. Okuchi[3], T. Hattori[4], and A. Sano-Furukawa[4]
[1]Geochemical Research Center, Graduate School of Science, The University of Tokyo; [2]Institute for Solid State Physics, The University of Tokyo; [3]Institute for Planetary Materials, Okayama University; [4]Neutron Science Section, Materials and Life Science Division, J-PARC Center, Japan Atomic Energy Agency

The Effect of Planar Rattling on Lattice Thermal Conductivity in $LaOBiS_{2-x}Se_x$

1. Introduction

Thermoelectric materials have attracted great attention in the field of energy conservation technology as they can convert heat directly into electric power. To realize the technology, further improvement of the thermoelectric performance is required. Thermoelectric properties can be described by the dimensionless figure-of-merit (ZT) defined as $ZT = S^2T/\rho\kappa$ where S is the Seebeck coefficient, ρ is the electrical resistivity and κ is the total thermal conductivity. To achieve high thermoelectric performance, good electric conductivity and poor thermal conductivity are required simultaneously. This conflicting condition can be realized, for example, by large vibration of atoms, the so-called, rattling. Rattling occurs in oversized cage compounds such as clathrates and filled skutterudites.

Recently, we found out that rattling occurs also in compounds without oversized cages. $LaOBiS_{2-x}Se_x$ exhibits extremely low lattice thermal conductivity with value of about 1 W/mK around room temperature [1], which is lower than that of vitreous silica. The extremely low lattice thermal conductivity positions $LaOBiS_{2-x}Se_x$ as a promising thermoelectric material with the ZT value of 0.36 at $T = 650$ K. Crystal structure refinements revealed that Bi atoms located at the center of basal plane of BiS_5-pyramid vibrate largely along c-axis [2]. We defined this as planar rattling to distinguish it from the rattling in oversized cages. To clarify the dynamics of planar rattling and the mechanism of suppressing lattice dynamics with planar rattling, we studied phonons of $LaOBiS_{2-x}Se_x$ using inelastic neutron scattering [3].

2. Experimental details

Polycrystalline samples of $LaOBiS_{2-x}Se_x$ (x = 0, 0.2, 0.4, 0.6, 0.8, and 1) were synthesized by solid-state reactions. Inelastic neutron scattering measurements were conducted using AMATERAS. The incident neutron energy was $E_i = 10.5$ meV. The energy resolution at elastic scattering was 0.69 meV. The temperature was $T = 300$ K. The data were processed using the Utsusemi visualization software. Phonon calculations based on density-functional theory and plane-wave basis set were performed to identify the phonon modes.

3. Results and discussion

Figure 1 shows contour maps of the scattering intensity of $LaOBiS_2$ at $T = 300$ K. The observed intensity is well reproduced by phonon calculations. Acoustic and optical phonon modes with steep and flat dispersions were observed, respectively. Phonon calculations revealed that the optical phonon modes around $E = 6$ meV were associated dominantly with large vibration of Bi atoms. To clarify the Se doping dependences of the Bi rattling modes, the contour map was sliced in the Q range of 2.75 – 2.85 A^{-1}. The energy spectra demonstrate that well-defined optical phonon peaks soften with Se doping (Fig. 2). This suggests that anharmonicity is enhanced with the doping. According to crystal structure refinements, Se doping induces in-plane chemical pressure to Bi atoms [2]. That is, the chemical pressure can enhance the Bi rattling. This is in contrast with the rattling in oversized cage compounds, where larger free space enhances the rattling motions [4-8].

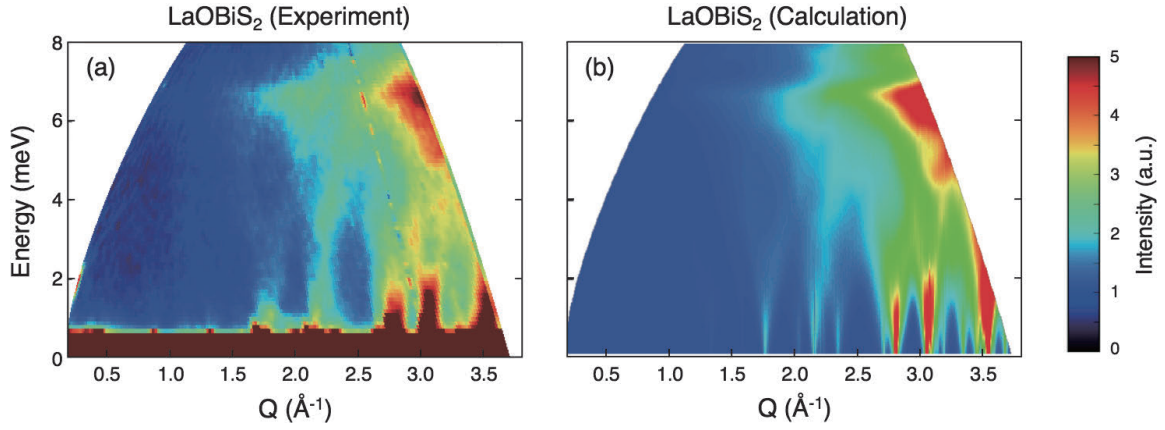

Figure 1. Contour maps of the scattering intensity of $LaOBiS_2$ at $T = 300$ K. (a) Observed map. (b) *ab initio* calculation convoluted with instrumental energy resolution. Reproduced from [3], with the permission of AIP Publishing.

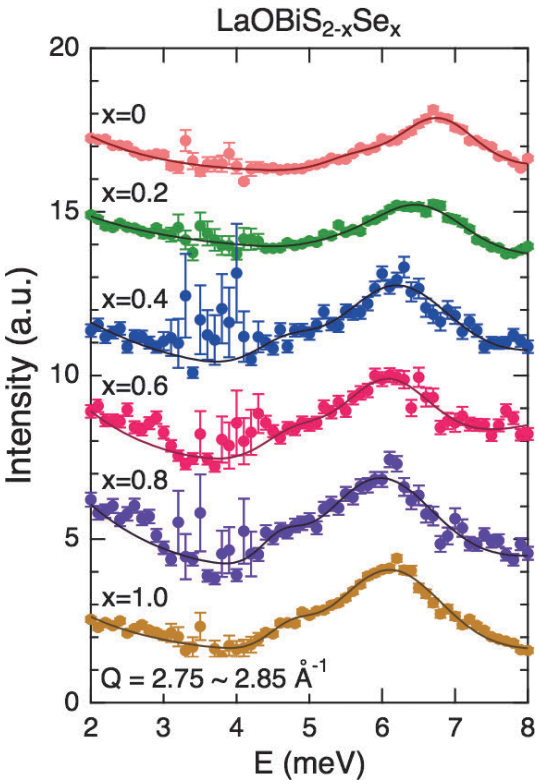

Figure 2. Se doping dependence of energy spectra of phonons at T = 300 K in the Q range of 2.75 to 2.85 A^{-1} for $LaOBiS_{2-x}Se_x$. Solid lines are Gaussian fits. Reproduced from [3], with the permission of AIP Publishing.

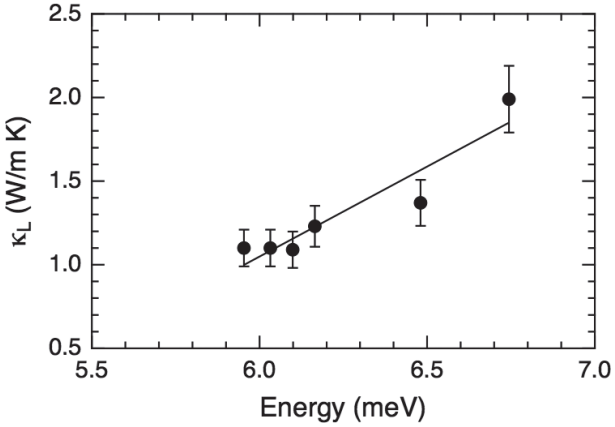

Figure 3. Bi rattling mode energy vs. lattice thermal conductivity at T = 300 K for $LaOBiS_{2-x}Se_x$. Reproduced from [3], with the permission of AIP Publishing.

Figure 3 shows rattling energy vs. lattice thermal conductivity (κ_L). The rattling energy softens linearly with decreasing κ_L, demonstrating that κ_L is suppressed by the Bi rattling modes. The results indicate that planar rattling is an essential factor for suppressing κ_L as rattling in oversized cage compounds.

4. Summary

We studied the phonon dynamics of $LaOBiS_{2-x}Se_x$, which exhibits extremely low κ_L. We observed that Bi planar rattling modes soften with decreasing κ_L, suggesting that the rattling modes are responsible for the low κ_L. In-plane chemical pressure enhances the planar rattling, in contrast with that in oversized cage compounds, where free space is essential.

References

[1] A. Nishida, O. Miura, C. H. Lee, and Y. Mizuguchi, Appl. Phys. Express 8, 111801 (2015).
[2] Y. Mizuguchi, A. Miura, A. Nishida, O. Miura, K. Tadanaga, N. Kumada, C. H. Lee, E. Magome, C. Moriyoshi, and Y. Kuroiwa, J. Appl. Phys. 119, 155103 (2016).
[3] C. H. Lee, A. Nishida, T. Hasegawa, H. Nishiate, H. Kunioka, S. Ohira-Kawamura, M. Nakamura, K. Nakajima, and Y. Mizuguchi, Appl. Phys. Lett. 112, 023903 (2018).
[4] K. Suekuni, M. A. Avila, K. Umeo, H. Fukuoka, S. Yamanaka, T. Nakagawa, and T. Takabatake, Phys. Rev. B 77, 235119 (2008).
[5] Y. Takasu, T. Hasegawa, N. Ogita, M. Udagawa, M. A. Avila, K. Suekuni, I. Ishii, T. Suzuki, and T. Takabatake, Phys. Rev. B 74, 174303 (2006).
[6] C. H. Lee, H. Yoshizawa, M. A. Avila, I. Hase, K. Kihou, and T. Takabatake, J. Phys.: Conf. Ser. 92, 012169 (2007).
[7] C. H. Lee, H. Yoshizawa, M. A. Avila, I. Hase, K. Kihou, and T. Takabatake, J. Phys. Soc. Jpn. 77, 260 (2008) Suppl. A.
[8] C. H. Lee, I. Hase, H. Sugawara, H. Yoshizawa, and H. Sato, J. Phys. Soc. Jpn. 75, 123602 (2006).

C. H. Lee[1], A. Nishida[2], T. Hasegawa[3], H. Nishiate[1], H. Kunioka[1], S. Ohira-Kawamura[4], M. Nakamura[4], K. Nakajima[4], and Y. Mizuguchi[2]
[1]National Institute of Advanced Industrial Science and Technology (AIST); [2]Graduate School of Science and Engineering, Tokyo Metropolitan University; [3]Graduate School of Integrated Arts and Sciences, Hiroshima University; [4]Neutron Science Section, Materials and Life Science Division, J-PARC Center

Vibrational States of Atomic Hydrogen in Bulk and Nanocrystalline Palladium

1. Introduction

The behavior of hydrogen in metals has attracted significant attention in fundamental and applied research areas. Palladium hydride (PdH_x; $x < 1$) is a typical metal-hydrogen system, which had been intensively studied for many decades. Pd has remarkable abilities to absorb plenty of hydrogen and to catalyze a broad range of chemical reactions. Metal nanoparticles are of current interest owing to their unique properties as compared with bulk materials. It has been demonstrated that the H absorption property of Pd nanoparticles is markedly different from that of bulk Pd and strongly depends on their size, shape, and surface structure. A key issue in metal hydride nanoparticles is to clarify the thermodynamic state and structure of the subsurface (a few layers below the surface), which are closely connected with the H absorption ability and the high catalytic performance.

We have investigated the structure [1] and diffusion [2] of hydrogen atoms by means of neutron scattering techniques for both bulk and nanocrystalline PdH_x/PdD_x. Neutron diffraction (ND) data of nanocrystalline $PdD_{0.36}$ (nano-$PdD_{0.36}$), taken on NOVA at MLF, suggested that hydrogen atoms were accommodated both at the octahedral (O) sites (1/2, 1/2, 1/2) and the tetrahedral (T) sites (1/4, 1/4, 1/4) in the face-centered cubic (fcc) lattice of Pd (see Fig. 1). This is in contrast to bulk $PdH_{0.7}$ with the occupation of only O sites [1]. It was also reported by our quasielastic neutron scattering (QENS) study that an additional fast diffusion process of the H atoms appeared in nano-$PdH_{0.47}$ [2]. It indicates that the H atoms diffuse faster near the surface, probably via the T sites. In this work, vibrational states of H atoms in bulk and nano-PdH_x were examined in a wide energy region $0 \leq \hbar\omega \leq 300$ meV by inelastic neutron scattering (INS), to gain insight into the shape of a potential well around the H sites [3].

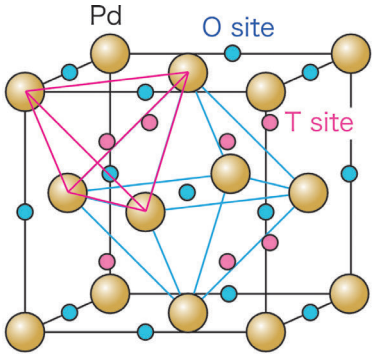

Figure 1. Interstitial hydrogen sites in an fcc Pd lattice: octahedral (O) and tetrahedral (T) sites.

2. Experiment

High-quality Pd nanocrystals with a narrow size distribution (8.0 ± 0.9 nm) were used in this work. They were basically the same as those in previous studies [1-2]. The INS spectra of bulk $PdH_{0.73}$, nano-Pd, and nano-$PdH_{0.42}$ were recorded at 10 K using a time-of-flight Fermi chopper spectrometer, 4SEASONS. The frequency of the Fermi chopper was set to 600 Hz and the phase was configured to select an E_i set of 942, 331, and 168 meV.

3. Results and discussion

Figure 2 shows the INS spectra of bulk $PdH_{0.73}$ and nano-$PdH_{0.42}$ at $Q \approx 10$ Å^{-1} and $T = 10$ K, taken with E_i of 331 meV. In bulk $PdH_{0.73}$, multiphonon processes up to 4th order ($n = 4$) are clearly visible. The excitation energy and intensity against n, estimated by multi-peak fitting, are roughly described by the quantum harmonic oscillator (QHO) model. In the model, the excitation energy is given by $n(\hbar\omega_0)$ and the fundamental energy $\hbar\omega_0$ is estimated to be 68 meV.

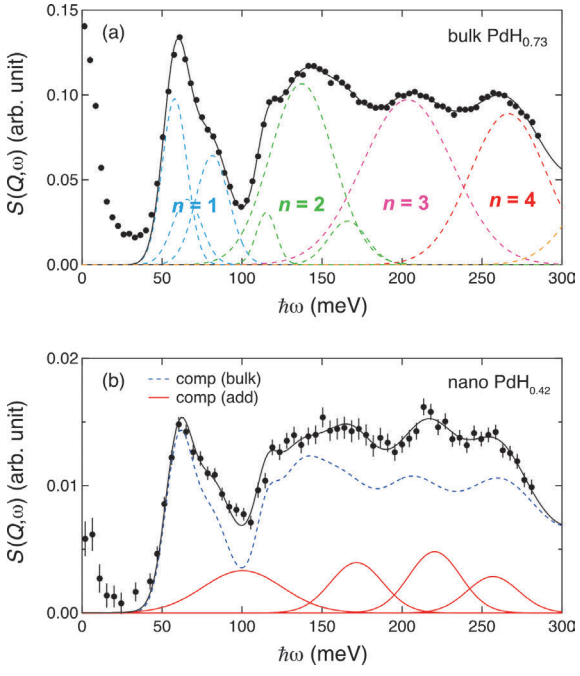

Figure 2. Inelastic neutron scattering spectra of (a) bulk $PdH_{0.73}$ and (b) nano-$PdH_{0.42}$ at 10 K.

The INS spectrum of nano-$PdH_{0.42}$ is different from that of $PdH_{0.73}$. We have analyzed the spectrum with the combination of the spectrum of bulk $PdH_{0.73}$ and the additional excitations, because the previous ND and QENS works suggest that most H atoms (70 – 80%) occupy the O sites and their behavior resembles the one observed in bulk. The additional excitations were found at energies above 80 meV (Fig. 2(b)). The energies and intensities of the additional states were not explained by the QHO model but were reasonably described as vibrations in a highly anharmonic trumpet-like potential (Fig. 3). The estimated $\hbar\omega_0$ was 122 meV that was significantly larger than that of bulk $PdH_{0.73}$. Such a remarkable change in $\hbar\omega_0$ cannot be explained by the small change in the lattice constant. In fact, the vibrational energy for the T site with the short H-Pd distance is expected to be higher than that for the O site. Therefore, it is reasonable to conclude that the additional vibrations are attributed to the H vibrations in the T sites near the surface of nanocrystals.

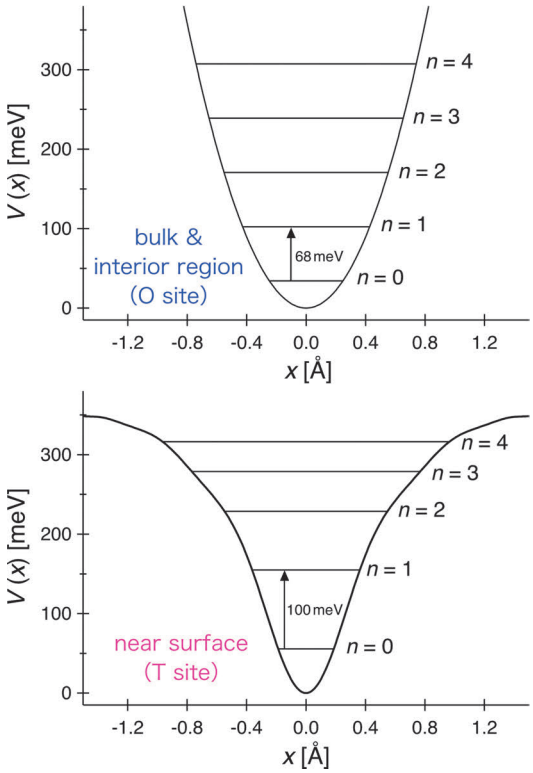

Figure 3. Potential energy as a function of the atomic displacements relative to the equilibrium position of the H atom.

4. Conclusion

We investigated the vibrational spectra of hydrogen atoms in bulk and nanocrystalline Pd. The H vibrations in bulk $PdH_{0.73}$ are roughly described by the QHO model. In $PdH_{0.42}$ nanocrystals, the excess excitations were found at higher energies in addition to the excitations, which resemble those observed in bulk $PdH_{0.73}$. The excess excitations are attributed to the hydrogen vibrations in a highly anharmonic trumpet-like potential, which is realized at the T sites in the near-surface region where the potential energy is substantially modified by surface strain/distortion effects.

Finally, our ND [1], QENS [2], and INS [3] works provided self-consistent results and would be the first comprehensive neutron scattering studies to gain insight into the behavior of H atoms in metal nanoparticles. Our findings can provide important information in a wide range of research fields, including hydrogen storage, surface science, and catalytic chemistry.

References

[1] H. Akiba, M. Kofu. H. Kobayashi, H. Kitagawa, K. Ikeda, T. Otomo and O. Yamamuro, J. Am. Chem. Soc., 138 10238 (2016); MLF Annual Report 2016, 11-12 (2016).

[2] M. Kofu, N. Hashimoto, H. Akiba, H. Kobayashi, H. Kitagawa, M. Tyagi, A. Faraone, J. R. D. Copley, W. Lohstroh and O. Yamamuro, Phys. Rev. B, 94 064303 (2016).

[3] M. Kofu, N. Hashimoto, H. Akiba, H. Kobayashi, H. Kitagawa, K. Iida, M. Nakamura and O. Yamamuro, Phys. Rev. B, 96 054304 (2017).

M. Kofu[1], N. Hashimoto[1], H. Akiba[1], H. Kobayashi[2], H. Kitagawa[2], K. Iida[3], M. Nakamura[4], and O. Yamamuro[1]

[1]Institute for Solid State Physics, University of Tokyo; [2]Department of Chemistry, Kyoto University; [3]Neutron Science and Technology Center, CROSS; [4]Neutron Science Section, Materials and Life Science Division, J-PARC Center

Dynamics of a Disease-causing Mutant of Troponin Studied by Quasielastic Neutron Scattering

1. Introduction

In the cardiac muscle, force generation is regulated in a Ca^{2+}-dependent manner by the protein, troponin (Tn), consisting of three subunits, TnC, TnI, and TnT. The main regulatory part of Tn is called the Tn core domain (Tn-CD), which consists of TnC, TnI, and TnT2 ($TnT_{183\text{-}288}$) (Fig. 1). Upon Ca^{2+}-binding to TnC, a series of structural changes occur within Tn, thereby transmitting the Ca^{2+}-binding signal to the other regulatory protein, tropomyosin (Tm). These Ca^{2+}-induced changes then allow interactions between actin and myosin, leading to force generation.

To date, more than 70 mutations in Tn are identified as causes of familial hypertrophic cardiomyopathy (HCM), which is associated with heart failure and/or sudden cardiac death [1]. These mutations modulate Ca^{2+}-sensitivity of force generation and/or the maximum force. While these mutation-induced functional aberrations have been widely studied, their detailed molecular mechanisms are poorly understood. Since the structural dynamics of Tn is crucial for the regulatory function [2], it is important to reveal the dynamics changes of Tn caused by these mutations.

While the time scale of the structural dynamics of proteins spans more than ten orders of magnitude from femtosecond vibrational modes to millisecond domain motions, picosecond dynamics serves as a lubricant for slower structural changes and thus an essential process for expressing protein function [3].

Quasielastic neutron scattering (QENS) is a powerful tool to study the picosecond dynamics of proteins. Due to large incoherent scattering cross-section, motions of hydrogen atoms are observed. Since hydrogen atoms are distributed quasi-uniformly in proteins, atomic motions averaged over a whole molecule are detected by QENS. In this study, we investigated how the dynamics of Tn is modulated by a HCM-causing mutation K247R of TnT, which increases the maximum force without changing the Ca^{2+}-sensitivity, using QENS [4].

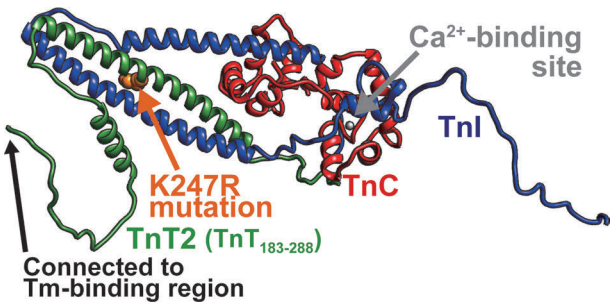

Figure 1. Structure of the human cardiac Tn core domain (Tn-CD). TnC, TnI, and TnT2 are shown in red, blue, green, respectively. The mutation site is represented by orange spheres. A Ca^{2+} ion bound to TnC is shown in a grey sphere.

2. Materials and Methods

The subunits of the human cardiac Tn-CD, expressed in *E. coli*, were purified, and reconstituted into the Tn-CD complexes containing the wild-type TnT2 (wtTn-CD) or the mutant of TnT2 (mtTn-CD). The D_2O-solutions of the wtTn-CD and mtTn-CD were prepared at ~20 mg/ml in both the $-Ca^{2+}$ and $+Ca^{2+}$ states. The QENS measurements were carried out using the BL02 near-backscattering spectrometer DNA at an energy resolution of 12 μeV at 300 K.

3. Results and Discussion

The measured QENS spectra $S(Q, \omega)$ (Q and ω are momentum transfer and energy transfer, respectively) were fit by the following equation:

$$S(Q,\omega) = [A(Q)\delta(\omega) + \{1 - A(Q)\}L_{local}(Q,\omega)] \otimes L_{global}(Q,\omega) \otimes R(Q,\omega) + B(Q), \quad (1)$$

where $A(Q)\delta(\omega)$ is the elastic component with $A(Q)$ being the elastic incoherent structure factor (EISF), from which amplitudes of local atomic motions are obtained, and $\delta(\omega)$ being the Dirac delta-function. $L_{local}(Q, \omega)$ and $L_{global}(Q, \omega)$ are the Lorentzian functions describing the local motions and the global diffusive motions of protein molecules, respectively. From the Q^2-dependence of the widths of $L_{global}(Q, \omega)$ and $L_{local}(Q, \omega)$, the apparent diffusion coefficient including translational and rotational motions of the entire molecules, and the residence time of local motions are obtained. $R(Q, \omega)$ denotes the instrumental resolution function and $B(Q)$ denotes the background.

Figure 2 shows an example of the measured spectra with the results of the fit using Eq. 1. The dynamics parameters obtained from these fits are summarized in Fig. 3. While there was no change in the apparent diffusion coefficients by either Ca^{2+}-binding or the mutation (data not shown), dynamics changes were observed for

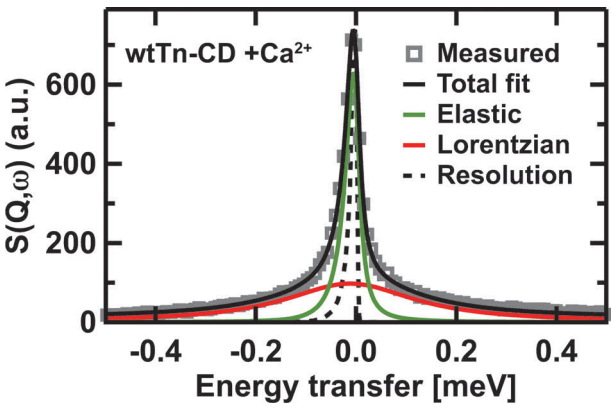

Figure 2. Examples of the QENS spectra. Those of the wtTn-CD in the $+Ca^{2+}$ state at Q = 1.375 [$Å^{-1}$] are shown. The measured data points are denoted by the grey open squares. The total fit, the elastic component, and the Lorentzian component are denoted by black, green and red solid lines, respectively. The resolution function is shown in black broken lines.

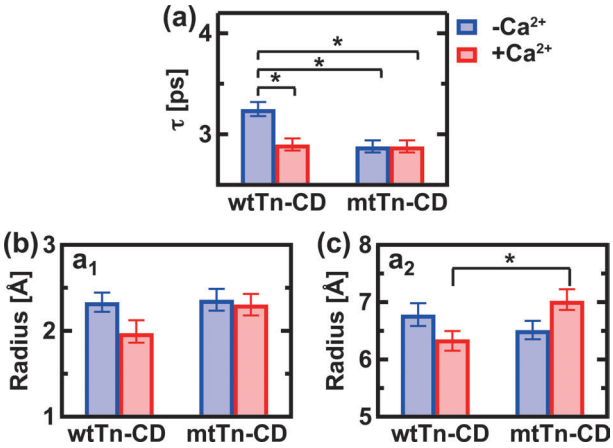

Figure 3. Summary of the dynamics parameters. (a) Residence times obtained from the QENS spectra. (b, c) Amplitudes of local atomic motions in the Tn-CD obtained from the EISF analysis. Asterisks show statistically significant differences at 95% confidence level by the Student's t-test.

local motions. In the case of the wtTn-CD, the residence time decreased upon Ca^{2+}-binding, suggesting that the frequency of the local motions increases by Ca^{2+}-binding (Fig. 3 (a)). On the other hand, the residence time of the mtTn-CD in the $-Ca^{2+}$ state was smaller than that of the wtTn-CD in the corresponding state and did not show any change upon Ca^{2+}-binding. This increased frequency of local motions caused by the mutation suggests that the Tn-CD molecules are destabilized by the disruption of hydrogen bond network around the mutation site.

Figure 3 (b, c) show the amplitudes of local motions obtained from the EISF analysis. Here, two kinds of populations of atoms moving inside spheres of radii of a_1 and a_2 were assumed. Both amplitudes of the wtTn-CD showed a decrease upon Ca^{2+}-binding. The amplitudes of the mtTn-CD in the $-Ca^{2+}$ state were similar to those of the wtTn-CD in the corresponding state. Upon Ca^{2+}-binding, however, the amplitudes of the mtTn-CD increased and as a result they exceeded those of the wtTn-CD. This suggests that the atoms of the mtTn-CD can explore larger conformational space than those of the wtTn-CD. Since the functional aberration is observed in the $+Ca^{2+}$ state, these larger amplitudes should be related to the pathogenesis of HCM.

We have previously shown that the main effect of the K247R mutation on Tn structure is in the orientation of $TnT_{183-225}$ region, which is connected to the Tm-binding region [5]. The large fluctuations of the mtTn-CD in the $+Ca^{2+}$ state detected here imply that the conformation of the mtTn-CD with the altered orientation of $TnT_{183-225}$ is unstable and thus Tn-Tm interactions are disturbed by the mutation. Since Tn-Tm interactions are crucial for the regulation of force generation, the disturbance of these interactions would modulate their abilities to control interactions between actin and myosin, leading to an increase in maximum force as observed for the K247R mutation. The present study has demonstrated that the dynamics of the Tn-CD is altered by Ca^{2+}-binding and a disease-causing mutation, emphasizing the importance of picosecond protein dynamics in both healthy and pathological conditions.

References

[1] Q.W. Lu et al., J. Geriatr. Cardiol., 10 91-101 (2013).
[2] A. Metskas & E. Rhoades, J. Mol. Biol., 428 2965-2977 (2016).
[3] G. Zaccai. Science, 288 1604-1607 (2000).
[4] T. Matsuo et al., Biochim. Biophys. Acta., 1865 1781-1789 (2017).
[5] T. Matsuo et al., Biophys. Physicobiol., 12 145-158 (2015).

T. Matsuo[1], T. Tominaga[2], F. Kono[1], K. Shibata[3], and S. Fujiwara[1]
[1]Quantum Beam Science Research Directorate, QST; [2]Neutron Science and Technology Center, CROSS; [3]Neutron Science Section, Materials and Life Science Division, J-PARC Center

Quasielastic Neutron Scattering Study of Microscopic Dynamics in Co-Crosslinked Rubber

1. Introduction

Rubber materials utilized in various industrial products are indispensable in the industries and our daily life. Fillers or functional agents are used to enhance the properties of pure rubber, such as mechanical strength, abrasion resistance, and deterioration resistance. Mechanical properties of rubber materials can be enhanced by an addition of crosslinking agents or reinforcing fillers, such as carbon black, silica, or clay [1]. The mechanical strength of polybutadiene rubber (BR) reinforced with zinc diacrylate (ZDA) (ZDA/BR) is known to be considerably higher than that of the typical carbon black or silica reinforced rubber [2]. Among them, the mechanism underlying the high mechanical strength attained using ZDA remains unknown despite the extensive studies. It has been conjectured that the failure to elucidate the reinforcement mechanism in ZDA/BR originates mainly from the lack of detailed information about both its static and dynamic structures. To overcome this shortcoming, first, we studied the structure of ZDA/BR through the complementary use of small-angle X-ray scattering (SAXS) and small-angle neutron scattering (SANS) techniques [3, 4]. In addition to the hierarchical structures of the ZDA aggregates and BR matrix, a hierarchical BR structure possessing a higher crosslinking density (HC-BR) than that of the BR matrix was observed for ZDA/BR. Furthermore, it was expected that such HC-BR region was mainly segregated on the surface of the ZDA aggregates.

In this work, we try to study the effect of concentration of reinforcing material (ZDA) on dynamics of ZDA/BR, which exhibit high mechanical strength through quasielastic neutron scattering (QENS). At present, the research of the concentration dependency of the reinforcing agent has been insufficient, due to various controlling parameters. Hence, tuning the concentration of the reinforcing agent, which depends on the specific fields where the BR product is used, is vital for its industrial application.

2. Experimental

We prepared a mixture of BR, ZDA, and dicumyl peroxide (DCP) as samples. ZDA monomer possesses carbon-carbon double bond (C=C) at its both ends. Firstly, the ZDA monomer was grafted to BR by reacting one C=C to BR, then ZDA aggregates with the size of several nm were subsequently formed by chain transfer reaction between the ZDA monomers. Secondly, the crosslinking of BR proceeded through further chemical reaction between other C=C end of ZDA and BR. DCP was used as an initiator for crosslinking reaction. Samples consisted of 0, 2.7, 5.3, 10.1, and 14.4 volume % of ZDA were named ZDA(0), ZDA(3), ZDA(5), ZDA(10), and ZDA(14), respectively. Figure 1 shows the relationship between the elastic modulus obtained by dynamic viscoelasticity measurements and the volume fraction of ZDA at 303 K. The elastic modulus increases dramatically above the volume fraction of 0.05. For clarity, we also added a solid line, which only holds for low ZDA contents in Fig. 1.

QENS measurements were carried out with an inverted geometry time-of-flight spectrometer (BL02 DNA) [5], installed at the Materials and Life Science Experimental Facility (MLF) in J-PARC, Tokai, Japan. The energy resolution (δE) defined as the full width at half maximum (FWHM) was estimated to be 4.0 ± 0.2 μeV for an elastic scattering spectrum measured at lowest temperature. The scattering contribution of each component was estimated based on the scattering cross section. For ZDA(14), which contained the highest volume fraction of ZDA among the investigated samples, the proportions of the total scattering cross-sections of BR, ZDA, and DCP were estimated to be 94.7:5.0:0.3. The large scattering contribution of BR were mainly due to the large incoherent scattering cross section of hydrogen atoms. Thus, the observable scattering intensity for ZDA/BR in this QENS study, would be dominated by the BR.

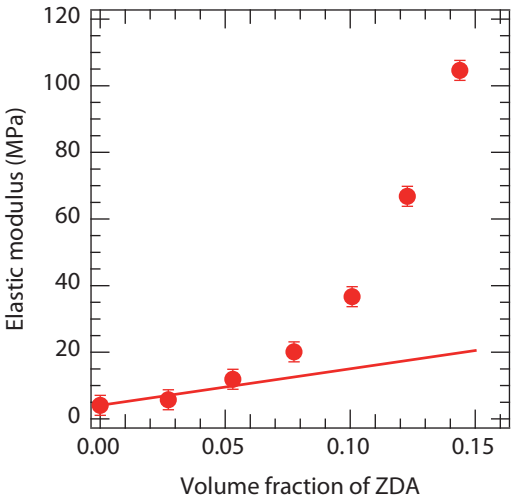

Figure 1. Relationship between the elastic modulus and volume fractions of zinc diacrylate (ZDA) [8].

3. Results and discussion

Figure 2 shows the dynamic scattering laws $S(Q, \omega)$ normalized by the peak intensity of the elastic scattering from different ZDA volume fractions at 310 K in the range of the scattering vector $Q = 1.48$ Å^{-1}. The increase in ZDA volume fraction, a narrowing of the $S(Q, \omega)$ is observed. To extract the parameters describing dynamical information from the $S(Q, \omega)$, we performed curve fitting to the observed $S(Q, \omega)$ at different ZDA volume fractions using an appropriate model function described by the Kohlrausch-Williams-Watts (KWW) equation [6].

$$S(Q, \omega) = A((1 - ecf)\ \mathcal{F}\{\exp[-(t/\tau)^{\beta}]\} + ecf\delta(\omega) \otimes R(Q, \omega) \quad (1)$$

where A, ecf, τ, and β are the amplitude of the relaxation function, the elastic component fraction, the relaxation time, and the distribution of the relaxation function, respectively. KWW function is defined in the time domain, necessitating that we adopt the Fourier-transformed KWW function ($\mathcal{F}$(KWW)) in the frequency region [7]. $R(Q, \omega)$ indicates the instrumental resolution function. In Fig. 3(a), the elastic fraction ecf increases with the ZDA volume fraction, suggesting that the elastic fraction mainly originates from the immobile region mediated by the cross links formed by the addition of ZDA. In addition, the deviation from the linear dependence of ecf above the volume fraction of ZDA of 0.05 was seen. Qualitatively, this tendency corresponds to that of the elastic modulus as seen in Fig. 1, indicating that the high ecf value observed at high ZDA content was related to high mechanical strength. As seen in Fig. 3(b), the average relaxation time $\langle\tau\rangle$ increases with the volume fraction of ZDA. At the same time, the parameter β, which represents the width of the distribution of relaxation time, decreases with increasing the ZDA volume fraction, implying the broadening of the distribution of relaxation time. In other words, the samples become dynamically heterogeneous with the increment of ZDA volume fraction.

To construct a plausible physical picture that could explain consistently the evaluated parameters, we referred to the structural information revealed in our previous work on SAXS and SANS [3, 4]. From small-angle scattering studies, the coexistence of BR regions having low and high crosslinking densities was revealed. In the above discussion on $S(Q, \omega)$, we used the mobile

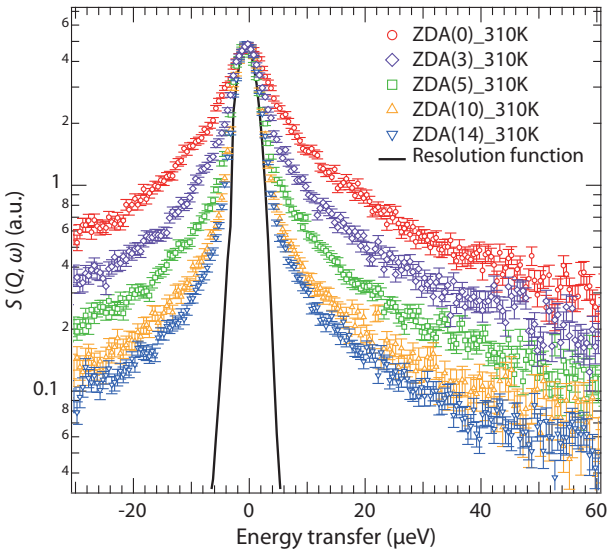

Figure 2. Dynamic scattering laws $S(Q, \omega)$ for ZDA(0) (○), ZDA(3) (◇), ZDA(5) (□), ZDA(10) (△) and ZDA(14) (▽) normalized at the peak top at 310 K in the range Q = 1.48 Å^{-1}. The line indicates the instrumental resolution function [8].

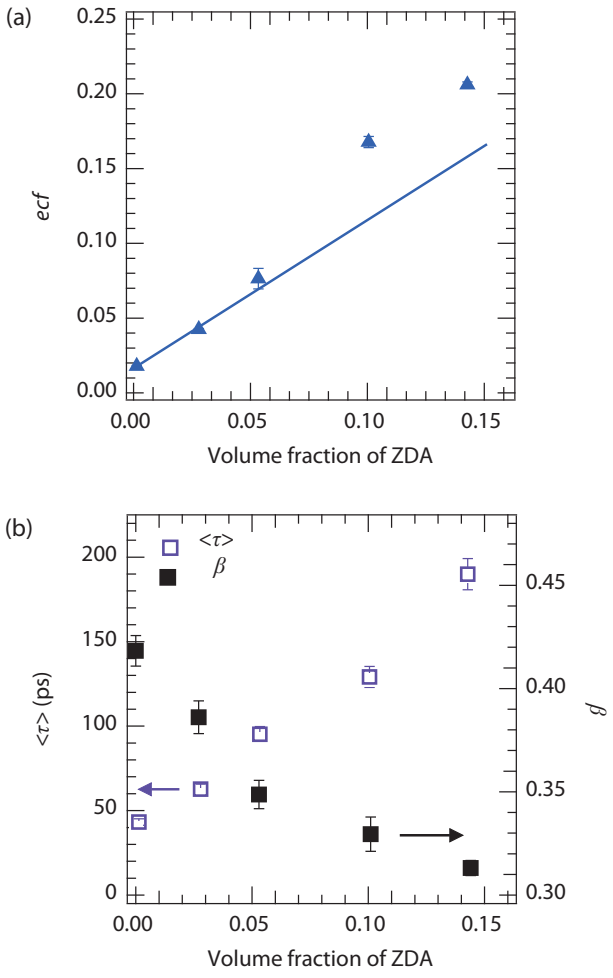

Figure 3. The volume fraction of ZDA dependence of (a) ecf (▲), (b) $\langle\tau\rangle$ (□) and β (■) at 310 K in the range Q = 1.48 Å^{-1} [8].

region and the immobile region for the low crosslinking density region and the highly crosslinked region, respectively. Based on this assumption, we reasoned that the mobile region originates from the low crosslinking density region (LC-BR) and the immobile region originates mainly from the high crosslinking density one (HC-BR), which is still in a glassy state in the present temperature range. As an increase in the elastic fraction was observed with the increasing ZDA volume fraction, a physical picture that assumes the coexistence of mobile and immobile regions in the ZDA/BR, is seemingly applicable to the observed dynamics. If the mobile and immobile regions are dynamically homogeneous for the ZDA/BR, the evaluated relaxation times or distributions of relaxation times must be constant, regardless of the volume fraction of ZDA. However, a slight increase in the relaxation time or broadening of the distribution of relaxation time with the increase in the volume fraction of ZDA was observed (see Fig. 3(b)). Thus, a contributing factor other than the coexistence of mobile and immobile component must be present in the ZDA/BR system. It is expected that the dynamics of BR near the HC-BR regions would be strongly perturbed by the HC-BR region in the glassy state, resulting in slower dynamics than that of neat BR. With increases in the volume fraction of ZDA, the contributions from such interfacial regions near HC-BR would increase. Thus, due to the gradient of dynamics mediated by the ZDA aggregates, more heterogeneous and slower dynamics are observed for ZDA/BR than those of the neat BR. The schematic representation of the ZDA/BR system, obtained from the results of our previous work and this QENS study, is shown in Fig. 4. In

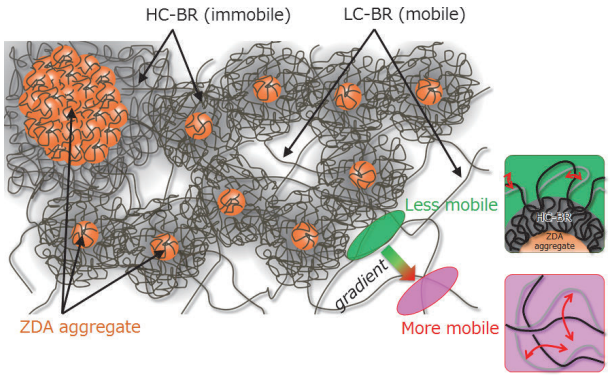

Figure 4. Schematic representation of the ZDA/BR system [8].

the case of ZDA/BR, the existence of chemical bonds between the BR and ZDA contributed to the effective, strong interaction between the BR and the reinforcement agents. Thus, tougher network-like structure is formed in ZDA/BR. Forming such network-like structure has also clearly supported the resulting dynamics as a function of ZDA concentration. Consequently, a higher mechanical strength was realized for ZDA/BR at a given volume fraction of reinforcement agents. The details of the present work can be obtained from reference [8].

References

[1] Y. Fukahori, Rubber Chem. Technol., **80**, 701 (2007).
[2] Y. Tsujita, et al., Macromolecules, **34**, 2220 (2001).
[3] R. Mashita, et al., Polymer J., **48**, 239 (2016).
[4] R. Mashita, et al., Polymer J., **45**, 57 (2013).
[5] K. Shibata, et al., JPS Conf. Proc. **8**, 036022 (2015).
[6] D. Richter, et al., J. Non-Cryst. Solids, **287**, 286 (2001).
[7] F. Alvarez, et al., Phys. Rev. B, **44**, 7306 (1991).
[8] R. Mashita, et al., Soft Matt., **13**, 7862 (2017).

R. Mashita[1], R. Inoue[2], T. Tominaga[3], K. Shibata[4], H. Kishimoto[1], and T. Kanaya[5]
[1]SUMITOMO Rubber Industries, LTD.; [2]Institute for Integrated Radiation and Nuclear Science, Kyoto University; [3]Neutron Science and Technology Center, CROSS; [4]Neutron Science Section, Materials and Life Science Division, J-PARC Center; [5]Material and Life Science Division, J-PARC Center, KEK

Quantitative Evaluation of Deformed Electron Density Distribution of Polydiacetylene Crystal on the Basis of the Organized Combination of X-ray and Neutron Diffraction Data

1. Introduction

Generally, it is quite difficult to obtain the accurate crystal structure information for semicrystalline synthetic polymers, which is indispensable for the prediction of physical property, because of the poor X-ray diffraction data. However, in a lucky case, a giant single crystal of a few mm size can be prepared in a solid-state polymerization reaction of the original monomer single crystal by the irradiation of γ-ray beam [1]. Polydiacetyele (PDCHD) with bulky carbazoryl side groups is treated here as the most typical case [2]. This polymer is electronically conjugated among the single, double and triple CC skeletal bonds. The accurate crystal structure analysis may determine the electron density distribution $\rho(\boldsymbol{x})$ along the skeletal chain, useful for understanding the physical property from the electron level. Since the electrons of the covalently-bonded atoms interact with each other, $\rho(\boldsymbol{x})$ deviates more or less from the original atomic nucleus positions. The quantitative evaluation of the deformed electron density distribution $\Delta\rho(\boldsymbol{x})$ may provide details about the chemical bonding along the polydiacetylene chain.

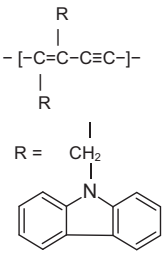

The $\Delta\rho(\boldsymbol{x})$ is estimated by subtracting the density $\rho_o(\boldsymbol{x})$ of the isolated atoms from the X-ray-analyzed density distribution $\rho(\boldsymbol{x})$.

$$\Delta\rho(\boldsymbol{x}) = \rho(\boldsymbol{x}) - \rho_o(\boldsymbol{x}) = (1/V)\Sigma\boldsymbol{q}_j\,[F_{obs}{}^X(\boldsymbol{q}_j) - F_{calc}{}^X(\boldsymbol{q}_j)]e^{i\boldsymbol{q}_j\boldsymbol{x}} \quad (1)$$

Here,

$$F_{calc}{}^X(\boldsymbol{q}) = \Sigma_j f_j{}^X(\boldsymbol{q})\exp(-i\boldsymbol{q}\boldsymbol{x}^X{}_j)\exp(-i\boldsymbol{q}\boldsymbol{U}^X{}_j) \quad (2)$$

is the structure factor calculated using the atomic scattering factors $f_j{}^X(\boldsymbol{q})$ of the isolated and non-interacting atoms without bondings. In the actual calculation the atomic positions ($\boldsymbol{x}^X{}_j$) and thermal parameters ($\boldsymbol{U}^X{}_j$) estimated by the X-ray analysis are assumed to be equal to those of the atomic nuclei. However, this assumption sometimes leads to an abnormal result of $\Delta\rho(\boldsymbol{x})$ due to the so-called *asphericity shift* effect [3]. The X-ray diffractions mainly generated from the valence (or outer-shell) electrons do not locate the exact positions of the nuclei, but they give information about the center of gravity of the electron clouds, which is not equal to the coordinates of the atomic nuclei. The exact positions of the atomic nuclei are obtained experimentally by analyzing the wide-angle *neutron* diffraction data. In this case, the $\Delta\rho(\boldsymbol{x})$ can be calculated as

$$\Delta\rho(\boldsymbol{x}) = (1/V)\Sigma\boldsymbol{q}_j\,[F_{obs}{}^X(\boldsymbol{q}_j) - F_{calc}{}^N(\boldsymbol{q}_j)]\,e^{i\boldsymbol{q}_j\boldsymbol{x}} \quad (3)$$

where $F_{calc}{}^N(\boldsymbol{q}_j)$ is the structure factor calculated from the isolated-atom X-ray scattering factors $f_j{}^X(\boldsymbol{q})$ combined with the parameters of nuclear positions $\boldsymbol{x}^N{}_j$ and thermal parameters $\boldsymbol{U}^N{}_j$ determined by neutron diffraction data analysis:

$$F_{calc}{}^N(\boldsymbol{q}) = \Sigma_j f_j{}^X(\boldsymbol{q})\exp(-i\boldsymbol{q}\boldsymbol{x}^N{}_j)\exp(-i\boldsymbol{q}\boldsymbol{U}^N{}_j). \quad (4)$$

Thus, the combination of the X-ray and neutron diffraction data provides accurate information of $\Delta\rho(\boldsymbol{x})$. This technique is called *X – N* method. We evaluated successfully the $\Delta\rho(x)$ of polydiacetylene single crystal using this method in our experiments [1]. Although various papers had been published about the application of the *X – N* method, most of them treat the inorganic and organic crystals of low molecular weight [3]. The present study is the first successful research of the synthetic polymers [1]. So far the electron state of the polymer substance was studied mainly using electron spectroscopy and quantum chemical calculation. The experimentally-obtained information of the electron density distribution is useful for interpretation of the physical properties of polymer from the electron level. This method is also useful for validation of the quantum chemical theoretical calculation.

2. Measurements and analysis

<Sample> A giant single crystal of PDCHD was prepared by irradiating 40 MRad γ-ray to the single crystal of 1,4-dicarbazoryl diacetylene (DCHD) monomer at room temperature.

<X-ray Diffraction Data> X-ray diffraction measurements were performed at room temperature by utilizing a Rigaku R-Axis Rapid II X-ray diffractometer with a graphite-monochromatized Mo-K_α line. The full-matrix least-squares refinement was performed to determine the final crystal structure based on 1882 observed reflections (*R* factor 4.29% and *wR* 11.5%).

<Neutron Diffraction Data> Neutron diffraction measurement was performed at room temperature using 2 systems: (A) BIX-3 (high resolution neutron diffractometer dedicated to biological macromolecules [4]), which is installed at the JRR-3 reactor hall of JAEA in Tokaimura, Japan. The 2D-detector used was a cylindrical imaging plate camera of 40 cm diameter. The neutron beam with wavelength of 1.51 Å was incident on the sample. The diffraction data were analyzed for all atoms including the H atoms. (B) iBIX (Ibaraki Biological Crystal Diffractometer) installed in beam

line 03 at the Material and Life Science Experimental Facility (MLF), J-PARC, Tokaimura, Japan [5]. The pulsed neutron beam was incident to the sample at 25 Hz. The proton acceleration power was 200 kilowatt. The wavelength range of the thus generated neutron was 0.7 ~ 4 Å. The 20 2-dimensional position-sensitive detectors were set around the sample for the TOF measurements. The crystal structure analysis was performed using the program SHELX-2013 (*R* 10.45% for all the observed diffraction spots).

3. Results and discussion

3.1 Crystal structure of PDCHD

Figure 1 shows the crystal structure and molecular conformation of PDCHD obtained by the X-ray data analysis. The unit cell parameters are $a = 12.8525(4)$ Å, $b = 4.88680(10)$ Å, $c = 17.3393(6)$ Å and $\gamma = 108.3690(10)°$, and the space group is $P2_1/c$- C_{2h}^5. The almost fully-extended planar-zigzag chains with bulk side groups are packed side by side in the unit cell. Neutron structure analysis was performed separately for the data collected with the BIX-3 and iBIX systems. The crystal structures derived by these methods displaced essentially the same accuracy of the atomic nuclear coordinates.

3.2 Evaluation of $\Delta\rho(\boldsymbol{x})$ by the *X* – *N* method

By utilizing the results of X-ray and neutron diffraction analyses, the *X* – *N* method was applied to evaluate $\Delta\rho(\boldsymbol{x})$ as shown in Fig. 2 (a). The 1-dimensional curve of $\Delta\rho(\boldsymbol{x})$ traced along the skeletal chain axis is shown in Fig. 2 (b). The electron density maximum is detected around the center positions of triple CC bonds. The lower but similar maxima are observed also on the single and double CC bonds. The $\Delta\rho(\boldsymbol{x})$ was calculated in parallel by the density functional theory (DFT) using a DMol³ software (Materials Studio 8.0, Biovia). Figure 2 (b) compares the 1-dimensional $\Delta\rho(\boldsymbol{x})$ curve obtained by the DFT calculation with that by the *X* – *N* method. The agreement between the observed and calculated results is excellent.

3.3 Evaluation of $\Delta\rho(\boldsymbol{x})$ by X-ray analysis

The $\Delta\rho(\boldsymbol{x})$ was calculated using only the X-ray analyzed result. The $\Delta\rho(\boldsymbol{x})$ was estimated using the atomic coordinates ($\boldsymbol{X}^X$) and thermal parameters ($\boldsymbol{U}^X$) derived by the X-ray data analysis. This method can be called the *X* – *X* method. As shown in Fig. 3, the maxima are observed for $\Delta\rho(\boldsymbol{x})$, in particular around the CC triple bond. As it is known from the comparison of structural parameters between X-ray and neutron data analysis, the atomic coordinates obtained by these two methods are slightly different from one another, resulting in a non-negligible difference in C-C, C=C and C≡C bond lengths. Then, a slight discrepancy occurs between the center positions of electron clouds and the atomic nuclear positions. The thermal parameters are larger for the X-ray results than the neutron ones. Figure 4 illustrates schematically how the abnormal density distribution is generated. In case of the *X*- *N* method, the relatively small electron density spheres are drawn at the nuclear positions. The thus-drawn $\rho_o(\boldsymbol{x})$ are subtracted from the whole electron density $\rho(\boldsymbol{x})$, then the maxima of $\Delta\rho(\boldsymbol{x})$ are generated on the middles of bonds. The result corresponds well to that shown in Fig. 2. In case of the *X* – *X* method, the spheres $\rho_o(\boldsymbol{x})$ are drawn at the centers of X-ray-derived electron density, where the radii of these spheres are relatively large because of the larger thermal parameters. Besides the CC distance is shorter (1.203 Å), resulting in the remarkable overlap of $\rho_o(\boldsymbol{x})$ between the neighboring spheres. The rest of electron density or $\Delta\rho(\boldsymbol{x})$ becomes almost zero in the middle part of C≡C bond. The $\Delta\rho(\boldsymbol{x})$ is rather higher in the center of C-C bond. These results give the abnormal distribution shown in Fig. 3. Thus, the usage of atomic nucleus positions revealed by the neutron data analysis is indispensable for the calculation of $\Delta\rho(\boldsymbol{x})$.

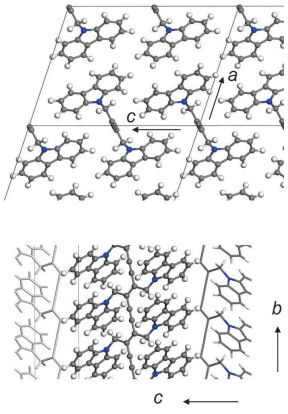

Figure 1. Crystal structure of PDCHD (copyright permission granted by ACS [1]).

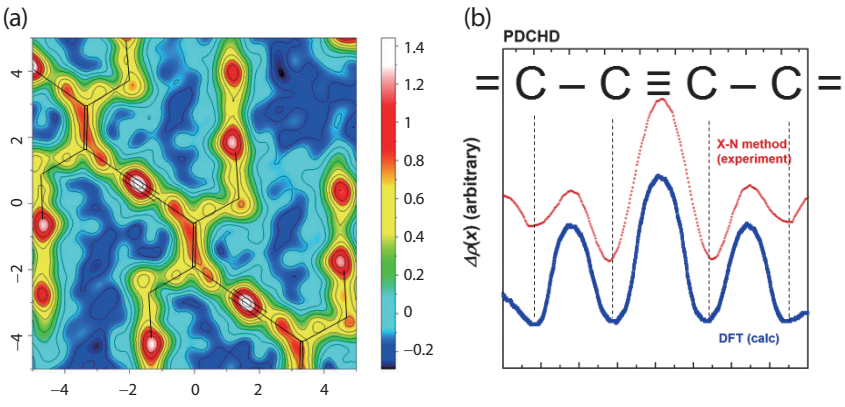

Figure 2. Deformed electron density distribution $\Delta\rho(x)$ and 1D profile along the PDCHD chain axis (copyright permission granted by ACS [1]).

How can we evaluate the correct $\Delta\rho(\boldsymbol{x})$ using the $X-X$ method? The X-ray atomic scattering factor consists of the contributions from core and valence electron clouds. The relative weight of diffraction from the core electrons is overwhelmingly large in the higher-angle region. If the X-ray diffractions in such high-angle region are used preferably in the analysis of electron core positions, the abovementioned asphericity shift might be removed as well. So, even the $X-X$ method might give us a reasonable evaluation of $\Delta\rho(\boldsymbol{x})$: the X-ray diffraction data collected in the lower-angle range reveals the whole electron density distribution $\rho(\boldsymbol{x})$ and the X-ray diffraction data in the higher-angle range shows the positions of the atomic cores or $\rho_o(\boldsymbol{x})$. Of course the effect of the atoms' thermal vibrations must be erased for drawing of smaller spheres $\rho_o(\boldsymbol{x})$. A diffraction measurement at adequately low temperature is required for it. In summary, the quantitatively accurate evaluation of $\Delta\rho(\boldsymbol{x})$ by the $X-X$ method needs the highly-accurate X-ray diffraction analysis with the diffraction data collected at a wide-diffraction angle and at a low temperature. The actual trial to PDCHD was made using a synchrotron X-ray beam [6].

3.4 Application of the $X-N$ method to general polymers

At present, the $X-N$ method (and also the $X-X$ method) is actually impossible to apply to the general partially-crystalline polymer substances, since the total number of observed diffraction spots is too small and the accurate evaluation of the diffraction intensity is also difficult [7]. So far the structure-property relation of polymers has been discussed mainly from the atomic level at best. It is desirable to shift this type of discussion toward the electron level for more precise interpretation of characteristic property of polymers. The concerted combination of X-ray and neutron diffraction methods is indispensable for this purpose as described in this report.

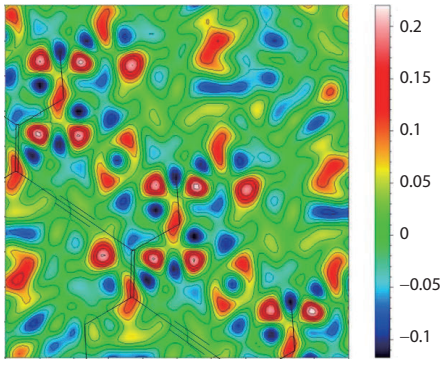

Figure 3. Deformed electron density distribution $\Delta\rho(x)$ of PDCHD derived by the $X-X$ method (copyright permission granted by ACS [1]).

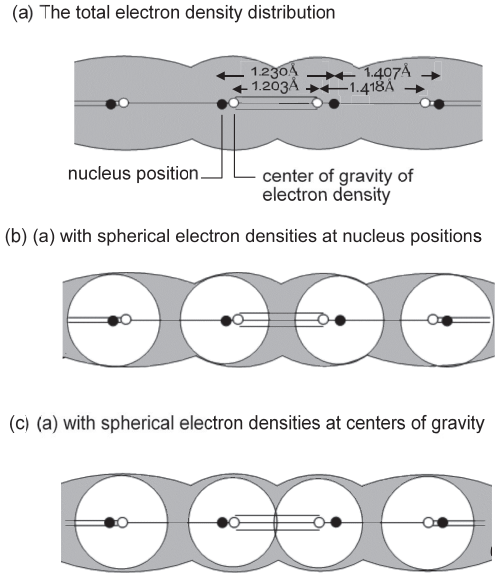

Figure 4. Schematic illustration to obtain the deformed electron density distribution of PDCHD (copyright permission granted by ACS [1]).

References

[1] K. Tashiro, K. Kusaka, T. Hosoya, T. Ohhara, M. Hanesaka, Y. Yoshizawa, H. Yamamoto, N. Niimura, I. Tanaka, K. Kurihara, R. Kuroki and T. Tamada, Macromolecules, 51, 3911-3922 (2018).
[2] V. Enkelman, Adv. Polym. Sci., 63, 91-136 (1984).
[3] P. Coppens, P. X-ray Charge Densities and Chemical Bonding. Oxford University Press Inc. (UK) (1997).
[4] N. Niimura, T. Chatake, A. Ostermann, K. Kurihara, I. Tanaka, J. Z. Kristallogr., 218, 96-107 (2003).
[5] K. Kusaka, T. Hosoya, T. Yamada, K. Tomoyori, T. Ohhara, M. Katagiri, K. Kurihara, I. Tanaka, N. Niimura, J. Synchrotron Radiat., 20, 994-998 (2013).
[6] B. Bagautdinov, H. Tanaka, C-H. Shih, K. Sugimoto, S. Sasaki, K. Tashiro, M. Takata, Acta Cryst., A67, C27-28 (2011).
[7] K. Wasanasuk, K. Tashiro, M. Hanesaka, T. Ohhara, K. Kurihara, R. Kuroki, T. Tamada, T. Ozeki, T. Kanamoto, Macromolecules, 44, 6441-645 (2011).

K. Tashiro[1], K. Kusaka[2], T. Hosoya[3], T. Ohhara[4], M. Hanesaka[1], Y. Yoshizawa[1], H. Yamamoto[5], N. Niimura[3], I. Tanaka[3], K. Kurihara[4], R. Kuroki[4], and T. Tamada[4]

[1]Department of Future Industry-Oriented Basic Science and Materials, Toyota Technological Institute; [2]Frontier Research Center for Applied Atomic Sciences, Ibaraki University; [3]Department of Biomolecular Functional Engineering, College of Engineering, Ibaraki University; [4]Research Unit for Quantum Beam Science Initiative, Japan Atomic Energy Agency; [5]Aichi Synchrotron Radiation Center, Aichi Science and Technology Foundation

Role of Molecular Weight in Shish-Kebab Formation

1. Introduction

Polymer materials are crystallized under various kinds of flow during processing, such as fiber spinning, injection molding and extrusion. In flow-induced crystallization processes, the so-called shish-kebab structures are often observed, which consist of a long central core (shish: extended chain crystal) surrounded by lamellar crystals (kebabs). The modulus and strength become higher as the number of shish-kebab structures increases. Therefore, it is believed that shish-kebab structures are the structural origin of ultrahigh strength and modulus of fibers. Extensive studies have been conducted to elucidate the shish-kebab morphology and mechanism of formation. The modulus and strength become higher when ultrahigh molecular weight components are added to the fibers, thus indicating that the ultrahigh molecular weight components enhance the formation of the shish-kebab structures.

In our previous paper [1] we have examined the effects of high molecular weight components on shish-kebab formation for polyethylene (PE) using small-angle neutron and X-ray scattering (SANS and SAXS) to conclude that the ultrahigh molecular weight component was mainly included in the shish. However, in the same month (May 2007), a completely opposite experimental result was published with blends of deuterated and hydrogenated isotactic polypropylene (d-iPP and h-iPP) by Sumitomo Chem. Co. group [2]. Their findings indicated that more of the low molecular weight component was included in the shish than the high molecular weight component. To disclose the contradiction, we conducted SANS and SAXS experiments on drawn PE blends of deuterated and hydrogenated PE (d-PE and h-PE) with various molecular weights.

2. Experimental section

d-PE with an average molecular weight of M_w = 600,000 and molecular weight distribution of M_w/M_n = 2 and h-PE with various molecular weights of M_w = 58,000, 300,000 and 2,000,000 and M_w/M_n = 8~12 were used in this experiment. The blend films were drawn at three drawing rates of 6 μm/s, 400 μm/s and 2.4 cm/s at 125°C.

SANS measurements were carried out using two machines. The first one was TAIKAN in MLF at J-PARC and the other one was a 40 m SANS machine at the HANARO reactor in Korea. SAXS and WAXS measurements were conducted using BL40B2 at SPring-8.

3. Results and discussion

On the basis of our previous experimental results, we considered a possible scenario for shish-kebab formation in which the low molecular weight component, rather than the high molecular weight component, was the major constituent of the shish. In the scenario, we also expected that the slower the drawing rate, the more of the polymer chains were included in the shish. On the basis of the considerations, we sought to confirm the scenario by using SANS and SAXS on drawn films of d-PE and h-PE with various molecular weights. From the experimental results, we had to distinguish between the two types of PE at the nanometer scale. Therefore, we used SANS and SAXS measurements for this experiment.

Figure 1 shows the 2D SAXS and SANS patterns for the drawn PE blend films. The 2D SAXS patterns showed weak two-spot patterns along the drawing direction corresponding to the distance between the kebabs (or lamellar crystals). The 2D SAXS patterns were very similar, thus suggesting that the small amount of added h-PE (3 wt%) did not affect the whole structure of the PE blends and functioned as a tracer. In contrast, in the 2D SANS patterns, streak-like scattering was observed normal to the drawing direction. Streak-like scattering corresponding to scattering from the h-PE was observed in addition to the two-spot pattern, thus suggesting that the shish mainly consisted of h-PE. At the same drawing rate, the streak-like scattering was enhanced as the molecular weight of the h-PE decreased. These results suggested that the low molecular weight component was more easily merged into the shish than the high molecular weight component. Furthermore, for the same molecular weight of h-PE (e.g., M_w = 58,000), the streak-like scattering was enhanced as the drawing rate decreased. The observed results qualitatively supported the picture predicted in the scenario.

To carry out a quantitative analysis, we evaluated the 1D SAXS and SANS intensities in the directions normal and parallel to the drawing direction. The SANS contrast in the present samples arises from the scattering length density difference due to the mass density difference and the scattering length density difference between the hydrogen (H) and deuterium (D). The form factor for the streak-like scattering normal to the drawing direction was approximately obtained as the difference between the SANS and SAXS intensities. The intensity differences are shown in Fig. 2.

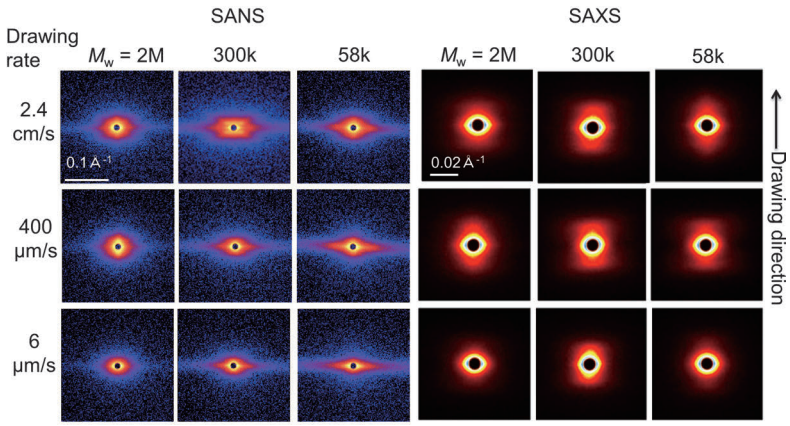

Figure 1. 2D SAXS and SANS patterns for the drawn PE blends containing 3 wt% h-PE with different molecular weights. The draw ratio is 7.0 for all samples.

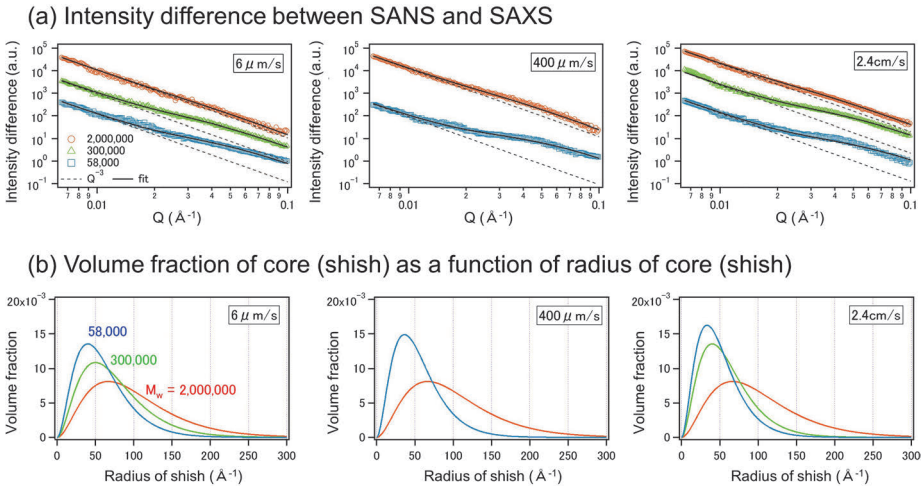

Figure 2. (a) Intensity differences between the SANS and SAXS results in the normal direction for the PE blends containing h-PE with different molecular weights. The solid curves are the results of the fits using the multicore-shell cylinder model. The dashed lines show the contributions of the large shell. (b) Volume fraction of the core (shish) as a function of the radius of the core (shish).

The multicore-shell cylinder model was applied to analyze the intensity differences in the normal direction. The illustration of the model can be found in Fig. 5 in ref. [1]. The results of the fitting are shown as black solid lines in Fig. 2. These results suggested that the observed results can be qualitatively explained with the scenario.

As mentioned in the introduction, this work was motivated by two contrary experimental results on the flow-induced crystallization of PE and iPP. Though we have not studied iPP or other flow conditions, it is clear that there are various mechanisms for shish-kebab formation that depend on factors such as the type of flow field, flow rate, type of polymer, temperature, molecular weight and molecular weight distribution. In various cases, the shish would be formed by either high-molecular or low-molecular weight components.

References

[1] T. Kanaya, et. al., *Macromolecules*, **40**, 3650 (2007).
[2] S. Kimata, et. al., *Science,* **316**, 1014 (2007).

T. Kanaya[1,2], M. Murakami[1], T. Maede[1], H. Ogawa[1,3], R. Inoue[1,4], K. Nishida[1], G. Matsuba[5], N. Ohta[3], S. Takata[6], T. Tominaga[7], J. Suzuki[7], Y.-S. Han[8], and T.-H. Kim[8]

[1]Institute for Chemical Research, Kyoto University; [2]Material and Life Science Division, J-PARC Center; [3]Japan Synchrotron Radiation Research Institute; [4]Research Reactor Institute, Kyoto University; [5]Department of Polymer Science and Engineering, Yamagata University; [6]Neutron Science Section, Material and Life Science Division, J-PARC Center; [7]Neutron Science and Technology Center, CROSS; [8]Korea Atomic Energy Research Institute, South Korea

Structure and Mechanical Properties of Elastomer Thin Films Bound to Carbon Interface

1. Introduction

The interface between polymers and inorganic materials is of pivotal academic and industrial interest. An example is the interphase in nanocomposites, a class of materials composed of polymers (matrix) and inorganic nanopowders (fillers). In general, the performance of a nanocomposite strongly depends on not only the physical properties of the matrix but also the interaction between the matrix and the filler material. It is noteworthy that the physical response of a composite can be modulated via the interactions resulting from the attachment/detachment of polymers on fillers. This means that an understanding of the interfaces between the polymer matrix and inorganic fillers is essential to construct highly functionalized nanocomposites.

A specific example are tire materials; because the rubber for tires consists mainly of a polymer elastomer matrix and carbon black fillers, an understanding of the interface between the polymer and carbon is important for quality improvement. It is well known that a nanometer-thick polymer layer, the so-called bound rubber layer (BRL), is formed on carbon fillers, and it is resistant to dissolution even in a good solvent for the polymer. As in the case of other nanocomposites, it is empirically known that the BRL plays an important role in improving the tensile strength, tear strength, fatigue resistance, and wear resistance of tires [1].

There have been significant efforts in the industry to manufacture well-performing tires by making a surface-modified filler. As the structure and/or thermal molecular motion of the polymer at the filler/polymer interface are affected by the interactions with the filler, it is believed that surface modification changes the property of the BRL, resulting in better tire performance. However, this is still a hypothesis because the evidence is still insufficient and the empirical data, especially about the influence of surface modification on the BRL, is not enough, moreover, the relationship between the BRL and the tire performance needs to be evaluated to develop a guiding principle to improve the tire performance. To answer this question, hydrophilization treatment of carbon is performed to change the surface free energy (γ), and investigate the influence of an elastomer bound to the surface, model BRL, on the structure and mechanical properties.

2. Experimental method

1,4-cis polybutadiene (PB) with a number-average molecular weight (M_n) of 190 kg/mol and molecular weight distribution of 2.3, and monodispersed deuterated 1,4-cis PB (d-PB) with a M_n of 90 kg/mol were used. The glass transition temperature (T_g) of PB and d-PB evaluated by differential scanning calorimetry were 170 K and 173 K, respectively. Si wafers were used as substrates, and carbon films were prepared on the Si wafers by plasma-enhanced chemical vapor deposition. Then, the carbon films were irradiated with a low-pressure mercury lamp with a wavelength (λ) of 185 nm and 254 nm in steam atmosphere at room temperature to change γ. To investigate the effect of the surface modification, three kinds of carbon layers were prepared. The γ of the carbon films were approximately 30, 45, and 58 $mJ \cdot m^{-2}$ (here we call these carbon layers carbon-30, carbon-45, and carbon-58), respectively. PB films were spin-coated on the carbon layers from a toluene solution and dried under vacuum for more than 12 h at room temperature. After that, the PB films were rinsed with a large amount of toluene 5 times to obtain residual layers (RLs) adhering on a carbon surface, which are model BRLs. Then, the specimens were dried under vacuum for more than 8 h at room temperature.

Interfacial diffusion of polymeric chains between the RLs and d-PB films on the RLs was examined by neutron reflectivity (NR) measurements with the SOFIA reflectometer installed at BL16. For the measurements, the d-PB films with a thickness of ca. 100 nm were spin-coated on the RLs from the toluene solution and dried under vacuum for more than 12 h at room temperature. After the measurements for the dried samples, the specimens were annealed under vacuum for more than 8 h at 453 K, and NR measurements were performed after annealing. Incident neutrons with a λ ranging from 0.25 to 0.88 nm were guided into the specimen. The reflectivity profiles depending on the scattering vector, $q = (4\pi/\lambda) \cdot \sin\theta$, were analyzed by fitting based on the scattering length density profile along the depth direction using the parratt32 software.

The normal force of the RLs was measured based on force-distance curves derived from atomic force microscopy (AFM) observations. A cantilever made of Si with a spring constant and Young's modulus of 1.6 $N \cdot m^{-1}$ and 169 GPa, respectively, was used to evaluate the normal

force, and an approach-retract scan was performed at a speed of 20 nm·s^{-1}. To avoid contamination of the cantilever by the PB films, each measurement was performed using a fresh cantilever.

3. Results and discussion

Figure 1 shows the NR profiles of the RL/d-PB bilayers on the carbon films before and after annealing at 453 K for more than 8 h. For clarity, each data set of the bilayers is offset by two decades. The schematic fitting model is illustrated in Fig. 1(c). Here, we focused on the scattering length density (b/V) of RL, $(b/V)_{RL}$, and the interfacial roughness between RL and d-PB, σ_{int}. Table 1 summarizes the $(b/V)_{RL}$ and σ_{int} values before and after annealing. For comparison, (b/V) of the RL before adding d-PB calculated from the mass density obtained from X-ray reflectivity of RLs are also listed in Table 1. First, $(b/V)_{RL}$ of the RL on carbon-58 after the formation of a d-PB layer was larger than that of the RL without the d-PB layer, and it increased upon annealing. This indicates that a part of the d-PB chains has already penetrated the RL during spin coating of the d-PB layer, and the intermixing of the molecules between the RL and d-PB layers is enhanced by the annealing. In contrast, no change in $(b/V)_{RL}$ was observed and only σ_{int} increased upon annealing in the case of the RL on carbon-45 and carbon-30 (the change in the NR profiles was mainly caused by the change in the roughness of the d-PB surface, $\sigma_{d\text{-}PB}$, for all the cases). Note here that σ_{int} of carbon-45 increased more than that of carbon-30; that is, the PB molecules in the RL on the carbon-45 were slightly more mobile than those on carbon-30. These results suggest that the mobility of the PB molecules in the RLs is strongly suppressed depending on the γ of the carbon films.

Figure 2 shows the force-distance curves of the RLs. In the case of the RL on carbon-58, the normal force slightly increased immediately after contact with the RL surface on approach, the slope becomes gradually steeper with closer contact, and the force curve presents a large hysteresis upon retraction. This suggests that the cantilever first detected the normal force of the RL, which has a thickness of 6.3 nm in the rubbery state; it then detected that of the carbon under the RL upon further contact and finally detected the one modulated by the rubbery RL adhesion upon retraction. In contrast, the slope of the force-distance curves immediately increased for the RLs on carbon-45 and carbon-30.

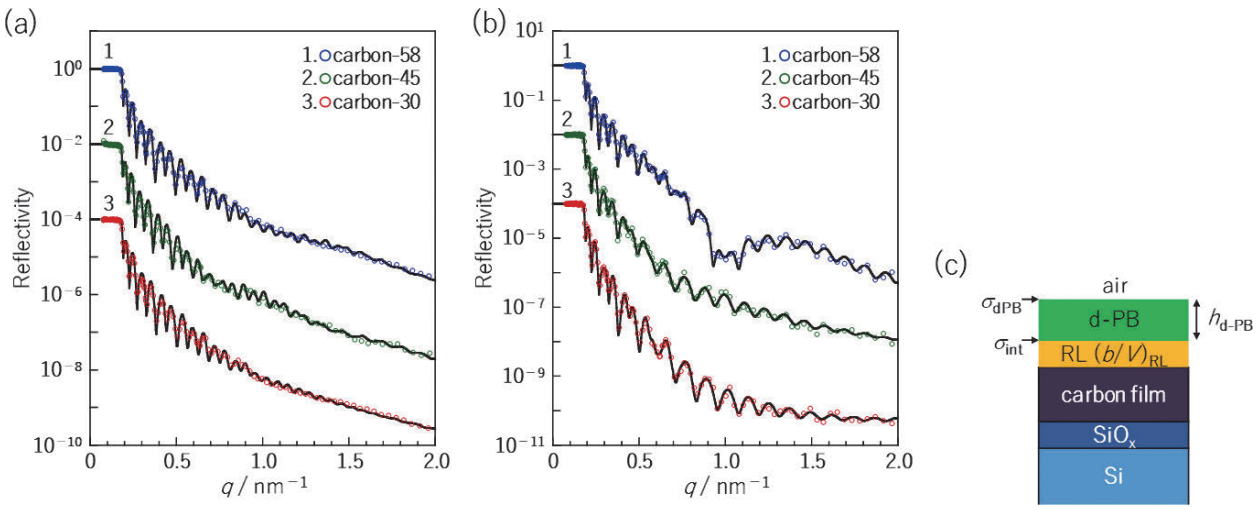

Figure 1. NR curves of (RL/d-PB) bilayer on the carbon film (a) before and (b) after annealing. Solid curves show calculated reflectivities based on model scattering length density profiles. (c) Schematic illustration of the model used for the bilayer.

Table 1. Scattering length density of RLs $(b/V)_{RL}$ and interfacial roughness of (RL/d-PB) interface σ_{int} before and after annealing.

	RL without d-PB layer	Before annealing		After annealing	
	$(b/V)_{RL}$ / nm^{-2}	$(b/V)_{RL}$ / nm^{-2}	σ_{int} / nm	$(b/V)_{RL}$ / nm^{-2}	σ_{int} / nm
RL(carbon-58)	$(0.43 \pm 0.08) \times 10^{-4}$	$(1.02 \pm 0.05) \times 10^{-4}$	1.3 ± 0.3	$(2.28 \pm 0.06) \times 10^{-4}$	2.6 ± 0.5
RL(carbon-45)	$(0.47 \pm 0.05) \times 10^{-4}$	$(0.47 \pm 0.05) \times 10^{-4}$	1.4 ± 0.2	$(0.48 \pm 0.05) \times 10^{-4}$	2.4 ± 0.4
RL(carbon-30)	$(0.50 \pm 0.06) \times 10^{-4}$	$(0.50 \pm 0.05) \times 10^{-4}$	0.9 ± 0.3	$(0.50 \pm 0.05) \times 10^{-4}$	1.2 ± 0.4

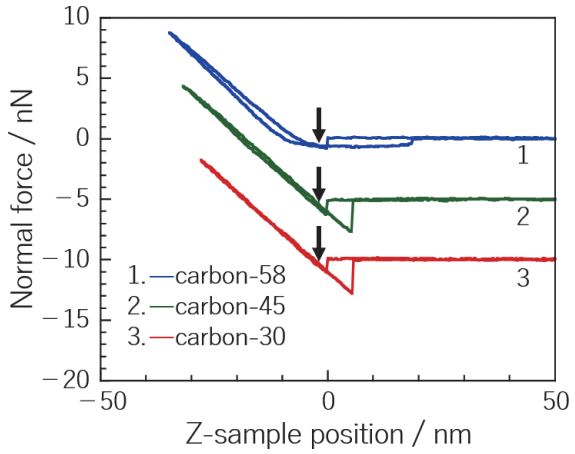

Figure 2. Force-distance curve of RL on carbon films. Downwards arrows denote positions where slope between Normal force and Z-sample position were obtained.

The slopes (m) of carbon-45 ($m = 0.31 \pm 0.02$) and carbon-30 ($m = 0.31 \pm 0.02$) were less than that of the carbon film ($m = 0.38 \pm 0.02$) but obviously more than that of the rubbery PB ($m = 0.03 \pm 0.01$). This increment of the slope, in other words, the enhancement of the stiffness for RL on the hydrophobic carbons, implies that the elevation of T_g is far above the bulk one. So far, the change in the polymer dynamics at various interfaces has been intensively studied and many experimental works have reported the increase in T_g and the suppression of the dynamics above the bulk T_g. To the best of our knowledge, the molecular orientation of the phenyl rings of a polystyrene (PS) film at an interface with a sapphire substrate did not change at 100 K above the bulk T_g [2], but our result suggests a greater elevation of the T_g. As a complete study of the elevation of the T_g at the interface lies outside the scope of this work, we leave these details for a future study, focusing instead on the mechanical properties of the RLs here.

4. Conclusion

Interfacial layers of PB films on bare and surface-modified carbon films and RLs on the carbon films were examined. Figure 3 is a schematic representation of the experimental results. An interfacial layer of PB was present near the carbon layer, with density and thickness identical to those of the RL after rinsing, in which case, a denser layer with more hydrophobic surface was formed on the carbon. The thermal diffusion between the RL and d-PB top layer, investigated by NR, indicated that the denser layer did not intermix significantly with the top layer. A consistent result was obtained for normal stress measurements based on AFM: the RLs on hydrophobic carbons were not in a rubbery state but presumably in a glassy state, whereas those on hydrophilic carbon were in a rubbery state. If the RLs on the hydrophobic carbons were glassy at room temperature, the transition temperature increased by more than 120 K [3].

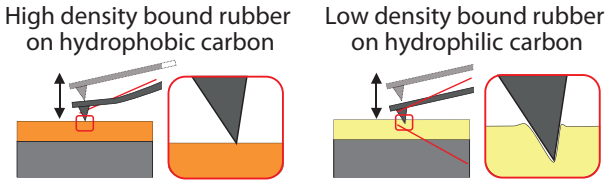

Figure 3. Schematic illustration of residual layers on hydrophobic and hydrophilic carbon.

Acknowledgement

This work was supported by the Photon and Quantum Basic Research Coordinated Development Program from the Ministry of Education, Culture, Sports, Science and Technology, Japan.

References

[1] S. T. Palinchaket al., Rubber Chem. Technol., 31, 374 (1958).
[2] K. S. Gautamet al., Phys. Rev. Lett., 85, 3854 (2000).
[3] K. Hori et al., Langmuir, 33, 8883, (2017).

K. Hori[1,2], N. L. Yamada[2,3], Y. Fujii[4], T. Masui[1], H. Kishimoto[1], and H. Seto[2,3]

[1]Chemical Analysis Center, Research & Development HQ. SUMITOMO RUBBER INDUSTRIES, LTD.; [2]Neutron Science Section, Materials and Life Science Division, J-PARC Center; [3]Institute of Materials Structure Science, KEK; [4]Department of Chemistry for Materials, Graduate School of Engineering, MIE UNIVERSITY

Analysis of Carbon Polygons by High-Resolution Pair Distribution Function Obtained from Neutron Diffraction

1. Introduction

Graphene is a basic building block for a variety of sp^2-carbon architectures with different dimensions: zero-dimensional (0D) fullerene C_{60} [1], 1D single-walled carbon nanotube [2, 3], 2D single-layer graphene [4, 5]. Moreover, it has been theoretically predicted that graphene is capable to form 3D frameworks (Fig. 1) known as Mackay crystals [6] or carbon Schwarzites [7]. A zeolite-templating method is expected to synthesize such imaginary 3D graphene frameworks as real materials [8, 9]. By replicating zeolite 3D nanochannels (Fig. 2) with carbon, zeolite-templated carbons (ZTCs) can be obtained, and the framework topology of ZTC accords to that of the zeolite nanochannels.

It is beneficial to understand how sp^2 carbons can be assembled into three-dimensional graphene-based frameworks in ZTC, towards the realization of carbon Schwarzites. We have previously reported that a typical ZTC obtained by using FUA zeolite has an open graphene framework, which is like the cross-linked buckybowls shown in Fig. 3 (denoted as Model-I), rather than a closed tubular framework [8]. Model-I was proposed as one of the possible structures, which meet many experimental characterization results. However, the crystalline Model-I structure cannot perfectly reflect the actual material, which contains amorphous structures. Thus, we proposed recently a new model denoted as Model-II, constructed by molecular dynamics (MD) simulation to include randomized irregularity/defects [10]. This short review expounds our recent report on the analysis of carbon polygons (pentagons, hexagons, heptagons, and octagons) included in the ZTC framework, which was elucidated by comparing a pair distribution function, g(r), of experiment with the ones of the aforementioned two models [10].

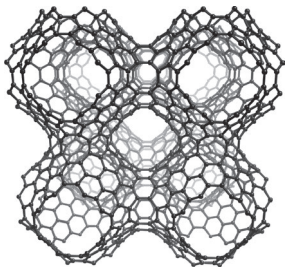

Figure 1. The structure of the Mackay crystal.

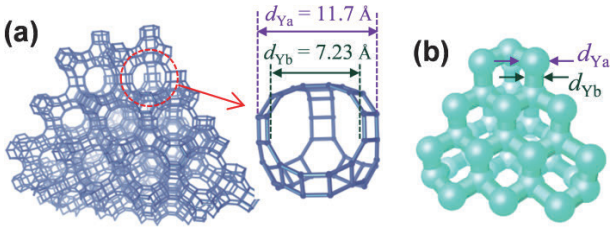

Figure 2. The structure of (a) FAU zeolite and (b) its nanochannel morphology. Reprinted with permission [10]. Copyright 2018 Elsevier.

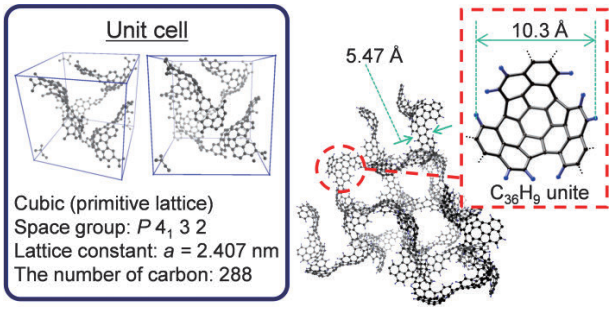

Figure 3. A geometric structure model for ZTC [Model-I]. Reprinted with permission [10]. Copyright 2018 Elsevier.

2. Experimental

ZTC was prepared by using the FAU zeolite as a template [8]. To discuss the presence of carbon polygons, a high-resolution g(r) was obtained by the neutron total scattering instrument, NOVA (BL21), at Material and Life Science Facility of J-PARC. The structure factor, $S(Q)$, was obtained from a measured diffraction profile after data correction [11], including background, self-attenuation, number of incident neutrons, solid angle of detectors, multiple scattering, and incoherent scattering cross-sections. To obtain g(r), $S(Q)$ was Fourier transformed in the Q range of 0.2–55.0 Å^{-1}.

3. Construction of Model-II

As shown in Fig. 4a, Model-II was constructed in the FAU zeolite framework (2×2×2 supercell with dimensions L_x = 48.14 Å, L_y = 48.14 Å, and L_z = 48.14 Å) by quench molecular dynamics simulation with the reaction state summation potential [12]. The details can be found in our previous publication [10]. A part of the resulting structure is cut out and shown in Fig. 4b. Some of the representative framework units corresponding to one zeolite supercage are shown in Fig. 4c-k.

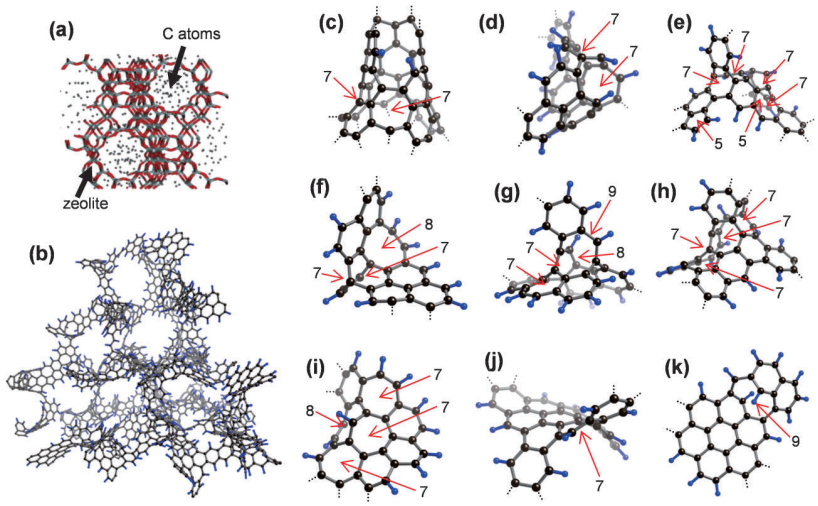

Figure 4. (a) The initial state of the calculation for the construction of Model-II. Carbon atoms are distributed in zeolite nanochannels. (b) A part of Model-II corresponding to Fig. 2b. Representative nine framework units are enlarged in (c-k). Carbon polygons, except hexagons, are indicated by the polygon numbers. Reprinted with permission [10]. Copyright 2018 Elsevier.

4. Carbon polygons

From the analogy of imaginary structures like Mackay crystals or carbon Schwarzites [6, 7], the presence of carbon heptagons and octagons is expected to realize a continuous open framework. On the other hand, carbon pentagons basically make a framework closed like C_{60}, though the Model-I realizes a continuous open framework only by carbon pentagons and hexagons. Thus, the ratio of carbon polygons in the ZTC framework is an interesting issue. Fig. 5a shows g(r) of ZTC, compared with those of the two models. As references, the experimental data of graphite and C_{60} are also shown. In Fig. 5a, the distances to the 1st, 2nd, 3rd, 4th, and 5th neighboring carbon atoms (d_{1st}, d_{2nd}, d_{3rd}, d_{4th}, and d_{5th}) in ZTC are denoted. Figs. 5b-e show d_{2nd} on the four types of carbon structures. In graphite hexagons (Fig. 5b), d_{2nd} is 2.46 Å, while d_{2nd} in C_{60} pentagons is 2.33 Å (Fig. 5c). Pentagons in Model-I (Fig. 5d) also have a short d_{2nd} (2.25–2.30 Å), and the difference from d_{2nd} of hexagons is 0.16–0.21 Å. On the other hand, d_{2nd} of carbon heptagons is 2.48–2.50 Å (Fig. 5e), and the difference from d_{2nd} of carbon hexagons is only 0.02–0.04 Å. Carbon octagons and larger polygons have very close d_{2nd} values to that of hexagons and thus, they cannot be distinguished each other in $g(r)$.

In Model-I, about 19% of carbon atoms are involved in carbon pentagons, while 81% are in hexagons. Thus, Model-I shows a peak corresponding to pentagons at 2.28 Å. Model-II contains carbon pentagons, hexagons, heptagons, and octagons, with ratios approximately 3%, 63%, 23%, and 11%, respectively, if further larger polygons are not considered. While the amount of the pentagons is too small to show an apparent peak, a heptagon shows a shoulder at 2.49 Å. In an actual

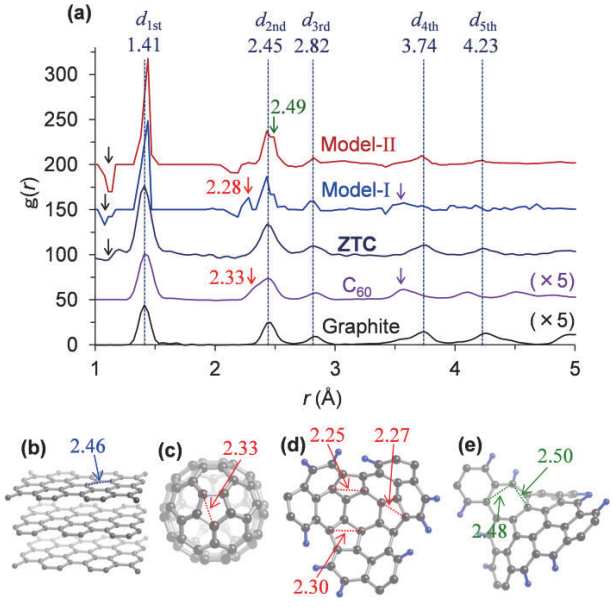

Figure 5. (a) Pair distribution function, g(r). Experiment: ZTC, C_{60}, and graphite. Calculation: Model-I and Model-II. Peaks corresponding to the 1st-5th nearest neighboring carbon atoms in ZTC are denoted. The peak positions of carbon pentagons (red font) and heptagons (green font) are described. Negative peaks are indicated by black arrows, and d_{4th} of C_{60} and Model-I is indicated by purple arrows. (b-e) Structure models of (b) graphite, (c) C_{60}, (d) Model I, and (e) Model II. The values of d_{2nd} [Å] are described for carbon pentagon (red), hexagon (blue), and heptagon (green). Reprinted with permission [10]. Copyright 2018 Elsevier.

experiment, however, the peak broadening is inevitable. Nevertheless, C_{60} barely shows a broad shoulder at 2.33 Å, corresponding to carbon pentagons, by the presence of significant amount of carbon pentagons (37.5%) and the high-resolution neutron diffraction measurement. The presence of pentagons appears also at d_{4th}. In C_{60}, d_{1st}, d_{2nd}, and d_{3rd} peaks corresponding to C–C distances inside carbon hexagons are the same as those of graphite. But, d_{4th}, involving two neighboring hexagon/pentagon rings, is noticeably shorter than that of graphite because of a positively curved framework induced by carbon pentagons. The d_{4th} position of Model-I is almost the same as that of C_{60} because Model-I includes carbon pentagons and has a positively curved framework. Thus, carbon pentagons can be distinguished from hexagons, if their amount is large enough in the present experiment. On the other hand, it is still difficult to distinguish carbon heptagons and larger polygons in the present resolution of the experiment.

ZTC does not show a peak/shoulder at 2.28–2.30 Å, and its d_{4th} is almost the same as that of graphite, indicating that the ZTC framework rarely contains carbon pentagons. Note that negative peaks at 1.08–1.11 Å in ZTC and two models are derived from negative correlation between C and H atoms. Apart from the amount of H, the overall ZTC g(r) related to the C–C correlation agrees well with that of Model-II rather than Model-I. Thus, Model-II represents very well the internal graphene microstructure of ZTC, and the results suggest an interesting possibility, *i.e.*, the presence of significant amount of carbon heptagons and octagons in ZTC. The framework topology of zeolite nanochannels, in which graphene growth is developed, is analogous to those of Mackay crystals and carbon Schwarzites, and it is hypothesized that such a geometrical restriction induces the inclusion of carbon heptagons and octagons rather than carbon pentagons in a hexagon-based sp^2 network.

5. Summary

The types of carbon polygons included in the ZTC framework are analyzed by comparing a pair distribution function, g(r), obtained by experiment with the ones of the two structure models. It is suggested that the ZTC framework contains a diverse range of carbon polygons such as hexagons, heptagons and octagons, while the number of the pentagons is small. Such distribution of carbon polygons demonstrates interesting similarities between the real three-dimensional graphene-based framework and the imaginary ones like Mackay crystals and carbon Schwarzites.

Acknowledgements

The neutron scattering experiment was approved by the Neutron Scattering Program Advisory Committee of IMSS, KEK (Proposal No. 2014S06). This work was supported by a Grant-in-Aid for Scientific Research (A), 17H01042 (H.N.); Dynamic Alliance for Open Innovation Bridging Human, Environment and Materials; and the Network Joint Research Center for Materials and Devices.

References

[1] H. W. Kroto, J. R. Heath, S. C. O'Brien, R. F. Curl and R. E. Smalley, Nature, 318, 162 (1985).
[2] S. Iijima and T. Ichihashi, Nature, 363, 603 (1993).
[3] K. Hata, D. N. Futaba, K. Mizuno, T. Namai, M. Yumura and S. Iijima, Science, 306, 1362-1364 (2004).
[4] K. S. Novoselov, A. K. Geim, S. V. Morozov, D. Jiang, Y. Zhang, S. V. Dubonos, I. V. Grigorieva and A. A. Firsov, Science, 306, 666-669 (2004).
[5] A. K. Geim and K. S. Novoselov, Nat. Mater., 6, 183-191 (2007).
[6] A. L. Mackay and H. Terrones, Nature, 352, 762 (1991).
[7] T. Lenosky, X. Gonze, M. Teter and V. Elser, Nature, 355, 333-335 (1992).
[8] H. Nishihara, Q.-H. Yang, P.-X. Hou, M. Unno, S. Yamauchi, R. Saito, J. I. Paredes, A. Martinez-Alonso, J. M. D. Tascon, Y. Sato, M. Terauchi and T. Kyotani, Carbon, 47, 1220-1230 (2009).
[9] E. Braun, Y. Lee, S. M. Moosavi, S. Barthel, R. Mercado, I. A. Baburin, D. M. Proserpio and B. Smit, Proc. Natl. Acad. Sci. USA, DIO: 10.1073/pnas.1805062115.
[10] H. Nishihara, H. Fujimoto, H. Itoi, K. Nomura, H. Tanaka, M. T. Miyahara, P. A. Bonnaud, R. Miura, A. Suzuki, N. Miyamoto, N. Hatakeyama, A. Miyamoto, K. Ikeda, T. Otomo and T. Kyotani, Carbon, 129, 854-862 (2018).
[11] T. Egami and S. Billinge, *Underneath the Bragg Peaks -Structural Analysis of Complex Materials*, Elsevier, 2012.
[12] Y. F. Shi, J. Chem. Phys., 128, 234707 (2008).

H. Nishihara[1], H. Tanaka[2], M. T. Miyahara[2], K. Ikeda[3], T. Otomo[3], and T. Kyotani[1]
[1]*Institute of Multidisciplinary Research for Advanced Materials, Tohoku University;* [2]*Department of Chemical Engineering, Kyoto University;* [3]*Institute of Materials Structure Science, High Energy Accelerator Research Organization (KEK)*

Linking Spin-Fluctuations in $Ba_{0.75}K_{0.25}Fe_2As_2$ to Electron Correlations

1. Introduction

Since the discovery of high-temperature superconductivity in iron-based superconductors (FeSC) in 2008 [1], many studies have been performed to elucidate their electronic and magnetic properties. Earlier studies have suggested that FeSCs are weakly correlated materials [2], in sharp contrast to cuprate superconductors, in which Mott physics is more fundamentally tied to superconductivity. However, increasing evidence suggests that electron correlations in FeSCs are much stronger than previously thought [3, 4]. The role of electron correlations is therefore the most interesting, yet not well understood, aspect of the physics of FeSCs.

Here, we use inelastic neutron scattering (INS) to study the effect of electron correlations on spin dynamics in hole-doped FeSCs $Ba_{0.75}K_{0.25}Fe_2As_2$. By combining angle-resolved photoemission spectroscopy (ARPES) measurements and first-principles calculations, we show that the measured spin excitations are heavily renormalized due to the correlated Fe-3*d* bands with enhanced effective electron masses. These results highlight the strongly correlated nature of FeSCs that should be considered for a realistic treatment of the spin dynamics. In addition, the consistency between the results of the two momentum-resolved spectroscopic methods, INS and ARPES, demonstrates a quantitative link between the magnetic response and the underlying electronic structure of FeSCs. This opens up new possibilities for using INS as a momentum-resolved spectroscopy for determining the correlated electronic structure [5].

2. Results and discussion

INS measurements of $Ba_{0.75}K_{0.25}Fe_2As_2$ were performed using BL01 4SEASONS installed at J-PARC. Figures 1 (a)-(d) compare the two-dimensional constant energy maps of spin excitations in the (*H, K*) scattering plane for various energy transfers. At low energies around $E = 60$ meV, spin excitations peak strongly at $\boldsymbol{Q} = (1, 0)$, which corresponds to the nesting vector between hole and electron FSs. As the energy increases, spin excitations form transversely elongated ellipses that lead to splitting into two branches. At even higher energies, these excitations broaden rapidly and form broad circular shapes centered at the zone boundary $\boldsymbol{Q} = (1, 1)$. These dispersive features are also confirmed by the constant energy cuts along the (1, 0) → (1, 1) high-symmetry direction in Fig. 1 (e), where a single commensurate peak centered at $\boldsymbol{Q} = (1, 0)$ at low energies ($E < 60$ meV) splits into a pair of two peaks with increasing energy, and eventually moves close to the zone boundary $\boldsymbol{Q} = (1, 1)$ at $E \sim 200$ meV.

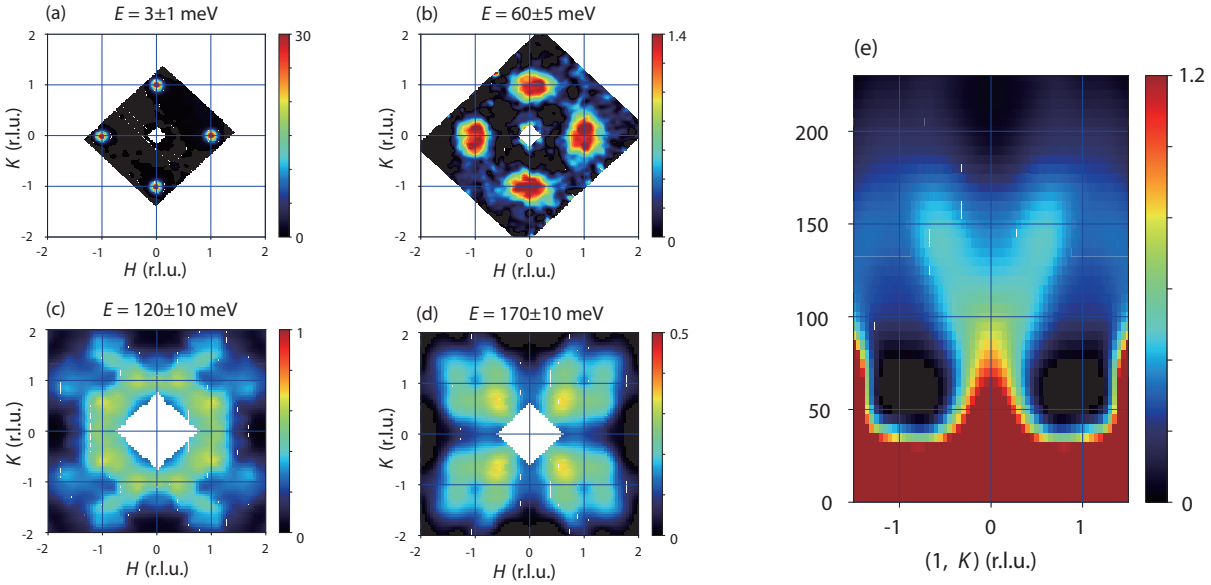

Figure 1. (a)-(d) Constant-energy maps of $Ba_{0.75}K_{0.25}Fe_2As_2$ in the (*H, K*) plane at energy transfers of $E = 3 \pm 1$ meV, $E = 60 \pm 5$ meV, $E = 120 \pm 5$ meV, $E = 170 \pm 10$ meV, respectively. (e) Energy-band dispersion of spin excitations along the (1,*K*) high-symmetry direction (see Ref [5]).

To understand the INS data, we provide a first-principles analysis of the spin excitation spectrum of FeSCs on the basis of the itinerant picture. As a first step, we construct an effective five-orbital model based on density-functional theory (DFT) calculations (see Fig. 2 (a)). Then, by considering Hubbard-type interactions (i.e., the intra-orbital Coulomb repulsion U, interorbital Coulomb repulsion U', Hund's coupling J, and pair hopping J') on top of the five-orbital model, we obtain the dynamical spin susceptibility $\chi_s(q, E)$ within the random-phase approximation (RPA) as

$$\hat{\chi}s(q,E) = \hat{\chi}_0(q,E)[\hat{I} - \hat{S}\hat{\chi}_0(q,E)]. \quad (1)$$

Here, S is the corresponding interaction vertex matrix and $\chi_0(q, E)$ is the irreducible susceptibility given as

$$\hat{\chi}_0^{l_1,l_2,l_3,l_4}(qE) = \sum_k \sum_{n,m} \frac{f(\epsilon^n_{k+q} - \epsilon^m_k)}{E + i\delta - \epsilon^n_{k+q} + \epsilon^m_k} \times U_{l_1,n}(k+q)U_{l_4,n}(k)U^\dagger_{l_2,m}(k)U^\dagger_{l_3,n}(k+q), \quad (2)$$

where $f(\varepsilon)$, $\varepsilon^m_{\boldsymbol{k}}$, and $U_{l,n}(k)$ are, respectively, the Fermi distribution function, energy dispersion, and elements of the unitary matrices from the orbital to the band basis. Figure 2 (b) shows a contour plot of the calculated $\chi_s(\boldsymbol{q}, E)$ along the high-symmetry directions. The spin excitations are markedly different in the two directions (1,0) → (1,1) and (1, 0) → (0, 0). This is consistent with the transversely elongated spin excitations seen in Fig. 1 (c). However, while our RPA calculation reproduces the spin-wave-like dispersive feature along the high-symmetry directions, it apparently overestimates the energy scale of the excitations. Along the (1, 0) → (1, 1) direction, the theoretical spin excitation peak extends approximately to ~ 600 meV, which is larger by a factor of ~ 3 than the experimental data.

This overestimation of the spin excitation energy in our RPA analysis has important implications for the electronic state of FeSCs. As it can be seen in Eq. (2), the electronic band structure $\varepsilon^m_{\boldsymbol{k}}$ determines the momentum- and energy-dependent structure of the dynamical spin susceptibility. The discrepancy between the experimental and theoretical spin excitations, therefore, suggests that the actual electronic structure of $Ba_{0.75}K_{0.25}Fe_2As_2$ deviates from the DFT-derived model. In principle, DFT provides a good starting point for modeling the electronic structure of the weakly correlated regime. However, when electron correlations become sizable, the low-energy bands near the Fermi level are heavily renormalized, which results in a substantial effective mass (m^*) enhancement [or equivalently, bandwidth (W) narrowing] relative to DFT calculations. Spectroscopic probes, such as ARPES, can provide direct information about the real single-particle spectra of the correlated materials, which cannot be accurately captured by DFT.

To gain more insight into the experimental electronic structure, we performed ARPES measurements on crystals from the same batch as that used for INS measurements. Figure 2 (c) shows the spectral image of $Ba_{0.75}K_{0.25}Fe_2As_2$ along the high-symmetry Z-X direction overlaid with DFT bands. The high-intensity region at the X point corresponds to the bottom of the $d_{xz/yz}$ electron band. From the ARPES data, one can notice that

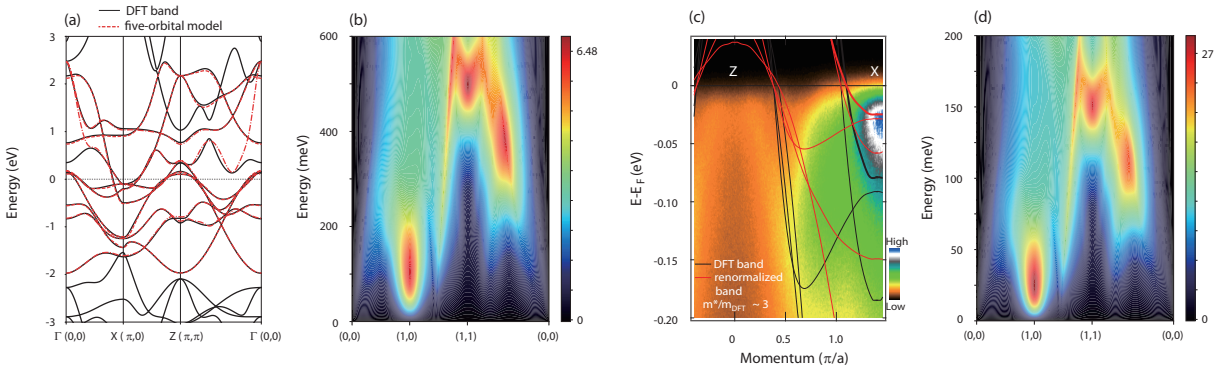

Figure 2. (a) Electronic band structure of $BaFe_2As_2$ along high-symmetry directions. The black solid lines denote the DFT band structure, whereas the red dotted lines denote the effective five-orbital model. (b) Energy-band dispersion of RPA dynamical spin susceptibility, $\chi_s(\boldsymbol{q}, E)$, along high-symmetry directions. The RPA calculation was performed for the original DFT derived band structure without mass renormalization ($m^*/m_{DFT} = 1$). (c) Comparison between ARPES and DFT band structures along the Z-X direction. The black and red lines denote the original ($m^*/m_{DFT} = 1$) and the renormalized ($m^*/m_{DFT} \sim 3$) DFT bands, respectively. The $d_{xz/yz}$ electron bands at the X point are denoted by the thick lines. (d) Energy-band dispersion of RPA dynamical spin susceptibility, $\chi_s(\boldsymbol{q}, E)$, along high-symmetry directions. To account for the ARPES-derived mass enhancement factor, the RPA calculation was performed for the renormalized ($m^*/m_{DFT} \sim 3$) DFT band structure (see ref [5]).

the experimental $d_{xz/yz}$ bandwidth is much narrower than the DFT-calculated one. As mentioned above, this is a manifestation of strong electronic correlation. The band renormalization factor (m^*/m_{DFT}), which quantifies the strength of electron correlation, is estimated by scaling the DFT band to fit the $d_{xz/yz}$ band bottom at *X*. This analysis yields $m^*/m_{DFT} \sim 3$, which is surprisingly close to the renormalization factor of the spin excitation bandwidth. Such consistency between the results of INS and ARPES has not been reported before.

Considering the strong sensitivity of the spin excitations to the underlying electronic structure, one can expect that the Fe-3*d* bandwidth narrowing due to electron correlations is directly reflected in the spin excitation energy scale. To confirm this, we re-evaluated the dynamical spin susceptibility under the scaling of the electron band energy as $\varepsilon^m_{\boldsymbol{k}} \rightarrow \varepsilon^m_{\boldsymbol{k}}/z$. (Here, $z = m^*/m_{DFT}$ is the ARPES-derived mass enhancement factor.) As shown in Fig. 2 (d), this scaling reduced the spin excitation bandwidth to ~ 1/ 3 of its original width, yielding a broadly consistent description of the observed INS data. The reasons for this consistency can easily be understood as follows. The dispersion of spin excitations is defined by the resonance condition in Eq. (2), in which the denominator of irreducible susceptibility becomes zero. If the electron band energy is renormalized as $\varepsilon^m_{\boldsymbol{k}} \rightarrow \varepsilon^m_{\boldsymbol{k}}/z$, correspondingly, a spin excitation peak energy, defined as $\varepsilon^n_{\boldsymbol{k+q}} \rightarrow \varepsilon^m_{\boldsymbol{k}}$, shows similar renormalization, much like the electron bands. This means that the concept of mass renormalization in the Fermi-liquid theory can be extended to dynamical spin susceptibility.

Our results thus demonstrate that it is possible to model the spin excitations of FeSCs by incorporating aspects of the low-energy quasiparticle renormalization that affect both single- and two-particle quantities. In addition, the consistency of the mass renormalization factors determined by independent INS and ARPES measurements highlights the potential capability of INS for characterizing the strength of electron correlations. The observed mass renormalization $m/m_{DFT} \sim 3$ is comparable to, or even larger than that of typical correlated metals such as $SrVO_3$ ($m^*/m_{DFT} \sim 2$) [6] and $Tl_2Ba_2CuO_{6+\delta}$ ($m^*/m_{DFT} \sim 3$) [7]. This means that FeSCs have stronger electron correlations than previously expected, and more importantly, such a correlated electronic state is a crucial aspect that must be taken into account for the realistic description of spin dynamics in these materials. With recent advances in modern INS spectrometers at spallation neutron sources, it is now becoming possible to experimentally determine the complicated spin susceptibility arising from the correlated electronic band structure, and in the future INS will allows us to discuss both electronic and magnetic structures on an equal footing.

3. Summary and perspectives

Historically, the development of experimental methods and instrumentation has greatly accelerated scientific progress, and this is also true for neutron spectroscopies. In particular, the availability of high-energy and high-flux neutrons at spallation neutron facilities offers a unique opportunity to use INS as a complementary spectroscopic probe to ARPES for the study of electronic band structures in the sub-eV range. The present work highlights the power and versatility of modern neutron spectroscopy as a bulk-sensitive probe of the electronic structure, by addressing some fundamental issues of electron correlation effects in FeSCs.

To date, J-PARC has ramped the operational beam power to 500 kW. The present beam power is not as high as expected, but when ramped up to its full-power capability of 1.0 MW, J-PARC will provide one of the most intense pulsed neutron beams in the world. The availability of more intense neutron sources in the next few years would further improve the potential of INS as a versatile and practical spectroscopic technique to investigate both electronic and magnetic structures on an equal footing.

References

[1] Y. Kamihara *et al.,* J. Am. Chem. Soc. **130**, 3296 (2008).
[2] W. L. Yang *et al.,* Phys. Rev. B **80**, 014508 (2009).
[3] Z. P. Yin *et al*., Nat. Mater.**10**, 932 (2011).
[4] M. Yi *et al*., npj Quantum Materials **2**, 57 (2017).
[5] N. Murai *et al.,* Phys. Rev. B **97**, 241112(R) (2018).
[6] T. Yoshida *et al.,* Phys. Rev. Lett. **95**, 146404 (2005).
[7] P. M. C. Rourke *et al.,* New J. Phys. **12**, 105009 (2010).

N. Murai[1], K. Suzuki[2], S. Ideta[3], M. Nakajima[4], K. Tanaka[3], H. Ikeda[5], and R. Kajimoto[1]
[1]Neutron Science Section, Materials and Life Science Division, J-PARC Center; [2]Research Organization of Science and Technology, Ritsumeikan University; [3]UVSOR Facility, Institute for Molecular Science; [4]Department of Physics, Osaka University; [5]Department of Physics, Ritsumeikan University

Tomonaga-Luttinger Liquid State in the Inequilateral Diamond-Chain Compound $K_3Cu_3AlO_2(SO_4)_4$

1. Introduction

Identifying spin liquid phases in the ground state is one of the hot topics in the field of low-dimensional quantum magnets. However, in most cases, experimental verification is difficult, because it is rare to have an ideal compound with negligibly weak inter-chain interactions. The distorted diamond-chain system is such a system. The ground state phase diagram of the distorted diamond-chain has been determined and it shows that there are three phases, a ferrimagnetic phase, an alternating tetramer-dimer phase, and an alternating dimer-monomer phase that represents the special case of a Tomonaga-Luttinger (TL) spin-liquid state [1, 2]. Azurite $Cu_3(CO_3)_2(OH)_2$ is considered to be one of the first experimental realizations of a spin-1/2 distorted diamond-chain system [3-6]. Therefore, a few theoretical works have also attempted to explain the unique magnetic properties of azurite, although none has yet been able to fully account for the experimentally observed behavior of this material [7, 8], due to the occurrence of relatively strong inter-chain interactions.

Recently, a highly one-dimensional (1D) inequilateral diamond-chain compound alumoklyuchevskite $K_3Cu_3AlO_2(SO_4)_4$ has been reported by some of the present authors [9].

The space group and structural parameters for the synthesized material are determined from single crystal XRD and synchrotron powder XRD [10]. Figure 1(a) and Fig. 1(b) show that $K_3Cu_3AlO_2(SO_4)_4$ contains magnetic Cu^{2+} ions in an inequilateral diamond-chain arrangement along the *a*-axis direction. The nearest-neighbor magnetic couplings, J_i ($i = 1$ to 5), are the superexchange interactions through Cu-O-Cu bonds, see Fig. 1(c). In addition, the exchange interactions through the Cu-O-S-O-Cu exchange paths are denoted by J_m, J_d, $J_{d'}$ in Fig. 1(c).

The magnetic susceptibility exhibits a double broad peak at around 200 K and 50 K. By analyzing the magnetic susceptibility, an effective model for $K_3Cu_3AlO_2(SO_4)_4$ has been proposed [11], where the dimer is formed by one of the four sides in the diamond and the remaining spins form a 1D Heisenberg chain, as shown in Fig. 1(d). The model is different from that for the azurite.

Here we report our detailed studies of $K_3Cu_3AlO_2(SO_4)_4$ through muon spin rotation/relaxation (μSR) spectroscopy and inelastic neutron scattering (INS). These experimental results indicate that $K_3Cu_3AlO_2(SO_4)_4$ is an appropriate model material for the investigation of the TL spin liquid state at low temperatures close to the ground state.

2. Experimental Details

Single phase polycrystalline $K_3Cu_3AlO_2(SO_4)_4$ was synthesized by solid-state reaction. The ZF and LF μSR experiments were performed using the spin-polarized pulsed surface-muon (μ^+) beam at the D1 beamline of the MLF of J-PARC. The INS experiments were performed on the HRC, installed at the BL12 beamline at the MLF of the J-PARC. A 400 Hz Fermi chopper was used to obtain a high neutron flux. A GM-type closed cycle cryostat was used to achieve 100 K and 4 K. The energies of incident neutrons were $E_i = 205.8$ meV and 45.95 meV (second frame), which yielded energy resolutions of $E = 5$ and 1 meV at the elastic position.

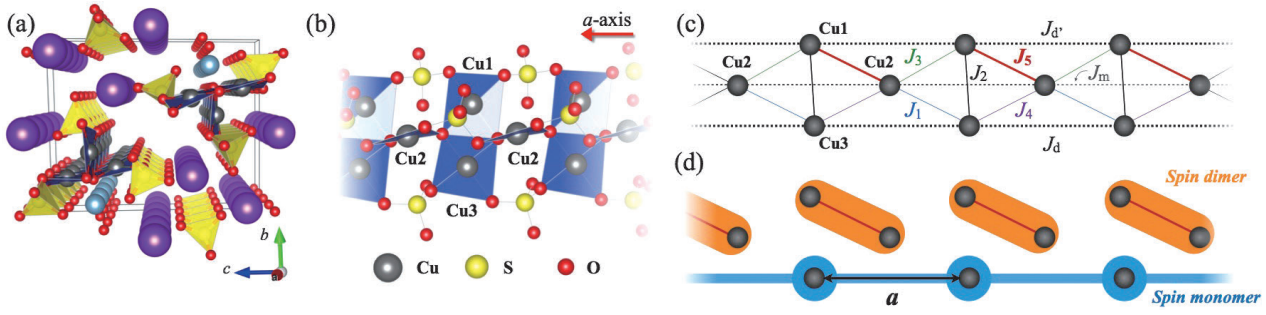

Figure 1. (a) Crystal structure of $K_3Cu_3AlO_2(SO_4)_4$ featuring a large inter-chain spacing. (b) The diamond chain of $K_3Cu_3AlO_2(SO_4)_4$, which consists of Cu^{2+} ions (grey spheres) along the *a*-axis with nearby oxygen (red spheres) and sulfur ions (yellow spheres). (c) Effective spin model of $K_3Cu_3AlO_2(SO_4)_4$ with the nearest-neighbor exchange couplings J_i ($i = 1$ to 5), and the next nearest-neighbor exchange couplings of J_m, J_d, and $J_{d'}$. (d) Spin configuration of the ground state for $K_3Cu_3AlO_2(SO_4)_4$.

3. μSR evidence for a quantum spin liquid state in $K_3Cu_3AlO_2(SO_4)_4$

Quantum spin fluctuations in $K_3Cu_3AlO_2(SO_4)_4$ are investigated by using ZF and LF μSR measurements for a powder sample in the temperature range from 90 mK to 300 K.

The ZF-μSR spectra are fitted by the stretched exponential function

$$a(t) = a_1 \exp[-(\lambda t)^{\beta}] + a_{BG},$$

where a_1 is an intrinsic asymmetry, a_{BG} is a constant background, λ is the muon spin relaxation rate, and β is the stretching exponent. The spectra at representative temperatures are presented in Fig. 2(a). The combined effect of these multiple nuclear dipole fields leads to a phenomenologically described relaxation function of the stretched exponential. The field distribution and the stretching exponent at high temperatures are approximately given by $\Delta_{nuclear} = \lambda / \gamma_{\mu} = 0.6$ G and $\beta \approx 2$, respectively, which are typical for a nuclear dipole field. The ZF spectrum at the lowest temperature 90 mK decreases continuously without oscillations up to 20 μs (see Fig. 2(b)). If this ZF spectrum is due to static magnetism, the internal field should be approximately 1.1 G. However, the relaxation is clearly observed, even in the LF at 0.4 T (see Fig. 2(c)), which is evidence for the fluctuation of Cu^{2+} electron spins without static ordering down to 90 mK.

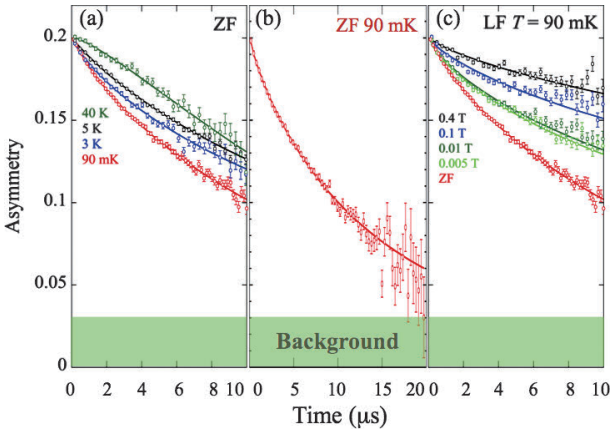

Figure 2. (a) ZF-μSR spectra at representative temperatures. The thick lines behind the data points are curves fitted by using the stretched exponential function (see text). (b) ZF-μSR spectrum measured at 90 mK, which decreases continuously without oscillations up to 20 μs. (c) μSR spectra measured at 90 mK under ZF and representative longitudinal magnetic fields.

4. Spinon continuum and spin-singlet dimer excitations in the inelastic neutron scattering spectra

The theoretical study predicted that a gapless low-energy spin excitation and gap excitation will be observed by an INS experiment, because the spin dimer together with a nearly isolated 1D Heisenberg spin chain characterizes the magnetic properties of $K_3Cu_3AlO_2(SO_4)_4$.

Figure 3(a) shows the magnetic scattering contribution at 4 K, which is obtained by subtracting the phonon contribution from the observed spectrum at 100 K. The strong flat signal is seen at approximately 10 meV, indicating that there is a van Hove singularity of spinon continuum edges at this energy. On the other hand, especially in the 1D system, powder orientational average obfuscates the INS intensity distribution and displaces considerably the Q position from the true q_{1D} position, where Q denotes the experimental wavenumber in powder experiment and q_{1D} is defined as the wavenumber along 1 chain direction. Thus, we also use a conversion method mitigating the powder average effect for a one-dimensional system [12]. This method enhances the vertically rising part of dispersion and corrects the Q position to the corresponding q_{1D} position on the basis of the differential with respect to Q. The converted result is shown in Fig. 3(b). The spinon continuum edges rise from the Brillouin zone centers in chain direction, $q_{1D} = \pi/a = 0.64$ Å^{-1} and $3\pi/a = 1.91$ Å^{-1}. In addition, the observed lower-energy boundary of the continuum is consistent with the theoretical line for the 1D spin-1/2 Heisenberg antiferromagnet given by $(\pi J_d/2)\,|\sin(Qa)|$ [13], indicating that the velocity of spin excitations of $K_3Cu_3AlO_2(SO_4)_4$ is an appropriate for the 1D spin-1/2 Heisenberg antiferromagnet.

Figure 3(c) shows the data measured with $E_i = 205.8$ meV. A signal is observed at around $E = 40$ meV and $Q = 1.0$ Å^{-1}. The signal due to magnetic excitations is generally enhanced at low-Q values, whereas phonon excitations are dominant at high-Q. Therefore, we consider that this signal comes from magnetic excitations.

The dynamical spin structure factor for the proposed model has been calculated by the dynamical density-matrix renormalization group [12]. In order to compare the calculated spectrum with the powder INS spectra in Figs. 3(a) and 3(c), we simulate the powder-averaged INS spectrum, including the magnetic form factor of Cu^{2+} , by using a conversion technique (see Eq. (2) of Ref. 13). Figure 3(d) shows the simulated powder-averaged INS spectrum. The agreement with

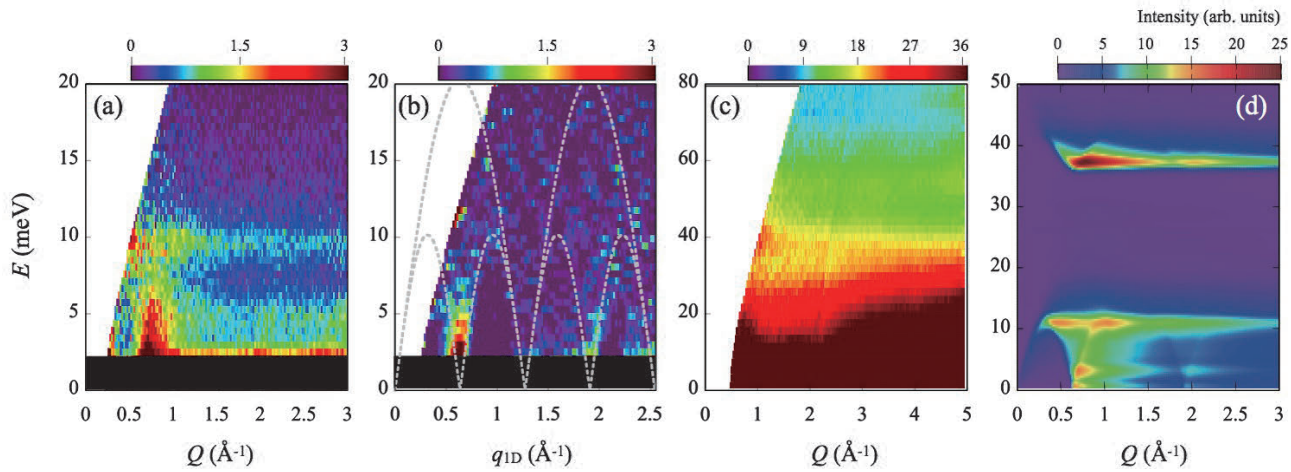

Figure 3. (a) INS spectra for $K_3Cu_3AlO_2(SO_4)_4$. (a) Magnetic scattering contribution extracted the 100 K data from the 4 K data corrected for the phonon population factor (E_i = 45.95 meV). (b) Single-crystal-like data obtained by applying the conversion method. The superimposed gray dashed lines indicate the lower and upper energy boundaries of the continuum given by $(\pi J_d/2)|\sin(Qa)|$ and $\pi J_d|\sin(Qa/2)|$ [13], respectively, where a is the lattice parameter in the chain direction. (c) Experimental raw data measured at 4 K with incident neutron energy of 205.8meV. (d) Simulated powder-averaged INS spectrum.

experimental data in Figs. 3(a) and 3(c) is fairly good. Therefore, we are confident that the proposed exchange interactions and the spin configuration shown in Fig. 1(c) are appropriate for this compound. In other words, the low-energy excitation is characterized by a TL spin liquid.

5. Summary

Spin-1/2 inequilateral diamond-chain compound $K_3Cu_3AlO_2(SO_4)_4$ has been experimentally examined by muon spin rotation/relaxation spectroscopy and inelastic neutron scattering. No three-dimensional long-range order is present down to 90 mK, $K_3Cu_3AlO_2(SO_4)_4$ is regarded as a typical compound that exhibits a TL spin liquid behavior at low temperatures close to the ground state. By comparing the INS experimental data with calculations for a theoretically proposed model, we have confirmed that the compound is described by a composite structure consisting of singlet dimers and a one-dimensional Heisenberg chain, which is different from an alternating dimer-monomer model corresponding to azurite. $K_3Cu_3AlO_2(SO_4)_4$ would further contribute to the experimental efforts in uncovering exotic properties of the TL spin liquid, such as spinon spin currents and ballistic thermal conduction.

References

[1] K. Okamoto, et. al., J. Phys.: Condens. Matter **11**, 10485 (1999).
[2] K. Okamoto, et. al., J. Phys.: Condens. Matter **15**, 5979 (2003).
[3] H. Kikuchi, et. al., Phys. Rev. Lett. **94**, 227201 (2005).
[4] K. C. Rule, et. al., Phys. Rev. Lett. **100**, 117202 (2008).
[5] K. C. Rule, et. al., Phys. Rev. B **83**, 104401 (2011).
[6] K. C. Rule, et. al., Phys. Rev. B **84**, 184419 (2011).
[7] B. Gu, et. al., Phys. Rev. Lett. **97**, 089701 (2006).
[8] H. Jeschke, et. al., Phys. Rev. Lett. **106**, 217201 (2011).
[9] M. Fujihala, et. al., J. Phys. Soc. Jpn. **84**, 073702 (2015).
[10] M. Fujihala, et. al., Sci. Rep. **7**, 16785 (2017).
[11] K. Morita, et. al., Phys. Rev. B **95**, 184412 (2017).
[12] K. Tomiyasu, et. al., *Appl. Phys. Lett.* **94**, 092502 (2009).
[13] B. Lake, et. al., *Nat. Mater.* **4**, 329–334 (2005).

M. Fujihala[1], H. Koorikawa[1], S. Mitsuda[1], K. Morita[2], T. Tohyama[2], K. Tomiyasu[3], A. Koda[4,5], H. Okabe[4,5], T. Yokoo[4,6], S. Ibuka[4], and S. Itoh[4,6]

[1]Department of Physics, Faculty of Science, Tokyo University of Science; [2]Department of Applied Physics, Faculty of Science, Tokyo University of Science; [3]Department of Physics, Tohoku University; [4]Institute of Materials Structure Science, KEK; [5]Muon Science Section, Materials and Life Science Division, J-PARC Center; [6]Neutron Science Section, Materials and Life Science Division, J-PARC Center

Magnetic Excitations from Two-Dimensional Interpenetrating Cu Framework in $Ba_2Cu_3O_4Cl_2$

1. Introduction

The elusive nature of high-temperature superconductivity continues to attract significant attention from the scientific community. At the heart of the most of these fascinating materials lies the copper-oxygen building block. To understand the electronic correlations originating from such plaquettes, closely related compounds, broadly referred to as cuprates, have received much attention. These materials are layered, possessing a square arrangement of Cu coordinated by O ions with various atoms separating the layers. Doping holes into the CuO_2 planes have been shown to drive many of these systems into complex phase space with regions in which the superconducting state is stabilized.

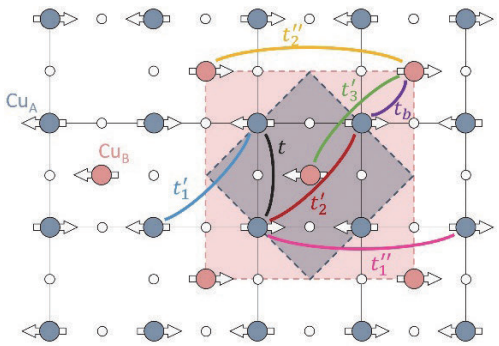

Figure 1. Depiction of the magnetic structure in $Ba_2Cu_3O_4Cl_2$. The blue and red circles represent Cu_A and Cu_B sites, respectively. The blank circles denote intermediate O atoms. The shaded blue and red outlines represent the magnetic unit cells when Cu_A and Cu_A-Cu_B are magnetically ordered, respectively. The hopping terms between ions used in our modelling are connected by colorized lines.

The planar crystal structure of $Ba_2Cu_3O_4Cl_2$ is somewhat peculiar, comprising of square lattice of Cu ions with O ions in-between mediating the exchange interactions. However, in addition there are Cu in the middle of every other square. This forms two interpenetrating Cu square lattices with an order of magnitude different coupling strengths. This arrangement is between closely related $Sr_2CuO_2Cl_2$ where no intermediate Cu ions are present and tetragonal CuO that possess Cu ions in the middle of every square. In order to characterise these compounds, we have performed a series of neutron scattering [1] and resonant x-ray experiments to map out the magnetic dispersions [2]. Using an extended one-band Hubbard model, we have been able to relate successfully the fundamental electronic correlations to derive the magnetic spectra in each compound.

2. Experimental details

Inelastic time-of-flight (TOF) neutron scattering measurements were performed using spectrometers: HRC at J-PARC, MAPS and MERLIN at ISIS. In the HRC measurements 5 crystals with a total mass of 4 g were coaligned. A Fermi chopper operating at 300 Hz was employed for the data presented herein. The MAPS and MERLIN measurements were carried out on 10 pieces of $Ba_2Cu_3O_4Cl_2$ with a combined mass of around 8 g. The Fermi chopper was set to 550 Hz and 500 Hz for the MERLIN and MAPS measurements, respectively. For all spectrometers, multi-rep mode was employed to obtain data at additional incident neutron energies E_i. The triple-axis spectrometer IN20 was used for magnetic field studies with both horizontal and vertical focusing of the Si(111) monochromator and PG(002) analyzer. A sample of co-aligned crystals totalling 8 g was mounted inside a 10 T vertical field magnet with field along the *c*-axis. A fixed final neutron energy of 14.7 meV was used for the measurements.

3. Inelastic neutron scattering results

Figure 2 shows the extracted magnon dispersion in $Ba_2Cu_3O_4Cl_2$. Our measurements suggest that the interaction between Cu_A and Cu_B must be rather small as we do not observe any magnetic zone folding or Cu_A branch splitting that would be otherwise expected. Strongly dispersive spin-waves emerge from the (0.5, 0.5) point due to coupling between Cu_A spins as it would be expected in the absence of Cu_B sublattice.

Tracking the Cu_A dispersion in energy transfer shows a maximum of around 250 meV at (0.75, 0.25) and close to 300 meV at (0.5, 0), see Fig. 2(a). The statistics of the data are poor above 300 meV and require closer examination using RIXS to complement this neutron scattering study [2]. A magnetic zone-boundary dispersion of at least 50 meV between (0.5, 0) and (0.75, 0.25) is found from our measurements. This effect has also been observed in closely related La_2CuO_4 and $Sr_2CuO_2Cl_2$ compounds and explained in terms of multi-spin exchange [3, 4]. To simulate the spin-wave spectrum, we set the hopping parameters, shown in Fig. 1, between the Cu_A sites to be the same as the

closely related $Sr_2CuO_2Cl_2$ compound. Examining the out-of-plane dispersion of the Cu_A modes and spin-gaps, we managed to constrain the exchange coupling between Cu_A spins along *c* to be 0.025(1) meV and the Cu_A-Cu_B sublattice coupling to be around $J_{AB} = -10$ meV. We found out that our model accounted well for the Cu_A dispersion over the entire magnetic Brillouin zone. Small differences, such as lower calculated spin-wave velocity at the zone center may be accounted for by (i) taking higher-order hopping parameters or (ii) inclusion of **Q**-dependence of the renormalization Z_c.

Now we turn to the low-energy dynamics of the weakly-coupled Cu_B sublattice. The Cu_B spin-waves emerge from (0.5, 0), and equivalent, positions in reciprocal space up to around 19 meV, as shown in Fig. 2(c). The excitations are gapped by 3.8(2) meV. In Fig. 2(c) we observe spin-waves from Cu_B as well as steeply rising Cu_A excitations at (0.5, 0.5). A strong magnetic zone boundary dispersion is found along (*h*, 0.25) which is shown in Fig. 2(a).

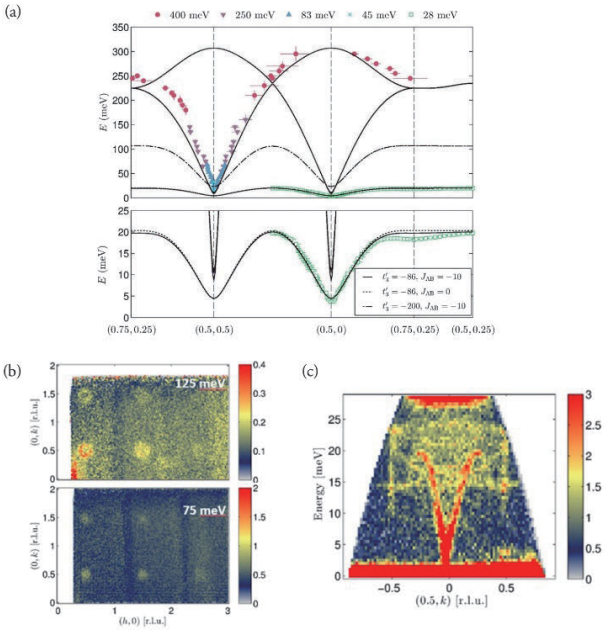

Figure 2. Dispersion along high-symmetry directions in the 2D Brillouin zone obtained at 6 K. (a) Extracted dispersion was obtained from TOF measurements using neutron incident energies in the 28–400 meV range. The simulated spin-wave spectrum is shown for different parameters of t'_3 and J_{AB} in units of meV. Other parameters were fixed to those shown in Table II and $J_\perp = 0.025$ meV. Data were collected using MERLIN, MAPS, HRC, and IN20 spectrometers. Panels (b) and (c) show representative cuts through the measured spectrum obtained from the HRC measurements. (b) shows rings from Cu_A lattice high-energy modes centred at (0.5, 0.5) while in (c) we show the gapped Cu_A modes and low-energy Cu_B dispersion.

The magnetic zone boundary in $S = 1/2$ square-lattice AFMs displays a number of intriguing quantum effects. This is reflected on the spectrum in the following ways: (i) the zone boundary at $(\pi,0)$ is around 8% lower than at $(\pi/2,\pi/2)$; (ii) half of the single-magnon intensity at $(\pi/2,\pi/2)$ is missing; and (iii) a continuum of intensity is found at $(\pi/2,\pi/2)$. The first is reproduced by the inclusion of quantum fluctuations using series expansion and quantum Monte Carlo methods for $S = 1/2$ square lattice AFMs [5-7]. The zone-boundary dispersion can also be modified by further neighbor interactions, as found for the Cu_A sublattice in $Ba_2Cu_3O_4Cl_2$ and other related materials [3,4,8-10]. However, the latter (ii) and (iii) seem to be robust for all realizations of $S = 1/2$ square-lattice AFMs studied in sufficient detail thus far. One possible origin of this effect is spinon deconfinement [11], though it may also be a spin-wave interaction effect [12].

In this framework, for sufficiently large magnetic fields, it may be possible to observe the confinement of $\Delta S = 1/2$ spinons into $\Delta S = 1$ spin waves. This is well out of reach for systems such as La_2CuO_4 and $Sr_2CuO_2Cl_2$ that would require magnetic fields far in excess of what is experimentally possible. To address this effect in $Ba_2Cu_3O_4Cl_2$, we have performed TAS measurements using a 10 T magnet with field along the crystallographic *c* axis. We observed what appeared to be a 5% sharpening of the mode at the zone boundary of the Cu_B sublattice at (1.25,0,0) — from a FWHM of 1.24(7) in zero field to 1.18(5) meV at 10 T as shown in Fig. 3. However, no clear signs of a continuum could be detected in our measurements.

In interpreting our results, we will first reflect on the seemingly missing continuum. Due to the phonon contribution, we would require polarized neutrons to conclusively exclude a continuum. However, the following considerations apply if indeed the continuum is missing. If the continuum is already suppressed in zero field, this would then explain why we also see no significant change upon applying a magnetic field. The reduction in quantum fluctuations would also impact the size of the ordered moment. Treating the Cu_B sublattice as a purely nearest-neighbor coupled Heisenberg AFM with an Ising anisotropy of 0.026 would result in an ordered moment of 0.73 μ_B, compared to the 0.6 μ_B for isotropic exchange coupling. However, our diffraction results that found a Cu_B moment of 0.6(1) μ_B cannot distinguish reliably between the two scenarios. The potential absence of a continuum could provide a promising direction for theoretical studies aiming to uncover the nature of quantum effects and we suggest both spinon

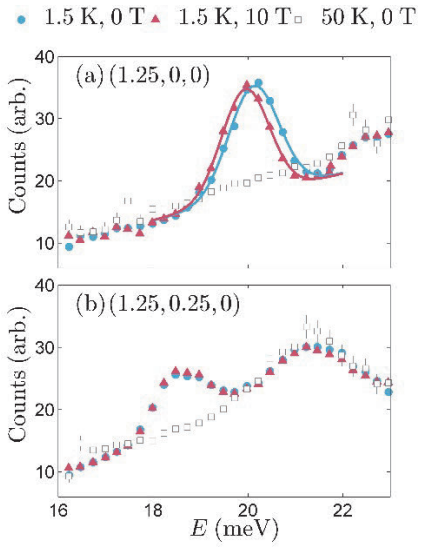

Figure 3. Magnetic field dependence of Cu_B sublattice. Constant wavevector measurements at high-symmetry points on the magnetic zone boundary, at (1.25,0,0) and (1.25,0.25,0), are shown in (a) and (b), respectively. Error bars on points for base temperature in 0 and 10 T are smaller than the point size. A Gaussian line shape is fitted to the magnetic excitations in (a).

and interacting-spin-wave based theories should investigate the effect of adding anisotropy.

4. Conclusion

Using neutron diffraction and spectroscopy we have characterized the static and dynamic magnetic properties of $Ba_2Cu_3O_4Cl_2$. Magnetic excitations are found to emerge from interpenetrating laminar sublattices of Cu_A and Cu_B spins each of which is arranged on a square-lattice. Lower energy excitations between 3 and 20 meV originate from the weakly coupled Cu_B spins and closely resemble the $Sr_2Cu_3O_4Cl_2$ spectra [13]. In addition, we track the Cu_A-like excitations up to 300 meV, which have not been previously studied in this family of materials. To characterize the spin dynamics, we employ a single-band Hubbard model from which we derive an effective spin Hamiltonian. A suitable parameterization of the magnetic spectrum is found using linear spin-wave theory. Careful analysis of the Cu_A and Cu_B spin-gaps provides us with the out-of-plane coupling, the strength of the Cu_A and Cu_B coupling as well as the exchange anisotropies. The interpenetrating Cu_B sublattice is found to be only weakly coupled to the Cu_A spins. Along the magnetic Brillouin zone boundary of weakly-coupled Cu_B spins we find a significant dispersion that we argue is a quantum effect that is beyond linear spin wave theory. On applying a magnetic field of 10 T we see a tiny magnon energy shift and sharpening. However, the effects are smaller than expected, which hints that anisotropy could be a useful parameter to tune and better understand this quantum effect.

References

[1] P. Babkevich et al., Phys. Rev. B **96**, 014410 (2017).
[2] S. Fatale et al., submitted.
[3] R. Coldea et al., Phys. Rev. Lett. **86**, 5377 (2001).
[4] M. Guarise et al., Phys. Rev. Lett. **105**, 157006 (2010).
[5] R. P. Singh and M. P. Gelfand, Phys. Rev. B **52**, R15695 (1995).
[6] O. F. Syljuåsen and H. Rønnow, J. Phys.: Condens. Matter **12**, L405 (2000).
[7] P. Babkevich et al., Phys. Rev. Lett. **117**, 237203 (2016).
[8] P. Babkevich et al., Phys. Rev. B **82**, 184425 (2010).
[9] B. D Piazza et al., Phys. Rev. B **85**, 100508 (2012).
[10] S. Moser et al., Phys. Rev. B **92**, 140404 (2015).
[11] B. D. Piazza et al., Nat. Phys. **11**, 62 (2015).
[12] M. Powalski, G. S. Uhrig, and K. P. Schmidt, Phys. Rev. Lett. **115**, 207202 (2015).
[13] Y. J. Kim et al., Phys. Rev. B **64**, 024435 (2001).

P. Babkevich[1], N. E. Shaik[1], D. Lançon[1,2], A. Kikkawa[3], M. Enderle[2], R. A. Ewings[4], H. C. Walker[4], D. T. Adroja[4,5], P. Manuel[4], D. D. Khalyavin[4], Y. Taguchi[3], Y. Tokura[3,6], M. Soda[7], T. Masuda[7], and H. M. Rønnow[1]

[1]Laboratory for Quantum Magnetism, Institute of Physics, École Polytechnique Fédérale de Lausanne (EPFL); [2]Institut Laue-Langevin; [3]RIKEN Center for Emergent Matter Science (CEMS); [4]ISIS facility, STFC Rutherford Appleton Laboratory; [5]Highly Correlated Matter Research Group, Physics Department, University of Johannesburg; [6]Department of Applied Physics, University of Tokyo; [7]Institute for Solid State Physics, University of Tokyo

Mono-Chiral Helimagnetism in $CsCuCl_3$

1. Introduction

Chiral helimagnetic structures, which form only one-handed screw magnetic structures, have attracted attention due to their characteristic magnetic textures such as Skyrmion lattices and chiral magnetic soliton lattices [1, 2]. Therefore, it is important to investigate the interplay between crystallographic and helimagnetic chirality since the sense of the rotation of helimagnetic structures strongly depends on the chiral crystal structures, which allow an anti-symmetric Dzyaloshinskii-Moriya (DM) interaction [3, 4]. However, there are not many experimental results due to the difficulty of synthesizing homo-chiral single crystals that have only right-handed (RH) or left-handed (LH) crystal domains.

Helimagnetic $CsCuCl_3$ has a chiral crystal structure with chiral space groups of RH $P6_122$ and LH $P6_522$, as illustrated in Fig. 1. Unpolarized neutron diffraction studies showed helimagnetic ordering with the magnetic propagation vector $\boldsymbol{k}_{mag} = (1/3, 1/3, \delta)$ ($\delta \sim 0.09$) below 10.5 K, suggesting a chiral screw structure with a period of 210 Å [5]. However, the interplay between crystal and magnetic chirality of $CsCuCl_3$ cannot be investigated because conventional crystal growth techniques produce racemic twinned crystals that have RH and LH domains in a sample. Here, we present a new technique to grow enantiopure single crystals and polarized neutron diffraction studies, probing a strong correlation between crystal and magnetic chiralities, which governs the nature of anti-symmetric DM interaction [6].

2. Sample preparation

Our two-step crystal growth technique for inorganic chiral compounds makes it possible to obtain centimeter-sized homo-chiral single crystals of $CsCuCl_3$ with the desired handedness. First, millimeter-sized seed crystals were synthesized by spontaneous crystallization with stirring. We succeeded in growing the homo-chiral crystals when the solution was constantly stirred in a beaker during the crystallization process [7]. Then, centimeter-sized homo-chiral crystals were obtained from the selected homo-chiral seed crystals. The spontaneous crystallization started with only one seed crystal in the saturated solution. The crystalline chirality of the obtained crystals matched that of the seed crystals. The large homo-chiral crystals made it possible to perform polarized neutron diffraction.

3. Experiments

To determine the helimagnetic chirality of the homo-chiral crystals of $CsCuCl_3$, polarized neutron diffraction experiments were performed on the BL15 (TAIKAN) in the MLF in Japan, and on the instrument POLI at the Maier-Leibnitz Zentrum (MLZ) in Germany. A single-crystal spherical neutron polarimetry technique using CRYOPAD was carried out at the POLI diffractometer operated in 2-axis mode. Neutron polarization and analysis were achieved by ^{3}He-spin filters in the incoming and scattered beams. The incomplete neutron polarization due to ^{3}He-spin filters was corrected by using a transmission monitor for the incoming beam and

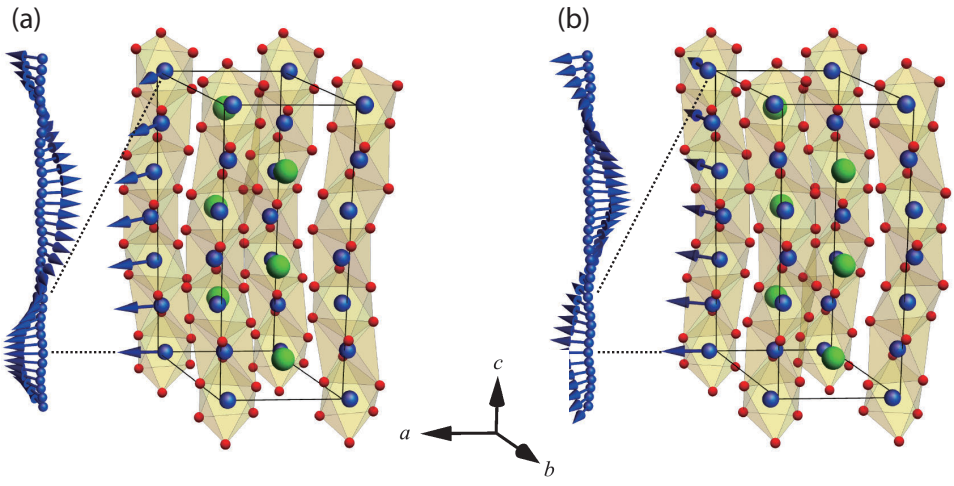

Figure 1. Crystal structures of (a) right-handed (space group: $P6_122$) and (b) left-handed (space group: $P6_522$) $CsCuCl_3$. The large, middle and small balls represent Cs, Cu and Cl ions, respectively. The arrows in a Cu chain shown in (a) and (b) represent right-handed and left-handed helimagnetic structures, respectively.

nuclear Bragg reflections for the scattered beam. The neutron spin polarization is analyzed along *i*,*f*, where *i* and *f* represent the incoming and outgoing neutron polarization, respectively. Here, *x* is one of three orthogonal directions and is parallel to the scattering vector *Q*.

4. Results and discussion

The omega-scan profiles of the spin-flip channels of the magnetic satellites are shown in Fig. 1. For the (1/3,1/3,6–δ) reflection in the RH crystal, shown in Fig. 2 (a), we observed the magnetic satellite peak only when the neutron polarization was along +*x*,–*x*. However, for the (1/3,1/3,6+δ) reflection, shown in Fig. 2 (b), the peak was observed only when the polarization was along –*x*,+*x*. The opposite behavior happened for the LH crystal, shown in Fig. 2 (c) and (d). These results indicated that the RH crystalline $CsCuCl_3$ forms purely RH helimagnetic structure, and the LH crystal forms purely LH helimagnetic structure.

Our experimental data revealed that the handedness of the magnetic helicity is coupled and directly controlled by the crystallographic lattice chirality. The results can be understood in terms of a DM interaction strongly coupled to the lattice.

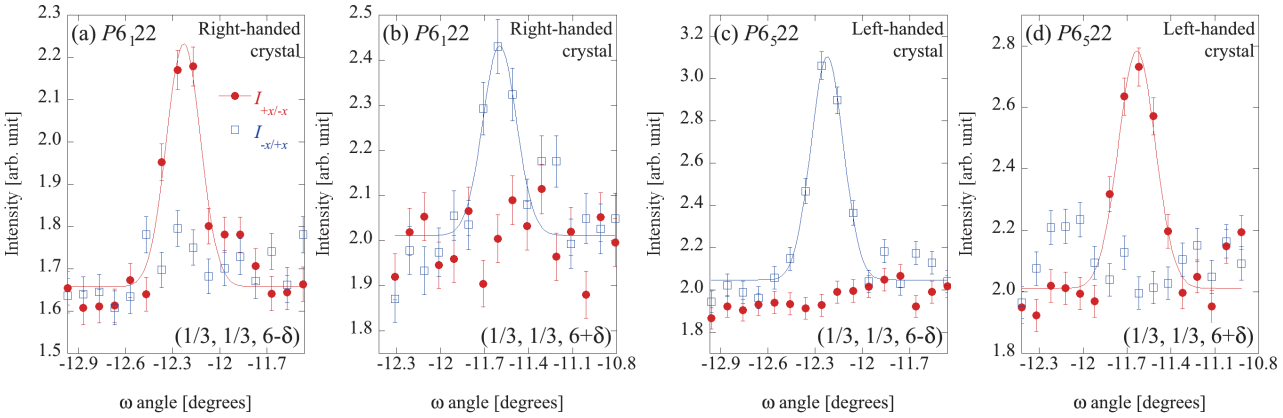

Figure 2. Omega-scan profiles of (a) $(1/3, 1/3, 6–δ) and (b) (1/3, 1/3, 6+δ) magnetic Bragg reflections for right-handed ($P6_122$) homo-chiral crystal and of (c) (1/3, 1/3, 6–δ) and (d) (1/3, 1/3, 6+δ) for left-handed ($P6_522$) homo-chiral crystal. The filled circles and open squares represent the measured intensities; the continuous lines are gaussian fits to the data.

References

[1] S. Muhlbauer, B. Binz, F. Jonietz, C. Pfleiderer, A. Rosch, A. Neubauer, R. Georgii, and P. Boni, Science **323**, 915 (2009).

[2] Y. Togawa, T. Koyama, K. Takayanagi, S. Mori, Y. Kousaka, J. Akimitsu, S. Nishihara, K. Inoue, A. S. Ovchinnikov, and J. Kishine, Phys. Rev. Lett. **108**, 107202 (2012).

[3] I. Dzyaloshinsky, J. Phys. Chem. Solids **4**, 241 (1958).

[4] T. Moriya, Phys. Rev. **120**, 91 (1960).

[5] K. Adachi, N. Achiwa, and M. Mekata, J. Phys. Soc. Jpn. **49**, 545 (1980).

[6] Y. Kousaka, T. Koyama, K. Ohishi, K. Kakurai, V. Hutanu, H. Ohsumi, T. Arima, A. Tokuda, M. Suzuki, N. Kawamura, A. Nakao, T. Hanashima, J. Suzuki, J. Campo, Y. Miyamoto, A. Sera, K. Inoue, and J. Akimitsu, Phys. Rev. Materials **1**, 071402 (2017).

[7] D. K. Kondepudi, R. J. Kaufman, and N. Singh, Science **250**, 975 (1990).

Y. Kousaka[1,2], T. Koyama[3], K. Ohishi[4], K. Kakurai[4], V. Hutanu[5], J. Campo[6], A. Sera[3], K. Inoue[2,3], and J. Akimitsu[1,2]

[1]Research Institute for Interdisciplinary Science, Okayama University; [2]Chirality Research Center, Hiroshima University; [3]Graduate School of Science, Hiroshima Univerisity; [4]Neutron Science and Technology Center, CROSS; [5]Institute of Crystallography, RWTH Aachen University and Jülich Centre for Neutron Science (JCNS) at Heinz Maier-Leibnitz Zentrum (MLZ); [6]Aragon Materials Science Institute (CSIC-University of Zaragoza)

Polarized Neutron Reflectometry Probe of the Structural and Magnetic Interfacial Inhomogeneity of Epitaxial ε-Fe_2O_3/GaN Films

1. Introduction

Hybridization of semiconducting and magnetic materials into a single heterostructure is believed to provide opportunities for designing novel functional spintronic devices. The iron oxides form a big family of magnetic materials exhibiting a rich variety of outstanding physical properties. The metastable ε-Fe_2O_3 is known to be the most intriguing ferrimagnetic and multiferroic iron oxide phase exhibiting a bunch of exciting physical properties both below and above room temperature [1]. The feasibility of growing the exotic ε-Fe_2O_3 phase along with three other iron oxide phases (Fe_3O_4, α-Fe_2O_3 and γ-Fe_2O_3) has been demonstrated [2]. Placing iron oxide film with controllable spontaneous magnetization / polarization next to the active zone of the GaN-based semiconductor devices is expected to add magnetic related functionality to these devices and attract attention to their potential use in novel designs for (opto-) electronic and spintronic applications.

2. Experimental

Polarized neutron reflectometry (PNR) experiments were performed at the SHARAKU time-of-flight instrument (beamline BL17) at the MLF [4] and D17 (ILL, France). The temperature and magnetic field at the SHARAKU instrument were controlled by a 4-T horizontal field cryomagnet (Fig. 1). The polarization of the direct beam was measured by analyzer for each value of the magnetic field used in the experiment. The amplitudes of the PNR curves were corrected for polarization efficiency. For quantitative discussions of the structure and magnetic properties of the ε-Fe_2O_3 samples the PNR data were fitted using the Parratt algorithm in the GenX software package [5].

3. PNR analysis of the nuclear and magnetic profiles of the ε-Fe_2O_3/GaN heterostructure

PNR curves R(Q_z) measured at temperatures 300 K and 10 K are shown in Fig. 2a. The splitting of $R^+(Q_z)$ and $R^-(Q_z)$ reflectivity components is proportional to the net magnetization of the film along the field direction. Because of the relatively small magnetic moment of the ε-Fe_2O_3 film, the splitting is hardly distinguishable at 300 K, but clearly observed after the sample

Figure 1. Horizontal 4 T cryomagnet installed at the SHARAKU beamline, MLF.

was cooled to 10 K in magnetic field of 2 T. For neutron reflectometry, the buffer GaN layer with thickness of 3 μm is considered the bulk medium. Thus, PNR data was fitted assuming the model consisted of GaN substrate, transition layer (interface) and ε-Fe_2O_3 layer. The resultant models are summarized in the nuclear scattering length density (SLD) and magnetic SLD profiles ($\rho_n(z)$ and $\rho_m(z)$, respectively) shown in Fig. 2b. The minimum found by the fitting algorithm corresponds to the model containing an interface layer with thickness of 37 ± 3 Å and roughness 24 ± 10 Å between iron oxide and GaN. The obtained density of the ε-Fe_2O_3 layer is reduced by 5% and GaN density is reduced by 1.5% compared to the literature values. The nuclear SLD of the interface layer is reduced compared to the main film of ε-Fe_2O_3 and close to the nominal value of ρ_n of $GaFeO_3$. The resultant magnetic $\rho_m(z)$ profile obtained at 10 K and 2 T is also shown in Fig. 2b. Interestingly, the

interface layer appears to be magnetically degraded in terms of the absolute magnetization and much softer compared to the main ε-Fe_2O_3 layer.

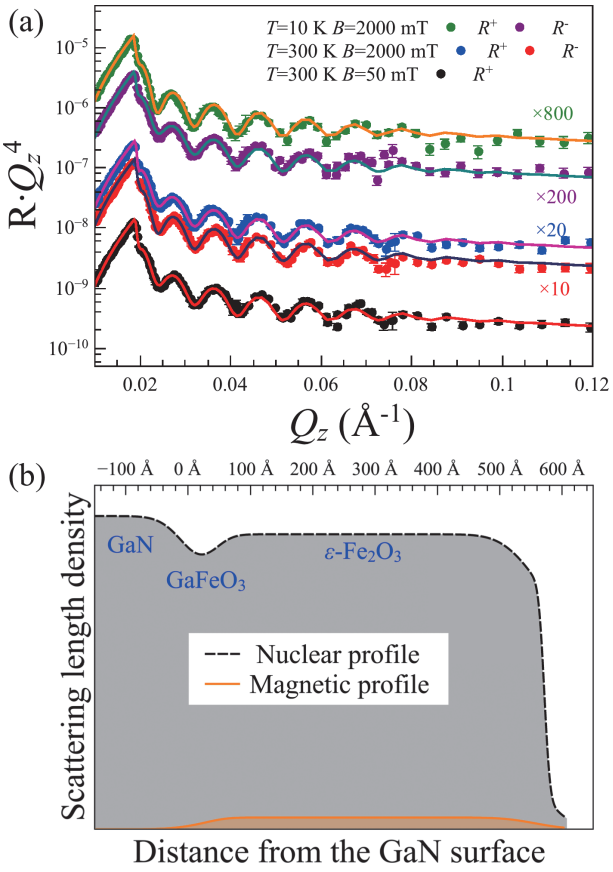

Figure 2. (a) PNR curves measured at 300 K (B = 50 and 2000 mT) and at 10 K (B = 2000 mT). Symbols represent the experimental data while the solid lines are calculated. The curves are shifted vertically for clarity. (b) Nuclear and magnetic SLD profiles delivered by fitting routine. Magnetic SLD profile obtained at 10 K and applied field 2 T is shown.

This result and the observations obtained by the complementary techniques [3] suggest that gallium substitutes iron in the interface region of the iron oxide layer leading to formation of $GaFeO_3$ compound isostructural to ε-Fe_2O_3. Formation of gallium ferrite is a probable scenario, which can explain both the magnetic degradation of the ε-Fe_2O_3/GaN interface region and the magnetization loop shapes similar to those reported for ε-Fe_2O_3 layers grown on $GaFeO_3$ buffer [6]. In the future, this issue can be further investigated by blocking Ga diffusion through introduction of a barrier layer, such as MgO or Al_2O_3 between GaN and iron oxide.

Acknowledgements

The neutron reflectivity measurements were performed on SHARAKU in J-PARC MLF under Project No. 2018A0199. We would like to thank N. Miyata, K. Akutsu, Y. Kawamura (CROSS) for the technical support and K. Kakurai (CROSS) for the fruitful discussion.

References

[1] Gich, M. et al., Advanced Materials, 26, 4645–4652 (2014).
[2] Suturin, S. et al., Physical Review Materials 2, 073403 (2018).
[3] Ukleev, V., et al., Scientific reports, 8,1, 8741 (2018).
[4] Nakajima, K., et al., Quantum Beam Science 1,3,9 (2017).
[5] Björck, M., Andersson, G., Journal of Applied Crystallography 40, 1174–1178 (2007).
[6] Thai, T. M. N. et al., Journal of Applied Physics 120, 185304 (2016).

V. Ukleev[1,2], S. Suturin[3], T. Nakajima[2], T. Arima[2,4], T. Saerbeck[5], and T. Hanashima[6]

[1]*Paul Scherrer Institut (Switzerland);* [2]*RIKEN CEMS;* [3]*Ioffe Institute (Russia);* [4]*Department of Advanced Materials Science, University of Tokyo;* [5]*Institut Laue-Langevin (France);* [6]*Neutron Science and Technology Center, CROSS*

3D Polarimetric Neutron Tomography (3DPNT)

1. Introduction

The knowledge of the inner 3D distribution of magnetic field directions and strengths inside bulk material cannot be obtained with conventional non-destructive methods. At the Energy-Resolved Neutron Imaging System BL22 beamline RADEN we have conducted the first proof-of-principle experiments that, in combination with newly developed reconstruction algorithms, have allowed us for the first time to measure the 3D magnetic field distribution of a current carrying solenoid with a technique capable of probing bulk material.

2. Underlying principle

Though electrically neutral, the neutron possesses an intrinsic magnetic moment, caused by its spin. The magnetic moment of the neutron will then precess in the presence of an external magnetic field with the precession angle being proportional to the magnitude of the magnetic field and the time spent by the neutron in the field. 3D Polarimetric Neutron Tomography (3DPNT) utilizes this effect by mapping an investigated magnetic field into the precession of the neutrons, which can be calculated from measurements of polarization for multiple initial spin orientations and projection angles.

3. Experimental set-up

Our experiments were performed at RADEN, BL22 [1], where polarizing super-mirrors and spin-rotators were used to select the initial and final spin states for polarization and analysis (see Fig. 1). The multiple spin-rotators were all ramped to be in sync with the pulsed neutron beam, so that the full polarization matrix could be measured for all wavelengths. The sample – a current carrying solenoid – was placed on a rotation stage and neutron intensity data with time-of-flight (ToF) information were recorded for 60 projection angles, each with 18 different combinations of directions of spin polarization and analysis.

4. Reconstruction technique

As the final neutron spin orientation depends not only on the strength and direction of the magnetic field regions it traverses, but also on the order by which these fields are passed through, standard filtered back-projection reconstruction methods cannot be applied directly. However, under the assumption of a relatively weak magnetic field linearized around **B**=0 (weak enough to not cause phase-wrapping, which is when neutron spin precession is larger than π), the recorded data can be transformed to an axis-angle representation, and the x, y, and z components of **B** can be reconstructed individually. The ToF information from the measurements was used to select the wavelength range in which no phase-wrapping occurred.

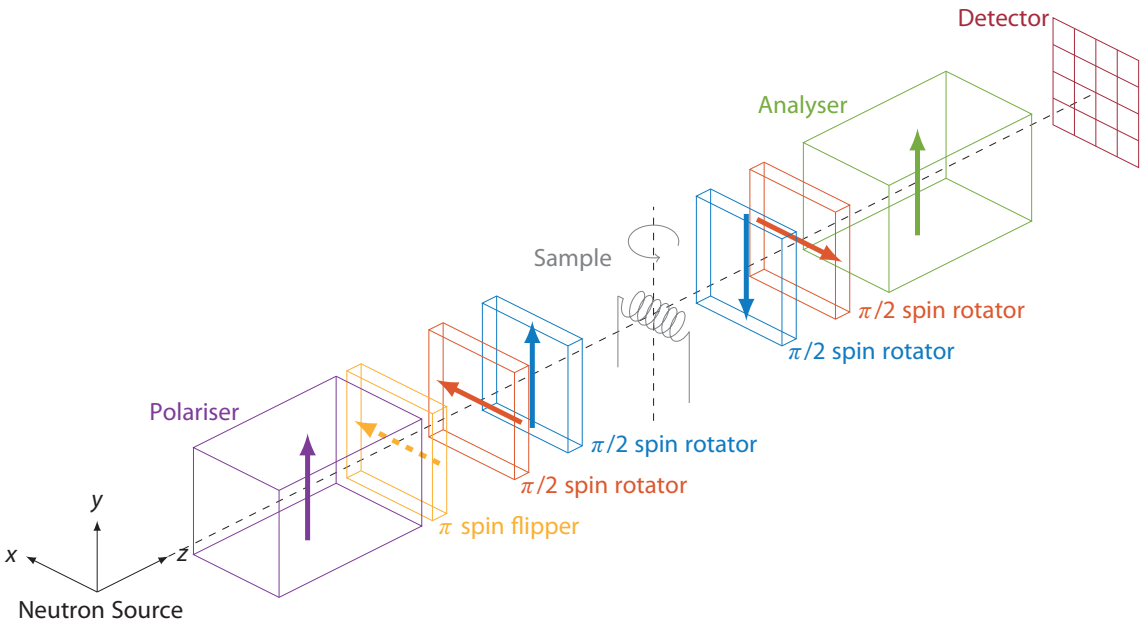

Figure 1. Schematics of the instrumental set-up. Super-mirror polarizers and analyzers, pulse-synced spin-rotators, and a both time- and position-sensitive multi-channel plate detector was used.

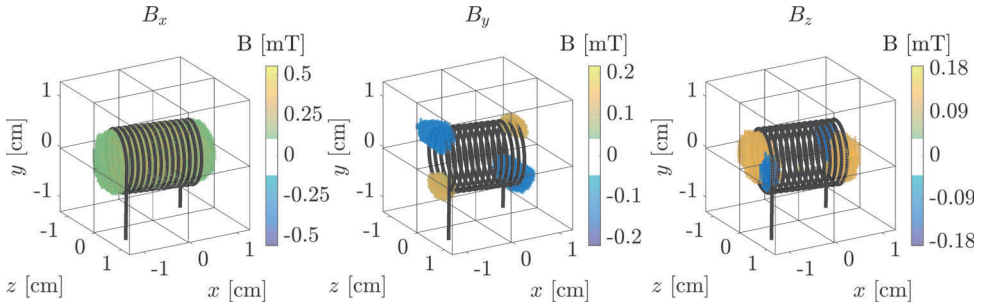

Figure 2. The reconstruction of a current carrying solenoid measured using 3DPNT. The three plots show the Bx, By, and Bz components of the magnetic field respectively.

5. Results

Figure 2 shows the reconstructed magnetic field from the current carrying solenoid measured with 3DPNT [2]. The main magnetic field, along the solenoid axis, as well as the magnetic field components, where the field wraps around the ends of the solenoid, are easily seen. Moreover, the magnetic field from the wires going to and from the solenoid was resolved as well. The reconstructed results were furthermore confirmed by finite element Biot-Savart law calculations of the magnetic field from a solenoid of the same shape and size, carrying the same current of 0.6 A.

6. Conclusion

Our work at RADEN has provided a solid proof-of-principle showing the possibilities of 3DPNT as a technique capable of revealing hitherto unattainable information of 3D magnetic field distributions and electric current flow. Such information can be of value in a range of scientific and material design disciplines such as the development of batteries and other energy materials, superconductors, shape-memory alloys, and in other investigations of the interplay between structural and magnetic sample compositions.

7. Future plans

The technique presented here is limited to the measurement of magnetic fields strong enough to cause resolvable spin precession while at the same time weak enough to not cause spin precession beyond π. To broaden the applicable range of 3DPNT, we are currently working on an iterative forward model optimization reconstruction algorithm taking full advantage of the ToF information at RADEN in order to reconstruct stronger magnetic fields. Furthermore, we have recently used the technique at RADEN to study the 3D electric current flow in a battery model.

References

[1] T. Shinohara et al., J. Phys.: Conf. Ser. **862**, 012025 (2017).

[2] M. Sales et al., Sci. Rep., **8**, 2214 (2018).

M. Sales[1], M. Strobl[2], T. Shinohara[3], A. Tremsin[4], L. Theil Kuhn[5], W. R. B. Lionheart[6], N. M. Desai[6], A. Bjorholm Dahl[7], and S. Schmidt[1]

[1]Department of Physics, Technical University of Denmark; [2]Laboratory for Neutron Scattering and Imaging, Paul Scherrer Institute, Switzerland; [3]Neutron Science Section, Materials and Life Science Division, J-PARC Center; [4]Space Sciences Laboratory, University of California at Berkeley, Berkeley, USA; [5]Department of Energy Conversion and Storage, Technical University of Denmark; [6]School of Mathematics, The University of Manchester, United Kingdom; [7]Department of Applied Mathematics and Computer Science, Technical University of Denmark

First Muon Acceleration Using a Radio-Frequency Accelerator

1. Introduction

Muon acceleration using radio-frequency (RF) accelerator has been discussed due to its potential advantages. For example, in muon collider and neutrino factory studies [1], it has been proposed that the large transverse emittance of the muon beam could be reduced through ionization energy loss and subsequent acceleration [2, 3]. In material and life sciences, one promising application of muon acceleration is in the construction of a transmission muon microscope. Transmission muon microscopes will become possible, if the muons can be cooled to the thermal temperature (ultraslow muon, USM) and subsequently re-accelerated [4]. Another application of USM acceleration is the precise measurement of the muon anomalous magnetic moment $a_\mu = (g_\mu - 2)/2$ and the electric dipole moment (EDM) [5] (Fig. 1). Muon acceleration is essential to realize these applications; however, it has not been demonstrated.

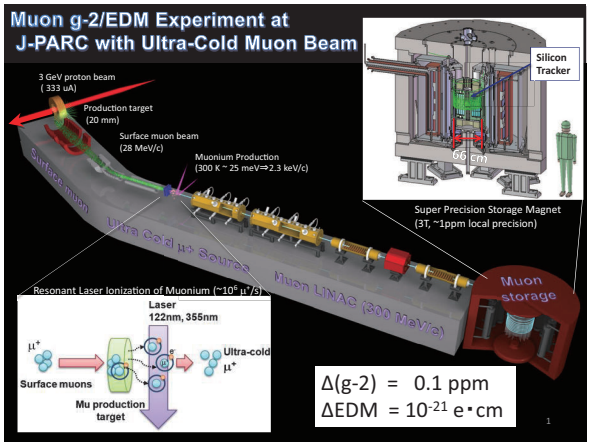

Figure 1. Overview of the J-PARC muon g-2/EDM experiment.

In October 2017, we successfully demonstrated the first negative muonium ions (Mu^-'s) [6], which will be reported in this paper.

2. Experimental setup

The experiment was conducted using a radio-frequency quadrupole linac (RFQ) installed at the MUSE D2 area. Figure 2 shows the experimental setup. A pulsed surface muon (μ^+) beam was injected into an aluminum degrader, and some portions form the Mu^-'s. The μ^+ energy was chosen to be 2.9 MeV to maximize the Mu^- emission yield on the basis of a separate experiment [7]. The Mu^-'s were extracted and accelerated to 5.6 keV by an electrostatic lens. They were then injected into the RFQ and accelerated to 89 keV. The accelerated Mu^-'s were detected by a micro-channel plate (MCP) detector after a diagnostic beamline. The diagnostic beamline consisted of a magnetic quadrupole pair (QM1 and QM2) and a bending magnet.

3. Results

Figure 3 shows the time of flight (TOF) spectrum with and without the RF operation after event selections. With the RF operation, a clear peak was observed at 830 ns. The TOF spectrum was confirmed with a series of simulations and it was consistent with the measurement within statistical error. The hatched histogram in Fig. 3 represents the simulated TOF spectrum of the accelerated Mu^-'s. The number of simulation events was normalized to the number of the incident muons in the data.

From these experimental results, it was concluded that the observed TOF peak was due to the Mu^-'s accelerated by the RFQ to 89 keV.

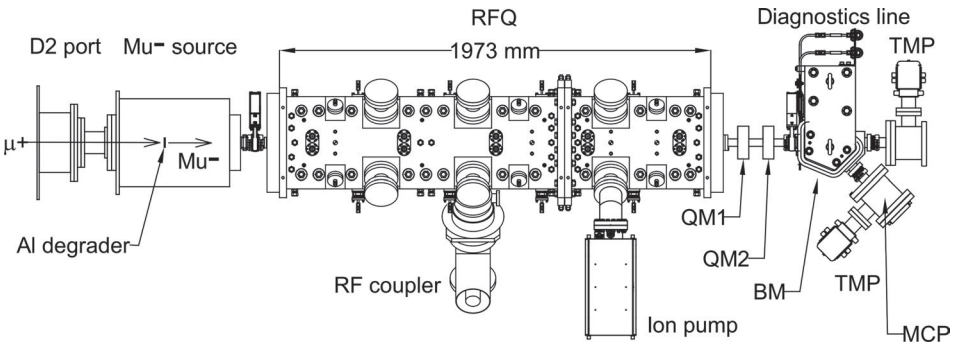

Figure 2. Schematic drawing of the experimental setup [6].

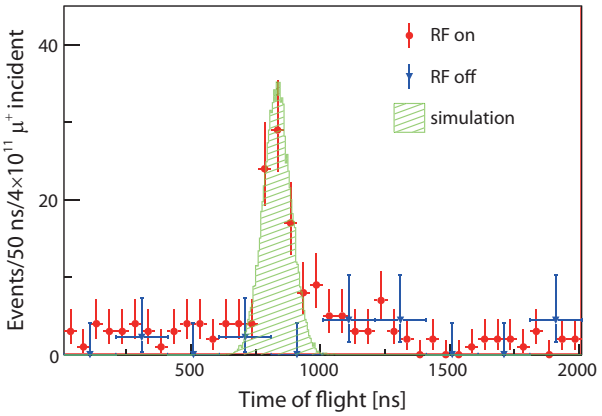

Figure 3. TOF spectra of the negative-charge configuration with RF on (rec circle) and off (blue rectangle) [6]. A simulated TOF spectrum of the accelerated Mu^-'s is also plotted (green hatched).

4. Conclusion and outlook

In summary, muons have been accelerated by RF acceleration for the first time. Slow Mu^-'s were generated through the electron capture process of the degraded μ^+'s in the D2 area of J-PARC MUSE, and accelerated with the RFQ up to 89 keV.

The intensity of the accelerated Mu^- in this experiment was limited by the very low conversion efficiency of μ^+ to Mu^-. With the construction of the new H line and assuming the design value of 1-MW beam power from the RCS, the intensity is expected to reach 2×10^{-2}/s. Finally, the laser-dissociation ultraslow muon source is expected to be installed in this beamline to obtain a muon rate of 10^6/s, the design intensity for the muon g-2/EDM experiment.

The results presented in this article are the first step toward making the low-emittance muon beam available as a powerful tool for application in material and life sciences and fundamental physics research.

Acknowledgements

This work was supported by JSPS KAKENHI Grant Numbers JP25800164, JP15H03666, JP16H03987, JP15H05742, JP16J07784, and JP18H03707. This experiment at the Materials and Life Science Experimental Facility of the J-PARC was performed under user programs (Proposal No. 2017A0263).

References

[1] M.A. Palmer, ICFA Beam Dynamics Newsletter, 55 (ICFA, 2011).
[2] D. Neuffer, Part. Accel. 14, 75 (1983).
[3] P. Franchini, Proc. of 9th International Particle Accelerator Conference, Vancouver, BC, Canada, pp. 4766 – 4768.
[4] http://slowmuon.kek.jp/MuonMicroscopy_e.html
[5] http://g-2.kek.jp/portal/index.html
[6] S. Bae et al., Phys. Rev. Accel. Beams 21, 050101 (2018).
[7] R. Kitamura et al., J. Phys. Conf. Ser. 85, 012055 (2017).

M. Otani[1,2], S. Bae[3], H. Choi[3], S. Choi[3], Y. Fukao[4,5], K. Futatsukawa[1,2], K. Hasegawa[6], T. Iijima[7], H. Iinuma[8], K. Ishida[9], N. Kawamura[10,11], B. Kim[3], R. Kitamura[12], H. S. Ko[3], Y. Kondo[6], S. Li[12], T. Mibe[4,5], Y. Miyake[10,11], T. Morishita[6], Y. Nakazawa[8], G. P. Razuvaev[13], N. Saito[14], K. Shimomura[10,11], Y. Sue[7], E. Won[15], and T. Yamazaki[10,11]

[1]Accelerator Division, J-PARC Center; [2]Accelerator Laboratory, KEK; [3]Seoul National University; [4]Particle and Nuclear Physics Division, J-PARC Center; [5]Institute of Particle and Nuclear Studies, KEK; [6]Japan Atomic Energy Agency; [7]Nagoya University; [8]Ibaraki University; [9]Riken; [10]Muon Science Section, Materials and Life Science Division, J-PARC Center; [11]Institute of Materials Structure Science, KEK; [12]University of Tokyo; [13]Budker Institute of Nuclear Physics; [14]J-PARC Center; [15]Korea University

μSR Study of $Sr_{2-x}La_xIrO_4$ Synthesized by Mechanical Alloying

1. Introduction

5d transition-metal oxides (TMOs) exhibit exotic phenomena because their spin-orbit coupling (SOC) is one order of magnitude larger than that of 3d TMOs. Recently, Kim et al. proposed a spin-orbit Mott state with a local $J_{eff} = 1/2$ in Sr_2IrO_4 [1]. Spin-orbital coupling Mott insulator Sr_2IrO_4 (SIO) shares with cuprates several distinctive features [2] that characterize high-temperature superconductors (HTSC). Due to the similar Mott physics between cuprates and iridates, Sr_2IrO_4 is a good candidate for exploring unconventional HTSC by carrier doping.

The physical properties of electron-doped Sr_2IrO_4 systems have been extensively studied in experiments by several groups. The neutron scattering study in single-crystalline samples of $Sr_{2-x}La_xIrO_4$ indicated that the long-range antiferromagnetic (AF) order was suppressed up to $x = 0.08$ and the short-range AF order persisted up to $x = 0.12$ due to the lack of a magnetic Bragg peak [3]. However, it was mentioned that the detection limit of magnetic scattering was 0.06 μ_B because of high neutron absorption of Ir. Thus, it remains unclear whether a short-range AF above $x = 0.08$ can be observed. Therefore, we have performed μSR experiments in $Sr_{1.9}La_{0.1}IrO_4$ to clarify the mentioned uncertainty.

2. Experiments

Polycrystalline samples of $Sr_{1.9}La_{0.1}IrO_4$ were prepared by conventional solid-state reactions. A mixture of $SrCO_3$, La_2O_3, and IrO_2 was ground and further mixed by planetary ball milling (Fritsch, P-7) at a rotation rate of 400 rpm for 3 h with 15 (5 mm-diameter) and 10 (10 mm-diameter) ZrO_2 balls. The resulting powders were calcined in air at 1150°C for 15 min. To examine the effects of mechanical milling on the morphology of polycrystalline $Sr_{2-x}La_xIrO_4$ samples, we characterized these samples by SEM. Comparing the mechanical alloying (MA) and non-MA samples, there were fewer grains in the MA samples at the same scale length, indicating that a post-MA reaction increased the size of the crystal grains and reduced the number of grain boundaries.

Zero-field (ZF)- and longitudinal field (LF)-μSR experiments were performed using the Advanced Research Targeted Experimental Muon Instrument at the S line (ARTEMIS) spectrometer [4] with a fly-past chamber at the Material and Life Science Experimental Facility (MLF), J-PARC, Tokai, Japan.

3. Results and discussion

Figure 1(a) shows selected ZF-μSR time spectra of $Sr_{1.9}La_{0.1}IrO_4$ in the temperature range 3.4–300 K. Non-oscillatory signals are present, indicating the absence of a long-range-magnetic order even below T_N (~180 K), which was also determined by magnetic susceptibility measurements. The oscillations are not completely absent, but the spectral damping becomes faster with decreasing temperature and the spectrum at 3.4 K shows a shallow "dip" that signals freezing of fluctuating random local fields, where the line shape is close to that of a quasi-static spin-glass state. The time evolution of the spectra above 14 K can be fitted by the following function:

$$A_{ZF}(t) = A_s \exp(-\lambda t)^{\beta} + A_{bg} \quad (1)$$

Here, A_s and A_{bg} are the positron decay asymmetries (amplitudes) of the sample ($A_s = 0.2048$) and background ($A_{bg} = 0.0293$, mainly from a silver plate) components, respectively; λ is the relaxation rate; and β is the stretching exponent.

Figure 1(b) shows the temperature dependences of λ and β. A three-step decrease appears in β as the temperature decreases. As evidenced in the lower panel of Fig. 1(b), β begins to decrease from approximately 300 K, suggesting the development of short-range spin correlations between the intralayer Ir ions. Subsequently, a gradual decrease of β from 0.8 to 0.6 appears around 180 K, corresponding to T_N. Because this behavior has often been observed in frustrated antiferromagnets, the magnetic state below T_N was determined as a short-range AF order coexisting with spin fluctuation that is detectable within the muon time scale. This situation can also be explained as a Griffiths phase, in which short-range AF clusters occur and grow upon cooling in the paramagnetic phase. Spin autocorrelation functions in the Griffiths phase can be described by a stretched exponential of the form $\exp(-\lambda t)^{\beta}$ with $\beta = 0.5$ [5], which is also consistent with our fitting results. As the temperature decreases further (to below 50 K), β reaches around 1/3, a typical value in dilute spin-glass systems.

To distinguish the low-temperature spin-glass state more clearly, we performed LF-μSR measurements on

$Sr_{1.9}La_{0.1}IrO_4$. As the LF increases, the persisting asymmetry is enhanced under restoration of the initial muon polarization; usually, this is called decoupling effect. The decoupling behavior in Fig. 1(c) clearly indicates that most of the Ir electronic spins are static in this state.

Before discussing the Ir moment size, we should determine where the implanted muon is located in $Sr_{1.9}La_{0.1}IrO_4$. The previous μSR study [6] indicated that there were two main types of muon sites in Sr_2IrO_4; one near the apical oxygen, the other near the in-plane oxygen. However, the implanted muons do not occupy these sites equally: more than 90% of the muons are located in the apical oxygen site of Sr_2IrO_4. We thus assume that all implanted muons occupy the apical oxygen site in $Sr_{1.9}La_{0.1}IrO_4$ (as in Sr_2IrO_4), because both crystal structures (x = 0 and x = 0.1) are nearly unchanged. We now estimate the Ir moment size of $Sr_{1.9}La_{0.1}IrO_4$. In Sr_2IrO_4, the moment size of the J_{eff} = 1/2 pseudospin is reduced to ~0.4 μ_B, as confirmed by previous μSR, RIXS, and neutron diffraction measurements. On the other hand, the effective Ir moment size of $Sr_{1.9}La_{0.1}IrO_4$ $|\mu_{Ir}|$ was determined as 0.0452(3) μ_B. This value is about one-tenth of that of Sr_2IrO_4 (0.4 μ_B), so the decrease of the Ir moment is attributed to the effects of electron doping by La substitution. This work has been published in PRB [7].

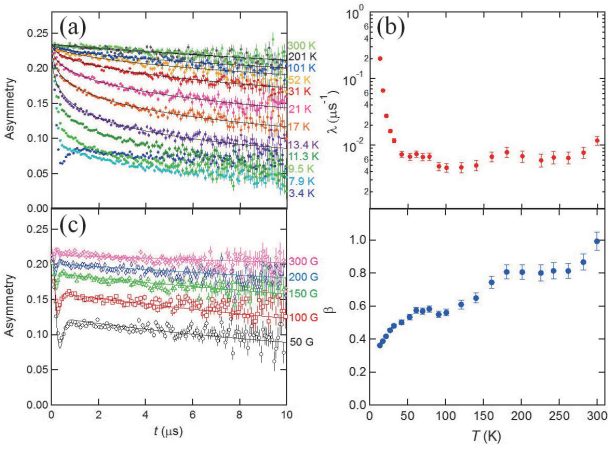

Figure 1. (a) Temperature dependence of ZF-μSR time spectra for $Sr_{1.9}La_{0.1}IrO_4$. (b) Temperature dependence of the λ and β. (c) LF-μSR time spectra

4. Future Plans

We summarized the magnetic phase diagram of $Sr_{2-x}La_xIrO_4$ determined by μSR and magnetic susceptibility measurements (Fig. 2). Although we have clarified the short-range magnetic order in $Sr_{1.9}La_{0.1}IrO_4$, it is still not clear how the long-range order changes to a short-range order with electron doping in the Sr214 system. To clarify the magnetic phase diagram in the Sr214 system, we will perform μSR experiments in electron-doped $Sr_{2-x}La_xIrO_4$ [x = 0.05 (T_N ~208 K), x = 0.075 (T_N ~198 K), and x = 0.13 (T_N ~114 K)] in a future work.

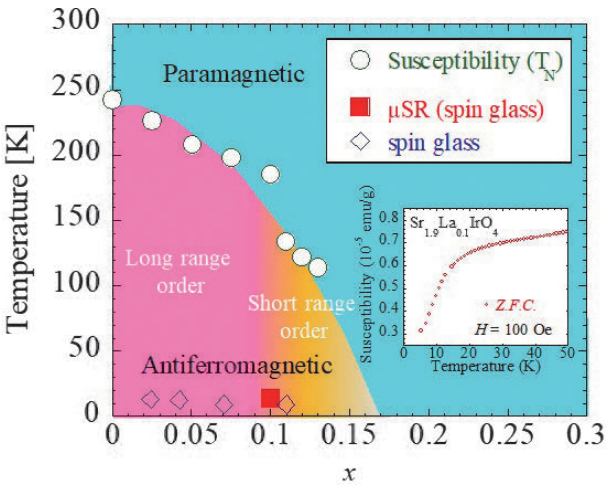

Figure 2. Magnetic phase diagram of $Sr_{2-x}La_xIrO_4$ detemined by magnetic susceptibility and μSR measurements. Inset shows the magnetic susceptibility data (x = 0.1) under a zero-field cooling process

References

[1] B. J. Kim et al., PRL. **101**, 076402 (2008).
[2] K. Terashima et al., PRB **96**, 041106(R) (2017).
[3] C. Chen et al., PRB **92**, 075125 (2015).
[4] K. M. Kojima et al., J. Phys. Conf. Ser. **551**, 012063 (2014).
[5] A. J. Bray, PRL. **59**, 586 (1987).
[6] M. Miyazaki et al., PRB **91**, 155113 (2015).
[7] K. Horigane et al., PRB **97**, 064425 (2018).

K. Horigane[1], M. Fujii[2], H. Okabe[3,4], K. Kobayashi[1,2], R. Horie[1], H. Ishii[5], Y. F. Liao[5], Y. Kubozono[1] A. Koda[3,4], R. Kadono[3,4], and J. Akimitsu[1]

[1]Research Institute for Interdisciplinary Science, Okayama University; [2]Graduate School of Natural Science and Technology, Okayama University; [3]Muon Science Section, Materials and Life Science Division, J-PARC Center; [4]Institute of Materials Structure Science, KEK; [5]National Synchrotron Radiation Research Center

Development of Ferromagnetic Fluctuations in Heavily Overdoped $(Bi,Pb)_2Sr_2CuO_{6+\delta}$ Copper Oxides

1. Introduction

It is well known in the hole-doped high-T_c superconducting cuprates that the superconductivity emerges through hole doping into the parent antiferromagnetic (AF) Mott insulator, suggesting that the superconductivity is mediated by AF spin fluctuations in the underdoped and optimally doped regimes. In the overdoped regime where the superconducting (SC) transition temperature T_c is depressed with hole doping, inelastic neutron-scattering [1] and muon spin relaxation (μSR) [2] experiments have revealed the weakening of the low-energy AF spin fluctuations with hole doping. A recent resonant inelastic x-ray scattering experiment, on the other hand, has revealed that high-energy AF fluctuations persist to the non-SC heavily overdoped regime [3]. This suggests that the suppression of superconductivity in the heavily overdoped regime might not be related to AF fluctuations.

Formerly, Sonier *et al*. have observed from zero-field (ZF) μSR measurements in the non-SC heavily overdoped $La_{2-x}Sr_xCuO_4$ single crystals that the relaxation rate of muon spins λ is enhanced at very low temperatures below 0.9 K [4]. Considering the ab-plane electrical-resistivity ρ_{ab} and magnetization results, they have proposed the formation of a three-dimensional ferromagnetic (FM) order of itinerant electrons in the non-SC heavily overdoped regime. This seems to be a challenge to the common understanding that a simple Fermi-liquid-like ground state without magnetism is realized in the non-SC heavily overdoped cuprates. The FM fluctuations might suppress the superconductivity in the heavily overdoped regime owing to the competition between AF and FM fluctuations [5]. Since the FM order appears at very low temperatures, however, its details, including the universality of this phenomenon in high-T_c cuprates, have not yet been investigated.

In order to investigate possible FM fluctuations, we have performed measurements of ρ_{ab}, magnetization, specific heat, μSR in heavily overdoped $(Bi,Pb)_2Sr_2CuO_{6+\delta}$ (Bi-2201) cuprates [6]. Single crystals of Bi-2201 were grown by the floating-zone technique. The hole concentration per Cu p was determined by the empirical equation and the thermoelectric power. ZF- and longitudinal-field μSR measurements were performed at J-PARC/MLF and the RIKEN-RAL Muon Facility in the UK.

2. Results and discussion

The static magnetization curve of heavily overdoped Bi-2201 have revealed that, while the magnetization curves are linear in the magnetic field above 20 K, it becomes nonlinear and tends to be saturated in high magnetic-field regions below 20 K. Considering no hysteresis in the magnetization curve down to 0.5 K, the saturated magnetization in high magnetic fields at low temperatures is probably a precursor phenomenon of the FM transition at a lower temperature.

For dynamic behaviors of spins, Fig. 1 shows the temperature dependence of λ of Bi-2201. It was found that λ increases with decreasing temperature below 200 K and the increase becomes larger with hole doping. These results suggest that spin fluctuations, probably FM fluctuations, are developed at high temperatures and are enhanced with hole doping in heavily overdoped Bi-2201.

The temperature dependence of ρ_{ab} in Bi-2201 have exhibited a $T^{4/3}$ behavior over a wide temperature range in the heavily overdoped regime. Figure 2 shows the p dependence of the exponent n obtained by expressing ρ_{ab} in the normal state as $\rho_{ab} = \rho_0 + AT^n$, where ρ_0 is the temperature-independent term and A is the temperature coefficient. It was found that $n \sim 1$ near the optimally doped regime and that n increases with overdoping and converges to 4/3 in the heavily overdoped regime, which is incompatible with the nonmagnetic

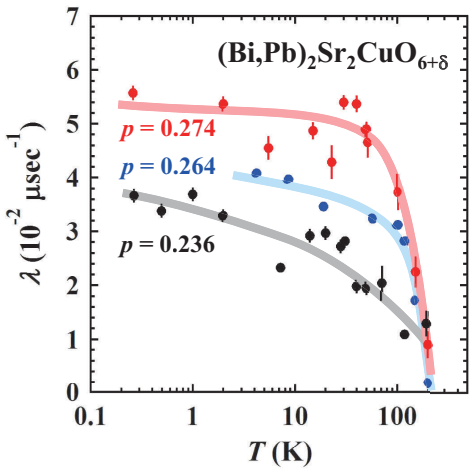

Figure 1. Temperature dependence of the relaxation rate of muon spins λ of $(Bi,Pb)_2Sr_2CuO_{6+\delta}$. The solid lines are included to guide the reader's eye.

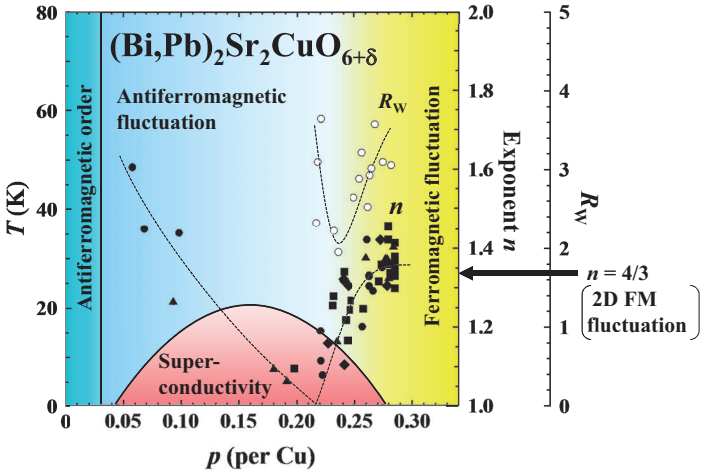

Figure 2. Schematic phase diagram of $(Bi,Pb)_2Sr_2CuO_{6+\delta}$. The open circles represent the Wilson ratio R_W. The closed circles, triangles, squares and diamonds represent the exponent n of $\rho_{ab} = \rho_0 + AT^n$. The dashed lines are included to guide the reader's eye.

Fermi-liquid-like T^2 behavior. According to the SCR theory, the $T^{4/3}$ behavior of ρ_{ab} is characteristic of metals with two-dimensional FM fluctuations due to itinerant electrons. The specific heat of Bi-2201 has also exhibited the behavioral characteristics of metals with two-dimensional FM fluctuations.

To obtain further insights into the FM fluctuations, we have estimated the Wilson ratio R_W relating to spin fluctuations from the static magnetic susceptibility and the electronic specific-heat coefficient. As shown in Fig. 2, surprisingly, R_W increases with hole doping in the heavily overdoped regime of $p > 0.23$, suggesting the enhancement of spin fluctuations.

The proposed new phase diagram of Bi-2201 is shown in Fig. 2. As characterized by the increase in R_W and the saturation of n around 4/3, the region of the FM fluctuations is shown in the heavily overdoped regime. It was found that the magnetic ground state changes from the AF to FM one with hole doping. The FM fluctuations exist even in the SC heavily overdoped regime, implying the interference between FM fluctuations and the electron paring mediated by AF fluctuations and resulting in the decrease in T_c with hole doping in the heavily overdoped regime.

The origin of the FM fluctuations has not been clarified yet. A possible candidate is the metallic ferromagnetism due to enhanced spin fluctuations as observed in R_W, the large density of states at the Fermi level suggested from angle-resolved photoemission spectroscopy [7] etc. and the good Fermi-surface nesting with the nesting vector of $q \sim 0$ suggested from the theoretical calculation [8].

3. Conclusion

FM fluctuations exist in heavily overdoped Bi-2201, suggesting the universal feature of the hole-doped cuprates. The magnetic ground state changes from the AF to FM one with hole doping. Moreover, the FM fluctuations are possibly related to the suppression of superconductivity in the heavily overdoped regime. The specific relationship between the FM fluctuations and superconductivity in cuprates should be clarified in the future.

References

[1] S. Wakimoto *et al.*, Phys. Rev. Lett. **92**, 217004 (2004).
[2] Risdiana *et al.*, Phys. Rev. B **77**, 054516 (2008).
[3] M. P. M. Dean *et al.*, Nat. Mater. **12**, 1019 (2013).
[4] J. E. Sonier *et al.*, PNAS **107**, 17131 (2010).
[5] A. Kopp *et al.*, PNAS **104**, 6123 (2007).
[6] K. Kurashima *et al.*, Phys. Rev. Lett. **121**, 057002 (2018).
[7] M. Hashimoto *et al.*, Phys. Rev. B **77**, 094516 (2008).
[8] D. Ogura and K. Kuroki, Phys. Rev. B **92**, 144511 (2015).

T. Adachi[1], K. Kurashima[2], I. Watanabe[3], M. Miyazaki[4], A. Koda[5], R. Kadono[5], and Y. Koike[2]
[1]Department of Engineering and Applied Sciences, Sophia University; [2]Department of Applied Physics, Tohoku University; [3]Meson Science Laboratory, RIKEN Nishina center; [4]Graduate School of Engineering, Muroran Institute of Technology; [5]Muon Science Section, Materials and Life Science Division, J-PARC Center and Institute of Materials Structure Science, KEK

Neutron Source

Progress of the Neutron Source Section

Fiscal year 2017 set in motion a new challenge to achieve a high-power operation by using a re-designed target vessel. The aim of the target operation was to establish a stable neutron production with a beam power from 300 to 500 kW. In the first half of the fiscal year, target vessel #2, which does not have a gas micro-bubbles injection system, operated at 150 kW continuously from the previous fiscal year until June 2017. The operation was calm and stable, without any serious problems.

In the summer shutdown period, target vessel #2 was replaced with a brand-new re-designed one. The proton beam window was also replaced with a new one. Details of the observation of damages induced on target #2 and the proton beam window replacement are described elsewhere in this activity report.

1. Mercury target operations with a re-designed target vessel

Figure 1 shows a photograph of the re-designed target vessel. It is the eighth target vessel in the fabrication order. To ensure more reliable structural integrity of the target vessel #8, a new fabrication method was introduced. The welding, previously used for coupling between the inner mercury vessel and the outer water shroud, was replaced by a monolithic structure in the forward part where high thermal stress is induced. In the rear part, the structure of the water shroud has also been improved by adopting a monolithic structure. Furthermore, all welding lines were inspected carefully with RT (Radiographic Test). In the end, target vessel #8 was delivered to the MLF on September 17, 2017.

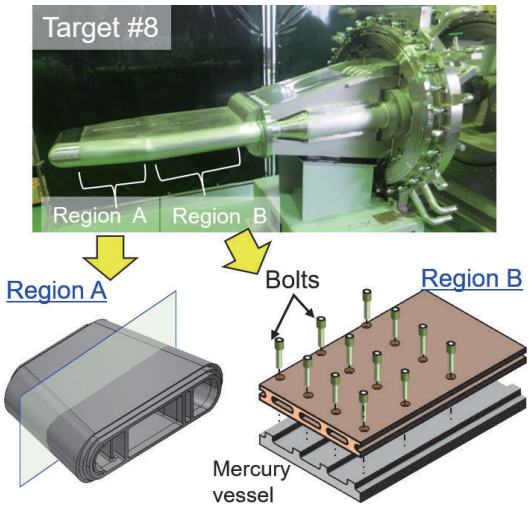

Figure 1. Photo of re-designed target vessel #8 with schematics of structures in the forward and the rear part (lower).

For target vessel #8, the following measures were taken to mitigate pitting damage at the beam window portion: 1) gas-micro-bubbles injection and 2) high speed mercury flow in a narrow channel formed with a double-walled window structure. These concepts are depicted in Fig. 2. In 2015, pitting damage with a depth of 25 μm was observed on the outer wall of target vessel #5, which has the same narrow channel structure as target #8, after an accumulated proton irradiation of 670 MWh with an average beam power of 407 kW. Therefore, it is quite important to investigate the damage on target vessel #8 for estimating its life time.

The neutron production operation using target #8 resumed with a power of 300 kW. During the operating period, we measured the temperature rise at the heat load of the target vessel and the effectiveness of the gas micro-bubbles injection on mitigation: the maximum temperature on the mercury with a proton beam injection was lower than the allowable value, as expected. As shown in Fig. 3, the displacement velocity at an upper position of the mercury vessel was reduced by about 1/3 with gas micro-bubbles injection. From the user operation in January, therefore, the proton beam power was increased to 400 kW. The target operations at 400 kW continued stably until the end of March 2018.

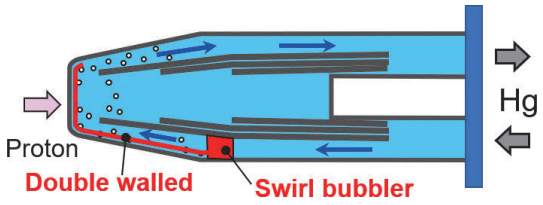

Figure 2. Horizontal cross-sectional view of target vessel #8.

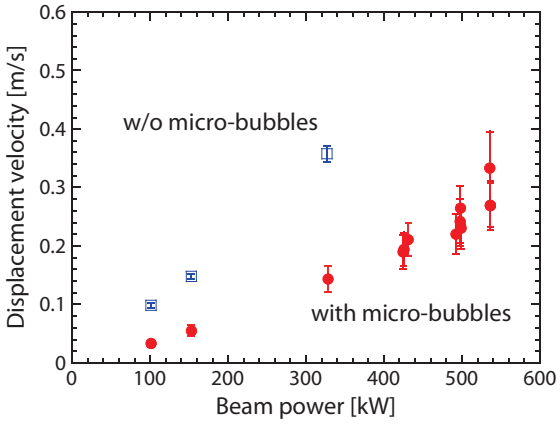

Figure 3. Displacement velocity at an upper position of target vessel #8 at the time of injecting the proton beam.

Then, from April, the beam power was ramped up to 500 kW. The total accumulated power on target #8 will reach 1800 MWh at the end of the operation.

2. Efforts to improve the target design

The fabrication of target vessel #9, which has the same structure as the one designed for target #8, had also been continued by the same vendor. It has been completed about half a year after the fabrication of target vessel #8. On the other hand, we have been designing a different type of target vessel. Its coupling-free structure between the inner mercury and the surrounding outer water shroud will remove the structural cause of generating high heat load on the target. The coupling-free structure uses the same design concept as the one applied for the mercury target at the SNS of Oak Ridge National Laboratory. However, the size of the target vessel at J-PARC is bigger than that of SNS. Realizing a 3-mm gap with a deformation of less than 1 mm between the mercury target and the surrounding water shroud was the key issue in both design and fabrication.

Our structural analyses confirmed that the specifications satisfied the requirement to enhance the rigidity of the water shroud by changing the cooling channel structure and the thicknesses of the inner and outer shroud plates. The resultant thicknesses of the inner and outer water shrouds are 3.5 mm and 3.5 mm with 8.5 mm in the rear part, respectively. Furthermore, we have reduced the volume of water manifold and added a cooling channel there to decrease the temperature difference, the source of thermal stress, between the beam dump and the end plate at the rear of the target vessel. Figure 4 shows a schematic of the coupling-free type target vessel. The fabrication of the coupling-free type target vessel is under way.

3. New storage building for used target vessels

At the Materials and Life Science Experimental Facility (MLF), the capacity of the storage room for the used mercury vessels is limited. Therefore, a new storage building, named RAM (Radio Activated Materials building), has been under construction near MLF in the J-PARC site for the last four years. It was completed on December 26, 2017. Figure 5 shows a photo of the RAM building.

Furthermore, we have designed a shipping container and a shielding container to transfer the used target vessel from MLF to the RAM building. The shielding container was designed to meet the regulation that the dose rate on the surface must be less than 2 mSv/h. The structural integrity of the shipping container is sufficient to endure the impact of a drop from a 1.6 m height when the shielding container is in it.

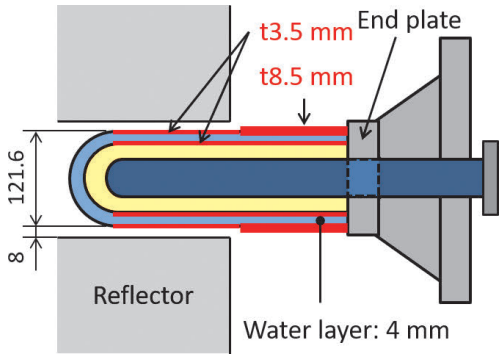

Figure 4. Vertical cross-sectional view of the coupling-free type target vessel.

Figure 5. Photo of the RAM building.

H. Takada
Neutron Source Section, Materials and Life Science Division, J-PARC Center

Progress of the Target Beam Window Cutting

1. Introduction

In the mercury target for the J-PARC neutron source, cavitation damage caused by the proton beam-induced-pressure waves degrades the structural integrity of the target vessel. The cavitation damage is likely to increase with the proton beam power and operating time. Since the thickness of the beam entrance portion of the target vessel is only 3 mm, the cavitation damage is a crucial factor to determine the lifetime of the target vessel and the necessary restriction on ramping-up the proton beam power. To reduce the cavitation damage in the mercury target, we have applied a technology of injecting gas microbubbles with radii less than 100 μm into mercury to suppress the pressure waves from target No. 3 (in fabrication order) operated from October 2012 [1]. In addition, from target No. 5 (operated from October 2014), the beam window was changed to a double-walled structure to suppress the growth of cavitation bubbles caused by high-speed flow and narrow gap [2].

The effect of these cavitation damage mitigation technologies had been investigated by inspecting the interior surface of the beam window portion after cutting out a specimen with an annular cutter. The specimen will be used to measure its mechanical properties in a post-irradiation examination.

Since the used target vessel No. 2 after operating up to 1048 MWh, was highly activated to 350 Sv/h at contact after 2 months cooling by the proton and neutron irradiation, cutting and inspection processes should be performed by full-remote handling.

The target vessel has a multi-walled structure consisting of outer and inner water shroud and mercury vessel. We cut the beam window from three used target vessels but faced the following difficulties: in 2014, the mercury vessel specimen fell inside the vessel for target No. 3 and the cutter's blade was broken by overheat because of dry-cutting for target No. 5 in 2015. For the cutting of target No. 2, therefore, we improved the cutting conditions through careful cold cutting tests and successfully cut out a specimen from the beam window portion without any troubles.

2. Cold cutting tests

Figure 1 shows a photograph of the cutting machine used for the cutting. It consists of a drill machine with an annular cutter, in which the outer/inner diameters of the cutter are 55/50 mm, a wireless system control unit, and a battery with a power convertor. The cutting was performed with fixing the target vessel to the target trolley as for the beam operation. The horizontal access is aiming to prevent a spill of the activated mercury and cooling water from the cut portion [3].

Prior to the actual cutting, we carried out cold cutting tests using a mock-up cutting machine to optimize the rotation speed, the feed rate of the forward motion and the frequency of feed of the cutter by changing them parametrically. Table 1 shows the parameters of cold cutting tests. During cutting in the past, the heat generated by the friction between the cutter and the beam window degraded significantly the cutter's blade. Therefore, a thermography was used to measure the temperature of the lateral surface of the annular cutter and a beam window mock-up of the cutting portion.

Under dry conditions, without using any lubricant, the cutting tests failed within all cutting parameters. As a remedy, we used a water-base lubricant to dissipate the heat. Figure 2 shows a typical example of the temperature distribution of the cutting portion and the time histories of the peak temperature in the square of the temperature distribution. It can be seen that the peak temperature is clearly reduced by splaying lubricant. As a result, we were able to cut out the specimen smoothly by adopting lubricant, regardless of the cutting conditions.

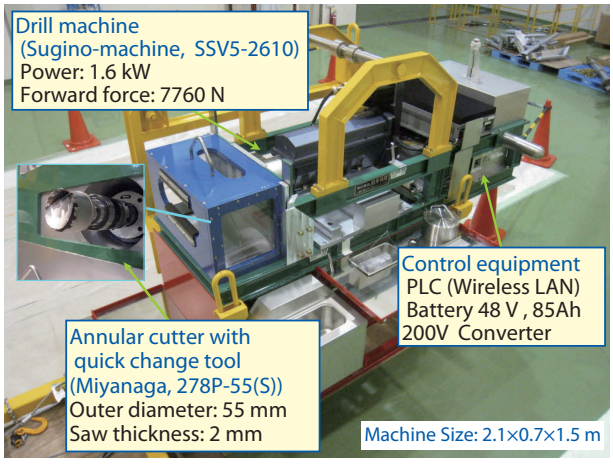

Figure 1. Photograph of the cutting machine.

Table 1. Parameters for optimizing cutting condition.

Rotation speed of cutter [rpm]	250, 400
Feed rate [mm/s]	0.1 [mm] for 0.1 [s], 0.1 [mm] for 3.0 [s]
Feed frequency [Hz]	0.111, 0.167, 0.250

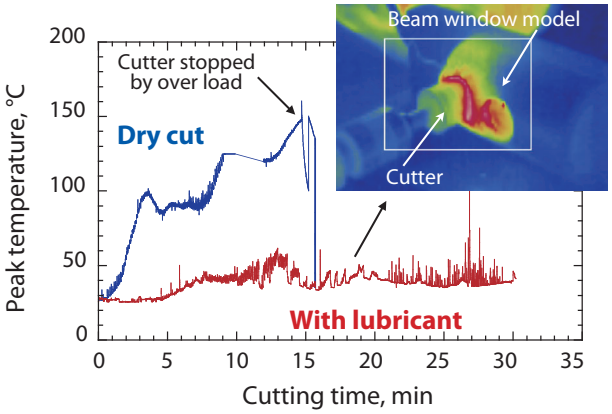

Figure 2. Time histories of surface temperature for cold cutting test.

3. Cutting of used target No. 2

For cutting out a specimen from an actual target in a hot cell at the MLF, we have employed a handy sprayer with a long hose to supply lubricant from outside of the hot cell, as shown in Fig. 3. The actual cutting of the used target No. 2 was completed without any troubles. The blades of the annular cutter after cutting did not change visually.

After cleaning the specimen using an ultrasonic bath with water, the specimen surface was directly observed using a HD video camera. Then, the damages on the specimen's surface were traced on a silicone rubber replica for detailed observation outside of the hot cell, because the highly-activated specimen cannot be removed from the hot cell.

Figure 4 shows the inferior surface of the mercury vessel after cleaning. It can be seen that the cavitation damages are distributed around the center and the top and bottom sides of the specimen. Furthermore, a localized deep pit is superimposed on the damage clusters. Although the details are not described in this report, the distribution of the cavitation damage cluster is well correlated with the saturation time of the negative pressure period, which is obtained by the FEM simulation [4, 5]. For target No. 2, we confirmed the correlation between the distribution of the negative pressure period and the cavitation damage clusters.

Figure 5 shows typical examples of the cavitation damage on replicated surface for the damage cluster and the localized deep pit obtained by a 3D laser scanner (Keyence, VR-3200). The measured depth of the localized deep pit was 234 μm. The homogenous erosion, accompanied with mass loss, can be calculated with an empirical equation, $D_{max} = 8MDE = MDE + d$, where D_{max}, MDE, d are the maximum damage depth, the mean depth of erosion, and the measured depth, respectively [6], the D_{max} of target No. 2 was concluded to be 268 μm since d = 234 μm. This result will be applied to improve the cavitation damage mitigation technologies and ensure a stable operation at high power.

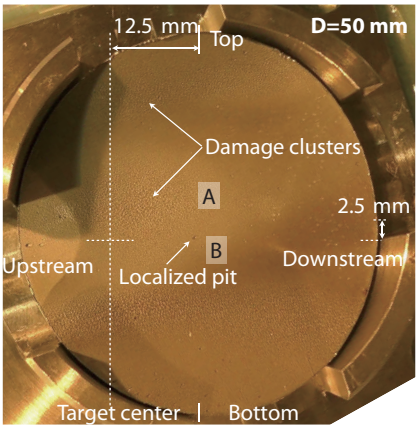

Figure 4. Cavitation damage on specimen cutout from the used target No. 2.

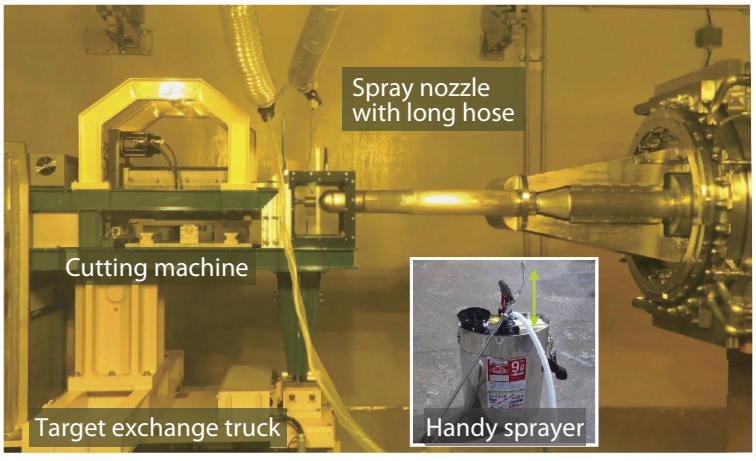

Figure 3. Cutting machine with remote sprayer tools for cutting of target No.2.

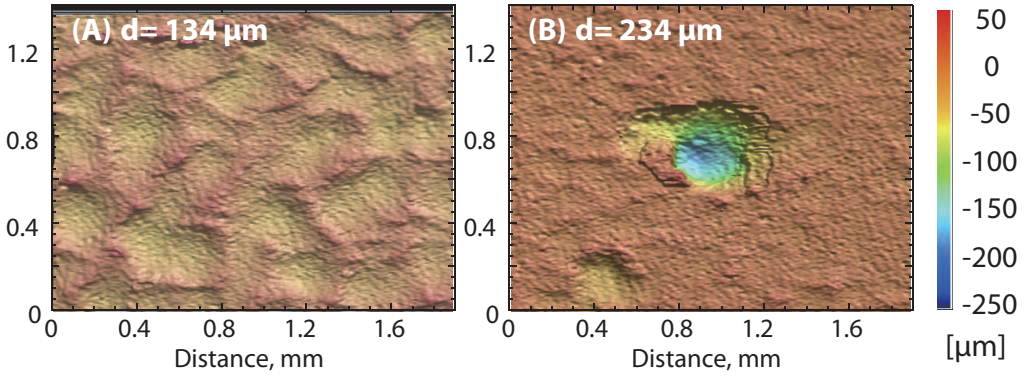

Figure 5. Depth contour of the replicated cavitation damage for (A) damage cluster and (B) localized deep pit.

References

[1] H. Kogawa, et al., J. Nucl. Sci. Technol., 54 (2017) 733-741.
[2] T. Naoe, et al., J. Nucl. Mater., 506 (2018) 35-42.
[3] H. Kinoshita, et al., Proceedings of ICANS-XX (2012).
[4] B. Riemer, et al., J. Nucl. Mater., 450 (2014) 183-191.
[5] T. Naoe, et al., J. Nucl. Mater., 450 (2014) 123-129.
[6] T. Naoe, et al., J. Nucl. Mater., 468 (2016) 313-320.

T. Naoe, H. Kinoshita, T. Wakui, H. Kogawa, M. Teshigawara, K. Haga, and H. Takada
Neutron Source Section, Materials and Life Science Division, J-PARC center

R&D of Electron Beam Welding on Moderator Vessel Fabrication

1. Introduction

The fabrication of a spare moderator and reflector has completed in 2017 to be ready for replacement scheduled around 2021, which is needed because these structural materials suffer accumulated irradiation damage.

A Gold-Indium-Cadmium (Au-In-Cd) decoupler was developed to reduce dramatically the radioactivity of the used components in comparison with the previous Silver-Indium-Cadmium (Ag-In-Cd) decoupler without sacrificing neutronic performance. The main issue was an implementation of (Au-In-Cd) alloy as a decopuler [1] and its assembly by welding in the spare moderator and reflector fabrication. Tungsten inert gas (TIG) welding was used previously to assemble the moderator-reflector, however, the TIG welding heat sometimes had an impact on the bonding region of the Au-In-Cd decoupler, causing cracks, exfoliation, deformation, etc., in the parts' manufacturing process, including the Au-In-Cd decoupler. In order to improve the welding conditions, electron beam welding (EBW) was applied specifically to manufacture these parts, including the Au-In-Cd decoupler. Here, we report the R&D of EBW on the moderator vessel fabrication.

2. Welding of decoupler vessel in decoupled moderator

As shown in Fig. 1 (a), the decoupled moderator, which is one of the three spare moderators, consists of four vessels. The third vessel (decoupler vessel) includes Au-In-Cd alloy. The Au-In-Cd alloy was bonded to aluminum alloy, A5083, a structural material of the vessel, added by the Hot Isostatic Pressing (HIP) technique.

This decoupler vessel was assembled previously by TIG welding at the welding position, as shown in Fig. 1 (b). However, the TIG welding heat sometimes affected the bonding region of the Au-In-Cd and A5083 alloys, causing cracks, exfoliation, deformation, etc., in the manufacturing process. We applied the EBW technique to improve the welding conditions for assembling the decoupler vessel. We performed R&D of EBW to obtain optimum EBW conditions, such as beam shape, power, focus position, welding speed, etc. Another issue that we found was that the welding did not reach full penetration but only partial one, preventing the required design weld thickness. Because there was a vacuum vessel inside the decoupler vessel, as shown in Fig. 1 (b), that was likely to cause problems, such as electron beam penetration to the vacuum vessel, contact of the penetration bead, etc.

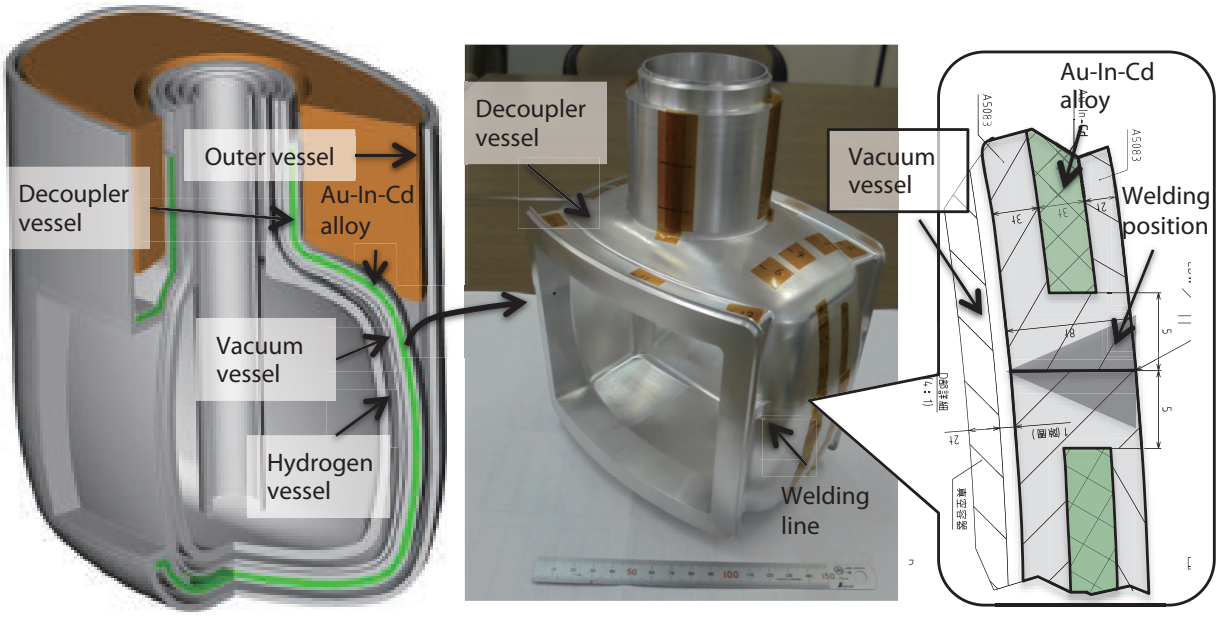

(a) Cutway view of decoupled moderator (b) Decoupler vessel and welding position in fabrication process

Figure 1. (a) Cutway view of decoupled moderator and, (b) Decoupler vessel and welding position in fabrication process.

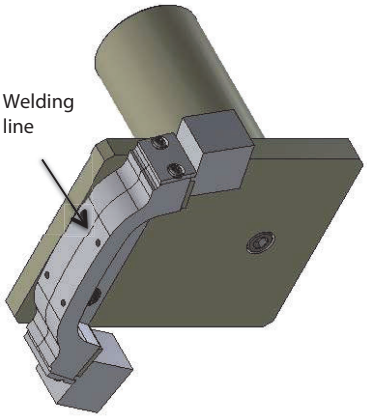

Figure 2. EBW element test model.

3. R&D of EBW

We performed an EBW element test to obtain optimum EBW conditions by using partial mockup model of the welding part, as shown in Fig. 2. We considered same thermal capacity as actual decoupler vessel in the mockup model, because the escape of heat in the welding area affected the EBW condition. An X-ray computed tomography (CT) scanning technique was also applied to confirm the state inside the welded area. We show a typical X-ray CT scanning image for unoptimized EBW condition, as shown in Fig. 3 (a) above. Many blowholes were observed at the focus position for the unoptimized one. We managed to reduce successfully the blowholes for the optimized EBW case, as shown in Fig. 3 (a), bottom. In the optimized case, we controlled the electron beam power from 32 to 48 mA with elliptical deflection beam according to the welding thickness and the focus position was 5 mm deep. Finally, we applied the obtained optimum condition to assemble an actual decoupler vessel, as shown in Fig. 3 (b).

Acknowledgments

We are grateful for the cooperation of Metal Technology Co. Ltd in the fabrication of the spare moderators and reflector. We also thank the Nippon Advanced Technology Co., Ltd. staff for their help in the preparation of the Au-In-Cd material.

Reference

[1] M. Teshigawara, et al., Nuclear Materials and Energy, 14, 14–21 (2018).

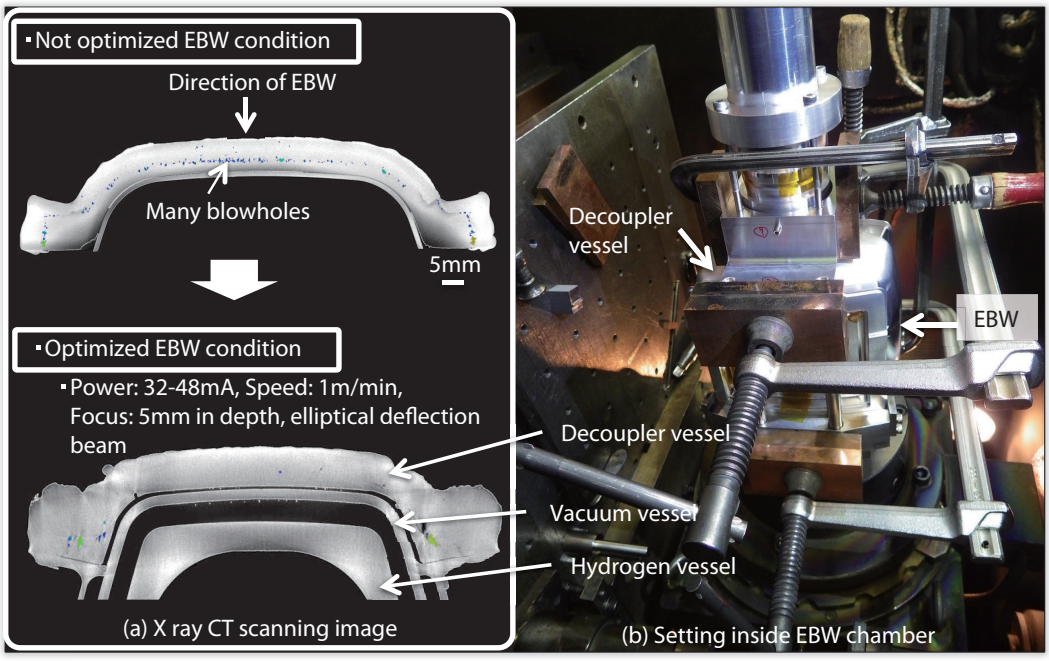

Figure 3. (a) X ray CT scanning image and (b)Setting inside EBW chamber.

M. Teshigawara, M. Harada, and M. Ooi
Neutron Source Section, Materials and Life Science Division, J-PARC Center

Replacement of the Proton Beam Window

1. Introduction

Proton beam window (PBW) is installed at the end of the proton beam line to divide high vacuum in the proton beam line of 10^{-6} Pa and the helium vessel, which contains a neutron target, moderator and reflector. As shown in Fig. 1, the window body of the PBW has a cylindrical shape with pillow seal, installed at the end of a shielding plug with a length of 3.8 m and total weight of 10 tons. The pillow seal kept airtightness by adhering the metal surface polished like a mirror surface with gas pressure. The window part of the PBW is made of two layers of aluminum alloy plates and is cooled by cooling water flowing between the aluminum plates. From previous evaluations of the irradiation damage of the aluminum alloy, lifetime of the PBW is supposed to be 2 years during a 1 MW operation [1]. The PBW is directly exposed to the proton beam, and because of the influence of neutrons generated in the neutron target, the PBW is highly activated. So, it is necessary to perform replacement work in the hot cell. Also, because the dose of the PBW is high, it is needed to move into the hot cell using a shielding transfer cask.

The total amount of the beam irradiation of PBW unit No. 2 is 2510 MWh, which is 1/4 of the expected lifetime. However, considering the effect of corrosion of the window caused by water leakage from the target container that occurred in 2015, we decided to replace it with PBW unit No. 3 in order to avoid breakage during the beam operation.

2. Replacement work

At first, the radiation shields over the He vessel was removed. Vinyl curing is applied on the floor surface and green house is built to control the tritium vapor. Local exhaust system and online tritium monitoring system are applied in the green house. This time, in order to prevent internal exposure of the worker, airline mask was worn during the manual removal of the pipes, which is shown in Fig. 2. The dose rate of the working area above the shielding plug was 3 μSv/h at maximum.

After removing the pipes, PBW unit No. 2 was moved to the hot cell by the shielding cask (Fig. 3), then stored in the drying room under the hot cell. Because PBW unit No. 3 was attached on another shielding plug, it was installed to the PBW position and the pipes and cables were connected.

Figure 4 shows the vacuum side of the PBWs, as well as the multi-wire profile monitor for measuring the proton beam profile. In the upper photo in Fig. 4 is PBW unit No. 2, and in the lower one is unit No. 3. We can see

Figure 2. The utility pipes of the PBW were removed manually. The workers were equipped with airline masks and anoraks, and worked in the greenhouse.

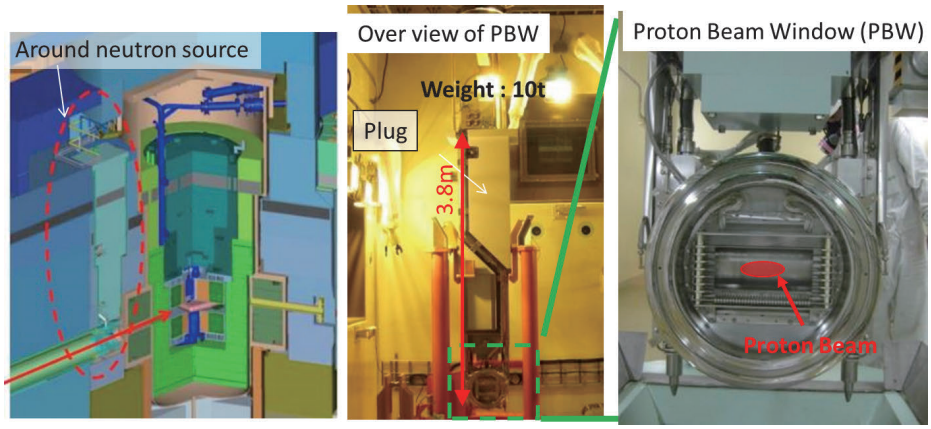

Figure 1. Overview of the PBW. PBW is placed before the neutron production target, its height is 3.8 m and the weight is 10 tons with the shielding plug. PBW is made with a circler pillow seal and aluminum beam window.

the beam footprint on PBW unit No. 2 and the wire of the profile monitor is winding. Such slackness would be caused by an error on the beam profile measurement, so we are planning to adopt a mechanism to suppress the wire slack in PBW unit No. 4.

Figure 3. PBW is stored in the shielding cask and moved to the hot cell with a 130-t crane.

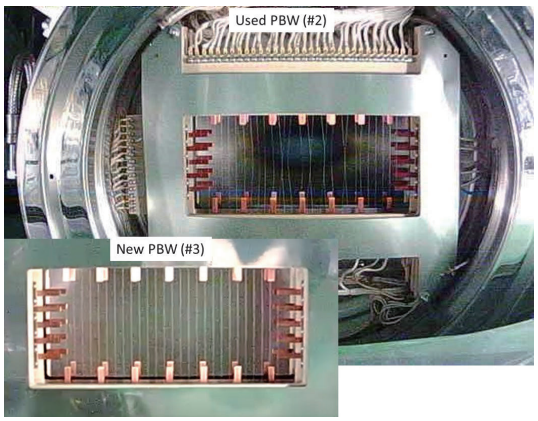

Figure 4. The vacuum side of PBW unit 2 (upper) and unit 3 (lower). An irradiation mark is shown in unit 2 and the wires of the profile monitors are distorted.

3. Dose and contamination of the PBW

There are some utility pipes for the PBW, such as cooling water pipes, middle exhaust vacuum pipes, He gas pipes for the pillow seal and beam monitor cables. The cooling water used in the PBW is a part of 6552 cooling water system in MLF, which contains 5.5×10^4 Bq/cc of tritium in the water. Before the replacement of the PBW, the cooling water was drained and dried with the vacuum method to reduce the tritium contamination and avoid internal exposure of the workers. Table 1 shows a results of the contamination measurement in the pipes. The tritium contamination of the water pipe is lower than that of the middle exhaust pipe of the He vessel side, it is assumed that the tritium come from the He vessel.

In order to measure the dose of the PBW, a dosimeter was installed at 50 cm from the extraction path of PBW. A dose rate of 202 mSv/h was observed at a maximum when the proton beam window was moved over the shield. After the PBW was stored in the shielding cask, the dose on the surface of the shielding cask was 0.8 μSv/h at the same height of the PBW, and the highest point was 20 μSv/h at 3 m from the floor shield.

Table 1. Results of surface contamination measurement of the water pipe and the vacuum pipe (middle exhaust) of PBW.

[Bq/cm²]

Position	β(γ)	Tritium
Water pipe	0.6	1.9
Middle exhaust (He Vessel side)	--	5.2
Middle exhaust (Vacuum side)	--	0.9

4. Future Plans

PBW unit No. 2 will be removed from the shielding plug, then the window body will be stored in the storage container after cutting the piping part. Then PBW unit No. 4 will be installed to the shielding plug for the next PBW replacement.

Reference

[1] S. Meigo et. al., J. of Nuclear Materials. 450(2014) 141.

M. Ooi, S. Meigo, H. Kinoshita, and M. Teshigawara
Neutron Source Section, Materials and Life Science Division, J-PARC Center

Neutron Science

Neutron Science Section

1. User program

After replacing the target with the older model No.2 in 2016 due to two target incidents of water leakage in 2015, we had to reduce beam power to around 150 kW. We operated this target safely until the summer shutdown in 2017. Then, we replaced the target with the newly-designed target No.8 and operated it with 300 kW until December and 400 kW from January, while maintaining a high level of beam availability over 90%.

For the general-proposal round for 2017A, 153 general proposals and 5 new user promotion proposals were approved from 228 submissions. For 2017B, 167 general proposals and 5 new user promotion proposals were approved from 291 submissions. Additionally, a new type of proposal was introduced in 2017B, the General Proposal (Long Term), also called Long Term Proposal. This Long Term Proposal, valid for three years, is called once a year, every B term. 8 Long Term Proposals were approved from 24 submissions.

A new proposal category for non-proprietary uses (free of charge) started at two pilot instruments, Super HRPD and NOVA, at the end of 2017B, which is a mail-in program called Fast Track Proposal. The users send their samples to MLF, and MLF staffs carry out experiments on the user's behalf and send the data.

2. Instruments

The layout of the neutron instruments at MLF, as of the end of JFY 2017, is shown in Fig. 1.

POLANO (Polarized Neutron Spectrometer) at BL23 is in the commissioning phase. On-beam commissioning, such as commissioning on the data acquisition system, was ongoing. In November 2017, a MIEZE part of the neutron spin-echo suit VIN ROSE (VIllage of Neutron ResOnance Spin Echo spectrometers) at BL06 moved into a user program phase (Fig. 2). Another line of VIN ROSE, the NRSE spin-echo line, was still under commissioning.

A measurement of the neutron lifetime is on-going on NOP (Neutron Optics and Fundamental Physics) at BL05 to achieve an accuracy of 1 s. The neutron lifetime is an important parameter for the big bang nucleosynthesis and the standard model for elementary particle physics. The first preliminary result was obtained as 896 +13/−14 s by analyzing data accumulated in 2014 - 2016. The data taking is still ongoing to reduce the uncertainty.

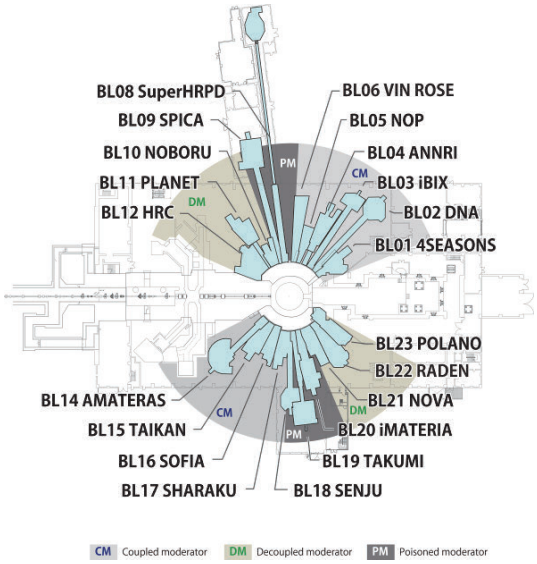

Figure 1. Layout of the neutron instruments at MLF as of JFY 2017. BL23 was in the commissioning phase.

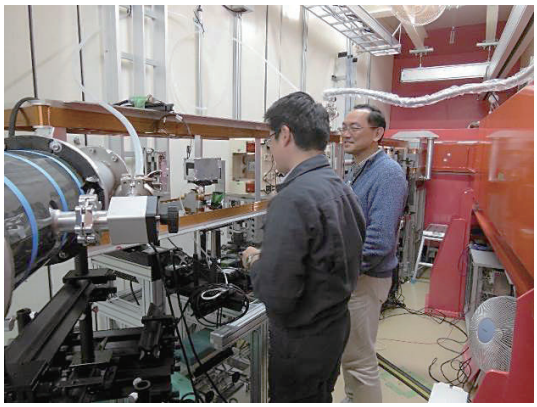

Figure 2. Users carrying out their experiment on a MIEZE spin-echo beam line at VAN ROSE.

Multiple-wavelength neutron holography with the time-of-flight technique was developed on NOBORU (NeutrOn Beamline for Observation and Research Use) at BL10 to provide information on local structures of materials. By using a single crystal of Eu-doped CaF_2, a clear three-dimensional atomic image around Eu^{3+} substituted for Ca^{2+} was obtained, revealing the local structure that allows it to maintain charge neutrality.

Since the increase of neutron flux is always an important issue for neutron instruments, the following work was done in that field. On 4SEASONS (4D-Space Access Neutron Spectrometer) at BL01, a part of the guide tube was improved and the neutron flux increased by 10 - 20%. On HRC (High Resolution Chopper Spectrometer) at BL12, the incident beam collimator as

well as the Fermi chopper were optimized, and the intensity gain was obtained for low angle experiments, such as neutron Brillouin scattering. On AMATERAS (Cold Neutron Disk Chopper Spectrometer) at BL14, 10 detectors were installed to extend the scattering angles from 4.9° to 3.4° for low angles and from 111.0° to 116.1° for high angles. On TAIKAN (Small and Wide Angle Neutron Scattering Instrument) at BL15, for chromatic aberration compensation, three magnetic lenses and two spin-flippers were utilized to control the focal length dependent on the wavelength. On SOFIA (Soft Interface Analyzer) at BL16, high resolution and high counting rate were achieved by the grazing incidence configuration of GEM (gas electron multiplier).

3. International activities

The 9th AONSA School / the 2nd Neutron and Muon School was held in November 16-20. Details about the school can be found on the web (https://neutron.cross.or.jp/9thAONSAschool/index.html). 49 young researchers and graduate students from Korea, Australia, Indonesia, India, China, Taiwan, Thailand, Malaysia, New Zealand, Viet Nam, Nepal, United Kingdom, Russian Federation, as well as Japan, participated in the school. The neutron science group contributed 10 neutron instruments for hands-on experiments and 43 of the 49 participants took part in neutron experiments (Fig. 3 and 4).

Figure 3. Dr. Yamada and his student enjoying hands-on experiment at DNA at BL02.

Figure 4. Dr. Hattori lecturing about the instrumental aparatus to students at PLANET at BL11.

J-PARC Center and CROSS hosted the J-PARC Workshop "Deuterated Materials Enhancing Neutron Science for Structure Function Applications" on October 19 and 20, 2017. We invited Dr. T. A. Darwish and D. Anthony from ANSTO, Australia, Dr. L. Anna from ESS, Sweden, and Prof. H. Sajiki from the Gifu Pharmaceutical University for plenary talks. 62 scientists paticipated in the meeting. Neutron studies on material and life siences by utlizing deuteration technology were discussed.

4. Resultant outcomes

The research activities in neutron science at MLF resulted in more than 160 articles, including 80 referred papers. This number includes papers in influential journals such as Nature Materials, Nature Communications and Scientific Reports.

The HRC beam line (BL12) group won the Technology Prize of the Japanese Society for Neutron Science for the development of the construction of high-resolution chopper spectrometer and implementation of neutron Brillouin scattering measurement.

The prize for development technology of Sumimoto Rubber Industries, Ltd. (Cooperation of SPring-8 / J-PARC / K-computer and Advanced tire developments) was awarded as Commendation for Science and Technology by the Minister of Education, Culture, Sports, Science and Technology, Japan in 2017. The technology has confirmed that atomic scale structure and dynamics of tire by neutron and X-ray and computer simulations could be used to improve the inconsistent performances of car tires. This group had won numerous awards. Based on these results, Sumitomo Rubber Industries decided to hire a fixed-term resident researcher, who works closely with J-PARC staffs; this initiative is called J-PARC/Sumitomo Fellowship program. The first fellow employed by this program was assigned in JFY 2017.

K. Nakajima[1], Y. Kawakita[1], S. Itoh[1,2], and T. Otomo[1,2]

[1]Neutron Science Section, Materials and Life Science Division, J-PARC Center; [2]Institute of Materials Structure Science, High Energy Accelerator Research Organization, KEK

BL01: 4D-Space Access Neutron Spectrometer 4SEASONS

1. Introduction

4SEASONS is a thermal neutron Fermi-chopper spectrometer for inelastic scattering measurements, and one of the Public Beamlines in MLF [1]. The momentum-energy region for this spectrometer occupies the middle of the momentum-energy space covered by all the MLF spectrometers [2, 3]. In 2017, 19 short-term proposals were approved for 4SEASONS: 16 General Use proposals, 2 Urgent Use proposals, and 1 New User Promotion proposal. Three types of full-year proposals, 1 Element Strategy Initiative Use proposal, 2 Project Use proposals, and 1 Instrument Group Use proposal, were approved as well. In addition, 4 reserved (short-term) proposals were given beamtimes. Most of the proposals were submitted for the fields of magnetism and strongly correlated electron systems, and a few proposals were for materials science or energy materials.

2. Beam transport update

The moderator-to-sample distance of 4SEASONS is 18 m, and a supermirror neutron guide is installed from 2.3 m to 15.8 m relative to the moderator. The guide has a square cross-section and an elliptically converging shape along the longitudinal direction to maximize the neutron flux reaching at sample. Unfortunately, however, we found that the observed neutron intensity at the sample was about 60% of the designed value [1], probably because of low reflectivity or misalignment of the supermirrors. Then, in 2017, we renewed the last 1.7-m section of the neutron guide (Fig. 1(a)). The designed shape and critical angle of the supermirrors ($m = 4$) in this new section are the same as those in the original design. In spite of the short length of this section (only 13% of the total neutron guide tube and less than 10% of the total flight path to sample), it contributes considerably to the neutron flux at the sample, because this section has the highest critical angle of supermirrors and the steepest slope in the neutron guide. Figure 1 shows the intensity ratio before and after replacing the last section of the neutron guide. The intensity ratio depends on neutron energy and no intensity gain was observed at energies higher than 500 meV where the supermirrors become ineffective, but we observed 10-20% intensity gain at < 100 meV. (Fig. 1(b)).

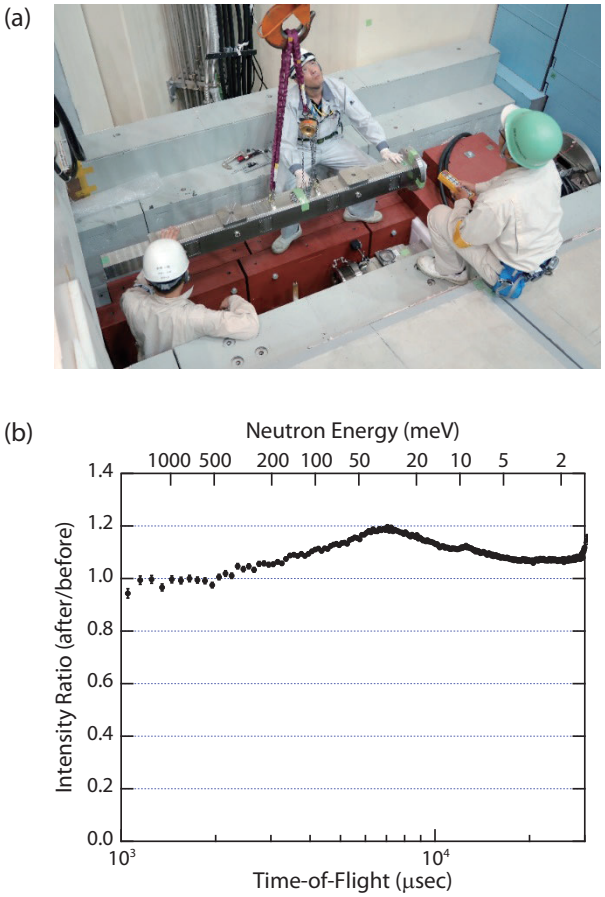

Figure 1. (a) A vacuum jacket with supermirror neutron guide is being removed by the technical supporting staffs of MLF. (b) Ratio of neutron scattering intensity from a vanadium sample measured using white neutron beam before and after the replacement of the neutron guide.

3. Preparation of the superconducting magnet

Because many iron components surround the sample area, and turbomolecular vacuum pumps with magnetic bearings are attached just below the sample position, it is difficult for 4SEASONS to use high-field magnets. We have been trying to mitigate the problem to make the MLF-SE vertical-field superconducting magnets (the maximum magnetic field is 7 T) available on this instrument. So far, we evaluated the stray fields from the magnet by calculation and performed a test operation below 1 T to validate the calculation [4, 5].

Because we found that the stray field on the turbomolecular pumps limits the available amplitude of the magnetic field, we decided to relocate the turbomolecular pumps. However, bending the exhaust path between the vacuum tank and the pumps would

degrade the pumping speed. Then, in 2017, we relocated the turbomolecular pumps downward as far as possible from the vacuum tank but kept the exhaust path straight (Fig. 2(a)). More specifically, we inserted a 25-cm long extension pipe between the pumps and the attachment flange on the tank. After the relocation of the pump, we performed a test operation of the magnet with the MLF Sample Environment (SE) team, measured the stray fields around the magnet and confirmed that the Fermi chopper, which also operates with a magnetic bearing, ran without problems under the magnetic field. From these tests, we concluded that the maximum available magnetic field on 4SEASONS was 3 T for the time being, although this value may change by future investigation. We will perform a test experiment with a real sample under magnetic fields in 2018, and if it is successful, we will accept proposals to use the MLF-SE magnet from the second half of 2018.

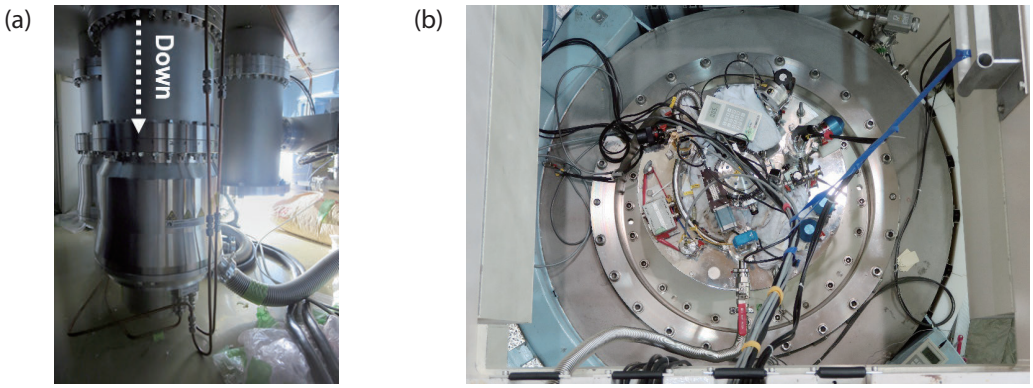

Figure 2. (a) Turbomolecular vacuum pumps below the vacuum tank of 4SEASONS. They have been relocated downward along the dotted arrow. (b) MLF-SE 7-T vertical-field magnet installed on the 4SEASONS sample flange.

References

[1] R. Kajimoto et al., J. Phys. Soc. Jpn. **80**, SB025 (2011).
[2] H. Seto et al., Biochim. Biophys. Acta, Gen. Subj. **1861**, 3651 (2017).
[3] K. Nakajima et al., Quantum Beam Sci. **1**, 9 (2017).
[4] R. Kajimoto et al., J-PARC Annual Report 2015, Vol. 2: Materials and Life Science Experimental Facility, pp. 67-68.
[5] R. Kajimoto et al., J. Phys.: Conf. Ser. **1021**, 012030 (2018).

R. Kajimoto[1], M. Nakamura[1], K. Kamazawa[2], Y. Inamura[1], K. Ikeuchi[2], K. Iida[2], M. Ishikado[2], N. Murai[1], T. Harada[1], H. Kira[2], and R. Takahashi[3]
[1]Neutron Science Section, Materials and Life Science Division, J-PARC Center; [2]Neutron Science and Technology Center, CROSS; [3]Technology Development Section, Materials and Life Science Division, J-PARC Center

Current Status of BL02 DNA in 2017

1. Introduction

DNA is a micro eV spectrometer designed to elucidate atomic and molecular dynamics, phonon and magnon excitations in −500 to 1500 micro eV range. A high energy resolution is achieved by a pulse shaping chopper with four slits (one 10 mm and three 30 mm slits) and Si111 back scattering analyzers. The first device makes DNA flexible to tuning energy resolution and enables the observation of a full energy range while keeping the energy resolution high. The second one is back-coated with Gd neutron absorber, which ensures an extra high signal-to-noise ratio of approximately 10^5. The accessible momentum transfer range is from 0.08 to 1.86 $Å^{-1}$ by using Si111 analyzer mirrors [1-3].

In 2017, the number of publications using DNA finally increased up to nine reviewed papers per year. These publications cover a variety of topics ranging from hard materials, such as spintronics material, Ionic Liquid, and thermoelectrics, to soft materials such as polystyrene thin films, clay, human hemoglobin and cardiac muscle. The results from the experiments described in those articles became possible due to the wide energy range and extra high signal to noise ratio of DNA.

2. User program in the periods 2017A and 2017B

Thirteen General Proposals (GP) including one New User Promotion (NUP) proposal, and twelve GPs, including one NUP, were approved for 2017A and 2017B, respectively. The portion of the approved beamtime in the total of the requested beamtime was 63% for 2017A and 64% for 2017B. The competition rate was approximately 1.6 which was almost average among all neutron instruments. During 2017B, one Urgent Proposal was conducted.

In addition, a General Proposal (Long Term) (hereafter LTP) Program, started in 2017B, calls every B term for a three-year project with a long-term strategy. One LTP project, which will continue till 2020A through an interim evaluation, was adopted at BL02.

The joint school of AONSA Neutron School and the 2nd Neutron and Muon School was held in mid-November. We at DNA accepted four students from Indonesia and Korea. They took part in a hands-on experiment on molecular dynamics of water on Nafion at DNA.

3. Beamline activities

Beamline

We relocated diffraction counters to the highest angle position to install Si 311 analyzer mirror bank. The diffraction data of LaB_6 powder was successfully confirmed.

Six years have passed since the commissioning of DNA and several pieces of equipment started to fail because of aging. Fast chopper No.2 stopped due to communication error between the control unit and the motor driver. Since the other chopper instrument with the same system had a similar problem, we were able to minimize the unexpected shut-down by replacing the control unit. Also, periodic maintenance was carried out for the slow choppers and the pumps for the fast choppers.

Sample environment

Low-temperature measurements are indispensable when DNA's fine energy resolution is used to study low-energy excitations. In the summer of 2017, we conducted a cooling test for MLF Sample Environment Team's ^{3}He cryostat and Dilution refrigerator with a new 2 K cryostat (Fig. 1). We achieved the lowest temperature of 300 mK (^{3}He) and 50 mK (Dilution), which opens doors to low-temperature measurement for general users.

We also performed feasibility measurements of the Paris-Edinburgh cell. The result received from an ionic liquid (C4mimPF6) is shown in Fig. 2. Even though the

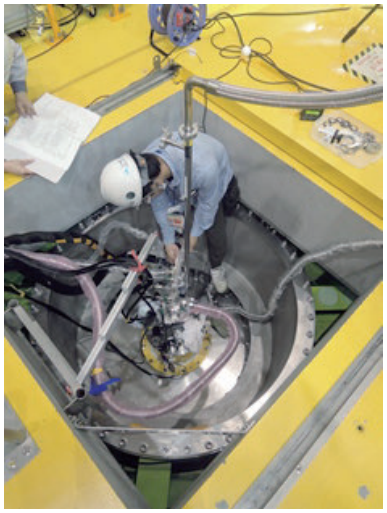

Figure 1. Photo of the commissioning work of MLF SE's dilution refrigerator with a new 2 K cryostat, summer of 2017.

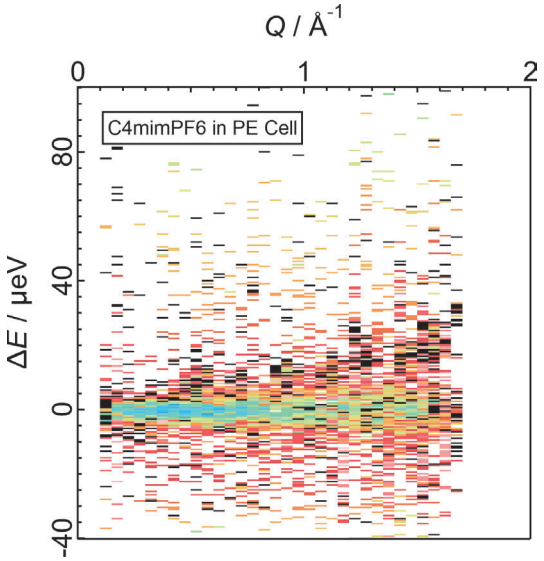

Figure 2. Feasibility test of the Paris-Edinburgh type pressure cell for QENS measurement. The sample was an ionic liquid C4mimPF6.

intensity is much weaker than that measured by the conventional cell due to the relatively narrow opening angle, we observed a quasi-elastic broadening caused by translational motion. Another type of cell for relatively low-pressure condition has been developed to increase the sample volume.

In DNA, the solution sample is usually sealed in an Al cell. Chemical reaction between our standard and the solution was found in a few cases due to a small amount of additive in the solution, which broke the Al cell. We strongly requested that the users precheck the sample's stability with Al (A1070). Pair of cylindrical quartz inner fits to be inserted into the Al cell has been developed for sample possibly interacting with aluminum. Currently we are working on the design of two thickness setups, approximately 0.2 mmt and 0.5 mmt each.

Due to the high sensitivity of DNA, the sample position could affect the spectrum. We found elastic position shifts in the time-of-flight spectrum when we rotated the non-straight sample stick. We have developed a system to evaluate the displacement of the sample stick by using line-lasers. In addition, we installed a cabinet to keep several of sample sticks straight. Now we are developing a new sample stick with high reproducibility of the sample position.

Software

QENSFit, the software for fitting of QENS profiles by some fitting functions convoluted with an instrument resolution function, has been updated. QENSFit is currently available for both MAC and Windows.

4. Future plans

The pulse-shaping chopper, one of the key instruments of DNA, will be upgraded in 2018. The current chopper was designed with the maximum rotational speed of 300 Hz; however, the highest speed is limited to 225 Hz due to large vibrations. Mr. Wataru Kambara, the chief engineer of MLF, developed successfully a new fast chopper, which ensures stable rotation at 300 Hz. The new device will improve the energy resolution by 30% with the new disk chopper.

Further, Si311 analyzer mirrors will be installed before the summer shutdown in 2019, which will extend the momentum transfer range to 3.8 $Å^{-1}$ with 12 micro eV with 10 mm slit.

5. Others

DNA received Interim Evaluation of Neutron Instrument. In MLF, the activity of each neutron instrument is evaluated every five years after opening to user program. The evaluation report stated that DNA has a world-class performance and the experimental support from the DNA team is satisfactory. However, considering the low number of publications, the leadership of the instrument group is expected to increase the volume of data analysis and expand the user community with scientists from many parts of the world.

The DNA group won the JAEA President Award 2017 for the construction of the DNA instrument and the outcomes from the pilot studies.

The access safety of the sample environment equipment on the top flange through the hatch was improved by redesigning the handrail and the ladder.

References

[1] Kaoru SHIBATA et al., JPS Conference Proceedings, 8 (2015), 036022.
[2] Kenji Nakajima et al., Quantum Beam Sci., 1 (2017), 9.
[3] Hideki Seto et al., Biochimica et Biophysica (BBA) General Subjects 1861 (2017), 3651.

Y. Kawakita[1], M. Matsuura[2], T. Yamada[2], T. Tominaga[2], M. Kobayashi[2], H. Nakagawa[1,3], and K. Shibata[1]
[1]Neutron Science Section, Materials and Life Science Division, J-PARC Center; [2]Neutron Science and Technology Center, CROSS; [3]Materials Sciences Research Center, JAEA

Current Status and Future Plans of iBIX

1. Introduction

The single-crystal neutron diffractometer is a powerful tool for obtaining the structure and magnetic information of various materials, including light elements. The IBARAKI biological crystal diffractometer, called iBIX, was constructed to accomplish high throughput single-crystal neutron structure analysis for biological macromolecules and organic compounds in various life processes [1]. A new photon-counting two-dimensional detector system using a scintillator sheet and wavelength-shifting fiber arrays for the X and Y axes has been developed with the cooperation of JAEA to achieve high measurement efficiency. In 2012, the installation of 30 detectors on the iBIX diffractometer was completed [2]. By the end of 2012, iBIX became available for user experiments on biological macromolecules, supported by the Frontier Research Center of Applied Atomic Sciences, Ibaraki University. The final specifications of the iBIX are shown in Table 1.

Table 1. Specifications of iBIX.

Moderator	Coupled
Wavelength of incident neutron (Å)	0.7 ~ 4.0 (1st frame) 4.0 ~ 8.0 (2nd frame)
Neutron intensity (n/s/mm^2) (@1 MW)	0.7×10^6
L_1 (m)	40
L_2 (mm)	500
Solid angle of detectors (% for 4π)	19.5
Detector covered region (deg.)	15.5 ~ 168.5
Detector size (mm^2)	133 × 133
Detectors pixel size (mm^2)	0.52 × 0.52
No. of detectors	30

2. Current status

The first period of the installation contract of iBIX for J-PARC, MLF expired in the end of 2017. The second period of the iBIX operation started in the beginning of 2018. In 2017, J-PARC was operated at accelerator power of 150 ~ 300 kW. The results from the experiments on the full data set of biological macromolecules for neutron structure analysis by using iBIX were as follows. We were able to collect a full data set of biological macromolecules for neutron structure analysis with around 2.0 Å resolution in about 14 days by using iBIX. The average volume of the sample measured by iBIX was 2.3 mm^3 (max. size: 4.7 mm^3, min. size: 0.67 mm^3). If the accelerator power reaches 1 MW, the total measurement time of the sample size will be reduced to one third of the previously necessary time. One organic compound and five biological macromolecules were provided for the diffraction experiments using iBIX. Some interesting scientific results were obtained from these investigations by applying neutron structure analysis, which will be covered in several papers to be published next year. We project that iBIX will become one of the world's best performing diffractometers under 1 MW operation.

We prepared a users' manual and a distribution package of the data reduction software "STARGazer", which will allow the iBIX users to perform personally data reduction in their laboratory [3]. At the same time, we also held a software workshop for iBIX users.

3. Development

We assumed that a full data set of a 2-mm^3 protein sample could be obtained by iBIX in about 2 to 4 days under the 1 MW operation. The assumption implied that iBIX was capable of achieving the designed target value. However, the sample size was still large and the measurement time was still long, especially for the users. We would like to reduce the difficulties of sample preparation as much as possible. In other words, it is necessary to further improve the measurement efficiency of iBIX by developing the beam line instrument.

As a simple and effective way to improve the measurement efficiency, we carried out the installation of the newly-added detectors. A maximum of 60 detectors can be installed on the support frame of the iBIX diffractometer without any design changes. In 2017, we stated to assemble the four newly-added detectors by ourselves. These have already been installed on the iBIX diffractometer (Fig. 1). The measurement efficiency with 34 detectors will become 1.13 times higher than that of the previous 30 detectors. Commissioning the without/with neutron beam has already finished. By using the four newly-added detectors, we could obtain the TOF diffraction data with the same accuracy as the current detectors. The new detectors will be available for users experiments in FY 2018.

We also started to develop a new scintillator unit with high sensitivity for the iBIX detector system. The scintillator unit consists of two scintillator sheets and

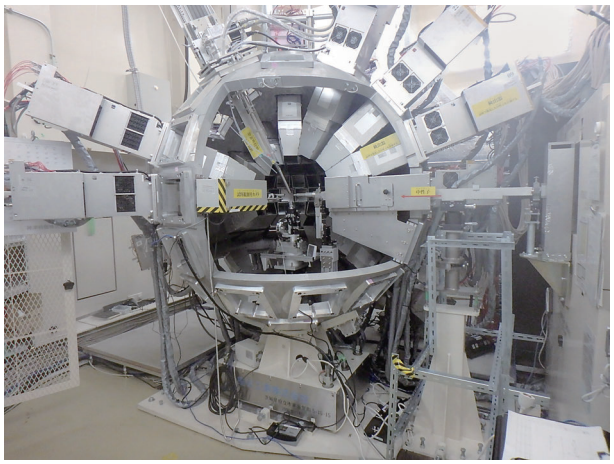

Figure 1. Current diffractometer of iBIX with new detectors.

wave-length sift fiber for X and Y axes. The scintillator sheet of the previous detectors is B_2O_2 scintillator. The new unit's scintillator was changed to a ^{6}LiF scintillator. Also, we optimized the material of the wave-length sift fiber for the new scintillator. In order to improve the position accuracy, we developed a method of fixation between neighboring WLSF. The development aim for the new scintillator unit is 1.2 ~ 1.4 times higher sensitivity than the previous one. We managed to demonstrate this increased sensitivity by performing neutron experiments on a test piece. Now, we will try to develop new scintillator sheets of practical size, to be fabricated later by a manufacturing company.

4. Future plans

It was demonstrated that iBIX achieved all design target values (max cell dimension, resolution, measurement efficiency etc.). iBIX will progress to the next stage, which is to continue achieving better scientific results that make a full use of the neutron diffraction experiment. In the future, the accelerator power of J-PARC will increase to about 1 MW. iBIX should be available regularly for full data-set measurement of samples with a volume of 1 mm^3. In order to speed up the better scientific results, we will continue to develop the data reduction software and the beam line instruments to improve the measurement efficiency and the accuracy of intensity data obtained from small samples. Specifically, we plan to install full detectors, a maximum of 60, and increase the number of incident neutrons to crystal samples.

References

[1] I. Tanaka, K. Kusaka, T. Hosoya, N. Niimura, T. Ohhara, K. Kurihara, T. Yamada, Y. Ohnishi, K. Tomoyori and T. Yokoyama, Acta Cryst. D66 (2010) 1194–1197.

[2] K. Kusaka, T. Hosoya, T. Yamada, K. Tomoyori, T. Ohhara, M. Katagiri, K. Kurihara, I. Tanaka and N. Niimura, J. Synchrotron Rad. 20 (2013) 994–998.

[3] N. Yano, T. Yamada, T. Hosoya, T. Ohhara, I. Tanaka, N. Niimura and K. Kusaka, Acta Cryst. D74 (2018) 1041–1052.

K. Kusaka[1], T. Yamada[1], N. Yano[1], T. Hosoya[1], I. Tanaka[1], T. Ohhara[2], and M. Katagiri[1]

[1]Frontier Research Center for Applied Atomic Sciences, Ibaraki University, Tokai; [2]Neutron Science Section, Materials and Life Science Division, J-PARC Center

Current Status of Accurate Neutron-Nucleus Reaction Measurement Instruments, ANNRI (BL04)

1. Introduction

Accurate data of neutron-capture cross sections are important in detailed engineering designs and safety evaluations of innovative nuclear reactor systems. Especially, nuclear data for minor actinides (MAs) and long-lived fission products (LLFPs) are necessary for burn-up analyses of nuclear fuels, improving the design and performance of advanced nuclear reactors and the nuclear transmutation [1]. However, accurate measurements of these cross sections are very difficult due to the high radioactivity of the samples.

To satisfy these demands, a time-of flight experimental instrument named "Accurate Neutron-Nucleus Reaction measurement Instrument (ANNRI)" has been constructed by the collaboration of Hokkaido University, Tokyo Institute of Technology, and Japan Atomic Energy Agency. Measurements of neutron-capture cross sections of MAs, LLFPs and some stable isotopes with high intensity pulsed neutrons began in 2008 [2]. In recent years, a measurement system for neutron total cross section and a new data acquisition system for the array of the Ge detectors have been developed. In this report, we provide an outline of the improvements in the ANNRI.

2. New method for total neutron cross-section measurement

In order to measure the total neutron cross-section, two Li-glass scintillators with different characteristics were prepared. The scintillator of the detector was GS-20 (^{6}Li enrichment higher than 95%) manufactured by Saint Gobain with dimensions of 50 mm × 50 mm and thickness of 1 mm. Additionally, to determine the background, an enriched ^{7}Li-glass detector was used. The scintillator of the ^{7}Li-glass detector was GS-30 (^{7}Li enrichment higher than 99.99%) manufactured by Saint Gobain with the same size and chemical component of the ^{6}Li-glass scintillator. The set-up of the detectors is shown in Fig. 1. The ^{6}Li-glass scintillation detector is installed at flight length of 28.7 m. The ^{7}Li-glass detector was set on the upstream side of the ^{6}Li-glass detector. The signals from the photomultipliers (HAMAMATSU: H7195) were analyzed using CAEN V1720 (12 bit 250 MHz) module with digital pulse processing software, DPP-CI. The module recorded a pulse height and a time of flight in "event-by-event" mode.

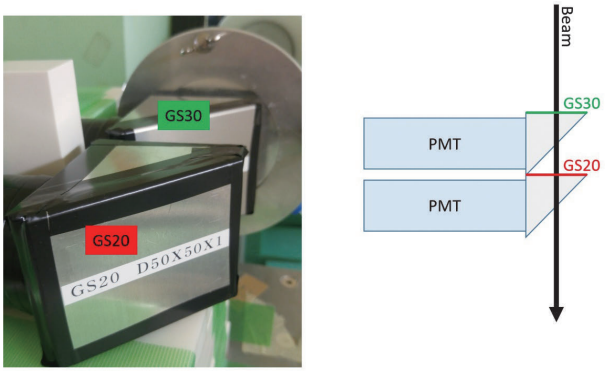

Figure 1. The photo and the schematic view of the Li-glass detectors for the total-neutron cross section measurement.

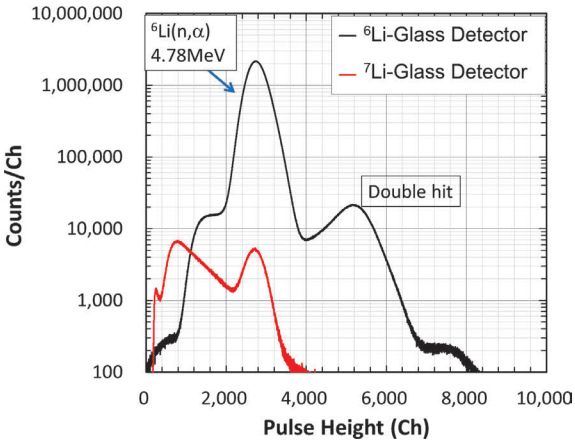

Figure 2. Typical PH spectra of the ^{6}Li detector and the ^{7}Li detector [3].

Typical pulse height spectra are shown in Fig. 2. The spectra are results of a 957 MBq ^{241}Am sample measurement with the ^{6}Li-glass and ^{7}Li-glass scintillation detectors. Using this new method, neutron total cross sections of ^{241}Am were reported in 2018 [3].

3. New data acquisition system

A new data acquisition system (DAQ system) in ANNRI was developed. The growing beam power of MLF in recent years allows the beam line users to obtain high quantity experimental data yields. By 2016, the beam current had increased by more than 25 times, compared to 2008.To match the strong beam power of MLF, a new DAQ system for the array of the Ge detectors in ANNRI is developed [4].

To digitize the detector signals, CAEN V1724 [5] (14 bit 100 MHz) module with a digital pulse processing

software, DPP-PHA has been introduced. A pulse height and a TOF were recorded in "event-by-event" mode with the module. Optical link connections are used for data transfer from the ADC boards to the PC using a CAEN A3818 PCI express board. The maximum data transfer rate is about 80 MB/s. Trigger signals issued from J-PARC were distributed to the DAQ in order to measure time-of-flight events.

The CAEN v1724 ADC works with fixed dead-time for each signal even, if the signal is not treated as a valid event (defined as "not invalid"). If the signal is treated as invalid (defined as "double pulses were detected but could not distinguish the pulse height information from each other"), only the time-stamp information is recorded. In order to estimate the count rate efficiency by the constant dead-time analysis method, we can use this time-stamp information as a starting point of the constant dead-time. In this case, the probabilities of the dead-time appearance are proportional to the real signal rates.

A test of the new DAQ system was performed using standard γ-ray sources and the ANNRI beam line. Figure 3 shows the counting efficiency. It depicts the Ge detector with different shaping time settings. Typically, the system works with 50 kcps for the Ge system.

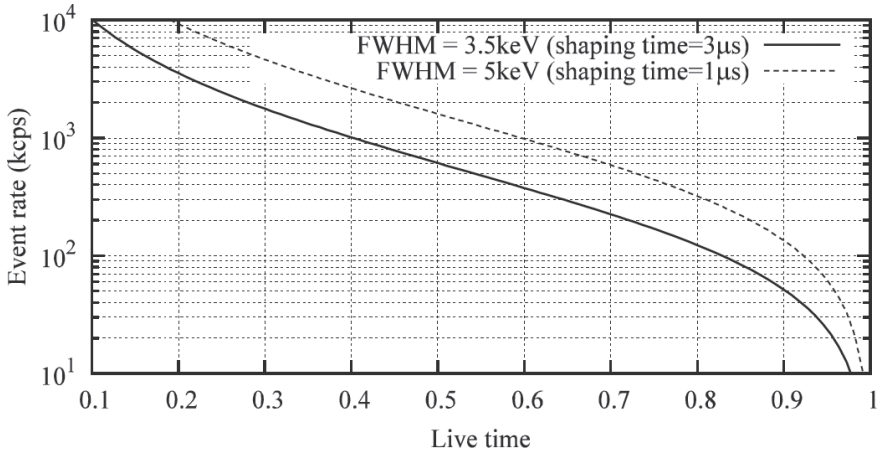

Figure 3. The counting efficiency of the DAQ system with different shaping time. The solid line represents the 3 μs shaping time setting. The dashed line shows the 1 μs case.

References

[1] M. Salvatore, R. Jacqmin, "Uncertainty And Target Accuracy Assessment for Innovative Systems using Recent Covariance Data Evaluations." WPEC-26, OECD NEA, (2008).

[2] H. Harada, et. al., J.Korean Phys. Soc. 59, (2011) 1547.

[3] K. Terada, et. al., Journal of Nuclear Science and Technology, (2018), https://doi.org/10.1080/00223131.2018.1485519

[4] T. Nakao, K. Terada, et. al., In Proceedings of the International Conference on Nuclear Data for Science and Technology (ND2016); 2016 September 11-16; Bruges, Belgium. EPJ Web of Conferences 2017;146:03021.

[5] http://www.caen.it/

A. Kimura

Nuclear Data Center, Nuclear Science and Engineering Center, JAEA

Status of Fundamental Physics Beamline BL05 (NOP) 2017

1. Introduction

"Neutron Optics and Physics (NOP/ BL05)" at MLF in J-PARC is a beamline for studies in the field of fundamental physics. The beamline is divided at the upstream into three branches, the so-called Polarized, Unpolarized, and Low-Divergence branches, used in different experiments in a parallel way [1-2].

A neutron lifetime measurement was being carried out at the Polarized beam branch with a spin flip chopper. Pulsed ultra-cold neutrons (UCNs) by a Doppler shifter are available at the Unpolarized beam branch. At the Low-Divergence beam branch, the search for an unknown intermediate force is performed by measuring neutron scattering with rare gases. The beamline is used also for R&D of optical elements and detectors [3].

2. Measurement of the Neutron Lifetime

A neutron decays into a proton, an electron, and an antineutrino. The decay lifetime is an important parameter for the unitarity of the CKM matrix and also for the primordial big bang nucleosynthesis. However, recently reported values for the neutron lifetime deviate significantly from the systematic uncertainties. An experiment to measure the neutron lifetime with a pulsed beam is ongoing at BL05 (NOP). The lifetime is measured as a ratio of the electron events of the neutron decay to the ^{3}He(n,p)^{3}H events caused by ^{3}He gas precisely doped in a time-projection chamber (TPC). Physics data have been collected for about four weeks by the TPC in 2016. By analyzing the data, we obtained our first preliminary result of the neutron lifetime as

$\tau_n = 896 \pm 10$ (stat.) $^{+14}_{-10}$ (sys.) [4].

3. Search for an Unknown Intermediate Force with Rare Gas Scattering

Since then, many experiments have been performed to measure the deviation from the inverse-square law of Newtonian gravity down to tens of micrometers. We are probing the short-range force in the nanometer scale by measuring the neutron scattering with noble gases.

In the simplest case with an unknown particle with a Compton wavelength of λ, the Yukawa force is expected to add to the Newtonian force so that the potential $V(r)$ between the masses of m and M can be described as

$$V(r) = -G_N \frac{mM}{r}(1 + \alpha e^{-r/\lambda}) \quad (1)$$

where r is the distance between the masses, and G_N is the gravitational constant. Neutron scattering is a unique probe to measure the short-range forces because it has no charge and small polarizability. The extra forces described as equation (1) increase the forward angular distribution in neutron-scattering outgas contamination in the noble gas samples for long time measurements. Two noble gases, He and Xe, were successfully measured in 2017. The results from the analysis by comparing the two gases were consistent with zero additional new forces [5].

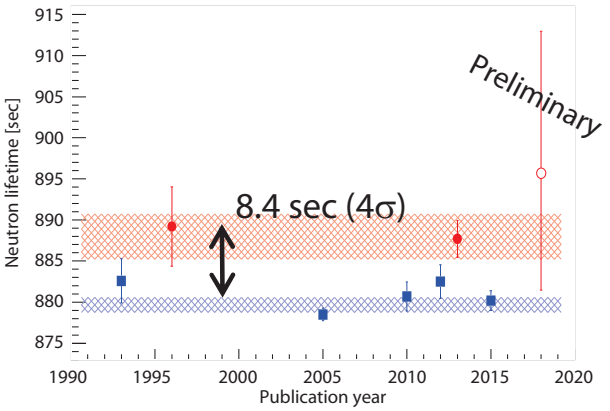

Figure 1. The neutron lifetime measurements in the 2017 PDG [1], the storage methods are denoted as blue squares, the proton counting is shown as closed red circles. The J-PARC preliminary result is shown as a red open circle [3].

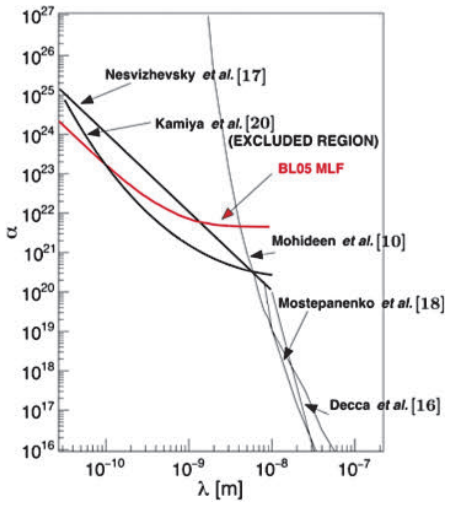

Figure 2. An exclusion line (red) in the α-λ plane resulting from the recent data acquired on BL05 [5].

References

[1] K. Mishima et al., "Design of neutron beamline for fundamental physics at J-PARC BL05," *Nucl. Instruments Methods Phys. Res. Sect. A*, vol. 600, no. 1, pp. 342–345, 2009.

[2] K. Mishima, "J-PARC Neutron fundamental physics beamline (BL05/NOP)," *Neutron Netw. news*, vol. 25, no. 2, pp.156–160, 2015.

[3] K. Mishima et al., Fundamental physics activities with pulsed neutron at J-PARC (BL05). Proceedings of International Conference on Neutron Optics (NOP2017) JPS Conference Proceedings, Vol. 22 (2018) 11033. (arXiv:1712.06351, 2017)

[4] K. Mishima et al., FUPA2018, in Nagoya, Japan.

[5] Haddock et al., Phys. Rev. D 97, 062002 (2018).

K. Mishima[1,2] on behalf of NOP collaboration

[1]*Neutron Science Section, Materials and Life Science Division, J-PARC Center;* [2]*Institute of Materials Structure Science, KEK*

BL06: Commissioning Status of VIllage of Neutron ResOnance Spin Echo Spectrometers (VIN ROSE)

1. Introduction

Neutron spin echo (NSE) is a variety of neutron spectrometry for high-resolution inelastic and quasi-elastic neutron scattering methods [1]. Since the energy resolution of the energy transfer measurement is not limited by the energy spectrum of the incoming neutrons in the NSE technique, a moderately (10-15% FWHM) monochromatic neutron beam is acceptable. In addition, the intermediate scattering function can be directly derived by NSE, so that the method is suitable for studying slow relaxation dynamics in condensed matter, and high-intensity and high-energy-resolution NSE spectrometers have been developed and realized [2].

Since 2011, Kyoto University and The High Energy Accelerator Research Organization (KEK) have been jointly constructing Beam Line 6 (BL06), consisting of two types of NSE spectrometers with neutron resonance spin flippers (RSFs), that is, a neutron resonance spin echo (NRSE) instrument and a modulated intensity by zero effort (MIEZE) instrument, at Materials and Life Science Experimental Facility (MLF), Japan Proton Accelerator Research Complex (J-PARC) [3]. NRSE uses RSFs, which can replace large magnetic precession fields with low-guide fields, therefore downsizing and adjacence of the spectrometers become possible [4].

In this report, the status of the MIEZE and NRSE spectrometers at BL06 in FY2017 is summarized.

2. Commissioning status at BL06 in FY2017

Time-of-flight neutron spectroscopy and MIEZE (TOF-MIEZE) is a novel approach. We have verified quantitatively fundamental characteristics of TOF-MIEZE [5]. In the 2017B proposal round, the user program has been partially started. In addition, we modified the arrangement of RSFs, that is, 4 RSFs were arranged sequentially with $\pi/2$-, π-, π-, $\pi/2$-flip conditions, as shown in Fig. 1. In this setup, the MIEZE-time-beating signal with frequency of 800 kHz can be observed by operating with 400 kHz frequency for the first π-flipper and 800 kHz for the second π-flipper. Figure 2 shows the observed 800 kHz TOF-MIEZE signal and the corresponding power spectrum obtained by Fourier transformation.

At the NRSE spectrometer, the two-dimensional ellipsoidal neutron-focusing supermirrors with $3Q_c$, where $x\,Q_c$ means that the critical angle is x times larger, were developed in close collaboration with the RIKEN center for

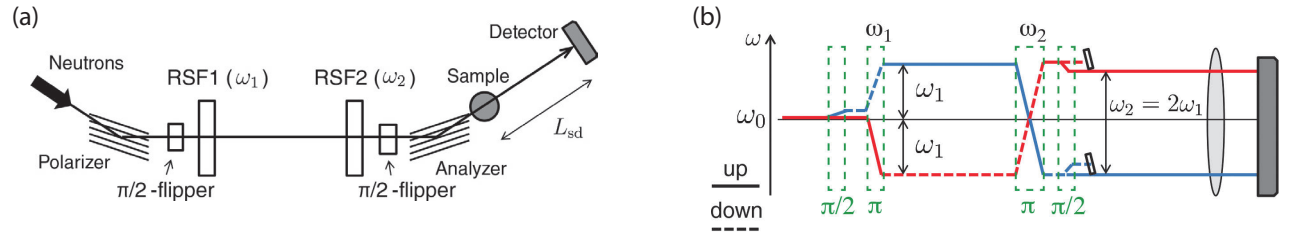

Figure 1. (a) Experimental setup of TOF-MIEZE measurement with effective 800 kHz. (b) Corresponding energy diagram.

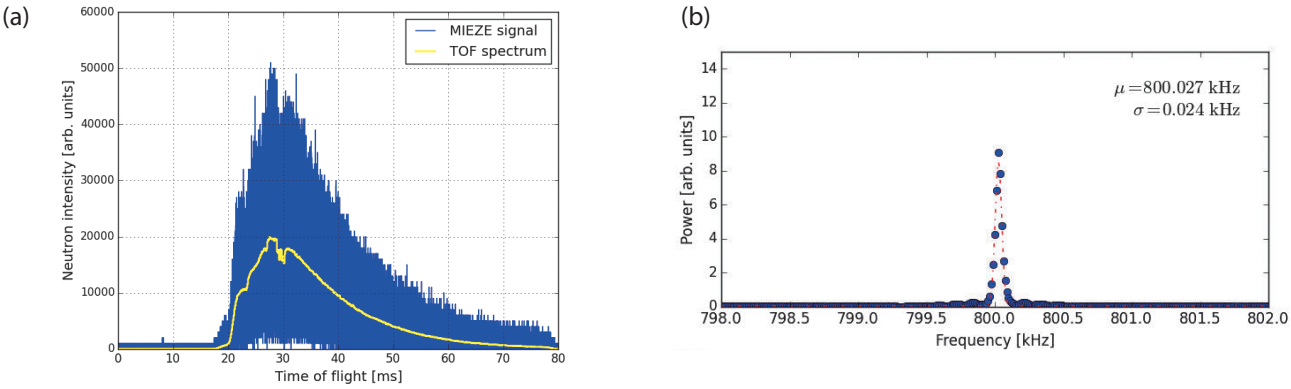

Figure 2. (a) 800 kHz MIEZE signal observed by the setup shown in Fig. 1. (b) Corresponding power spectrum obtained by Fourier transformation.

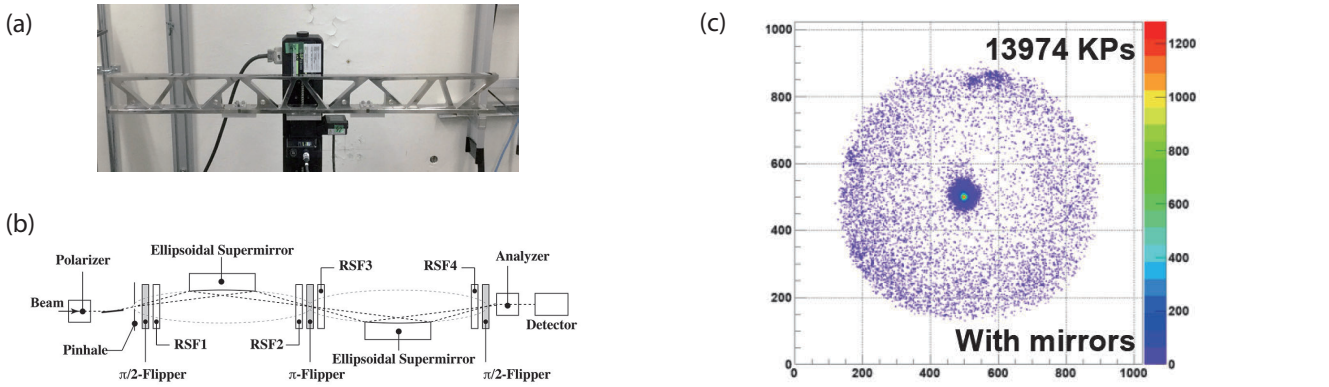

Figure 3. (a) Picture of 900 mm-length metallic two-dimensional elliptic supermirror with $3Q_c$. (b) Experimental setup of the NRSE spectrometer. (c) Focusing beam profile with a pair of the mirrors where the pinhole (ϕ = 1 mm) to detector length is 5 m.

advanced photonics [6]. The optical design is 1250 mm semi-major axis and 65.4 mm semi-minor axis with 900 mm length as shown in Fig. 3 (a). The ellipsoidal supermirrors are essential for NRSE with high-energy resolution, which were installed before and after the sample position symmetrically to correct the path difference, see Fig. 3 (b). In Fig. 3 (c), the focusing beam profile is shown, which clearly shows the required characteristics of the mirrors can be achieved. The beam was restricted by an initial pinhole with 1 mm ϕ, and passed the first focusing mirror, then focused at the sample position (the center π-flipper in this case) and refocused again by the second mirror at the detecting position, where the length between the pinhole to the detector was 5 m. By using this system, we tested the NRSE. RSFs were operated with 50 kHz for the $\pi/2$-flippers and the π-flipper and 100 kHz for RSF1 ~ RSF4, so that the effective frequency became 150 kHz in this case. The repetition rate of the pulsed neutron was tuned to 25/3 Hz by using a band chopper for observation of the neutron wavelength band. Figure 4 shows the observed neutron spin echo signal as a function of the position of RSF4 with 0.05 mm steps, where the wavelength band is from 0.7 nm to 1.6 nm and the intensity is normalized by the mean intensity. This observation is an important step in developing the NRSE spectrometer.

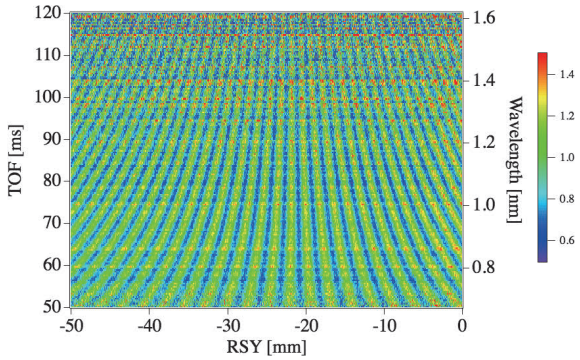

Figure 4. Time-of-flight neutron spin echo signal as a function of the position of RSF4.

3. Summary

This was a brief report about the current status of BL06 VIN ROSE. In FY2017, the public use with the MIEZE spectrometer has been started partially, and 800 kHz TOF-MIEZE signal was observed. At the NRSE spectrometer, the first NRSE signal was observed with ellipsoidal neutron-focusing supermirrors, which was a technical hurdle for the development of NRSE with high-energy resolution. Based on these successful achievements, we will work intensely on the commissioning in FY2018.

References

[1] F. Mezei ed., Neutron Spin Echo, Lecture Notes in Physics, (Springer, Berlin) 128 (1982).
[2] D. Richter, M. Monkenbusch, A. Arbe, J. Colmenero, *Adv. Polym. Sci.* 174, (2005) 1-221.
[3] M. Hino, T. Oda, M. Kitaguch, N. L. Yamada, H. Sagehashi, Y. Kawabata, H. Seto, *Physics Procedia* **42**, (2013) 136.
[4] R. Gähler and R. Golub, J. Phys. France, 49, (1988) 1195-1202.
[5] T. Oda, M. Hino, H. Endo, N. L. Yamada, Y. Kawabata, H. Seto, *J. Phys. Soc. Conf. Proc.* in press.
[6] T. Hosobata, M. Hino, H. Yoshinaga, T. Kawai, H. Endo, Y. Yamagata, N. L. Yamada, S. Takeda, *J. Phys. Soc. Conf. Proc.* in press.

H. Endo[1,2], M. Hino[3], T. Oda[3], N. L. Yamada[1,2], H. Seto[1,2], and Y. Kawabata[3]
[1]Neutron Science Division, Institute of Materials Structure Science, KEK; [2]Neutron Science Section, Materials and Life Science Division, J-PARC Center; [3]Institute for Integrated Radiation and Nuclear Science, Kyoto University

Commissioning of a New 4K Cryostat at S-HRPD

1. Introduction

S-HRPD (BL-08), installed at MLF, J-PARC, is a neutron powder diffractometer with the highest resolution in the world ($\Delta d/d \sim 0.03\%$) [1]. It is very useful for high-resolution experiments, for example, investigation of structural transition together with very small distortion, and structure analysis of low-symmetry material whose profile contains many overlapped Bragg peaks on diffractometers with conventional resolution. Although the resolution of the neutron powder diffraction (NPD) is inferior to that of the synchrotron XRD, NPD has advantages over XRD for some samples (e.g. material containing adjacent elements, and one containing light and heavy elements) and sample environment. Especially, NPD can demonstrate diffraction experiment at low temperature.

A new GM cryostat, with a better performance than the old one, was installed on S-HRPD in the end of FY2016. We performed commissioning of the cryostat and found several problems. The fatal problem was with the sample temperature. We were not able to control the real sample temperature by sample heater in reasonable time. Offline tests revealed the cause of the temperature problem, which we solved by using an additional large vanadium holder and confirmed that it performed NPD of magnetic transitions using 2014S05's beam time. The details are covered below.

2. Offline test

We installed a new 4 K GM cryostat with cooling power of 1.5 W at 4.2 K. We can control the temperature with a 100-W heater installed on the top of the cold-head. The cryostat has two jackets, one is the outer vacuum chamber (OVC), the other is the inner Al tube (ϕ124 mm) for the radiation shield. The incident neutron beam passes two vanadium windows (with thickness of 100 μm) at the front and back of OVC.

First, we did an offline operation check without sample holder. Because the cooling power was sufficiently strong, it was possible to go from room temperature (RT) to 4 k in about 90 minutes. On the other hand, when we measured NPD for samples with an enclosed V-Ni 6-mm sample holder with helium gas at 1 atm, a problem with the temperature emerged. Whereas the monitor displayed a temperature of 3 K, we could not observe magnetic peak of one sample with T_N = 5 K. When the cold-head temperature was changed from 20 K to 50 K, the Bragg peaks were gradually shifted in 6 hours; it took at least 6 hours to reach a thermal equilibrium of the real sample temperature. There are two possible explanations: i) the thermal conduction from cold-head to sample is too weak, and ii) the position and temperature of the radiation shield are not suitable.

Next, we tried to check the real sample temperature in an offline test. The V-Ni sample holder containing helium gas was mounted to the cold-head. The cell was checked by helium gas detector and there was no leakage. The cryostat has two temperature sensors, one (sensor A) is at the center of the cold-head, the other (sensor B) is on the tip of cold-head. We moved sensor B to the bottom of the sample holder to record the real sample temperature. In this setting, large differences between the temperatures of sensor A and sensor B were observed; although sensor A showed 3 K as the lowest temperature, sensor B showed 19 K (Fig. 1). Then the holder was heated up to RT while keeping the temperature of sensor A at several points. Whereas the response of sensor A was quick, the response of sensor B was very slow. In addition, at above 200 K, the temperature of sensor B was lower than that of sensor A. We concluded that the major cause for the sample temperature problem was weak thermal conductivity of the V-Ni sample cell. To stabilize a temperature of sample position, copper stick imitating a sample cell was used. There was almost no difference between the temperatures of the two sensors and the temperature response of sensor B was good.

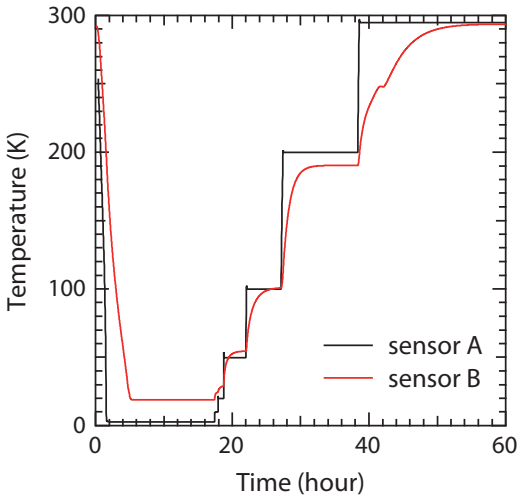

Figure 1. Temperature log of the offline test.

3. Online test

To realize good thermal coupling, we prepared additional 10-mm vanadium holder, the layout is shown in Fig. 2. The V-Ni 6-mm holder was enclosed in the 10-mm cell together with helium gas. Because it was impossible to check the real sample temperature using a temperature sensor, we performed diffraction measurement as an online test. We used as a reference sample of the temperature points, a powder sample of the geometrical frustrated compound $Co_2(OD)_3Br$ [2]. Its crystal structure was hexagonal (*R-3m*) and had a tetrahedral arrangement of S = 3/2 Co^{2+} ions. There were two magnetic transitions at $T_{N1} = 6.2$ K, $T_{N2} = 4.8$ K. Each magnetic transition T_{N1} and T_{N2} was related to a magnetic peak indexed $\boldsymbol{k}_1 = (1/2\ 0\ 1/2)$ and $\boldsymbol{k}_2 = (0\ 0\ 3/2)$, respectively, thus, we could check two temperature points. Figure 3 shows NPD profiles at 10 K and 3 K. We performed Rietveld analysis to refine the crystal and magnetic structures using Z-Rietveld program [3]. The results showed a good agreement with the reference for both crystal and magnetic structures. The temperature dependence of the integrated intensity of two kinds of magnetic peaks are shown in Fig. 4. Both transition temperatures could be reproduced in this experiment. We also checked the response of the sample temperature during the heating process. The temperature (sensor A) was set up to 10 K, 20 K, 40 K, 100 K, 150 K, 200 K and 250 K with 3 hours' measurement at each temperature point. Before this measurement, sensor B was put back to the original position. Table 1 shows the elapsed time from the moment of setting a new temperature point to the start of the next measurement, when the temperature of sensor B is stable. The time-sliced data sets with 5 minutes' interval are shown in Fig. 5. Only the first 5 minutes' profile shows a slight peak shift, so it is enough to wait for about additional 5 minutes after stabilizing the temperature.

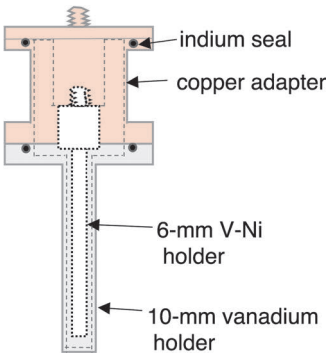

Figure 2. The sample setting for the online test.

Table 1. The elapsed time of the temperature increasing process.

start T (K)	set T (K)	elapsed time (min.)
10	20	4.2
20	40	4.2
40	100	9.7
100	150	12.5
150	200	14.1
200	250	15.8

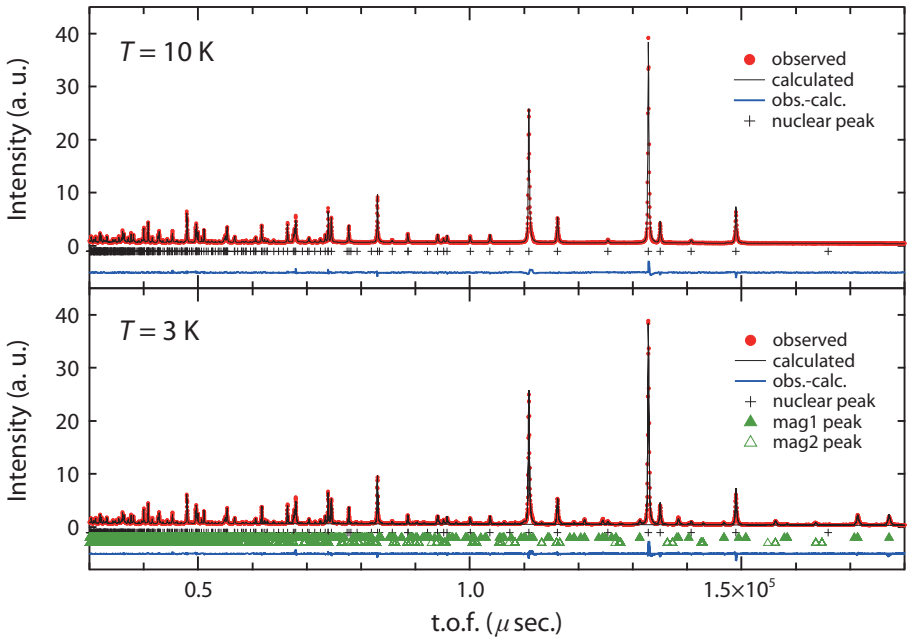

Figure 3. The NPD profile of back scatter bank and Rietveld refinement result on $Co_2(OD)_3Br$ at (up) 10 K and (down) 3 K.

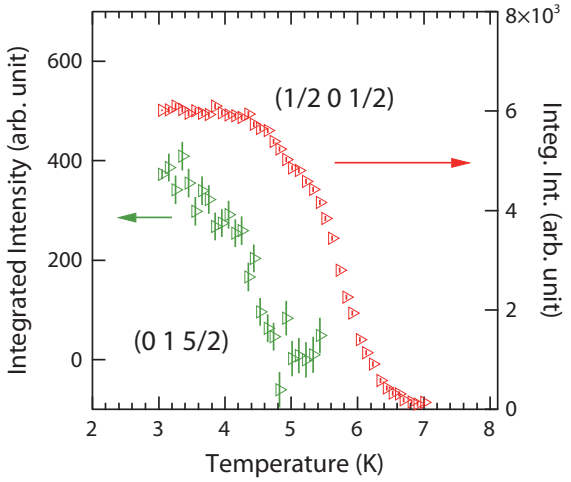

Figure 4. The temperature dependence of integrated intensity of two magnetic peaks. The (1/2 0 1/2) and the (0 1 5/2) reflection is related to $\boldsymbol{k}_1$ = (1/2 0 1/2) and $\boldsymbol{k}_2$ = (0 0 3/2) order, respectively.

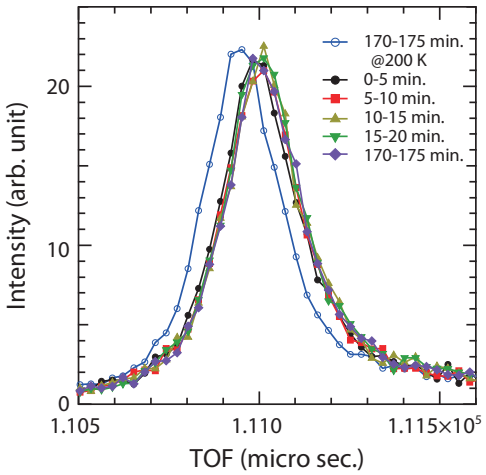

Figure 5. The peak profiles of (2 0 4) reflection on $Co_2(OD)_3Br$. The profiles were collected at 250 K, except for the purple line (200 k).

4. Summary

We did commissioning of a new 4 K GM cryostat and improved the accuracy and response of the sample temperature. We provided the cryostat to user programs and several user groups used it. An ongoing problem is that it takes a long time to change a sample. When the sample temperature reaches RT after cooling, the most part of the cryostat is still cold, so we need to wait for several hours to open the OVC. The background signal is high because of scattering from the OVC and the inner Al tube. We will solve these problems in the future.

References

[1] S. Torii *et. al., J. Phys. Soc. Jpn.* **SB020** SB020-1-4 (2011).
[2] M. Hagihala *et. al., Phys. Rev.* **B** 82 214424 (2010).
[3] R. Oishi-Tomiyasu *et. al., J. Appl. Crystallogr.* **45** a299-308 (2012).

M. Hagihala[1,2], S. Lee[2], S. Torii[1,2], and T. Kamiyama[1,2]
[1]Neutron Science Section, Materials and Life Science Division, J-PARC Center; [2]Institute of Materials Structure Science, KEK

Current Status of Special Environment Powder Diffractometer, SPICA

1. Introduction

The battery is a key technology in society because the consumer and business electronic devices, like mobile phones, laptop computers and even an electric vehicles (EV) work only with batteries as energy sources. Currently, the lithium-ion battery (LIB) is the best system to store large energy density. An all-solid-state battery, which has more powerful output performance, is also being developed for commercial usage as the next battery system. And some other advanced battery systems, like metal-air and fluoride ones, have been proposed and are in the process of research. However, it will take a long time before they are ready for practical use.

Neutron *operando* measurements to observe directly inside a battery and detect key issues to improve its performance in operative conditions are important for current and future studies. BL09, SPICA is the only beamline in the world, solely dedicated to battery study. The *operando* measurements have already been performed and some results were reported [1, 2]. For the next step in improving the *operando* measurements, a limited space volume measurement is being developed. To define space as a gauge, volume, width, height, and depth are necessary. The sizes of the width and height are defined by the size of the beam slits in front of a sample. They cannot limit the depth along the incident-beam direction. If only 90 banks are used for the limited space volume measurements, a radial collimator is very effective to define the gauge volume in the time of flight (TOF) diffraction technique. In this development, we tried to apply 3D-printing technique to create the radial collimator.

2. Development of the Radial Collimator as space definitory

The radial collimator has many neutron-absorber blades in cylindrical locus, to define the gauge volume. It is suitable equipment to limit the sight-view of depth along an incident beam direction, especially in the TOF diffraction technique at 90° banks. Figure 1 shows an illustration of the limited space volume technique in the TOF diffraction measurements. An incident neutron beam passes through four quadrant-multi slits in front of a sample. The slits, made by sintered B_4C plates with thickness of 10 mm, define the width and the height of the beam. The depth along an incident beam direction is limited by a radial collimator.

Three different radial collimators with 2, 5, and 10 mm sight-view sizes, respectively, were developed on SPICA. A basic design of a radial collimator was reviewed by Dr. Torii, Dr. Moriai and S. Harjo [3-5]. The radial collimators for BL09 were designed in 2014 on basis of their reports in 2014 [6].

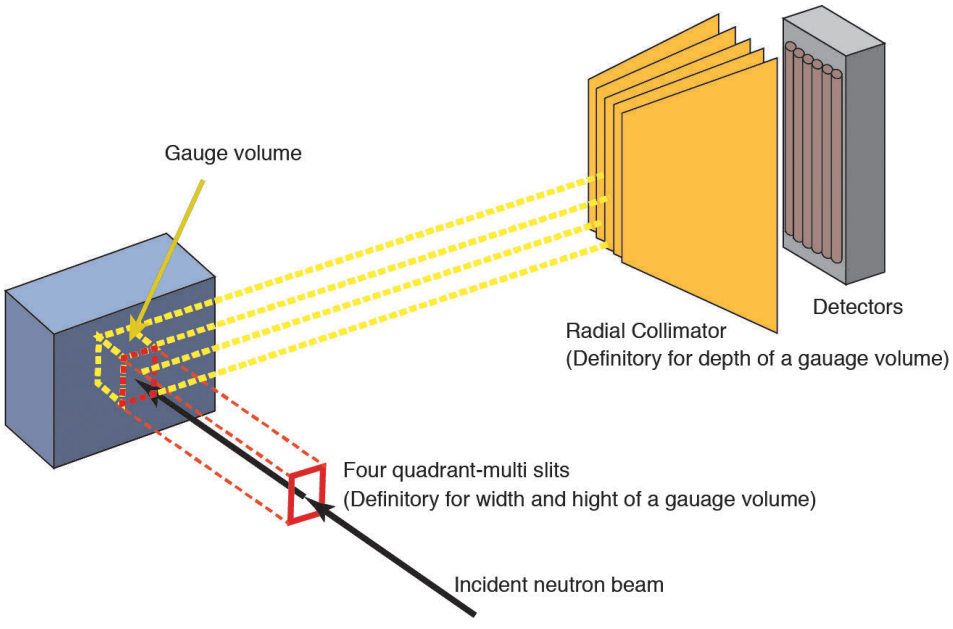

Figure 1. The illustration of the limited space volume measurements in the time-of-flight technique. The radial collimator is the key device to define the depth of the sample to measure.

SPICA uses rough course collimators to reduce the air-scattering level in front of all detector-banks, except the back-scattering ones. It is possible to install the new radial collimators in two different locations, between the vacuum sample chamber and the detector-banks or in the chamber. In the 2014 design, we considered the location between the chamber and the detector-banks. However, the experimental conditions may require removal of the collimators. But in the 2014 design, it was not easy to remove them because they were confined to a limited space due to overhung upper-detector-banks. Therefore, the new ones were redesigned to be placed in the sample chamber.

The basic parameters of the new ones are show in Table 1. The blades of the collimators are located between 200 to 400 mm from the center of the sample position. The gap between each of the blades was calculated based on the previously reviewed papers [3-6]. These radial collimators were designed to cover an angle from 60° to 120°. Figure 2(a) shows the design picture of the 10-mm one. The basic shapes of radial collimators in this development are the same as seen in Fig. 2. The 2, 5, and 10 mm sight-view collimations were obtained from the different slit gaps. The narrow slit-size was consistent with the narrow sight-view. A pair of these collimators was installed at a 90° angle position.

Figure 2(b) shows the real collimators created by the 3D-printer, AGILISTA-3100 (KEYENCE corporation), which were placed at the Mechanical Engineering Center in the High Energy Accelerator Research Organization (KEK). The price for this collimator was less than one fourth of the price for a manufactured radial collimator. The benefits from 3D-printing are 1) short time to create, 2) create easily a complicated structure component and 3) low weight. This 3D-printer creates an object from organic polymer. The weight of the developing collimator (one set of one side) is approximately 10 kg, which is amazingly low. The blade was formed by organic polymer materials. The hydrogen in the organic polymer became a neutron absorber. Therefore, it was not necessary to coat them with an extra neutron absorber.

Table 1. The basic parameters of the radial collimators on SPICA.

Distance of blades		
from the sample center (mm)		200
to the ends of collimators (mm)		400
Gap between each blade		
Depth	Near side	Far side
2 mm	0.90	1.80
5 mm	2.25	4.50
10 mm	4.50	9.00

4. Performance of the 3D-printed radial collimator

The 3D-printed radial collimators were installed on BL09 with 5-axis goniometer. Neutron diffraction data were taken when a tandem of two different metals with diameter of 10 mm shifted each sample position from + 25 mm to − 25 mm with 1 mm steps along the neutron beam direction. The collected diffraction data with the 5-mm radial collimator is shown in Fig. 3.

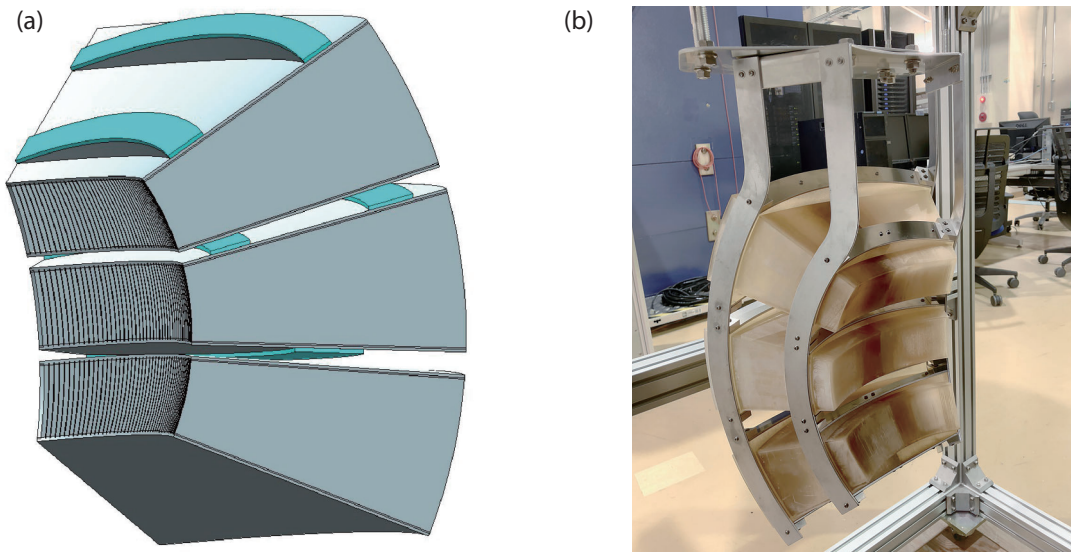

Figure 2. The illustration of the radial collimators in this development. (a) The 3D-design picture of 10 mm radial collimators. 90° banks have a 3 detector-bank (upper, middle and lower) at both the left and right sides. (b) Photograph of the 3D-printed radial collimators.

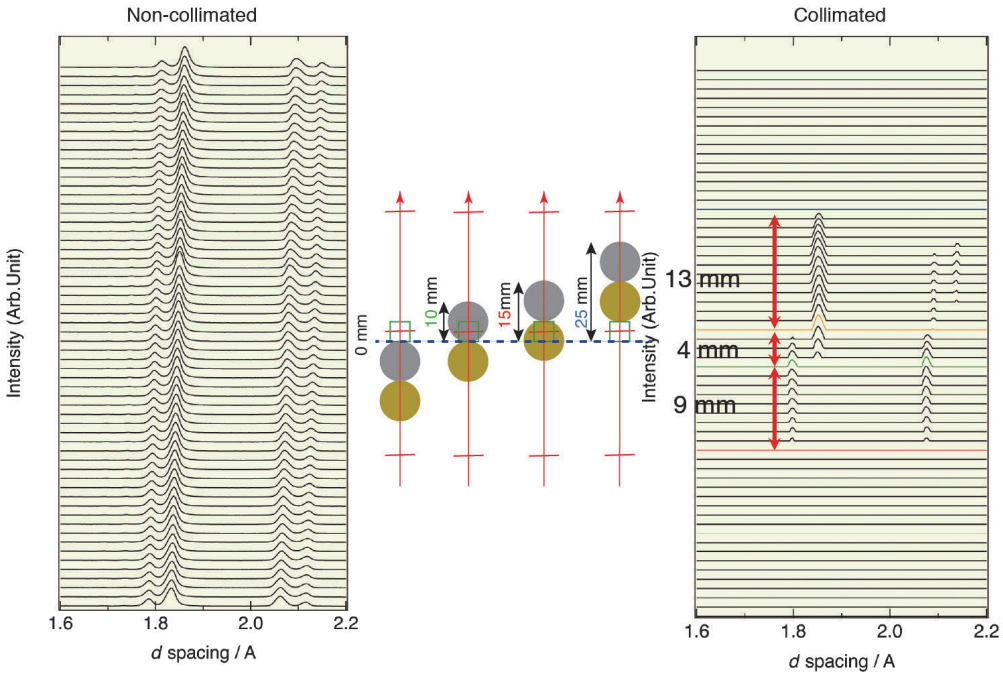

Figure 3. The neutron diffraction data, non-collimated and collimated by the 5 mm radial collimators in this development.

Figure 3 indicates that the radial collimator worked successfully. In non-collimated conditions, the diffraction peaks from the tandem of two different metals appeared in all sample positions. On the other hand, the diffraction peaks from these metals were only observed when these metals passed through the collimated sight-vision area by the radial collimators. These results indicated a depth resolution of 4 mm against the 5 mm in the designed resolution. However, both metals having same diameter were observed in different path-length, 9 and 13 mm, as shown in the Fig.3. These differences might come from geometrical misalignment of the collimator. The sample position and height were correct. However, the collimator was located at a slightly higher level than the sample position. To understand what happened, we will repeat the experiment with a correct geometry condition.

Acknowledgements

This work was supported by the Research and Development Initiative for Scientific Innovation of New Generation Batteries (RISING2) project of the New Energy and Industrial Technology Development Organization (NEDO). The neutron scattering experiment was approved by the Neutron Scattering Program Advisory Committee of IMSS, KEK (Proposal No. 2014S10).

References

[1] S. Taminato, et. al., Scientific Reports, 6, Article# 28843 (2016).
[2] S. Shiotani, et. al., Journal of Power Sources, 325, 404–409 (2016).
[3] S. Torii, et. al., JAEA-Technology, 2005-004.
[4] S. Torii, et. al., Physica B, 385-386, 1287–1289 (2006).
[5] S. Harjo, et. al., JAEA-Technology, 2008-004.
[6] N. Suzuki, et. al., JPS Conf. 8, Article# 03010 (2015).

M. Yonemura[1,2,3], Y. Ishikawa[4], H. Kawamata[5], M. Yamanaka[5], and T. Kamiyama[1,2,3]

[1]Institute of Materials Structure Science, KEK; [2]Sokendai (The Graduate University for Advanced Studies); [3]Neutron Science Section, Materials and Life Science Division, J-PARC Center; [4]Neutron Science and Technology Center, CROSS; [5]Mechanical Engineering Center, KEK

BL10: NOBORU

1. Introduction

In FY 2017, twenty general-use proposals and three project-use proposals, in addition to the postponed three proposals from FY 2016B, were carried out at NOBORU. The user program was not disrupted by any technical problems with the instruments.

This year, we did not add any beamline device. The proton beam power was not increased because of the acceptance limitation of the mercury target, so the dependence of the neutron beam intensity on proton beam intensity was not examined. Instead, we carried out the other neutronic performance test described here in Section 2.

We also carried out the continuing test of the 2012 model lithium-6 time analyzer neutron detector (LiTA12) system [1] at NOBORU. Its purpose is to provide high efficiency at epi-cadmium cut-off energies and a high counting rate with a reasonable spatial resolution. The result of the maximum counting rate estimated in 2017 is reported in Section 3.

2. Dependence of neutron beam intensity on the proton beam profile and the injection position

Neutron intensity depends on the profile and position of the proton beam injected into the mercury target. Therefore, we measured the neutron intensities during changes of the proton beam profile and position (Fig. 1).

The experiment was conducted at NOBORU with a monitor-type He-3 detector (Efficiency: 10^{-3}) located at 13.0 m from the moderator. A rotary collimator with 'tiny' size aperture (3.2 × 3.2 mm^2) and a duct collimator with small size aperture (20 × 20 mm^2) were adopted. A disk chopper was used to suppress the frame overlap neutrons. In the measurement, the proton beam conditions were changed as follows:

Vertical proton beam position:

y = –4, –2, 0, 2, and 4 mm.

Proton beam profile:

Flat distribution (with octupole magnet) and Gaussian distribution (without octupole magnet).

The results are shown in Fig. 2. The neutron intensities were integrated between 1 meV and 20 meV. As the vertical position of the proton beam rises, the neutron intensity increases. As shown in Fig. 1, the reason was that the decoupled moderator providing neutrons to NOBORU was located above the target. On the other hand, the flat profile of the proton beam provided a higher neutron intensity than the gaussian profile. The possible reason for it was that the flat distribution of protons provides a smaller proton beam loss than the gaussian distribution of protons. These results have been presented at the 2018 Fall Meeting of the Atomic Energy Society of Japan.

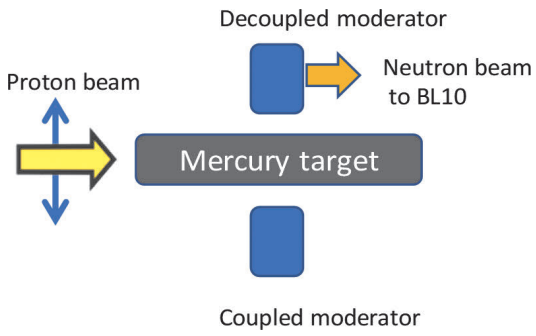

Figure 1. Vertical relation of proton beam, target and moderators.

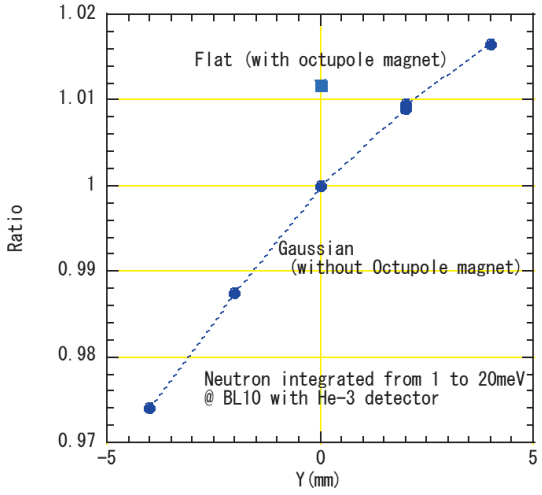

Figure 2. Relative neutron intensity integrated between 1 meV and 20 meV during the change of the proton vertical position and the proton beam profile.

3. Maximum counting rate of LiTA12 system

A ^{6}Li-glass scintillator (GS20) of 1 mm in thickness with a multi-anode photo multiplier tube (Hamamatsu Photonics K.K.: H9500 series, detection area 49 × 49 mm^2) was set at the 13.4 m position of NOBORU. The proton beam power was 150 kW. The spatial resolution of this system using the center-of-gravity calculation was estimated to be 0.7 mm for the energy at 4.9 eV as reported last year [2]. The maximum counting rate was estimated by measuring neutron spectra with varying neutron intensity by the rotary collimator and a filter device [3].

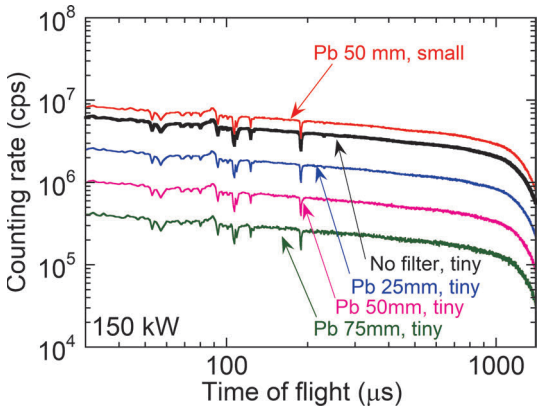

Figure 3. Neutron counting rates as a function of neutron flight time for different neutron intensities controlled by selection of 'tiny' or 'small' through-apertures in the rotary collimator and through various thicknesses of the lead (Pb) filters.

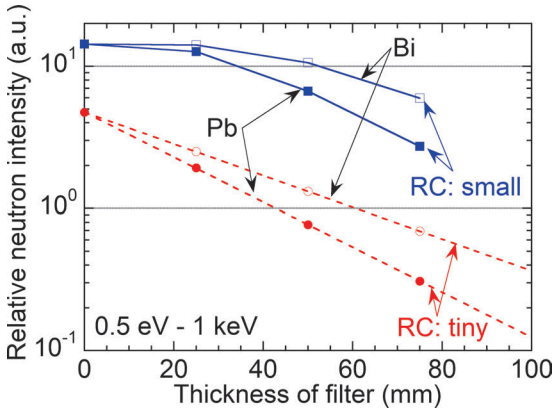

Figure 4. Neutron intensity as a function of the thickness of the lead (Pb) or bismuth (Bi) filters with 'tiny' or 'small' rotary collimator apertures. The values are integrated between 0.5 eV and 1 keV. The dashed lines for the 'tiny' cases are fitted ones, the solid lines for the 'small' are an eye-guide.

The rotary collimator has a revolver equipped with four through-apertures in a 400-mm long stainless-steel cylinder. Apertures designated 'small' and 'tiny' with cross sections of 10 × 10 and 3.2 × 3.2 mm^2, respectively, were used. The neutron intensities increased roughly tenfold by changing the aperture from 'tiny' to 'small' expected from the ratio of cross sections of them. The filter device has four linear stages with two filters each. A cadmium filter (thickness 2 mm) was used for all measurements. The thicknesses of lead (Pb) or bismuth (Bi) used in the measurements with the 'tiny' or 'small' apertures were 0, 25, 50 and 75 mm.

Neutron counting rates as a function of time-of-flight were measured in various neutron intensity conditions to find the maximum counting rate. Figure 3 shows those measured with the 'tiny' aperture and Pb filters of 0, 25, 50 and 75 mm in thickness, and with the 'small' aperture and 50-mm thick Pb filter. The range of flight time in the figure corresponds to the neutron energy range between 1 keV and 0.5 eV. The shapes of these spectra were almost the same, indicating that those measurements were performed without counting loss. Some deteriorations in the spectra were recognized in the 'small' aperture cases without filter, with the 25-mm thick Pb and Bi filters, and with the 50-mm thick Bi one. The highest counting rate of 8 Mcps was recorded by the 'small' aperture with the 50-mm thick Pb filter [4].

Figure 4 shows the neutron intensities integrated between 0.5 eV and 1 keV as a function of the filter thickness. In the near future, we plan to increase the neutron intensities 6.67 times by increasing the proton beam power from 150 kW to 1 MW. The values in Fig. 4 were normalized so that the value of the 'small' aperture with the 50-mm thick Pb filter was 6.67 to project the availability of the LiTA12 system at the higher beam power. At a proton beam power of 1 MW, the LiTA12 system is expected to be available with intensity conditions with relative values below 1.0. In the case of 500 kW, the limit is 2.0. It indicates that the 'tiny' aperture with the 50-mm thick Pb filter is recommended for measurements at epi-cadmium cut-off energies in the future 1 MW operation.

References

[1] S. Satoh, Development of a 2012 model for the 6Li time analyzer detector system, Phys. Procedia 60, 363 (2014).
[2] MLF Annual report 2016, 98 (2016).
[3] M. Harada, et al., JPS Conf. Proc. 1, 014015 (2014).
[4] T. Kai, et al., Physica B, to be published (Proceedings of ICNS2017).

M. Harada[1] and T. Kai[2]
[1]Neutron Source Section Materials and Life Science Division, J-PARC Center; [2]Neutron Science Section Materials and Life Science Division, J-PARC Center

BL11: Development of High-P Experiments Using a Paris-Edinburgh Cell

1. Introduction

Since the start of the beamline operation at 2013, accessible pressure and temperature range have been extended by developing high-pressure devices, such as a six-axis press and diamond anvil cells [1,2]. Now we can routinely collect diffraction data up to about 18 GPa [3]. However, the users' demands are still expanding. To satisfy them, we tackled the following challenges this year:

a. Extend the maximum pressure limit by using a Paris-Edinburgh (P-E) cell equipped with smaller top anvils.
b. Increase the data quality by avoiding freezing of pressure-transmitting medium (PTM) using a heating system.
c. Correlate the pressure change with neutron data acquisition.

Here, we will introduce these results in detail.

2. Extension of the maximum pressure limit with use of smaller top anvils for a P-E cell

In principle, pressure is equal to the force divided by the area which the force is applied to. Therefore, higher pressure is generated by applying the force to a smaller area. So far at PLANET, anvils whose top are 4 mm or 6 mm in diameter have been normally applied in the experiments using a P-E cell, which makes possible the structure analysis at pressures up to 18 GPa [3]. To extend this pressure limit, we tested the pressure generation and data acquisition using anvils whose tops are 3 mm and 2.5 mm in diameter.

Figure 1 shows the diffraction patterns of a mixture of NaCl and MgO compressed with a PTM of the methanol/ethanol mixture. Thanks to the narrow beam collimation, clean diffraction patterns were obtained up to about 30 GPa. The generated pressures were calculated from the lattice parameters of the sample based on the previously reported equation of state [4, 5]. Figure 2 shows pressure generation curves obtained in this study (purple and green), together with those for the anvils with a larger top size. Results showed that the maximum pressure has been extended to 30 GPa without degrading the quality of the diffraction pattern. Comparison of the pressure generation curve among the different top anvils revealed that the pressure generation efficiency was proportional to the inverse area of the top of the double toroid anvils (described as DT in Fig. 2). Based on this relationship, it is expected that

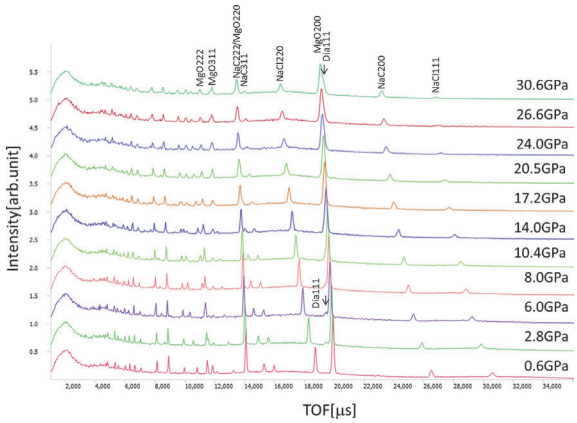

Figure 1. Diffraction patterns of a mixture of NaCl and MgO taken with 2.5 mm-top sintered diamond anvils.

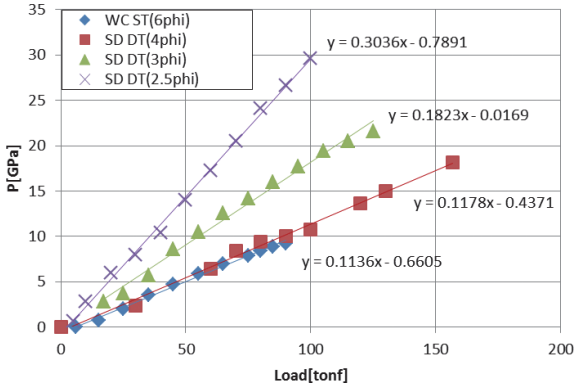

Figure 2. Pressure generation curves for different anvil tops (WC ST: single toroidal tungsten carbide anvils, SD DT: double toroidal sintered diamond anvils).

100 GPa can be generated by applying load of 50 ton with 1-mm-top anvils in future.

3. Increase of the data quality by avoiding the freezing of pressure-transmitting medium using a heating system

Normally, in the experiments using P-E cell, the sample is compressed with liquid PTM to avoid broadening of the diffraction peaks due to the collision of crystal grains, which makes the precise structure determination difficult. For this reason, liquid that has high freezing pressure is preferable as PTM, and a mixture of deuterated methanol and ethanol (ME) in volume ratio of 4:1 is normally used. This PTM works well at pressures below 10 GPa, but at higher pressures it freezes, and hydrostatic condition is no more present. We actually encountered this situation when extending the maximum

pressure range above 10 GPa. Heating of the PTM could efficiently overcome this problem. Previously reported pressure dependence of melting temperatures of ME mixture suggests that the freezing pressure point can be extended to 17 GPa by heating it to 100°C [6]. For this purpose, we built a sample heating system for a P-E cell. Figure 3 shows the system configuration and the enlarged view of the anvil parts. The system consists of wire heaters (Watlow,130 W), DC power supplies (Takasago Den-netsu, ZX-400MAN) and PID controllers. Each heater is attached to an upper or lower anvil via an adapter. To transfer the heat effectively, each anvil is press fitted into the adapter via a tapered ring. The temperature of the anvil is monitored with a K-type thermocouple attached to the anvil and is PID controlled individually. By using this system, the PTM (and the sample) can be heated to 100°C.

To illustrate the effectiveness of heating, the pressure dependence of the 220-diffraction peak of MgO taken with and without heating are shown in Fig. 4. Without heating (upper left in Fig. 4), the peak becomes broader above 10 GPa. On the other hand, the peak with heating shows no marked broadening even above 10 GPa (upper right in Fig. 4). To show the difference more quantitatively, the pressure dependence of the FWHM is shown in Fig. 4. Contrary to the significant increase of FWHM above 10 GPa in the case without heating, the FWHM remains almost unchanged in the case with heating.

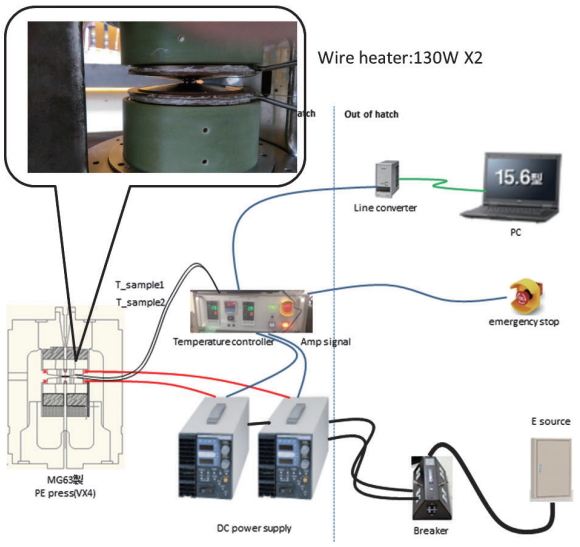

Figure 3. Configuration of the heating system and the enlarged view of the anvil parts.

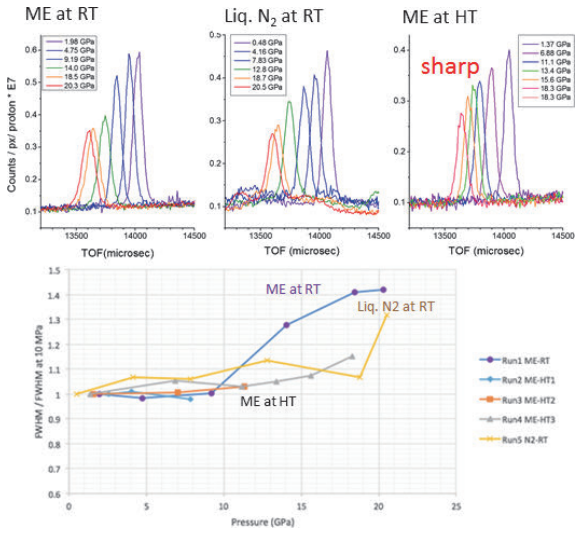

Figure 4. Pressure dependence of the profile of MgO 220 peaks (upper) and the FWHM (lower) with and without heating.

4. Correlation of pressure change with neutron data acquisition

Usually in the experiments using a P-E cell, the diffraction data at high pressures are collected in the following sequences:

1. Compress the sample to the desired load.
2. Move back the sample position to the center of goniometer to compensate sample drift by compression.
3. Collect the diffraction data.

The typical exposure time is from 3 h to 12 h, thus users had to come the beamline each time to execute the above process manually. It's often time consuming and exhausting. If the amount of drift is known in advance, these procedures can be done automatically by correlating pressure change with data acquisition. To make it possible, we have implemented pressure change commands in our software "Experimental Scheduler", which uses batch control. Thanks to this development, now a series of high-pressure data are collected once the users plan the experiments.

References

[1] T. Hattori, *et al.*, MLF Annual Report 2013, 93.
[2] T. Hattori, *et al.*, MLF Annual Report 2016, 99.
[3] T. Hattori, *et al.*, MLF Annual Report 2014, 93.
[4] J. M. Brown, J. Appl. Phys., 86, 5801 (1999).
[5] I. Jackson, Geophys. J. Int., 134. 291 (1998).
[6] S. Klotz *et al.*, High Press. Res., 29, 649 (2009).

T. Hattori[1], A. Sano-Furukawa[1], S. Machida[2], J. Abe[2], and K. Funakoshi[2]
[1]Neutron Science Section, Materials and Life Science Division, J-PARC Center; [2]Neutron Science and Technology Center, CROSS

Status of High Resolution Chopper Spectrometer, HRC, in FY2017

1. Introduction

The High Resolution Chopper Spectrometer (HRC) is being operated at BL12 to study dynamics in condensed matters with high resolutions using relatively high energy neutrons. A research project using HRC is being conducted to observe wide range of correlated electron systems. In FY2014, we entered the second phase of our project , where we will improve the performance of HRC in the following points: (1) detector system at low angles for high energy experiments, (2) Fermi choppers for higher resolution and lower background, (3) sample environments, (4) completion of installing detectors at high angles, and (5) computational environment for easy operation of experiments. In this phase, using these instrumentations, we are improving the neutron Brillouin scattering (NBS) experiments and realizing inelastic neutron scattering experiments under external fields.

2. Instrumentation in FY2017

NBS is inelastic neutron scattering near to the forward direction. This technique is effective for observing coherent excitations in non-single-crystal samples, such as ferromagnetic spin waves in powder samples. After the recent success of NBS [1], the neutron intensities for NBS experiments were increased by the doubled array of PSDs, the less deformed slit package of the Femi chopper and the longer incident beam collimator [2]. On HRC, one of the two Fermi choppers, which are the high-intensity chopper and the high-resolution chopper, can be selected to optimize every experiment. The performance of the high intensity chopper has been well established by the recent instrumentation. To improve the performance of the NBS experiment, the parameters of the slit package of the high-resolution chopper, which are the slit width and the slit curvature, were optimized so that the intensity at $E_i = 100$ meV can be doubled with unchanged energy resolution to reach $\Delta E/E_i = 2\%$. Also, the long collimator was replaced by one with better transmission. As shown in Fig. 1, the neutron flux greatly increased. Moreover, the best energy resolution was achieved to be 1% something with a reasonable neutron flux by rotating the chopper faster.

Realizing inelastic neutron scattering experiments under external fields is another important issue on HRC. We performed inelastic neutron scattering experiments under high pressures. A standard sample can contains a cylindrical pressure cell with a sample crystal cooled with a 1 K refrigerator. We confirmed a pressure-induced phase transition and successfully observed magnetic excitations at 1.4 GPa in $CsFeCl_3$ [3, 4], as shown in Fig. 2.

Magnetic field is also one of external fields, under which inelastic neutron scattering experiments are to be performed on HRC. The superconducting magnet was repaired due to vacuum leak. According to the

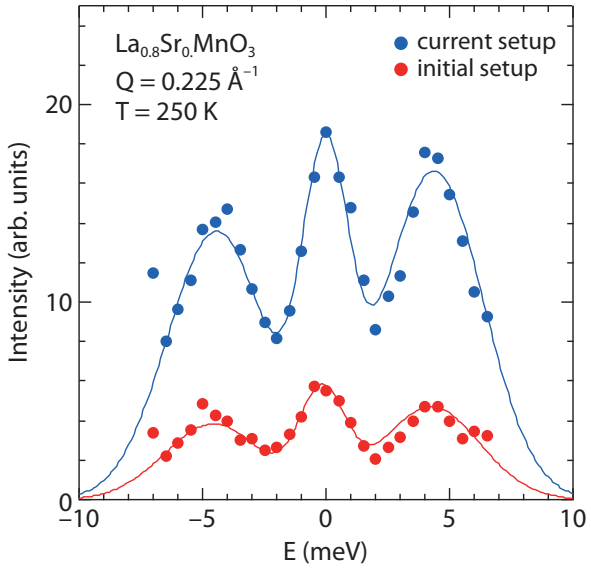

Figure 1. NBS spectra for ferromagnetic spin waves in $La_{0.8}Sr_{0.2}MnO_3$ in the current improved set-up and in the initial set-up when the NBS experiment was started on HRC for the first time. The experiments were performed with $E_i = 100$ meV and $\Delta E/E_i = 2\%$.

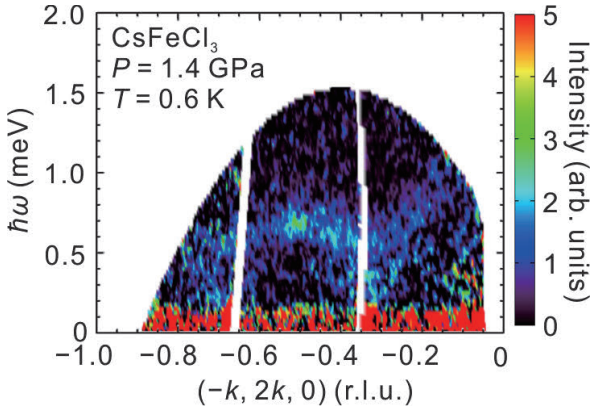

Figure 2. A preliminary result of inelastic neutron scattering from $CsFeCl_3$ at P = 1.4 GPa and T = 0.6 K. The scattering intensities related to the ordering wave vector (1/3, −2/3, 0) can be seen.

manufacturer, the vacuum leak may have been caused by a deformation due to applying magnetic fields on HRC, which contains a large amount of iron materials. The manufacturer evaluated the maximum magnetic field to be 5 T under the HRC environment. Based on this report, we plan to perform experiments using this magnet in the next fiscal year.

At the secondary flight path L_2 = 4 m on HRC, 256 pieces of position sensitive detectors (PSDs) with 2.8 m long, 3/4 inch diameter and 1.8 MPa of ^{3}He gas pressure are mounted at the scattering angles from 3° to 62° and from −13° to −31°. Some PSDs showed inhomogeneous positional dependence of neutron intensities due to distorted central wires, some PSDs did not work due to broken wires, and therefore, 26 pieces of these defective PSDs were located randomly in the scattering angles. Several PSDs could be repaired because of funding and several new PSDs were provided by the manufacturer, so the number of defective PSDs was reduced to 10. The PSDs were reconfigured so that good PSDs can be located continuously by moving the defective PSDs to the side of the detector bank from −13° to −31°.

For the Fermi chopper control system, the control algorithm was improved to realize a good phase control performance and the power of the uninterruptible power supply was increased to ensure safe slowdown of the rotation of the chopper in case of power failure.

We experienced some breakdowns. Since the cryopump for the vacuum scattering chamber, the turbo molecular pump for the Femi chopper, and the 1 K refrigerator failed, they were repaired. The flexible tubes for helium gas circulation in the GM refrigerator for the sample cooling were twisted and broken, causing leak of helium gas. This problem was also fixed.

The cooling water of the T0 chopper installed on BL04, that is the same type as those installed on BL09, BL12, BL21 and BL23, leaked at the coupler. The couplers were tightened too much and electrical erosion occurred by the difference of the ionization tendencies of the brass coupler of the water hose and the stainless-steel coupler of the body of the T0 chopper. Then the coupler was damaged. All brass couplers were changed to ones made of stainless steel and the torques of tightening were properly controlled for the T0 choppers installed on BL09, BL12, BL21 and BL23.

3. Scientific results

The following scientific results were obtained from the S-type project on HRC. Pressure-induced quantum phase transition was detected, and magnetic excitations were observed under the pressure in a quantum antiferromagnet $CsFeCl_3$ [3, 4]. The Stoner excitations were observed in metallic antiferromagnets γ-Fe_xMn_{1-x} [5, 6]. Crystalline electric fields (CEF) as well as low energy coherent excitations were observed in breathing pyrochlore antiferromagnet $Ba_3Yb_2Zn_5O_{11}$ [7]. The CEF level scheme of the non-centrosymmetric $CePtSi_3$ was determined [8]. The magnetic and thermodynamic properties of the charge and spin ordering in the highly hole-doped layered cobalt oxide $La_{2-x}Sr_xCoO_4$ were investigated [9].

References

[1] S. Itoh et al., J. Phys. Soc. Jpn. 82 (2013) 043001.
[2] S. Itoh et al., MLF Annual Report 2016, p.101.
[3] S. Hayashida, Doctoral Thesis, The University of Tokyo (2018).
[4] S. Hayashida et al., Phys. Rev. B 97 (2018) 140405(R).
[5] S. Ibuka et al., Phys. Rev. B 95 (2017) 224406.
[6] S. Itoh et al., Physica B, in press.
[7] T. Haku et al., J. Phys.: Conf. Series 828 (2017) 012018.
[8] D. Ueta et al., Physica B 536 (2018) 21.
[9] M. Yoshida et al., Physica B 536 (2018) 338.

S. Itoh[1,2], T. Yokoo[1,2], T. Masuda[3], H. Yoshizawa[3], T. Hawai[1,2], M. Yoshida[3], S. Asai[3], D. Kawana[3], R. Sugiura[3], T. Asami[3], and Y. Ihata[4]
[1]Institute of Materials Structure Science, KEK; [2]Neutron Science Section, J-PARC Center; [3]The Institute for Solid State Physics, The University of Tokyo; [4]Technology Development Section, J-PARC Center

BL14 AMATERAS

1. Introduction

FY2017 was the ninth year of operation of AMATERAS [1, 2], a cold-neutron disk-chopper spectrometer. We continued the user program out-reach activities. As it happened the previous year, this fiscal year we encountered again some mechanical problems with the equipment of AMATERAS. There were changes in the staff of AMATERAS. From this fiscal year, we accepted a post-doctoral fellow from a company, Sumitomo Rubber Industries, Ltd., Dr. Tatsuya Kikuchi, by using the "Industrial Post-Doctoral Fellow" program, which was launched by MLF to promote further industrial users' activity.

2. User program, international activities & out-comes

The number of general proposals submitted for the 2017A and 2017B periods was 23 (accepted: 10, reserved: 13) and 28 (accepted: 8, reserved: 20), respectively. Among the proposals, the studies on magnetism dominated and the number of proposals, related to energy materials increased. As a result, in FY2017, 24 general proposals (including two urgent proposals) and three JAEA project proposals were carried out on AMATERAS.

In the second Neutron and Muon School held in November, five foreign students took part in a hands-on experiment at AMATERAS (Fig. 1). The students carried out inelastic neutron scattering measurement for single crystal of one-dimensional antiferromagnetic compound. They learned how to measure and analyze the collective spin dynamics using the time-of-flight chopper spectrometer. The students reported their results at the presentation session held on the last day of the school and won the second prize of the presentation awards.

In 2017, 10 refereed papers covering the woks at AMATERAS were published. Furthermore, two master theses, based on experiments at AMATERAS, were completed. The research topics included frustrated magnets, 4f electron systems, perovskite solar cells, and polymer membranes.

3. Instrumental activities

AMATERAS has three sets of fast-disk choppers, whose maximum frequency is 300 Hz in conventional use. In 2016, we limited the maximum frequency of one of them, called CH03, to 275 Hz because of anomalous vibration. In JFY2017, its maximum frequency was restored to 300 Hz after replacing a disk.

We also encountered several problems with the cryopump, which is involved in the pumping system of the vacuum scattering chamber. Although they were fixed within JFY2016, we faced yet another problem with it: a heater warming up the cold heads was broken. In conventional operation, we warm up the system to room temperature (RT) using the heater to vent the scattering chamber before introducing air into the chamber. However, due to this problem, we were forced to warm them up by letting helium gas into this huge scattering chamber instead of using the heater and to introduce air before the system is warmed up to RT to save time. The repair of the heater and refurbishment of some parts were completed during the summer shutdown , and the system recovered before restarting the beam operation. As these problems were detected in two consecutive years, we plan to replace it with a new cryopump in near future.

Figure 1. Students participated in the second Neutron and Muon School and staff members of AMATERAS.

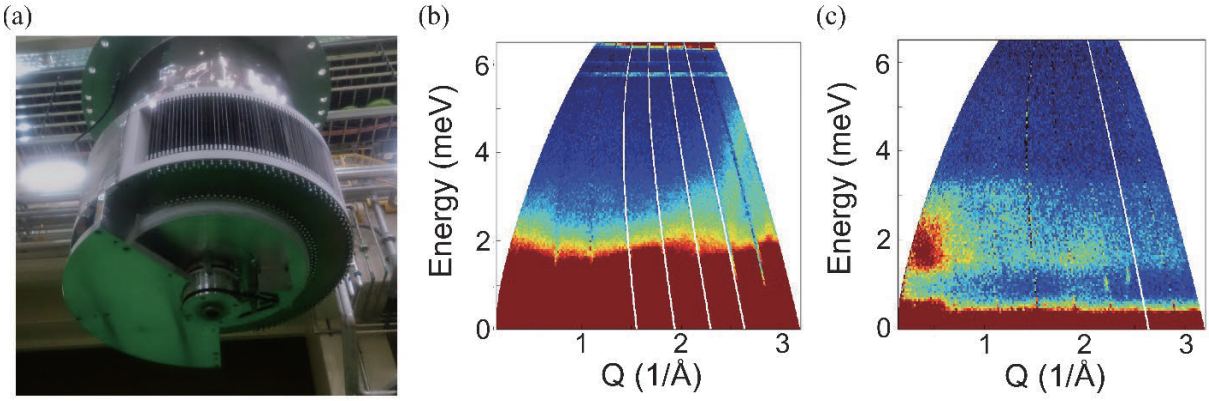

Figure 2. (a) The oscillating radial collimator of the superconducting magnet. Inelastic neutron scattering spectrum taken at experiments using the superconducting magnet (b) without and (c) with the collimator. Inelastic signal observed around 2 meV in (c) is a real magnetic signal which can hardly be detected in (b).

Since 2008, the number of detectors installed to AMATERAS was only 60% (266) of the final specified capacity (448). In JFY2017, 10 additional detectors were installed: four detectors were installed to the low-angle side, while six to the high-angle side.

Recently, the number of users' proposals that require non-standard sample environment (SE), such as a dilution refrigerator and superconducting magnet, had gradually increased. As an oscillating radial collimator (ORC) of the superconducting magnet (Fig. 2 a) managed by the SE team has just been ready for inelastic neutron scattering (INS) measurements, we carried out commissioning on this magnet with the ORC. This ORC was quite effective for the INS experiment. The background, mainly due to the thick Al walls of the magnet, registered in the previous commissioning without the ORC, was drastically reduced, and a magnetic excitation spectrum was clearly observed (see Fig. 2 b and c). After this commissioning, a general users' experiment under magnetic field was performed in the 2017B period.

References

[1] K. Nakajima, S. Ohira-Kawamura, T. Kikuchi, M. Nakamura, R. Kajimoto, Y. Inamura, N. Takahashi, K. Aizawa, K. Suzuya, K. Shibata, T. Nakatani, K. Soyama, R. Maruyama, H. Tanaka, W. Kambara, T. Iwahashi, Y. Itoh, T. Osakabe, S. Wakimoto, K. Kakurai, F. Maekawa, M. Harada, K. Oikawa, R. E. Lechner, F. Mezei, and M. Arai, J. Phys. Soc. Jpn. **80**, SB028 (2011).

[2] K. Nakajima, RADIOISOTOPES **66**, 101 (2017).

K. Nakajima[1], S. Ohira-Kawamura[1], M. Kofu[1], T. Kikuchi[1,2], Y. Inamura[1], and D. Wakai[3]

[1]Neutron Science Section, Materials and Life Science Division, J-PARC center; [2]Chemical Analysis Center, Research & Development HQ, Sumitomo Rubber Industries, Ltd.; [3]Nippon Advanced Technology Co., Ltd.

Upgrading TAIKAN

1. Introduction

The small and wide angle neutron scattering instrument TAIKAN (BL15) has been developed and upgraded at J-PARC to analyze precisely and efficiently the microstructures or hierarchical structures of substances in various scientific fields with a 1 MW spallation neutron source [1]. In FY2017, it was upgraded further to perform high-*q* measurement, also, the mid-term evaluation of TAIKAN was carried out.

2. Upgrading for high-*q* measurement

The detector system of TAIKAN is composed of 5 detector banks: small-, middle-, high-, ultra-small-angle, and backward detector banks. On the high-angle detector bank, 96 ^{3}He PSD tubes were additionally installed. The measurement efficiency of the high-angle detector bank increased about twofold. The number of ^{3}He tubes then increased to 768, 592, 200, and 48 for the small-, middle-, high-angle, and backward detector banks, respectively. The installation ratios of the ^{3}He tubes became 84, 82, 36, and 60% for the small-, middle-, high-angle, and backward detector banks, respectively. Figure 1 shows a photo of the high-angle detector bank after installing the ^{3}He tubes.

Figure 1. High-angle detector bank.

3. Mid-term evaluation

The mid-term evaluation of TAIKAN was carried out on December 18, 2017. In the evaluation committee, we introduced the history of conceptual study of TAIKAN with a community of neutron science, the past performance of the instrument group members, and the technical progress of neutron optics and detector applicable to TAIKAN. After the introduction, we explained the aim of the development of TAIKAN, the configuration and components of TAIKAN, and the performance of TAIKAN (such as performance of T0 and disk choppers, neutron flux at the sample position, background, *q* range, beam focusing for extension of the *q* range, *q* resolution, measuring time, etc.), number and field of application, results obtained with TAIKAN, and future prospects.

The committee evaluated TAIKAN as follows:

a. TAIKAN has been developed as a high level of small and wide angle neutron scattering instrument, which can perform precise and efficient measurement in a wide *q* range.
b. Many research outcomes are expected in the next five years, focusing on the following two points:
   b-1. Promoting academic researches using wide-*q* measuring capabilities
   b-2. Research achievements in usual small-angle scattering studies
c. The instrument group members are expected to lead research projects and joint researches with power users and produce academic results, which can only be obtained with TAIKAN.

4. Future prospects

The improvement of the measurement efficiency by the installation of high-angle detectors makes precise measurement in a high-*q* range easier. We, the instrument group members, will do our best to meet the expectations of the evaluation committee and conduct researches with the cooperation of users.

Reference

[1] S. Takata, J. Suzuki, T. Shinohara, T. Oku, T. Tominaga, K. Ohishi, H. Iwase, T. Nakatani, Y. Inamura, T. Ito, K. Suzuya, K. Aizawa, M. Arai, T. Otomo and M. Sugiyama, JPS Conf. Proc. 8, 036020 (2015).

J. Suzuki[1], S. Takata[2], K. Ohishi[1], H. Iwase[1], T. Morikawa[1], Y. Kawamura[1], and M. Sahara[1]
[1]Neutron Science and Technology Center, CROSS; [2]Neutron Science Section, Materials and Life Science Division, J-PARC Center

0.1 mm Focusing Elliptic Mirror with Large Area for Neutron Reflectometry at BL16

1. Introduction

Neutron reflectometry (NR) is very useful for investigations of structures of surfaces and buried interfaces composed of soft materials. SOFIA is a horizontal-type neutron reflectometer constructed at Beamline 16 (BL16) of the Materials and Life Science Experimental Facility (MLF) of the Japan Proton Accelerator Research Complex (J-PARC) [1, 2]. Due to the high-flux beam of J-PARC, less than one hour is needed for taking a full *Q*-range data and only a few seconds for a limited *Q*-range data in the case of a sample with 3 inches (76 mm) in diameter; even though the beam power is still one-third of the planned value, 1 MW. However, several hours are still needed for a small sample such as 10 mm × 10 mm, which is a typical size of a sample for X-ray reflectometry.

For further upgrade of the SOFIA reflectometer, we have been developing an elliptical focusing mirror to illuminate a sample with a neutron beam with a large beam divergence. In the case of conventional double slit collimation, the optimal beam divergence decreases according to the sample size. Hence, the focusing optics with the mirror has an advantage on the beam flux especially for small samples. The planned specifications of the focusing mirror and detector are a beam size of 0.1 mm at a sample position with divergence of 2.5 mrad.

So far, we developed a prototype focusing super-mirror capable of focusing neutrons with a width of 0.34 mm [3], and modified mirror with 0.17 mm in full width at half maximum (FWHM) [4]. These mirrors work well as focusing devices, however, the focusing size is insufficient for our needs. Here, we discuss a new mirror satisfying the specification of 0.1 mm focusing.

2. Manufacture

We employed an aluminum alloy as a base plate for the focusing mirror. First, the base plate was machined with a single diamond tool to produce a rough surface shape, in which the surface follows the central part of an ellipse with a long axis of 4300 mm and a short axis of 430 mm. Then, the plate was coated with nickel phosphorous by electroless plating process and finished by an ultrahigh precision cutting (UPC) process. The surface was polished before coating the super mirror to create a smooth surface of less than 1 nm in root mean square (RMS) roughness. The super mirror with an m-value of 3 was deposited on the substrate using an ion beam sputtering instrument at the Kyoto University Research Reactor Institute [5]. Since the mirror size, 550 mm in length and 60 mm in width, was too large to coat the super mirror, the mirror was divided into two pieces and assembled into one unit after the processes above were completed with the kinematic coupling developed earlier [4].

3. Results

First, we checked the surface roughness of the super-mirror, which is sensitive to the reflectivity of neutrons. Figure 1(a) shows the surface roughness map measured using white-light interferometer (NewView 7200, ZYGO). Remarkably, the RMS of the roughness was only 0.105 nm in this field of view and the average of 10 different points on the mirror was 0.108 nm ± 0.009 nm (standard deviation), that is, the roughness was better than the commercially available Si substrates over the whole mirror surface. Surprisingly, the neutron reflectivity at 20 different points with the area of 20 mm × 25 mm was almost the same over the large area and more than 80% below the critical angle as shown in Fig. 1 (b), which is comparable with a neutron guide mirror. The low roughness was not the only reason for this result; another contribution was the fabrication process of the super-mirror, which focused on the homogeneity of the reflectivity, as well as the considerable progress achieved compared with the former mirrors [4, 5], which were inhomogeneous and had less reflectivity.

Next, we evaluated the distribution of the slope error. As the slope error is the difference of the incident angle from the ideal value to reflect neutrons on a focal point, the distribution is closely linked to the minimum size of the focal image. Figure 2(a) shows the slope error map on one segment of the mirror. Due to the property of the UPC process, the waviness arose with the spatial frequency of a few millimeters. Even though the waviness was reduced in the polishing process, it could not be completely removed and was still dominant on the slope error. To estimate the minimum size of the focal image, the frequency distribution of the slope error was estimated as shown in Fig. 2(b). The distribution followed a Gaussian well and the FWHM was 24 μrad. As the distance between the mirror and the focal point, that is, the sample position, is designed to be 2150 mm, the minimum beam size is expected to be 50 μm to satisfy the specification value, 0.1 mm.

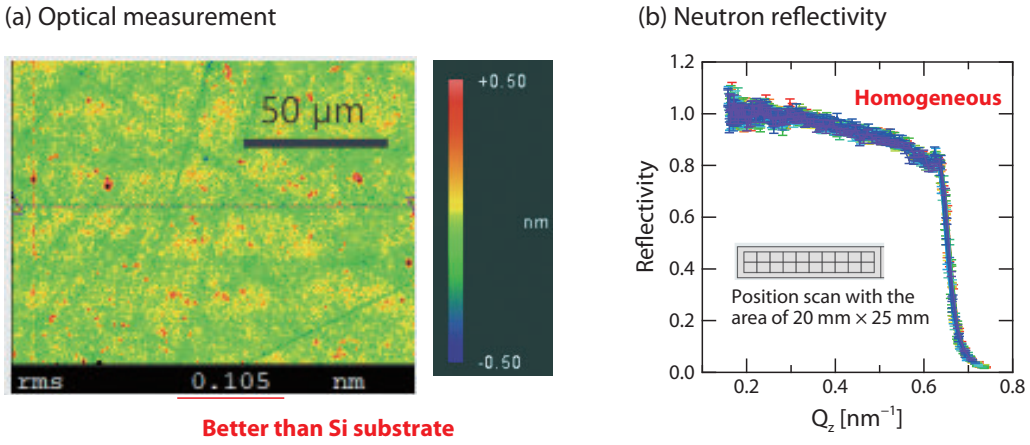

Figure 1. Evaluation of surface roughness and neutron reflectivity of a mirror segment: (a) the surface roughness map measured using white-light interferometer and (b) neutron reflectivity at 20 different points with an area of 20 mm × 25 mm.

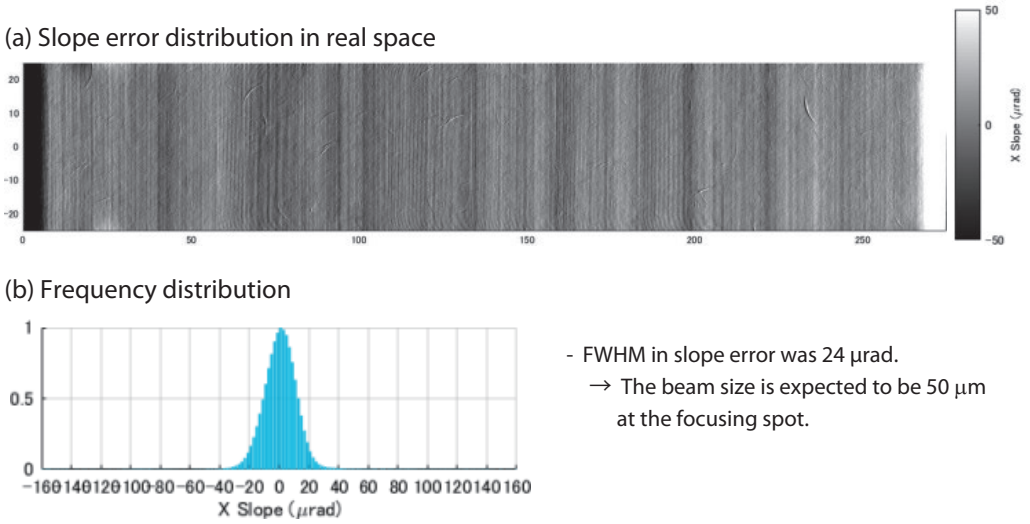

Figure 2. Evaluation of slope error of a mirror segment: (a) the slope error map and (b) frequency distribution of the slope error.

Finally, we conducted the focusing measurement with neutrons at BL16. Although the two segments of the focusing mirror were fixed with the kinematic coupling developed before, the positions of focal images of the segments were not coincident at the focal point because of the misalignment of the relative tilt. Hence, this time, one segment in the upstream side was removed for the measurement. Figure 3 presents the FWHM of the focal images evaluated with changing the slit aperture working as the virtual source. The beam size at the focal point decrease with the source size, and the minimum beam size in the experiment was 83 μm, which satisfied the requested specification.

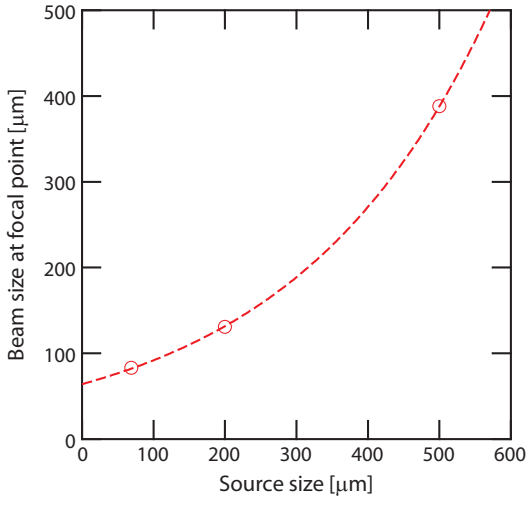

Figure 3. Beam size at the focal point evaluated with changing the slit size working as the virtual source.

4. Future Plans

Here, we reported on the improvement of the focusing mirror developed for the neutron reflectometer SOFIA. The roughness of the new base-plate for the mirror was approximately 0.1 nm in RMS over the whole surface, and a homogeneous super-mirror was fabricated on it. Owing to these developments, high and homogeneous neutron reflectivity was achieved over the whole surface of the mirror. Concerning the focusing capability, the figure errors of two segments composing the focusing mirror were low enough to realize the focusing image smaller than 0.1 mm according to the optical measurement. In fact, it was confirmed by the neutron beam that one segment of the mirror was capable of focusing with a width of 83 μm in FWHM. On the other hand, we still have a problem with aligning of the two segments into one mirror unit. We continue our work to overcome the problem with the alignment of the segments and install the focusing mirror to the SOFIA reflectometer in near future.

References

[1] N. L. Yamada *et. al.*, *Euro. Phys. J. Plus*, **44** (2011) 9424.
[2] K. Mitamura *et. al.*, *Polymer J.*, **45** (2013) 100.
[3] S. Takeda *et. al.*, *Opt. Express*, **24**, (2016) 12478-12488.
[4] T. Hosobata *et. al.*, *Opt. Express*, **25**, (2017) 20012-20024.
[5] M. Hino *et. al.*, *Nucl. Instr. and Meth. A*, **797** (2015) 265.

Norifumi L. Yamada[1,2], Takuya Hosobata[3], Masahiro Hino[4], Koichiro Hori[1,2], Fumiya Nemoto[1,2], Toshihide Kawai[3], and Yutaka Yamagata[3]

[1]Institute of Materials Structure Science, KEK; [2]Neutron Science Section, Materials and Life Science Division, J-PARC Center; [3]RIKEN Center for Advanced Photonics, Wako, Japan; [4]Kyoto University, Kumatori, Japan

BL17: Current Status of Polarized Neutron Reflectometer, SHARAKU

1. Introduction

SHARAKU, installed at BL17 in Materials and Life Science Experimental Facility (MLF), is a neutron reflectometer with vertical sample geometry used to investigate nanometric structures in thin film samples [1, 2]. Since SHARAKU has a pair of a spin polarizer and a flipper for both of incident and reflected/scattered neutrons, it can be employed to analyze the magnetic structure of magnetic thin films [3, 4]. In SHARAKU, the neutron intensity reflected at the sample film has been detected by a zero-dimensional (0D) ^{3}He tube detector. The low noise of the 0D detector allows a specular NR measurement down to a reflectivity of 10^{-7}; however, it cannot be used for an off-specular measurement. Therefore, the installation of a two-dimensional position sensitive neutron detector was needed. Over the last few years, the commissioning of a two-dimensional neutron detector, multi-wire proportional counter (MWPC), has been carried out and it is ready for use in the specular and off-specular observation.

In this fiscal year, we developed a data reduction environment for the NR measurement using the MWPC. The data correction considering the position sensitive information allows the efficient and reliable measurement of NR profiles. Moreover, a sample exchanging system was developed for an automated measurement of a number of samples.

2. Data reduction system for specular NR profile measured by MWPC

In the NR experiment using MWPC, the NR profile should be constructed considering the position data of the detected neutrons. This year, we developed a data reduction system to achieve fast data acquisition with high q resolution.

The neutron beam has a finite divergence of an incident angle in the reflectometry measurement. The increase in the beam divergence, $\Delta\theta$ (shown in Fig. 1a), increases the intensity of the reflection signal. However, the 0D detector detects the sum intensity at the reflection angle range from $\theta - \Delta\theta/2$ to $\theta + \Delta\theta/2$, resulting in decrease in the q resolution of the obtained NR profile. On the other hand, the position sensitive detection by MWPC can resolve the divergence of the reflected neutron beam. Figure 1b shows an intensity map of the reflected neutron from a 100-nm thin film of polystyrene

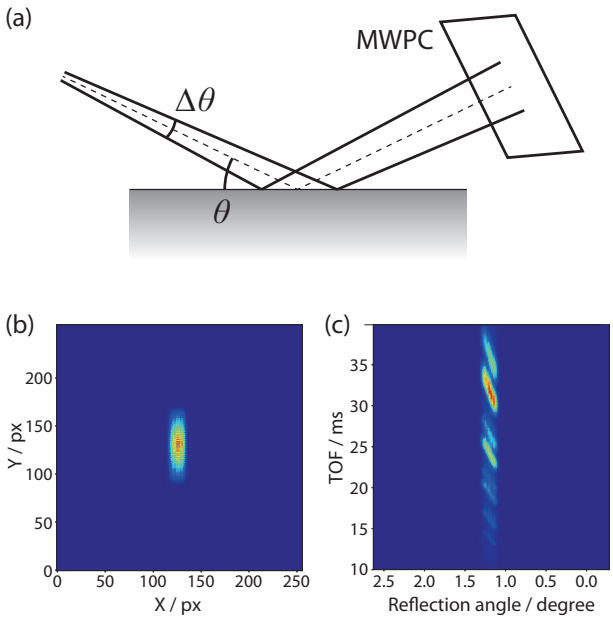

Figure 1. Illustration of reflection of a neutron beam at an incident incidence angle θ and a divergence $\Delta\theta$ (a), detected neutron intensity on the detector plane (b), and relation between the reflection angle and TOF (c).

on a silicon wafer at an incident angle of 1.2° with a divergence, $\Delta\theta/\theta$, of 0.20. In SHARAKU, a sample is mounted vertically, therefore, the neutron beam is spread in the X direction due to the large incident angle dispersion. Figure 1c shows the reflection intensity dependent on the reflection angle and the time-of-flight (TOF) of the reflected neutron. This indicates that the reflected TOF profile is dependent on the reflection angle.

Figure 2 shows the NR profiles at a q-range of 0.2 – 1.4 nm^{-1} obtained by the 0D detector and MWPC. The black and blue curves show the data taken by the 0D detector at beam divergence conditions of $\Delta\theta/\theta = 0.06$ and 0.20, respectively. This indicates that the increase of the incident angle divergence results in the decrease of the q resolution of the reflection profile. The structure in the sample film cannot be analyzed from the NR spectrum with $\Delta\theta/\theta = 0.20$. On the other hand, the NR profile constructed from the MWPC data considering the reflection angle divergence due to the incident beam (the red curve in Fig. 2) is in good agreement with that obtained by the 0D detector, indicating similar q resolution. The reflection intensity detected by MWPC was 2-times higher than that by the 0D detector. This indicates that the MWPC reduces the measurement time without the q resolution of the reflection profile

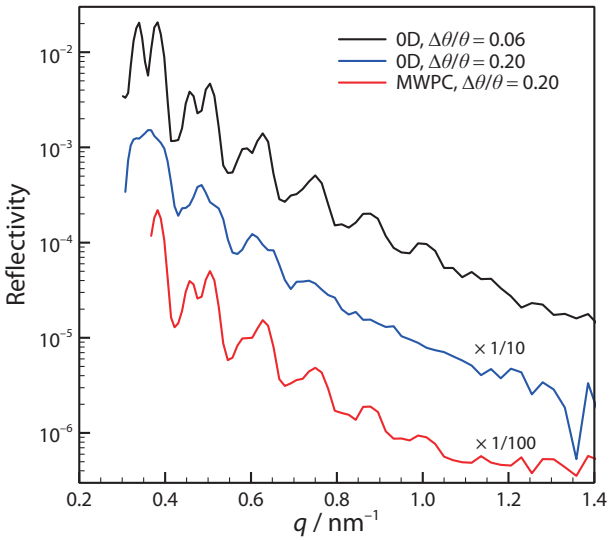

Figure 2. NR profiles for a polystyrene thin film deposited on a silicon wafer observed by the 0D detector and MWPC.

by using a strong incident neutron beam with a large divergence. Moreover, the background signal can be evaluated from the neutron signal detected at the outside of the reflected beam. By the background subtraction, reflectivity of less than 10^{-7} can be observed.

3. Sample Changer

The increase of the neutron beam power of MLF reduces the measurement time. For example, a specular NR profile for a polymer thin film deposited on a 2-inch silicon wafer can be obtained in 30 – 60 min at an operating power of 500 kW. In BL17, a typical time to change a sample and to adjust the beam alignment is about 30 min, which is comparable to the measurement time. Therefore, in order to reduce the total experiment time, the time for the sample exchange must be shortened. This year, the sample-exchanging and auto-alignment systems were installed. Figure 3a shows a photograph of the sample changer, which is a one-dimensional translation stage with a stroke of 200 mm. With this system, the sample exchange and the beam alignment process can be completed in about 10 min. A standard sample holder for a 2-inch silicon wafer has a thickness of 10 mm and can be stacked as shown in Fig. 3b. A sequential measurement of up to 16 samples can be carried out automatically.

Figure 3. Photographs of a 200-mm translation stage for a sample exchange (a) and stackable sample holders for a 2-inch silicon wafer (b).

4. Summary

We developed a data reduction system for the NR measurement using MWPC and automatic sample changing system, which enables fast data acquisition with high q resolution and reduction of the time required for sample exchange, respectively. Their combined use would improve the measurement efficiency.

References

[1] K. Akutsu, T. Niizeki, S. Nagayama, N. Miyata, M. Sahara, A. Shimomura, M. Yoshii, and Y. Hasegawa, *J. Ceram. Soc. Jpn.*, **124**, 172 (2016).
[2] Y. Sakaguchi, H. Asaoka, and M. Mitkova, *J. Appl. Phys.*, **122**, 235105 (2017).
[3] K. Amemiya, M. Sakamaki, M. Mizusawa, and M. Takeda, *Phys. Rev. B*, **89**, 54404 (2014).
[4] V. Ukleev, S. Suturin, T. Nakajima, T. Arima, T. Saerbeck, T. Hanashima, A. Sitnikova, D. Kirilenko, N. Yakovlev, and N. Sokolov, *Sci. Rep.*, **8**, 8741 (2018).

H. Aoki[1,2], K. Soyama[1], D. Yamazaki[1], N. Miyata[3], K. Akutsu[3], T. Hanashima[3], S. Kasai[3], and J. Suzuki[3]
[1]*Materials and Life Science Division, J-PARC Center;* [2]*Institute of Materials Structure Science, KEK;* [3]*Neutron Science and Technology Center, CROSS*

Status of SENJU 2017

1. Introduction

SENJU is a TOF single-crystal neutron diffractometer designed for precise crystal and magnetic structure analyses under multiple extreme environments, such as low-temperature, high-pressure and high-magnetic field, as well as for taking diffraction intensities of small single crystals with a volume of less than 1.0 mm^3 down to 0.1 mm^3 [1]. Ever since SENJU was launched in 2012, continuous commissioning and upgrading operations have been carried out.

In 2017, we upgraded two important components of SENJU. One was the software for data processing, STARGazer for SENJU, and the other was the DAQ-computer system of SENJU. In addition to the upgrade, we also report on the purposes for which the instrument beam-time for SENJU was used.

2. Upgrade of the data processing software STARGazer for SENJU

Software for data processing, i.e., making a reflection file (called "HKLF file") from raw data and data visualization, is one of the essential components for a single-crystal diffractometer. For SENJU, a program called "STARGazer for SENJU" is used for data processing and visualization.

In FY2017, we upgraded some functions of STARGazer for SENJU. The major areas of the upgrade were as follows:

1. Showing major candidates of true UB-matrix in the UB-matrix finding process.
2. Goniometer-angle correction in the UB-matrix refinement process.

The first one was developed to find the true cell-parameters and UB-matrix more easily. Before the upgrade, STARGazer for SENJU showed only the most likely candidate of the true UB-matrix in the "Find-Cell" component. While upgrading, we modified the Find-Cell component to show several candidates of the true UB-matrix.

The second one was developed to define only one UB-matrix for all data-set of one sample. Although each axis of the goniometers for SENJU outputs their current rotational angles, those angles were usually different from the true angles (±10°). Consequently, we had to define an UB-matrix when we changed the rotational angle of goniometers. It means that we could not define a common UB-matrix for one data-set. During the upgrade, we added to STARGazer for SENJU a new component to search the true goniometer angles of each diffraction data and define a common UB-matrix. For example, when we measure diffraction data with three settings of goniometer angles, an UB-matrix of one of the three settings is defined as a standard UB-matrix. For the other two settings, the goniometer angles are adjusted to make their UB-matrixes match the standard UB-matrix. Finally, the standard UB-matrix becomes the common UB-matrix for the three settings.

3. Virtualization of the DAQ-computer system

The DAQ-computer system of SENJU, installed in 2010, just before the Earthquake of March 2011, was already "obsolete". In 2017, we replaced the DAQ-computers of SENJU and built up a new "virtualized" DAQ-computer system to improve the system's redundancy. The DAQ-computer system of SENJU is composed of four DAQ control servers. In the replacement, each server is constructed in a virtual-PC software and all four virtual-PC systems operate on two physical servers (Fig. 1). After the virtualization, the neutron events detected at the detectors are successfully stored in

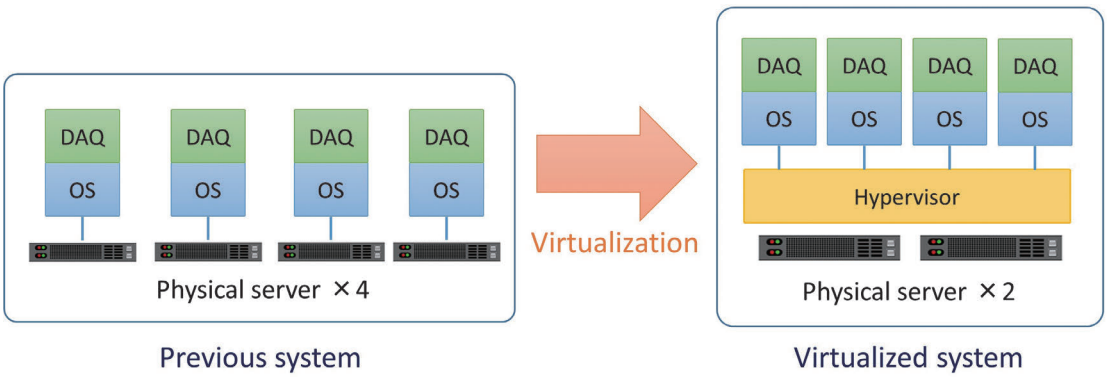

Figure 1. Schematic image of the virtualization of the DAQ-computer system at SENJU.

the storage system of SENJU and the data-processing speed of the new system is almost the same as the one before the replacement and sufficient for data processing in the 1 MW operation.

The major advantage of the virtualization is the improvement of redundancy. In case of any computer problem, we only need to copy the virtual-PC software, in which a DAQ control server is installed, to another computer.

4. Use of the instrument beam-time

In 2017, the instrument beam-time was mainly used for measurements of standard samples, a vanadium-nickel alloy and a C12A7 single crystal, for instrument calibration. The latter was for the oscillational radial collimator developed in 2016. 40 diffraction data of a C12A7 were measured with 0.5° interval with the collimator to clarify the intensity change of the same Bragg peak by the collimator. The analysis of the obtained data is now in progress. In addition, we used the instrument beam-time to compensate beam-time of some general-use proposals lost due to usage problems of sample environment devices.

Reference

[1] T. Ohhara et al., J. Appl. Cryst., 49 120 (2016).

T. Ohhara[1], R. Kiyanagi[1], A. Nakao[2], K. Munakata[2], T. Moyoshi[2], K. Moriyama[2], I. Tamura[1], and K. Kaneko[1]
[1]Neutron Science Section, Materials and Life Science Division, J-PARC Center; [2]Neutron Science and Technology Center, CROSS

Status of TAKUMI, BL19

1. Introduction

TAKUMI, BL19 is an engineering diffractometer, a type of powder diffractometer installed as a pair of 90° scattering detector bank, dedicated for engineering materials.

There are three stress-loading instruments in TAKUMI, BL19. The first one is a versatile type with temperature range from nitrogen level to 1300 K, the second one is a compact type with temperature range from room level to 1000 K, and the third one is a dedicated instrument for low temperature up to 6 K. These instruments are used to study the deformation mechanism and mechanical properties of various kinds of metal and composite materials under normal deformation speed and temperature control. On the other hand, there is demand to study the optimized manufacturing process of metals, such as steel, under the conditions of high-speed deformation and temperature control. Therefore, over the last few years, we have worked on the conceptual design of a new stress-loading instrument with high-speed deformation and temperature control. Finally, we decided to adopt a high-frequency heating system for temperature control.

In FY 2017, we introduced at BL19 high-frequency heating type stress-loading equipment with cooling gas blowing function, which can perform high-speed deformation, high-speed heating/cooling for high temperature stress-loading instrument of steel, etc.

2. Specification of the new stress-loading instrument

The new stress-loading instrument consists of a stress load device and high-frequency heating system. The main specifications of the instrument are shown below.

(1) Stress-load device

1) Sample size

Tensile test:

Parallel part diameter 6 × 20 mm,

Approximately 80 mm

Compression test:

Diameter 6 × length 10 mm

Total length 20 mm

Deformation test method:

Horizontal uniaxial swing mechanism type

Deformation maximum load:

Tension 50 kN, Compression 50 kN

Deformation speed:

0.01 mm/mim – 500 mm/min

Deformation mode:

Tension, Compression,

Tension/compression, Fatigue, Creep

Control method:

Load control, Displacement control,

External extensometer control

(2) High-frequency heating system

Heating rate:

20 K/s or more

Cooling rate:

30 K/s or more

Maximum temperature:

1570 K or higher

Thermal band (length):

20 mm or more

Isothermal holding time:

12 hours or more

Atmosphere:

Inert gas (Ar gas, nitrogen gas) atmosphere

3. Expected application

The new stress-loading instrument is fully fitted to TAKUMI, because the horizontal uniaxial loading method was adopted in its design, as a result, it can be used for standard simultaneous measurements in radial and axial directions of neutron diffraction, which is necessary for understanding the mechanical behavior.

Expected proposals using the new stress-load instrument include, for example, elucidation of the dynamic ferrite transformation mechanism of low-carbon steel at high temperature and evaluating thermal fatigue characteristics by thermal fatigue test (accelerated test) of materials used in thermal cycling environment. Also, it can be used to observe the solidification process and phase separation of alloy under high-speed cooling.

4. Future plans

Now, off-beam commissioning about the basic performance at the J-PARC research building is ongoing. We plan to perform commissioning of the new stress-loading instrument using neutron beams after passing the instrument safety check by the MLF safety team in FY 2018. And we would like to open it to general proposals as soon as possible.

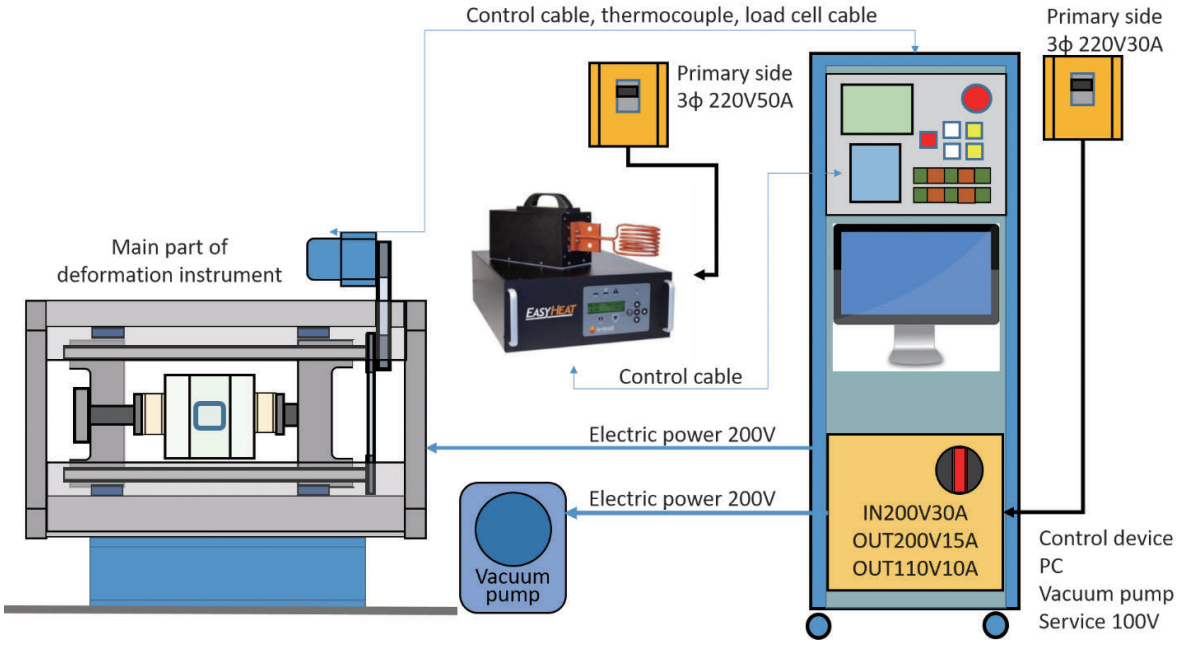

Figure 1. Schematic layout of the new stress-loading instrument.

K. Aizawa[1], S. Harjo[2], and T. Kawasaki[2]

[1]Technology Development Section, Materials and Life Science Division, J-PARC Center; [2]Neutron Science Section, Materials and Life Science Division, J-PARC Center

The Current Status of the Versatile Neutron Diffractometer, iMATERIA

1. Introduction

Ibaraki Prefecture, local government of Japan's area where the J-PARC sites are located, has decided to build a versatile neutron diffractometer (IBARAKI Materials Design Diffractometer, iMATERIA [1]) to promote industrial applications for the neutron beam in J-PARC. iMATERIA is planned to be a high-throughput diffractometer that could be used by materials engineers and scientists in their materials development work, including chemical analytical instruments.

The applications of neutron diffraction in materials science are (1) to do structural analyses of newly developed materials, (2) to clarify the correlation between structures and properties (functions), and (3) to clarify the relation between structural changes and improvements of functions, especially for practical materials. A diffractometer with super high resolution is not required to achieve those goals. The match of features like intermediate resolution around $\Delta d/d = 0.15\%$, high intensity and wide d coverage is more important.

This diffractometer is designed to look at a decoupled-poisoned liquid hydrogen moderator (36 mm, off-centered) (BL20), and it has an incident flight path (L1) of 26.5 m, with three wavelength selection disk-choppers and straight neutron guides with a total length of 14.0 m. The instrumental parameters are listed in Table 1. There are four detector banks, including a low-angle and small-angle scattering detector bank. The angular coverage of each detector bank is also shown in Table 1. The rotation speeds for the disk-choppers are the same, with a pulse repetition rate of 25 Hz for the most applications (SF mode). In this case, the diffractometer covers $0.18 < d$ (Å) < 2.5 with $\Delta d/d = 0.16\%$ and covers $2.5 < d$ (Å) < 800 at three detector banks of 90-degree, low-angle and small-angle with gradually changing resolution. When the speed of the wavelength selection disk-choppers is reduced to 12.5 Hz (DF mode), we can access a wider d-range, $0.18 < d$ (Å) < 5 with $\Delta d/d = 0.16\%$, and $5 < d$ (Å) < 800 with gradually changing resolution with doubled measurement time compared to the SF mode.

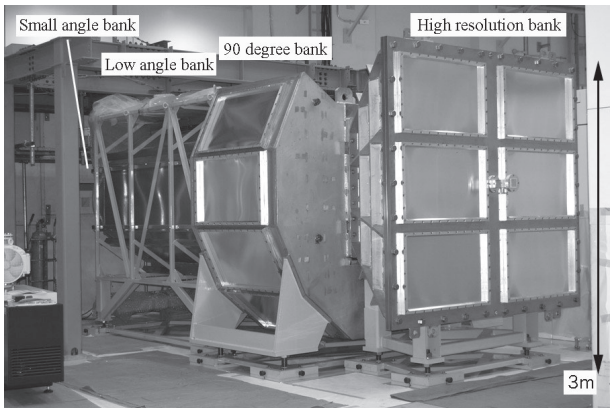

Figure 1. IBARAKI Materials Design Diffractometer, iMATERIA without detector for each bank and instrument shielding. The high-resolution bank, special environment bank (90-degree bank), and low-angle bank, can be seen from right to left. The small-angle detector bank, which is not shown in the picture, is situated in the low-angle vacuum chamber (left-hand side of the picture).

Table 1. Instrumental parameters of iMATERIA. L2 is the scattered flight path. The d-range (q-range) for each bank is the maximum value for 2-measurement mode.

L1		26.5 m
Guide length		14 m (3section)
Position of Disk choppers		7.5 m (double) 11.25 m (single) 18.75 m (single)
High Resolution Bank	2θ	$150^\circ \le 2\theta \le 175$
	L2	2.0 - 2.3 m
	d-range	$0.09 \le d$ (A$^\circ$) ≤ 5.0
Special Environment Bank	2θ	$80^\circ \le 2\theta \le 100^\circ$
	L2	1.5 m
	d-range	$0.127 \le d$ (A$^\circ$) ≤ 7.2
Low Angle Bank	2θ	$10^\circ \le 2\theta \le 40^\circ$
	L2	1.2 - 4.5 m
	d-range	$0.37 \le d$ (A$^\circ$) ≤ 58
Small Angle Bank	2θ	$0.7^\circ \le 2\theta \le 5^\circ$
	L2	4.5 m
	q-range	$0.007 \le q$ (A$^{\circ -1}$) ≤ 0.6

2. Current status

All of the four banks, high-resolution bank (BS bank), special environment bank (90-degree bank), low-angle bank and small-angle bank, are operational. It takes about 5 minutes (in DF mode) to obtain a 'Rietveld-quality' data in the high-resolution bank at 500 kW beam power for about 1 g of standard oxide samples.

Figure 2 shows a typical Rietveld refinement pattern for $LiCoO_2$ sample, cathode material for lithium ion battery (LIB), at the high-resolution (BS) bank by the

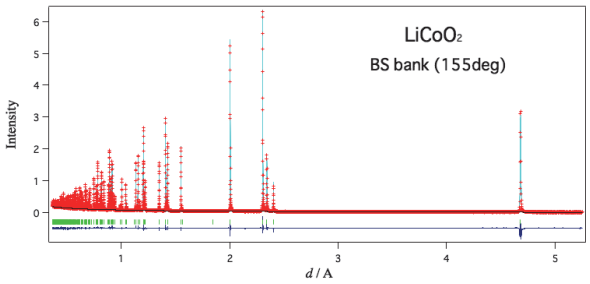

Figure 2. Rietveld refinement pattern for $LiCoO_2$ at the high-resolution bank of iMATERIA.

multi-bank analysis function of Z-Rietveld [2]. It takes 20 min in DF mode to collect the available Rietveld data, due to the high neutron absorption cross section for natural Li ($\sigma_s^{Nat} = 70$ barn).

3. Sample Environments

The automatic sample changer is the most important sample environment for high-throughput experiments. Our automatic sample changer [3] consists of a sample storage, elevating system of two lines, two sets of pre-vacuum chambers and a sample sorting system. We can handle more than 600 samples continuously at room temperature without breaking the vacuum of the sample chamber.

The V-furnace (~900°C), the gas flow furnace (~1000°C), the cryo-furnace (4K) and the 1K cryo are ready for experiments. The in-operando experiment system for LIB with a sample changer is available in cylindrical and coin types of batteries.

Recently, the rapid heating and cooling furnace with automatic sample changer also became available for texture measurement.

References

[1] T. Ishigaki et al., Nucl. Instr. Meth. Phys. Res. A 600 (2009) 189-191.
[2] R. Oishi et. al., Nucl. Instr. Meth. Phys. Res. A 600 (2009) 94-96.
[3] A. Hoshikawa et al., J. Phys.: Conf. Ser. 251 (2010) 012083.

T. Ishigaki, A. Hoshikawa, T. Matsukawa, and Y. Onuki
Frontier Research Center for Applied Nuclear Sciences, Ibaraki University

Status of the High Intensity Total Diffractometer (BL21, NOVA)

1. Introduction

Total scattering is a technique created to analyze non-crystalline structure in materials with atomic Pair Distribution Function (PDF). NOVA was designed to perform total scattering and is the most intense powder diffractometer with reasonable resolution ($\Delta d/d$ ~ 0.5%) in J-PARC. It is easy to adapt NOVA to a very wide range of fields: liquids, glass, local disordered crystalline, magnetic structure of long lattice constant and so on. The observation of the hydrogen position in materials is one of the most important scientific themes of NOVA.

Sample temperature and gas pressure are controlled by various environments at NOVA (Table 1), but a radiation shield or a vacuum chamber degrades the signal-to-noise ratio and diminishes the statistical accuracy. Hence, a radial collimator was introduced to NOVA, as an effective device to reduce the background signal.

Table 1. Sample environmental equipment of NOVA.

Apparatus	Specification
Sample Changer	sample: 10 or 40 (RT)
Temperature controlled Sample Changer	sample: 18 temp.: 20 ~ 750 K
Top Load Cryostat	temp.: 5 ~ 700 K
PCT (hydrogen gas atm.)	press.: max. 10 MPa H_2/D_2 temp.: 50 ~ 473 K
Vanadium Furnace	temp.: max. 1273 K
2 K cryostat (MLF SE)	temp.: 1.8 ~ 300 K

2. Design of the radial collimator

NOVA covers a wide-Q range with detector banks from small-angle to high-angle and short wavelength neutron (λ ~ 0.12 Å) for total scattering. However, there is no shielding material for a radial collimator to keep the performance and decrease the background. Additionally, it is difficult to install collimator blades along the Debye-Scherrer rings in the small-angle or high-angle direction. Therefore, as the first step of the radial collimator development, 50-μm-thick Cd coated 100-μm-thick Al plates were placed only around the 90° bank at intervals of 2° (Fig. 1).

Figure 1. Radial collimator installed at NOVA.

3. Performance of evaluation

The shielding effect of the radial collimator was examined for the vanadium furnace environment at NOVA. Figure 2 shows incident proton numbers normalized neutron counts scattered from vanadium foils in the furnace without sample. The detected neutrons are reduced by about an order due to the radial collimator. The shielding effect is not enough below 0.4 Å because Cd indicates cut-off energy of 500 meV. The neutron transmittance at 1 Å was evaluated for 4.7%, which corresponds to shielding by 3 or 4 blades. It is insufficient in case of scattering path of fewer blades.

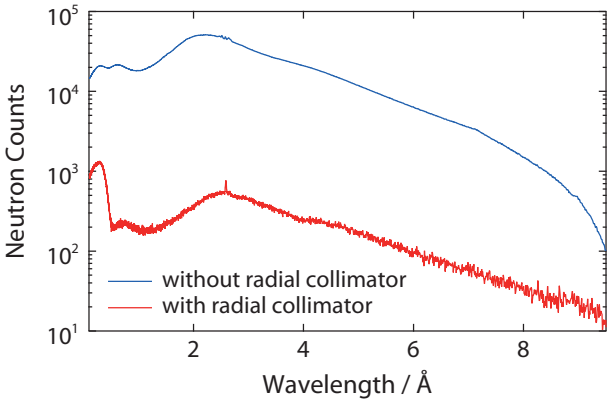

Figure 2. Scattering intensity from vanadium furnace.

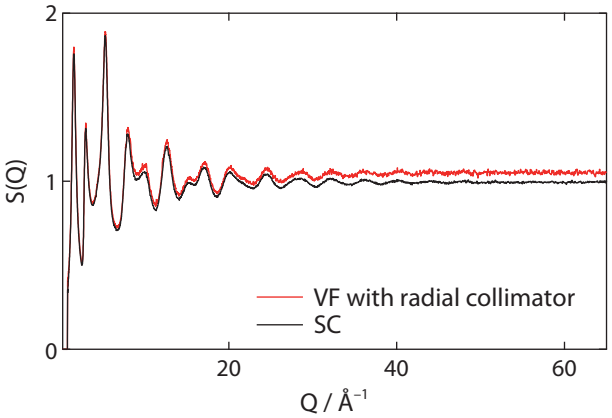

Figure 3. S(Q) of SiO_2 glass rod measured under vanadium furnace (VF) with the radial collimator and sample changer (SC) environments.

Structure factor, *S*(*Q*), of SiO_2 glass rod was measured under the vanadium furnace with the radial collimator and sample changer environments, as shown in Fig. 3. Both *S*(*Q*) are valid and similar PDFs are derived, even though there is a slight difference. However, the shielding effect of the radial collimator for a 2 K cryostat is low compared to the vanadium furnace in the small-angle and high-angle direction, because the cryostat has a vacuum chamber with a larger diameter and the scattering neutron passes through deficient shielding blades. Though it is necessary to reinforce the shielding ability, the basic performance of the radial collimator was confirmed to be available for the experiments.

Acknowledgement

The authors would like to thank Mr. Kambara for his helpful assistance in manufacturing the radial collimator. The operation and developments of NOVA were performed under the S1-type program (2014S06) approved by the Neutron Scattering Program Advisory Committee of IMSS, KEK.

K. Ikeda[1,2], T. Otomo[1,2,3], T. Honda[1,2], H. Ohshita[1,2], M. Tsunoda[3], N. Kaneko[1,2], T. Seya[1,2], and K. Suzuya[2]

[1]Institute of Materials Structure Science, KEK; [2]Neutron Science Section, Materials and Life Science Division, J-PARC Center; [3]Graduate School of Science and Engineering, Ibaraki University

Present Status of the Energy-Resolved Neutron Imaging System RADEN

1. Introduction

The energy-resolved neutron imaging system "RADEN", installed at beam line BL22 in the Materials and Life Science Experimental Facility (MLF) of J-PARC, is a dedicated instrument for wavelength/energy-dependent neutron imaging experiments with full utilization of the short-pulsed neutron's nature, such as broad available neutron energy range and narrow pulse shape [1]. RADEN provides capabilities to conduct the following energy-resolved neutron imaging (ER-NI) techniques: Bragg-edge, neutron resonance absorption, and polarized pulsed neutron imaging. In addition, neutron phase imaging based on a Talbot-Lau interferometer has recently been adapted to the wavelength dependence analysis for effective and precise determination of phase change [2]. In this report, we will cover the current status of RADEN's activities, including technical developments and application studies.

2. Improvement of neutron imaging detector systems

Owing to continuing studies on improving the performance of imaging detectors, the counting-type detector system with fine time resolution, which is important for energy-resolved neutron imaging experiments, and good spatial resolution up to 100 μm, similar to the conventional camera-type detector system, became available without sacrificing the neutron beam intensity due to their limited count rate. Figure 1 shows neutron transmission images of a Gd test target [3] obtained by three different detector systems [4]. At RADEN, the nGEM detector was initially used due to its stable performance, but now the μNID detector is near completion, ready to provide five times higher counting rate performance and 1/10 the spatial resolution of the nGEM detector. Moreover, to achieve a much higher counting rate capacity, a new detector system with the same micro-pattern readout plane as the μNID is being developed. Its neutron conversion medium (i.e., the material that converts incident neutrons into charged particles that can be detected) has been changed from ^{3}He gas to a solid, thin ^{10}B layer (B-μNID). Because the alpha particle produced by the neutron-^{10}B reaction travels a shorter distance than the particles released in the neutron-^{3}He reaction, the number of hit channels per one neutron event is reduced. Consequently, a very high neutron count rate capacity of over 20 Mcps could be obtained. Since currently the ^{10}B conversion layer is very thin, its efficiency is not high, but it can be improved by increasing the thickness of the ^{10}B layer relative to the incoming neutron beam direction.

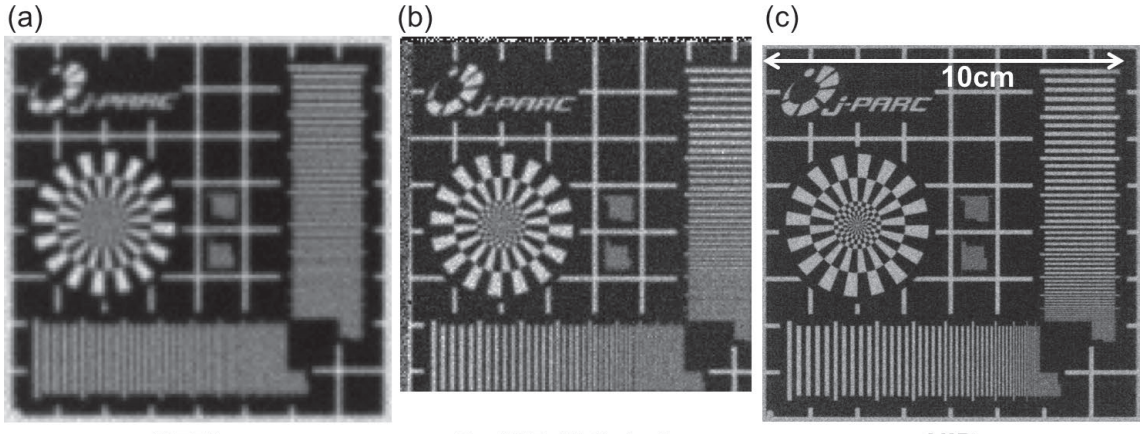

Figure 1. Neutron transmission images of a Gd test target taken by three counting-type neutron imaging detectors: (a) nGEM detector, (b) μNID detector using ^{10}B converter, and (c) normal μNID detector.

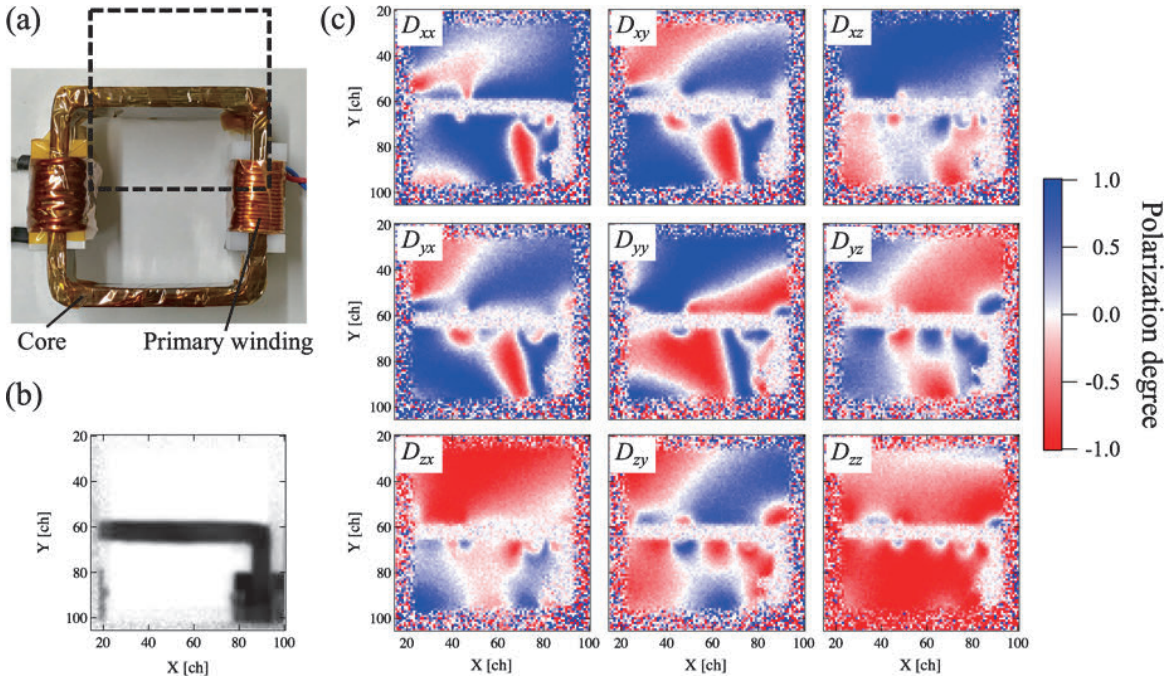

Figure 2. (a) Photograph of the model electric transformer. The dashed square indicates the FoV. (b) Neutron radiograph of the transformer. (c) Polarization image for each element of the spin rotation matrix **D** [9] obtained at a wavelength of 2.51 Å. The wavelength resolution (Δλ) is 0.043 Å [8].

3. Application studies of energy-resolved neutron imaging

After RADEN started its user program in FY 2015, 63 proposals have been approved through FY 2017. More than half of the beam time for the user programs was used for experiments using wavelength/energy analysis. Especially, new application studies of ER-NI, e.g., in-situ observation of liquid/solid interface and segregation of elements during the single-crystal growth process [5] and applications of tomography techniques to visualize the three-dimensional distribution of strain in a steel sample in combination with Bragg-edge imaging [6] or of both magnetic field strength and direction in a solenoid coil with TOF polarimetric imaging [7], have been successfully carried out. Another remarkable achievement is the application of ER-NI to industrial objects. The leaked field from an electric transformer has been observed by using the polarized neutron imaging technique [8]. Figure 2 shows polarization imaging results of a small transformer with a direct current applied (c), together with a photograph of the small transformer sample (a) and a neutron radiograph (b). Apparently, a change in polarization could be found in the polarization images around the top part of the transformer core, where a gap in the wrapped electric steel sheet is located, and in the primary winding. This change indicates leakage of magnetic fields from the wrapping part and the primary coil. Moreover, spatial distributions of both strength and direction of the leakage field could be evaluated by analyzing the oscillatory behavior which appeared in the wavelength dependent polarization at each point in the image.

4. Summary and future plans

Now, RADEN is under user operation and is being continuously upgraded. The detector performance improves year after year, and we will continue the development in order to achieve finer spatial resolution and higher count rate. Another ongoing project at RADEN is the development of new imaging techniques utilizing wavelength/energy dependence, especially the combination of ER-NI and computed tomography. In the future, we will develop a general technique to visualize the three-dimensional distribution of strain, magnetic field, elemental composition, and temperature. The application of ER-NI techniques has started to spread widely in both scientific and industrial disciplines. In-situ or in-operando observation experiments are expected to be very important subjects for RADEN, because they can utilize the advantages of neutron imaging. We are going to improve the RADEN instrument and prepare an easy-to-use environment to promote these kinds of application studies.

Acknowledgements

This work was partially supported by the JST ERATO Momose Quantum Beam Phase Imaging Project and by the Photon and Quantum Basic Research Coordinated Development Program from the Ministry of Education, Culture, Sports, Science and Technology, Japan.

References

[1] T. Shinohara et al., J. Phys: Conf. Series 746 012007 (2016).
[2] Y. Seki et al., J. Phys. Soc. Jpn. 86 044001 (2017).
[3] M. Segawa et al., JPS conference proceedings (accepted).
[4] J. D. Parker et al., JPS conference proceedings (accepted).
[5] A. S. Tremsin et al., Crystal Growth & Design 17 6372 (2017).
[6] J. N. Hendriks et al., Phys. Rev. Materials 1 053802 (2017).
[7] M. Sales et al., Scientific Reports 8 2214 (2018).
[8] K. Hiroi et al., JPS conference proceedings (accepted).
[9] M. Th. Rekveldt: Z. Physik 259 391 (1973).

T. Shinohara[1], T. Kai[1], K. Oikawa[1], M. Segawa[1], T. Nakatani[1], K. Hiroi[1], Y. Su[1], H. Hayashida[2], J. D. Parker[2], Y. Matsumoto[2], Y. Seki[1], and Y. Kiyanagi[3]

[1]Neutron Science Section, Materials and Life Science Division, J-PARC Center; [2]Neutron Science and Technology Center, CROSS; [3]Graduate School of Engineering, Nagoya University

Commissioning Started on New Spectrometer POLANO

1. Introduction

POLANO is a brand-new spectrometer being constructed in MLF with polarization analysis capability [1-4]. The polarization analysis technique in the field of inelastic neutron scattering was formerly developed in the end of the 1960s and in the early 1970s at reactor-based neutron sources. At that time, a new generation of high-flux neutron reactor became available and it brought a resurgence of interest in polarization methods. The first new technique to appear was one-dimensional polarization analysis in 1969 [5]. After many years of the successful experiments in reactor-based polarization, the application of the polarization method to accelerator-based neutron sources (time-of-flight method) was commenced [6]. The reactor-based and accelerator-based neutron methods are in principle similar but there are many big differences in terms of techniques. POLANO was designed to realize the polarization analysis in inelastic neutron scattering up to higher energy (100 meV) beyond the reactor-based method.

The construction of POLANO was initiated in 2013. Before that, we had many discussions about the project, designs, technical issues and numerous other items. Also, the preliminary construction and R&D of the required devices began within a limited budget. In 2012, we successfully obtained a large amount of funding for the instruments, and the construction process was accelerated after 2013. The major part of the construction of the instrument was completed by 2016, and radiation assessment was conducted. In 2017, POLANO accepted the first neutron beam and started on-beam commissioning as well as device tests.

2. Present status of POLANO

As mentioned above, we just accepted the first neutron beam in June 2017. After the summer shutdown, we started running tests, electrical communication tests, operational tests, and so on.

Vacuum Chamber System

POLANO has a 20 m^3 class vacuum chamber and vacuum system as other chopper type instruments. Figure 1 shows the vacuum chamber (right) and the evacuation test results. Ten minutes after starting pumping by mechanical dry pumps, the vacuum of the tank reached the so-called crossover pressure where the cryo-pump can be safely started (main gate valve opens). Once the main valve opens, the vacuum immediately goes down to the order of 10^{-3} Pa, at which point we can start cooling the sample down. This vacuum chamber is used for the following two reasons. First, to avoid air scattering in the neutron flight paths and second, for vacuum insulation for sample environment devices such as cryostat, furnace, and magnet. For the above purposes, the vacuum obtained in these tests is sufficiently low. When the main valve is closed, the vacuum abruptly increases (at around 3000 min in the plot of Fig. 1). This is simply because of the gases coming out of many components inside the tank, such as B_4C shielding liner, the analyzer mirror and its rotational system. This type of out-gas can be reduced by repeating the evacuation process many times.

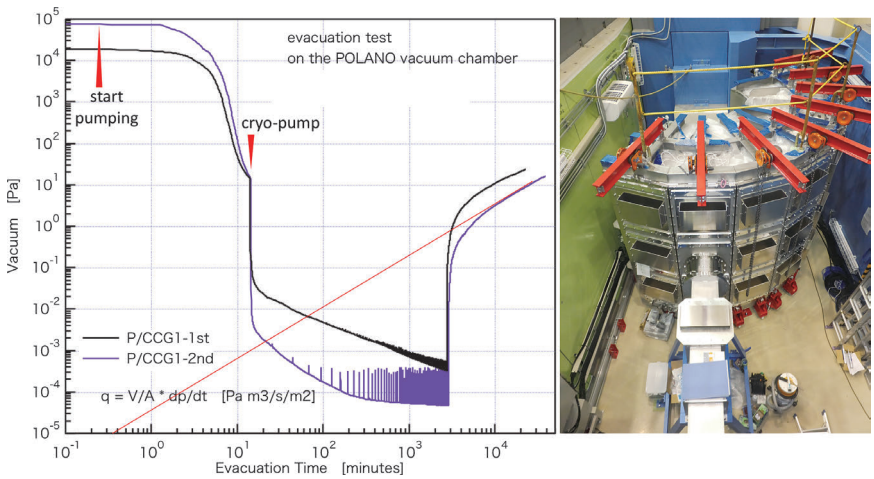

Figure 1. (left) Evacuation test of the POLANO vacuum chamber. Time evolution of the vacuum (pressure) in the chamber. The black line shows the result of the first trial, and the purple line is the second trial.
(right) POLANO vacuum chamber viewed from downstream.

Detector Alignment

We adopted so-called PSD (position sensitive detector) system. PSDs are placed at the very end of the vacuum chamber detecting the scattered neutron with reasonable spatial resolution. POLANO detectors are composed of three layers of 60 cm PSDs as shown in Fig. 2 on the right. The detector efficiencies of adopted PSD conditions (SUS tube, 0.35 mm, 3/4" diameter, ^{3}He 10 atm) can be calculated as shown in Fig. 2 left. Even with 100 meV of the neutron energy, nearly 80% efficiency is expected, which is a reasonable performance. The assembled PSDs were tuned with cadmium slit jigs. In Fig. 3 left, perfectly aligned three slit patterns are presented. Since ^{3}He gas for the detectors is extremely expensive, we purchased only a part of full detectors. The black area of the upper and lower detector layer represents blank space. Figure 3 right shows the actual measurement of a vanadium sample translated to the reciprocal space Qb (transverse to the incoming beam direction) and Qc (vertical direction). A clear Debye-ring pattern originating from aluminum can be observed in addition to the scattering from vanadium.

Other Devices

Much effort and time were also spent for the newly installed chopper system. Four different types of choppers will be used in POLANO. Three types of choppers, excluding the statistical chopper, were tested at the beam line. It was confirmed that they worked properly and performed according to expectations. Remote control and status logging of POLANO devices including above choppers were successfully operated by newly developed device controlling software YUI for POLANO. The data visualization and analysis software HANA for POLANO was also checked and Fig. 3 are the results from HANA.

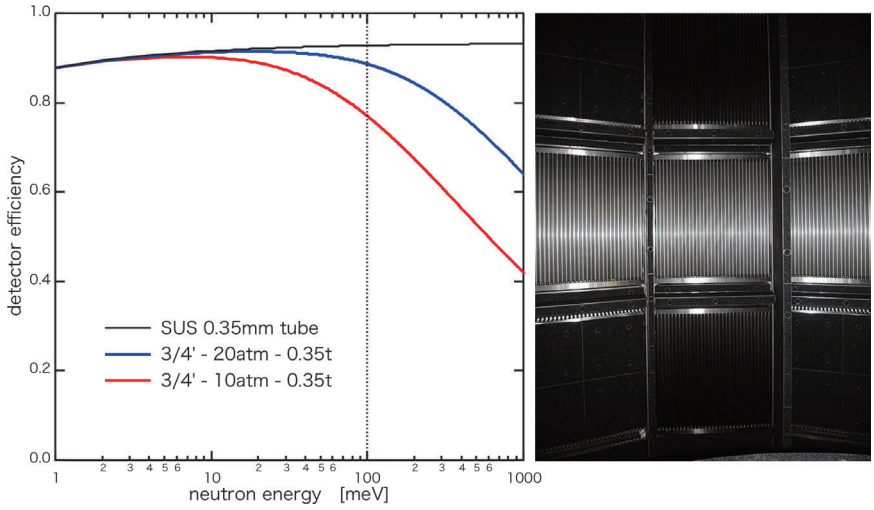

Figure 2. (left) Calculated position sensitive detector (PSD) efficiencies as a function of incoming neutron energy. The detector condition presented by the red line is adopted in POLANO.
(right) PSD arrangement on the large vacuum chamber wall. 60 cm effective length PSDs are layered to make a 2-dimensional detector array.

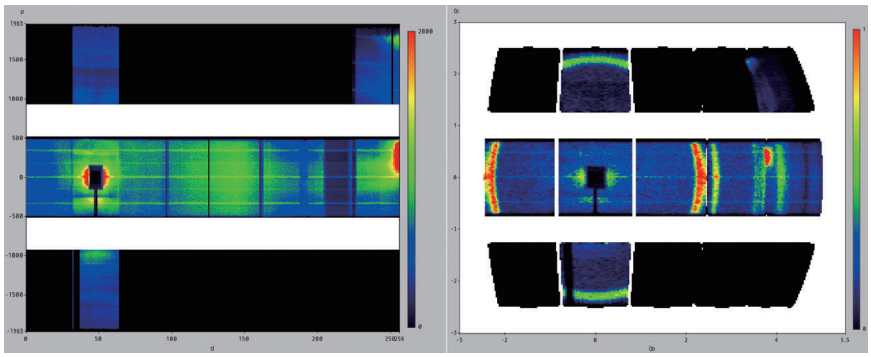

Figure 3. (left) Detected neutrons by tuning of PSDs. 3 lines from cadmium slits can be observed.
(right) Reciprocally translated observed signal in Qb-Qc plane. Part of the ring patterns (arcs) are due to the isotropic diffractions from aluminum.

3. Future plans

Still there are many things to take care of for the routine operation of the beam line. We are specifically focusing on improvement of devices to realize on-beam experiments and user programs, such as sample environment devices and data-acquisition, data-analysis software.

References

[1] T. Yokoo et al., AIP conference proceedings **1969** 050001 (2018).
[2] H. Seto et al., Biochimica et Biophysica Acta **1861** 3651 (2017).
[3] T. Yokoo et al., EPJ Web of Conferences **83** 03018 (2015).
[4] T. Yokoo et al., J. of Physics Conf. Series **502** 012043 (2014).
[5] R. Moon et al., Phys. Rev., **181** 920 (1969).
[6] J. R. Stewart et al., J. Appl. Cryst. **42** 69 (2009).

T. Yokoo[1,2], Y. Ikeda[3], N. Kaneko[1,2], M. Ohkawara[3], T. Ino[1,2], S. Sugai[1,2], S. Itoh[1,2], and M. Fujita[3]
[1]*Neutron Science Section, Materials and Life Science Division, J-PARC Center;* [2]*Institute of Materials Structure Science, KEK;* [3]*Institute for Material Research, Tohoku University*

Development of an *in-situ* Polarized ^{3}He Neutron Spin Filter for POLANO

1. Introduction

A ^{3}He neutron spin filter (NSF) is a key component for polarized neutron scattering in POLANO. Pressurized ^{3}He gas is polarized *in-situ* by the spin-exchange optical pumping (SEOP) method [1] to keep the incident neutron beam at a constant polarization. A compact *in-situ* polarized ^{3}He NSF, suitable for the limited space in POLANO, was developed [2], and off-line tests are underway (Fig. 1).

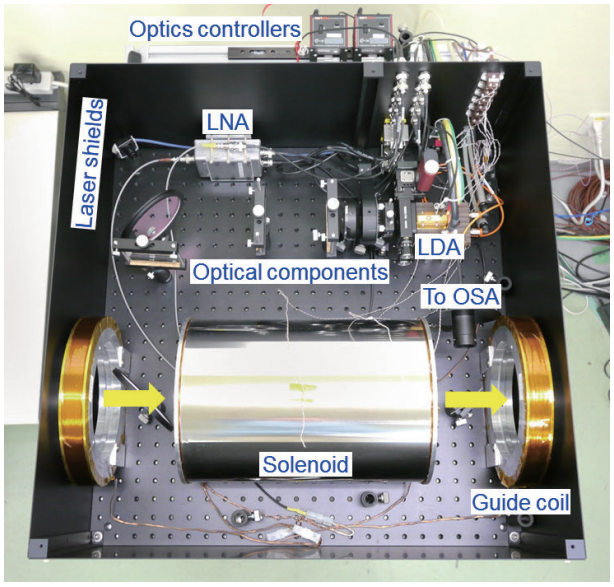

Figure 1. An *in-situ* polarized ^{3}He NSF for POLANO in laboratory testing. The essential components are packed in a laser shield box, 60 cm long, 60 cm wide, and 25 cm high (the top shield plate is detached). A ^{3}He cell is placed inside the magnetically-shielded solenoid. A laser diode array (LDA) and optical components provide circularly-polarized light of up to 70 W power for SEOP. The circularity and wavelength of the laser can be controlled remotely. The ^{3}He cell transmission light is continuously monitored with a fiber coupled optical spectrum analyzer (OSA). A low-noise amplifier (LNA) is for the NMR measurements of polarized ^{3}He gas. The neutron beam is shown as arrows.

2. AFP NMR system

In polarized neutron scattering, it is indispensable to reverse neutron spins to make the spin-up and spin-down measurements. It is often done by using a neutron spin flipper that may introduce a systematic error unless otherwise the neutron spins are perfectly reversed. With a use of a ^{3}He NSF, it can be done by reversing the spins of polarized ^{3}He instead of flipping the neutron spins. Unlike neutron spin flippers, the ^{3}He spins can be almost perfectly reversed by using the technique called adiabatic fast passage or AFP [3]. In AFP, an oscillating magnetic field is applied perpendicular to the static magnetic field that holds the ^{3}He nuclear spins, and by sweeping the oscillating field frequency or the static field strength so that either passes through the Larmor resonance of the ^{3}He nuclei, the ^{3}He spins are instantaneously reversed. The AFP spin reversal causes little depolarization of ^{3}He spins, but it can be drastically reduced by modulating the strength of the oscillating field. In addition to the AFP spin reversal, the ^{3}He polarization can also be measured by using a nuclear magnetic resonance (NMR) technique. The ^{3}He NSF for POLANO is equipped with such an AFP NMR system that reverses the ^{3}He spins and simultaneously performs ^{3}He polarization measurements (Fig. 2).

The frequency of the oscillating magnetic field is swept linearly, while the strength (amplitude) is modulated by a trapezoidal function; the amplitude is increased in the beginning, kept constant around the Larmor resonance, and decreased to zero in the ending. The increase and decrease rates of the oscillating field amplitude, as well as the frequency sweep rate, are key

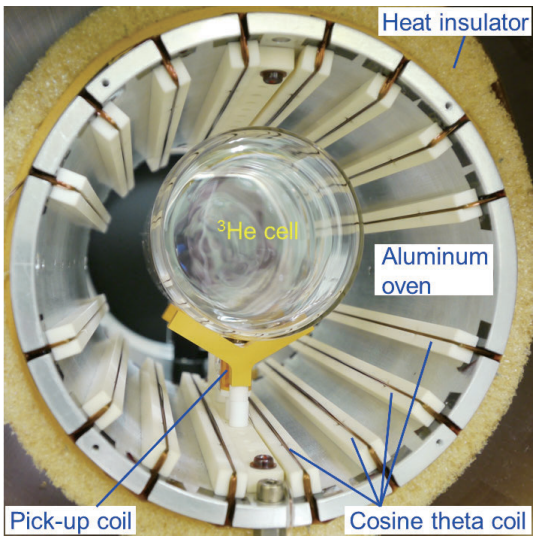

Figure 2. A cosine theta coil (AFP drive coil) arranged inside an aluminum oven generates an oscillating magnetic field perpendicular to the static magnetic field. A small pick-up coil is placed under the ^{3}He cell for NMR measurements. Note that the ^{3}He cell diameter is 60 mm.

parameters to minimize the ^{3}He depolarization during the AFP spin reversal. As for the NMR measurement, it is important not to change the amplitude around the Larmor resonance frequency to distinguish the NMR signal by the rotating ^{3}He spins from the background signal caused by the oscillating field itself, since the signal amplitude of the background is nearly constant, while that by the rotating ^{3}He spins follows the square root of the Lorentzian function to the sweep frequency.

In the NMR measurements, the signal detection is generally done with a lock-in-amplifier, but in the AFP NMR system for POLANO, it is performed in software on a PC with a USB oscilloscope, which has eliminated an expensive lock-in-amplifier (Fig. 3). A simple algorithm that detects NMR signals in real time has been developed. It has made the AFP NMR system compact, low cost, and flexible.

The ^{3}He depolarization by the AFP spin flip was determined to be less than 10^{-4} in one spin-flip, which is practically negligible. It is also worth noting that the ^{3}He spins are flipped in less than 0.1 seconds. The ^{3}He NSF will be installed in POLANO soon.

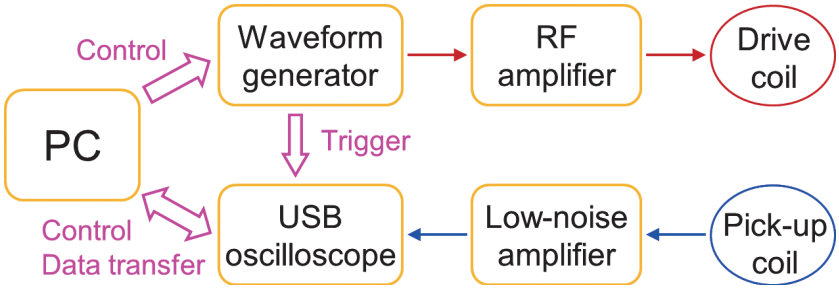

Figure 3. A schematic diagram of the AFP NMR system. A modulated oscillating current is generated, amplified, and applied to a drive coil for AFP. The rotating ^{3}He spin signal is sensed by a pick-up coil, then amplified, and stored in a USB oscilloscope for the NMR detection on a PC.

References

[1] T. R. Gentile, P. J. Nacher, B. Saam, and T. G. Walker, Rev. Mod. Phys. **89**, 045004 (2017).

[2] T. Ino, M. Ohkawara, K. Ohoyama, T. Yokoo, S. Itoh, Y. Nambu, H. Kira, H. Hayashida, K. Hiroi, K. Sakai, T. Oku and K. Kakurai, J. Phys.: Conf. Ser. **862**, 012011 (2017).

[3] A. Abragam, The Principles of Nuclear Magnetism, Oxford University Press (1961).

T. Ino[1,2], M. Ohkawara[3], Y. Ikeda[3], M. Fujita[3], S. Itoh[1,2], and T. Yokoo[1,2]

[1]Institute of Materials Structure Science, KEK; [2]Neutron Science Section, Materials and Life Science Division, J-PARC Center; [3]Institute for Materials Research, Tohoku University

Development of the Magnetic Field Environment System for Polarized Neutron Experiments on POLANO

1. Introduction

Although the polarized neutron spectrometer, POLANO, is under commissioning, we reached the first milestone, namely, standard unpolarized neutron experiments become available on BL23. The next goal is to realize polarization analysis experiments on BL23, so that it is indispensable to develop neutron-polarization devices, such as an in-situ polarized ^{3}He neutron spin filter (SEOP), a magnetic field environment system (guide field), and the analyzer. In this report, we present the status of the construction of the magnetic field environment system.

Figure 1 shows the configuration of the magnetic field environment devices on POLANO. Here, the guide coil, longitudinal-field guide magnet, fan-shaped guide magnet and magnetic housing of the supermirror analyzer have been installed into the beam line, while the SEOP-type spin filter and a Helmholtz coil are under construction. The completed Helmholtz coil consists of a split-pair longitudinal field coil and three transverse field coils. By tuning the current ratio, the magnetic field direction can be controlled three dimensionally in the range of ±50 Gauss at around the sample position. Since the Helmholtz coil is installed into the vacuum chamber, a cooling system is required to remove the Joule heat at the coil.

2. Design and Model Calculation of the Cooling System

We examined the cooling efficiency of the water-cooled flange prior to the construction of the system. The left panel in Fig. 2 show results of the calculation of the temperature profile. In this model, we assumed that the cooling water was kept at 25°C and the total heating of 327 Watts was generated at the coil as a standard experimental condition. Furthermore, we inserted a higher thermal conducting material (heat pipe) into the aluminum-A5052 columns to assist the efficient heat transfer from the coil to the cooling flange. In this case, the maximum temperature was estimated to rise up to ~55°C at the bottom of the Helmholtz coil. Next, we investigated the earthquake-resistant strength of the cooling system. As a typical case, we calculated the distribution of the principal stress when the acceleration of 1/4 G was transversely applied to the cooling system, which roughly corresponds to the seismic earthquake intensity of 3~4. As seen in the right panel of Fig. 2, the maximum principle stress was estimated as ~5.5 MPa at the connection area of the aluminum columns. This value was sufficiently smaller than the mechanical strength of the main material of the cooling system (c.f. yield strength of A5052 is 215 MPa). Based on the above simulations, we then constructed the cooling system.

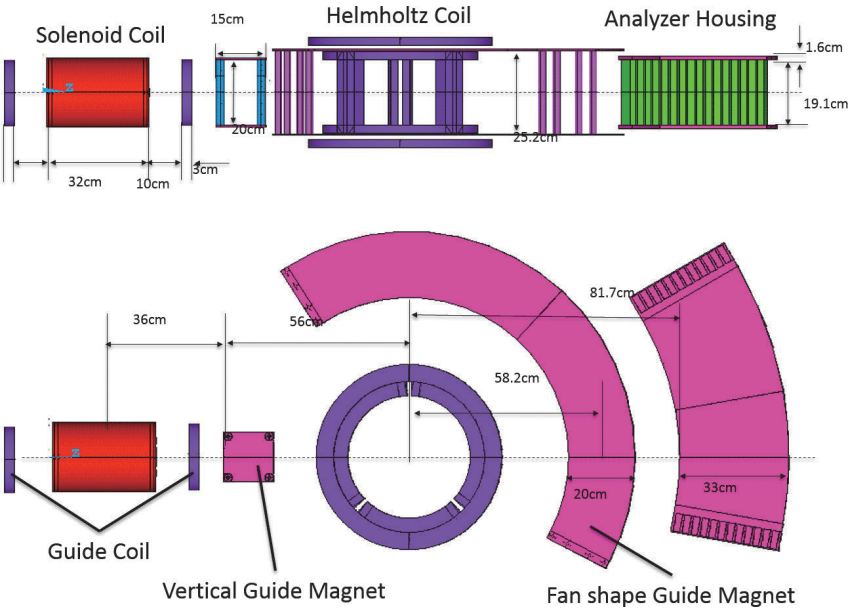

Figure 1. Configuration of the magnetic field environment system on POLANO.

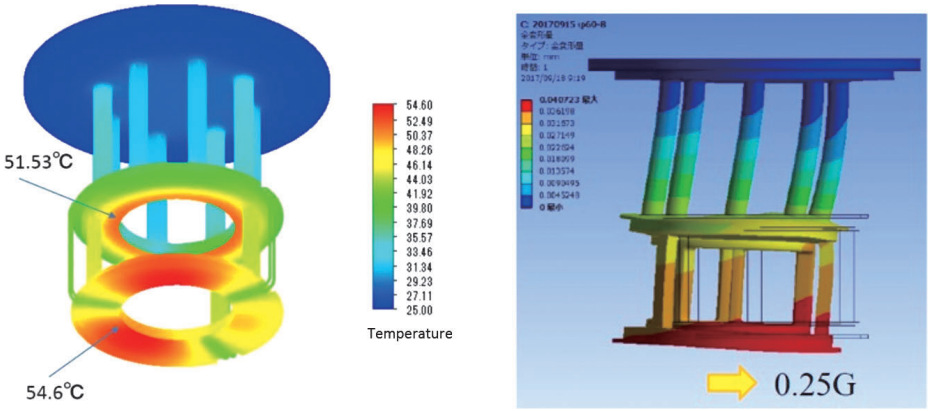

Figure 2. (Left) Simulations of the temperature profile of the cooling system. (Right) Calculation of the distribution of the principle stress for the case when the transverse acceleration of 1/4 G is applied.

3. Interlock and Monitoring System

We prepared the interlock and monitoring systems for safe operation. These systems monitor the current value of the Helmholtz coil, the temperature of the cooling system, and the flow rate of the water. When these monitoring values deviate from the limit, the interlock system immediately shuts down the power sources of the Helmholtz coil.

4. Performance Test

We carried out a performance test by using the constructed system. The left panel of Fig. 3 shows the time evolution of the temperature on the Helmholtz coil when the current of 10 A is applied to the three transverse field coils. Meanwhile, the right panel of Fig. 3 displays the results for another case when the current of 8 A is applied to the split-pair longitudinal field coil. As seen in these figures, the maximum temperature at a steady state is estimated to be 65 ~ 95°C, which is substantially lower than the maximum safe operating temperature of the coils.

5. Future

Now, we work on passing the safety review for the magnetic field environment system. The constructed system will be installed on POLANO soon after the safety examination is finished.

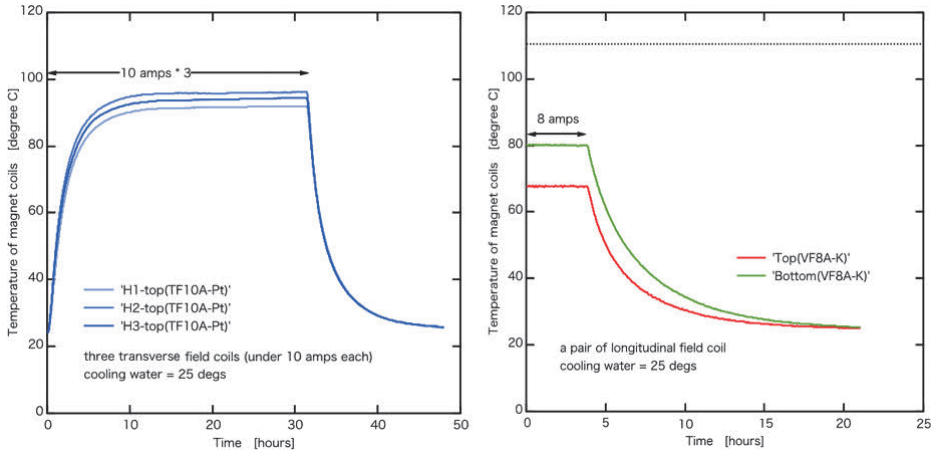

Figure 3. Time evolution of the temperature on the Helmholtz coil for (Left) 10 A on the three transverse field coils, and (Right) 8 A on the longitudinal field coil.

M. Ohkawara[1], T. Yokoo[2,3], Y. Ikeda[1], N. Kaneko[2,3], S. Itoh[2,3], and M. Fujita[1]

[1]Institute for Materials Research, Tohoku University; [2]Institute of Materials Structure Science, KEK; [3]Neutron Science Section, Materials and Life Science Division, J-PARC Center

Improvement of the Computing Environment System on POLANO

1. Introduction

The polarized neutron spectrometer, POLANO, has been designed with the ability to perform polarization analysis capable of utilizing the advantages of a pulsed-neutron beam [1]. In this report, we present the commissioning of the computing environment system on POLANO.

2. Improvement of the computing environment system

The device diagram of POLANO is shown in Fig. 1: here, grey-colored devices are under construction or not implemented. As seen in this figure, the hardware device for "unpolarized-neutron" experiments has been almost completely installed. Indeed, we have carried out various test measurements with unpolarized neutron beam and succeeded in observing magnetic excitation spectra from $CsVCl_3$ as a standard one-dimensional antiferromagnet [2].

To improve the computing environment system, we customized the control program of the Gifford-McMahon type refrigerator installed on BL23. Due to this update, users can carry out a standard low-temperature measurement from $T = 4$ K to room temperature. In addition, we improved the usability of the log visualization program on BL23 (Fig. 2). After this update, the graph-expansion (reduction) function and the export function of log data are available.

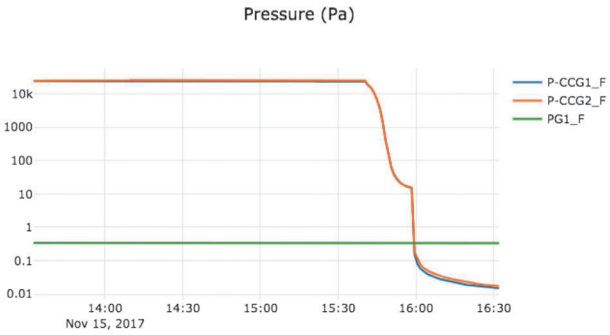

Figure 2. Improved log visualization program on BL23. Due to the update, the extension/reduction of the graph and the export function of the log data were improved.

3. Maintenance and Debugging

For preserving the colossal amount of event data, POLANO has two network-attached storage (NAS) servers of 30 TB with redundant arrays of inexpensive disks (RAID60). Unfortunately, unidentified warnings frequently occurred in the components of NAS. This hardware problem was solved by updating the firmware and replacing the defective hard disks.

When neutrons are detected at the position-sensitive detectors, the electronic signals are converted into event data (i.e. detected position and time). In the position calculation, we found an incorrect calculation process. Because of the incorrect calculation, the detected neutron positions were distorted, as shown in the top panel of Fig. 3. By modifying the calculation program,

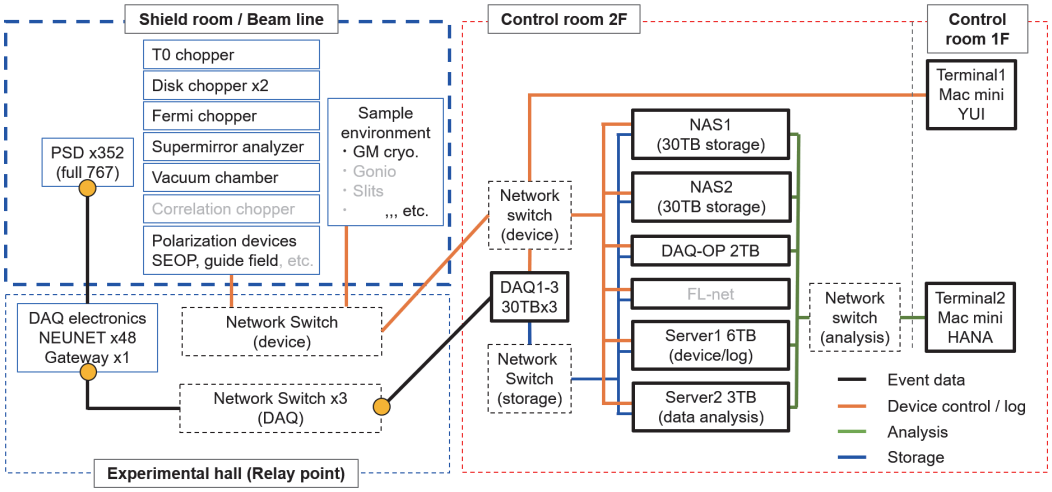

Figure 1. Device diagram and computing environment system on POLANO. Grey-colored devices are under construction or not implemented. Bold-solid lines indicate the flow of data/signals.

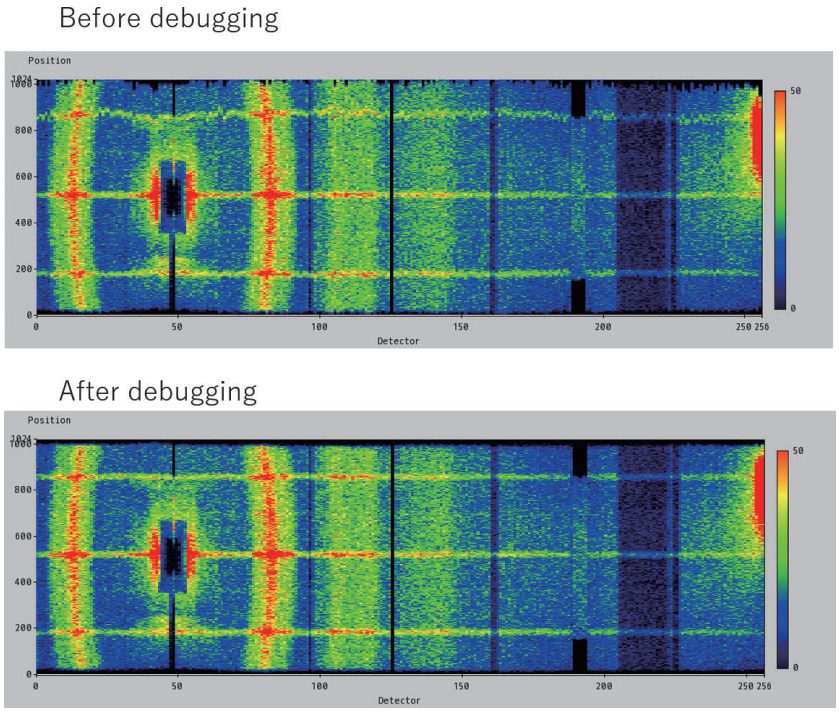

Figure 3. Debugging position calculation algorithm on the data visualization program HANA.

we were able to obtain a correct result, as seen in the bottom panel of Fig. 3.

4. Future plans

In the near future, we plan to install several core devices for "polarized-neutron" experiments, such as an in-situ polarized ^{3}He neutron spin filter (SEOP) device [3], a magnetic field environment system (a Helmholtz coil and its control system) [4], and a special cryostat. To operate such core devices, further development of the control programs is needed. In addition, further improvement on the data analysis program is indispensable for polarization analysis experiments. In particular, since it is difficult to install a wide-angle spin-flipper system, we must devise an ingenious analysis method to realize XYZ polarization analysis on POLANO. As a feasible analysis method, the Schärpf equations may be useful [5].

Acknowledgement

We acknowledge the support of D. Kawana (ISSP), KENS-DAQ group, and Bee Beans Technologies Co., Ltd. (Tsukuba, Japan).

References

[1] T. Yokoo, K. Ohyama, S. Itoh, J. Suzuki, K. Iwasa, T. J. Sato, H. Kira, Y. Sakaguchi, T. Ino, T. Oku, K. Tomiyasu, M. Matsuura, H. Hiraka, M. Fujita, H. Kimura, T. Sato, J. Suzuki, M. Takeda, K. Kaneko, M. Hino, and S. Muto, J. Phys. Soc. Jpn. **82**, SA035 (2013).

[2] T. Yokoo et al., presentation on WINS (2018); see also the related document in this annual report.

[3] T. Ino et al., (private communication) see the related document in this annual report.

[4] M. Ohkawara et al., see the related document in this annual report.

[5] O. Schärpf and H. Capellmann, Phys. Stat. Sol. A **135**, 359 (1993).

Y. Ikeda[1], T. Yokoo[2,3], S. Itoh[2,3], M. Fujita[1], N. Kaneko[2,3], and M. Ohkawara[1]

[1]Institute for Materials Research, Tohoku University; [2]Neutron Science Section, Materials and Life Science Division, J-PARC center; [3]Institute of Materials Structure Science, KEK

Sample Environment at MLF

1. Introduction

The sample environment (SE) team is in charge of the preparation, maintenance and development of the beamline (BL)-common SE equipment, and aids the users in operating the equipment. The team has thirteen members: seven from JAEA, four from CROSS and two from an outsourcing company, and is divided into sub-teams of cryogenics and magnets, high temperature, high pressure, soft-matter, pulsed magnet, light irradiation and ^{3}He spin filter. The status and activities of the SE team in JFY 2017 are summarized in this report.

2. Cryogenics and magnets

As of cryogenics and magnets, we have operated a top-loading ^{4}He cryostat, a bottom-loading ^{3}He cryostat, a dilution refrigerator (DR) insert and a superconducting magnet. The number of users' experiments we supported increased significantly over the past year. In JFY2017, the ^{3}He cryostat was operated for eight experiments, the DR insert for four experiments and the magnet for eleven experiments, including instrument proposals. The ^{4}He cryostat, into which the DR insert can be set, was used for seven experiments until January 2018. However, when preparing a users' experiment in January 2018, a serious leakage was found on this cryostat. Because the combination of the ^{4}He cryostat and DR insert is in high demand among users, we requested that the manufacturer repair it and are preparing an alternative cryostat.

3. High temperature equipment

The high temperature sub-team has a niobium furnace for quasi-elastic neutron scattering and inelastic neutron scattering measurements as the BL-common SE equipment. The niobium furnace is used with a radial collimator, allowing the elimination of unwanted background from the furnace. However, it is difficult to eliminate such background at the small-angle region because the line-of-sight from the detector to the sample and that to the background source are very close to each other in the small-angle region. Therefore, we recently developed a furnace for small-angle neutron scattering, which enables us to obtain small-angle neutron scattering data with a very low background level (Fig. 1). In JFY2017, we supported five users' experiments at BLs14, 15 and 18 using these furnaces.

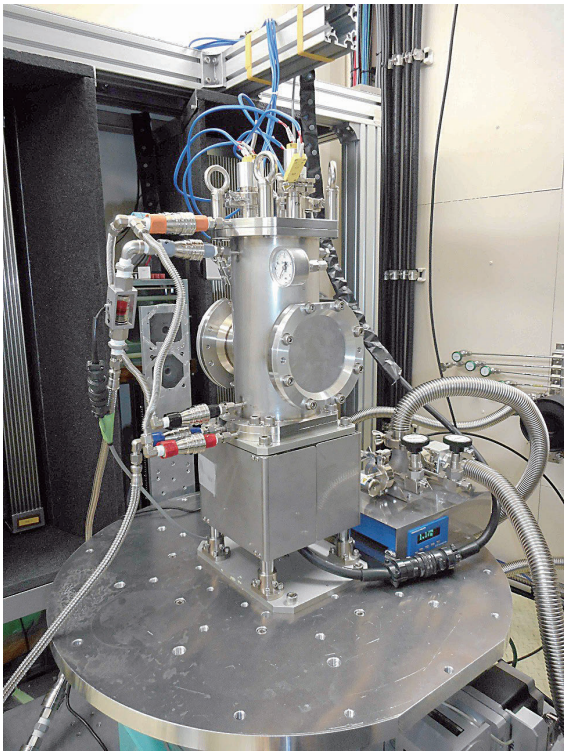

Figure 1. Furnace for small-angle scattering and neutron reflectivity measurement.

4. A pulsed magnet system

We have developed a prototype of a general-use pulsed magnet system of 30 T at the maximum. The pulsed magnet system consists of a solenoid coil, a sample stick and a pulsed power supply. The pulse width of the generated current is 2.65 msec at 50% of peak. Neutron scattering pulsed magnet experiments were carried out at NOBORU (BL10) in this fiscal year. As samples, a triangular lattice antiferromagnetic material and a heavy electron system superconducting material were employed. The main objective of the pulsed magnet equipment is to demonstrate repetitive firing by automatic operation of the pulsed power supply using control device in this experiment. Figure 2 shows the screen of the touch panel on the control box. In the automatic operation, the charged voltage was set to 700 V, output peak current and the peak magnetic field were 2.3 kA and 5.84 T, respectively. As a result, each shot was fired every 75 seconds (approximately 50 shots per 1 hour) and150 continuous automatic shots were successfully fired in approximately 3 hours; the total was 2000 shots in approximately 2.5 days.

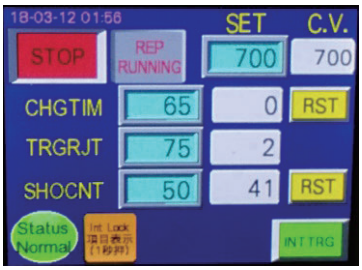

Figure 2. The touch panel on the control box.

5. Light irradiation

In JFY2017, we installed a new mercury lamp, which provides strong ultra-violet illumination (Fig. 3). Also, a photodetector was installed to "stamp" the time when a light shutter was open and closed, synchronized with the data acquisition system at the MLF.

Figure 3. The mercury lamp.

6. ^{3}He spin filter

We have been developing a spin-exchange optical-pumping (SEOP) based polarized ^{3}He neutron spin filter (^{3}He-NSF) for efficient utilization of pulsed neutrons at J-PARC.

In 2017JFY, we started the assembly of a ^{3}He gas filling station to fabricate hybrid cells with Rb and K.

A laser lab for laser pumping based on the SEOP was prepared in the beam hall of MLF in 2016. However, the problem was that the relaxation time of the ^{3}He polarization was too short and the achieved polarization was not high enough for polarized neutron experiments. In 2017, therefore, we investigated the causes of the problem, and found out that the situation could be improved drastically by setting a noise-cut transformer in the electric power supply line, thus, we managed to obtain adequate ^{3}He relaxation time and the necessary polarization.

In 2017, we performed a demonstrative study of polarized-neutron single-crystal diffraction measurement at BL18 (SENJU). The sample was a single crystal Fe. In the results, the expected flipping ratios of Bragg peaks were not observed. To understand the results, we thought of the possibility that severe depolarization of neutrons had occurred in the sample. To check the idea experimentally, we performed a depolarization experiment of neutrons transmitted through the sample at BL10. Then it was found out that neutrons were severely depolarized in the sample, which was almost magnetically saturated under an applied magnetic field of 4.2 kG. This result indicated the existence of some domains whose magnetization is not oriented in the direction of the applied magnetic field even in the field of 4.2 kG.

T. Oku[1], M. Watanabe[1], R. Takahashi[1], S. Ohira-Kawamura[1,2], M. Ishikado[4], K. Ohuchi[4], Y. Yamauchi[5], M. Nakamura[5], S. Takata[1,2], Y. Sakaguchi[4], H. Kira[4], K. Sakai[1,3], T. Aso[1,3], and K. Aizawa[1]

[1]Technology Development Section, Materials and Life Science Division, J-PARC Center; [2]Neutron Science Section, Materials and Life Science Division, J-PARC Center; [3]Neutron Source Section, Materials and Life Science Division, J-PARC Center; [4]Neutron Science and Technology Center, CROSS; [5]Nippon Advanced Technology co.

Development of a Remote Data Access Based on the Cloud Environment

1. Introduction

The remote access environment for data retrieval, download, and analysis plays an important role in the research workflow after experiments in MLF. Such an environment allows the facility users to perform the analysis smoothly and effectively in their home institution. However, building such an environment is quite challenging because, in addition to adequate management of large and diverse experimental data acquired by neutron instruments in the whole facility, it requires secure, quick and easy data access via network from the outside of the facility.

In recent years, we have been developing the remote access environment based on the public cloud. Owing to the recent rapid progress and spread of public clouds such as Amazon Web Service (AWS) and Microsoft Azure, it is possible to develop effectively more advanced systems and applications using various services provided by public clouds.

This year, we completed two developments for the remote data access using Amazon Web service (AWS). One is a development of the data delivery function of the MLF experimental database (MLF EXP-DB) [1]. The MLF EXP-DB is the integrated system creating a metadata catalog for data management and access. The other is a development of the general-purpose framework for a web-based analysis environment. In addition, to confirm the feasibility of this system, we have conducted a performance test for load distribution. This framework consists of two components, which are a web interface, called "Nokiba" and processing backend, called "Shigure" [1]. Using this framework, facility users can execute various types of analysis software according to the experiment, as well as perform analysis through a browser.

2. Development of data delivery service

A new data delivery function of the MLF EXP-DB utilizes the cloud service provided by the AWS. The MLF EXP-DB centrally manages the experimental data generated in neutron instruments by cataloging it as a metadata catalog. The cataloged data files are stored in the data repository of the facility. Since the MLF EXP-DB is a web-based integrated system, the management operation can be performed using a web browser.

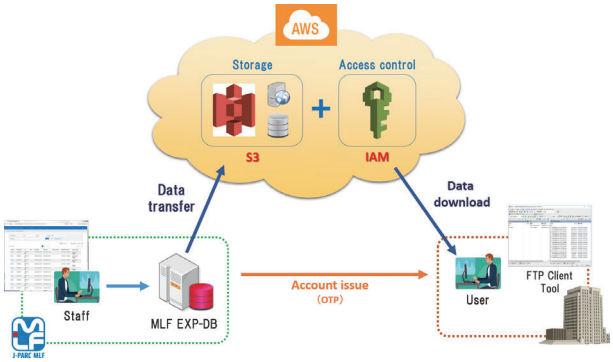

Figure 1. The schematic view of the data delivery service.

Figure 1 shows schematic overview of the data delivery using the new function. This function transfers the data selected from the metadata catalog by the instrument staff through the browser from the facility data repository to the storage service AWS S3 [2] on demand. The access to the data preserved on the AWS S3 is controlled by the Identity and Access Management service AWS IAM [3]. The facility user is issued an ID and one-time password (OTP) to access the AWS S3. Data download using a general-purpose FTP client tool is possible. In addition, the data on the AWS S3 can be archived for a long term and fast downloaded from a distance by using other services and foreign regions of the AWS.

3. Development and performance tests of the remote analysis environment

Since a large number of facility users will perform data analysis on the remote analysis environment after the experiment, this environment should be able to process large amounts of analysis activities by simultaneous access. Therefore, we have constructed the remote access environment using our framework as a scalable clustered system on the cloud.

Using the Elastic Computing Cloud service AWS EC2 service [4], we constructed the environment of the analysis server × 10 (640 core) and developed the program execution environment as a cluster by Docker swarm. For the analysis program, we converted event data to histograms in parallel using UTSUSEMI [5, 6] developed in MLF. We performed the histogram processing in parallel using analysis software called UTSUSEMI, developed in MLF. The AWS S3 service was used for

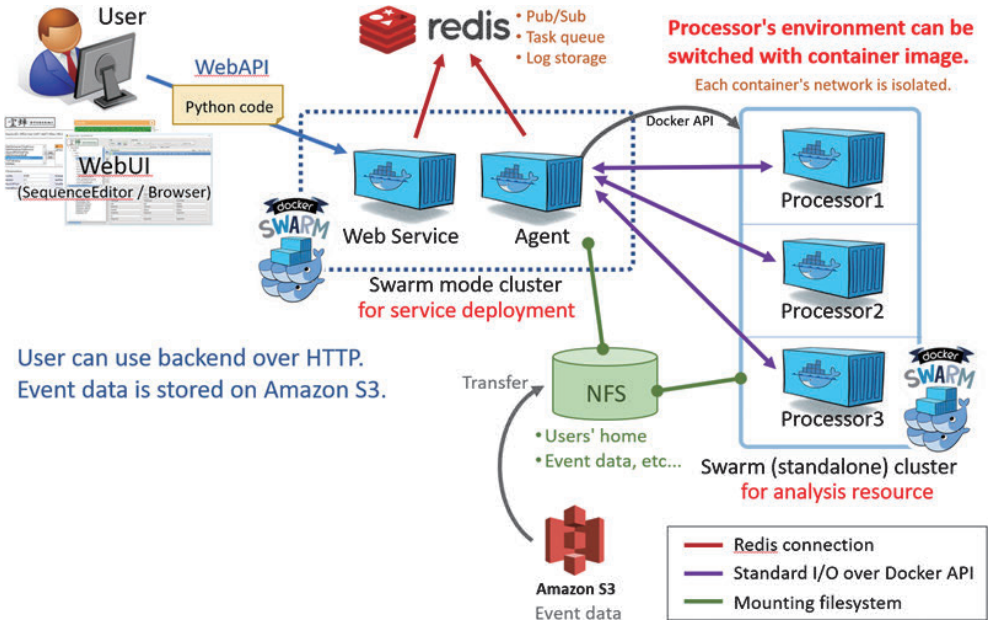

Figure 2. The configuration of the remote analysis environment for the performance test.

object storage. Originally, we were building a cluster with Docker swarm standalone [7], but due to a change in the number of Sessions, but the Docker service itself crashed due to insufficient memory, so in Docker swarm mode [8], to fix the number of sessions, we decided to overcome the memory shortage problem by limiting the number of replicas.

In the performance tests, it was assumed that analysis processing of 6 sessions could be performed simultaneously on each beam line, and the goal was to accomplish simultaneous processing of 6 sessions × 23 beam lines = 138 sessions or more.

As a result, concurrent processing could be done in up to about 200 sessions at the maximum, but memory shortage occasionally occurred depending on the situation, so it was possible to finally carry out stable processing in up to 180 sessions.

According to the results of this experiment, a stable operation was achieved with the configuration combining Docker swarm mode and standalone (Fig. 2). In this configuration, swarm mode is for the Web service (entry point) and Agent. On the other hand, a cluster composed of swarm standalone is assigned as a computing resource. Cloud resources used in this work was provided in the Demonstration Experiment of Cloud Use conducted by National Institute of Informatics (NII) Japan (FY2017).

4. Conclusion and future plans

In FY2018, as our first attempt to use the cloud, we will make this service available to the instrument users of BL18 and we also plan to extend the service to other instruments in stages. In addition, we have developed the remote data analysis environment as the flexible clustered system on the cloud and conducted the performance test. Based on the result of this test, we plan to develop a more user-friendly web interface in the future.

References

[1] K. Sakasai et. al., Quantum Beam Sci. 2017, 1, 10.
[2] https://aws.amazon.com/s3/?nc1=h_ls
[3] https://aws.amazon.com/iam/?nc1=h_ls
[4] https://aws.amazon.com/ec2/?nc1=h_ls
[5] Y. Inamura et. al., J. Phys. Soc. Jpn. 2013, 82, SA031-1-SA-031-9.
[6] J. Suzuki et. al., Nuclear Inst. and Meth. Phys. Res. 2009, 600, 123.
[7] https://github.com/docker/swarm
[8] https://docs.docker.com/engine/swarm

K. Moriyama and N. Okazaki
Neutron Science and Technology Center, CROSS

"Live Data Reduction" Project

1. Introduction

Since the commissioning of the first neutron beam at MLF, we, the computing group, have successfully produced a lot of software for facility users to improve the efficiency of measurement and data analysis. On the other hand, there are some users' requests left on the computing environment at MLF. One of the strong users' demands is real-time data processing during a measurement. Because the measurement time becomes shorter with the increase of the neutron beam intensity, users want to analyze and visualize their current data while conducting their measurement to decide the next measurement conditions.

To see the current data of measurements in the original data acquisition system (DAQ) adapted at MLF, we had to access directly the data files during DAQ system writes. This access can potentially damage the recorded data. To reduce such risks, we have started a new project, named "Live data reduction", which treats and visualizes current data with "Safety", "Speed" and "Flexibility" in real time. This real-time processing method is used not only in the real-time analysis but also for automated executions of the measurement schedule by cooperation with instrument control software. In this report, we share the results of our work on this project, accomplished in FY2017.

2. Developments

MLF has adopted the event-recording method by means of DAQ middleware [1] for the data acquisition system. The DAQ middleware gathers event-recorded data (event data) produced by the electric module of neutron detectors and devices installed in a beam line instrument to store the data into the storage as a file. We attempted before to implement real-time data processing by using differential events reading methods as an online monitoring system [2]. Under this method, the software reads the differential events in data files updated by the DAQ system at regular intervals to execute some data processing steps using only differential data. This method certainly reduces the access to data files and the damage risk. However, the method was not good enough because it still involved file access.

To achieve our targets for data processing with "Safety", "Speed" and "Flexibility" in real-time, the system requires high throughput with safety and flexibility. Therefore, we've decided to adopt software architecture, based on "Publish – Subscribe" pattern with a message-oriented middleware, which is used in many internet services. In this model, the data senders, called publishers, and data receivers, called subscribers, are connected loosely through a broker. Publishers and subscribers do not communicate with each other directly, which means that the publishers do not need to wait for a reaction from subscribers and the latter do not need to know the status of the publishers. In addition to this flexibility, this method has high scalability to increase easily the number of both publishers and subscribers by any request.

As a broker in our system, we chose the open source "Redis" [3], which is an in-memory database for faster processing and has interfaces in various languages. Next, we decided to treat events data produced from DAQ directly as messages (data) sent by the publishers. This decision simplifies the structure of publishers' activities and ensures the flexibility of subscribers. We, therefore, started to develop publisher software as a module working in the DAQ middleware. By using this module, we can introduce another data stream which is different with a stream to write data into files, as shown in Fig. 1. This means that we are able to access the current data without the danger of data files' destruction. In

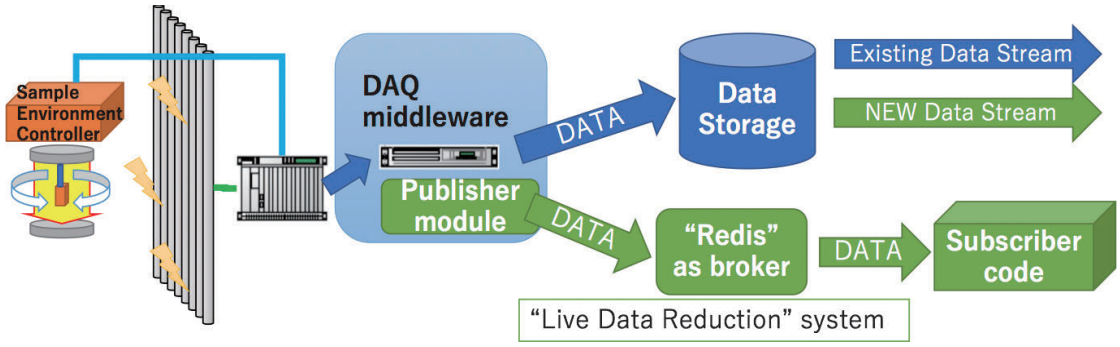

Figure 1. The structure of the DAQ middleware and the live data reduction system.

addition, it's easy to install this publisher module into a beam line using the DAQ middleware. In FY2017, these base components had already passed the long-term stability examination and were introduced in some actual beam lines. As subscribers, we are able to develop software suitable for each beam line adopting our live data reduction system using Python or C++. We show some applications of our system in the next section.

3. Applications of the live data reduction

Here, we introduce some applications using the live data reduction system.

The first example is the online beam monitor for the 2-dimensional neutron detector installed in BL17 (Fig. 2). As the subscriber for a 2-dimensional detector, a member of the beam line staffs wrote by himself some Python codes to get event data from the Redis server to count kicker events for the time normalization and to make histograms for plotting. These subscribers are simple Python codes with several tens of lines and their processing speed is fast enough to check the status of the measurements.

The second example is the online visualization on the web browser used at BL21. In this system, the subscriber was written in C++. The subscriber obtains event data from the Redis server and then makes some histograms with ROOT [4]. To visualize those histograms on the web browser as shown in Fig. 3, JSROOT are used. Users can see the 2-dimensional profile of the incident beam and the intensity map for each detector bank in the middle of their measurement. This visualizations system has already been working successfully. The next step is to add the functions to execute some data reduction codes to calculate a structure factor S(Q).

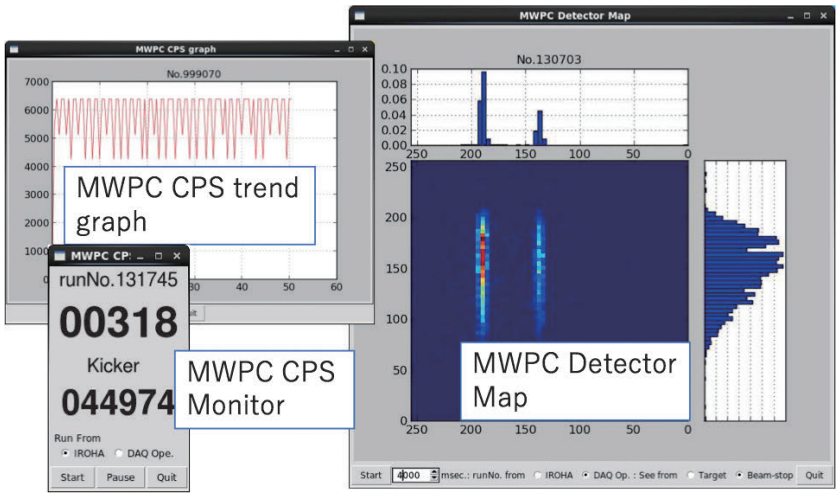

Figure 2. Screen shots of the online monitoring software for the 2D detector (MWPC) in BL17 (Sharaku).

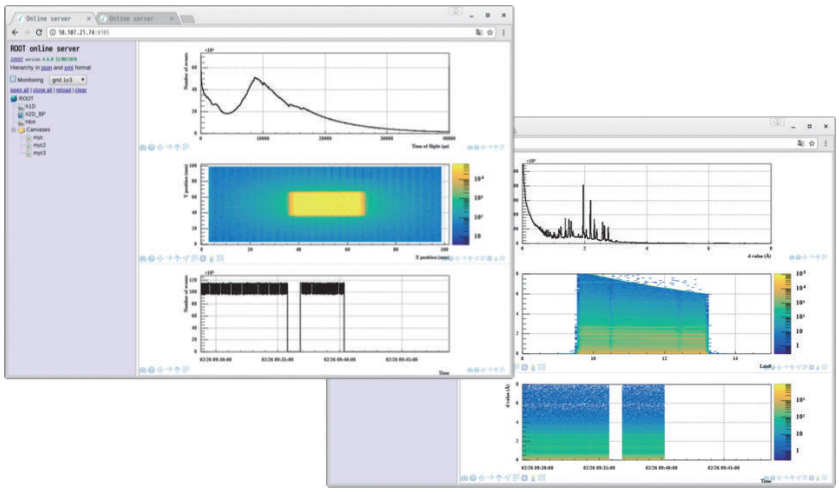

Figure 3. Screenshots of the online monitoring software in BL21 (NOVA).

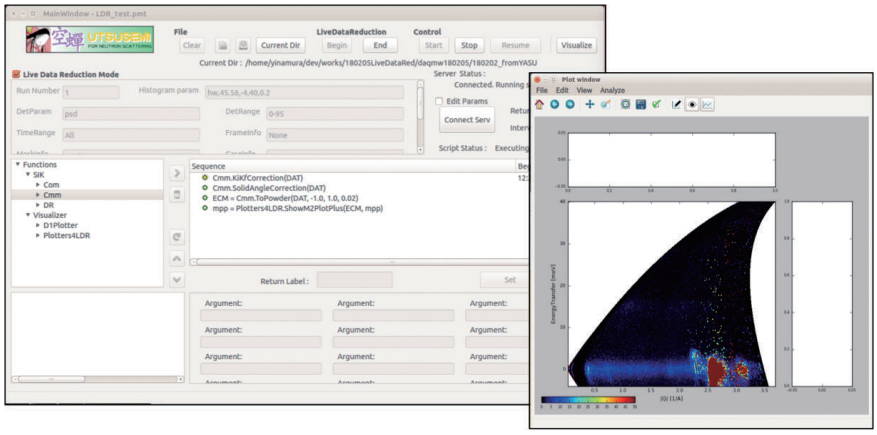

Figure 4. Screen shots of GUI and the plotter of the live data reduction on Utsusemi.

The last example is the attempt to add the subscriber function into Utsusemi software, which is a series of software to analyse and visualize the event data with a graphical interface and is introduced in a lot of beam lines in MLF [5]. One of important functions of Utsusemi is the flexible conversion from the event data to the histogram format data filtered by the various experimental conditions. Utsusemi is normally utilized as offline analysis software, which means the codes in Utsusemi treat only static data files in a storage. On the other hand, as mentioned before, we have already implemented the differential events reading method in Utsusemi. We, therefore, appended a subscribe function to this method instead of the function to read data from data files for the live data reduction. As a result, Utsusemi receives the differential events from the Redis server at regular intervals, and then converts the events to histogram format to do the data reduction codes, for example various data corrections, background subtraction, time normalization and so on. It should be noted that all the offline data reduction codes can be used for the live data reduction without code modification. This means that the results of the live data reduction process match completely the ones derived from offline data reduction. In other words, this method allows the users to get the analyzed data immediately after the users' measurements are completed. This new function in Utsusemi had been already demonstrated in the actual beam line with enough results. In near future, we will make it available to users.

4. Summary and future plans

In this project, we produced successfully a base system for the live data reduction and introduced it in some actual beam lines. However, there are many problems to be solved. One is the issue of the timing for subscribing. In the current system, if the software subscribes after publishing by the publishers, the data stream before subscribing is lost. When we implement the actual live data reduction system, we must develop a system that will let the subscribers cooperate with publishers in the DAQ system. We will continue our work to refine the system and make it more useful.

References

[1] Y. Yasu et. al., J. Phys. Conf. Ser., 219, 022025 (2010).
[2] Y. Inamura, et. al., J. Phys. Conf. Ser., 1021, 12015 (2018).
[3] https://redis.io
[4] https://root.cern.ch
[5] Y. Inamura, et. al., J. Phys. Soc. Jpn. 82, SA031-1 (2013).

Y. Inamura[1], S. Kasai[2], H. Ohshita[1,3], and Y. Yasu[3]
[1]Neutron Science Section, Materials and Life Science Division, J-PARC Center; [2]Neutron Science and Technology Center, CROSS; [3]Institute of Materials Structure Science, KEK

Bump Cathode Element for Two-Dimensional Neutron Detector

1. Introduction

Neutron scattering experiments that measure neutron-induced signals near high-intensity direct beams require two-dimensional neutron detectors that have particular features, such as a high counting rate, a good spatial resolution, a high detection efficiency, and a superior signal-to-noise (S/N) ratio. Gas-based two-dimensional neutron detectors using a multiwire- and micropattern-element are candidates for use in these neutron-scattering experiments, and we have developed a gas-based position-sensitive neutron-detection system that consists of a two-dimensional detector element and can read out an individual signal line [1]. In a gaseous neutron detector for the neutron scattering experiment, a conversion gap, a reaction length between neutron and neutron converter, should be made as small as possible, because the gap causes the parallax effect of incident neutrons. At the same time, the gas pressure should be increased to obtain a high-detection efficiency performance, though the increase of the gas pressure causes the decrease of the output signal. To measure the decreased output signals, the gaseous amplification and/or charge collection efficiency must be increased. In the present study, we developed a dedicated two-dimensional detector element using circular cathode bumps for charge collection and performed preliminary neutron irradiation experiments.

2. Bump cathode element

The developed element has triangularly arranged, small-sized circular cathode bumps, which are linked together in the x- and y-directions for the individual signal line readout. The photograph and the magnified schematic view of a developed bump cathode element are shown in Fig. 1.

The developed bump cathode element consisted of a polyimide insulator and circular cathode bumps (pads) made from Cu on the insulator. A polyimide layer with a thickness of 0.025 mm was used as the substrate and the thickness of the bumps was 0.02 mm. Two types of circular bumps, with diameters of 0.6 and 0.65 mm, were triangularly arranged on the surface of the polyimide. The 0.65- and 0.6-mm bumps were linked in lengthwise direction on the bottom of the substrate using 0.1 mm lines, and the crosswise direction on the surface of the substrate using 0.05 mm lines, respectively. Both lines were arranged orthogonally. As a result, the 0.65- and 0.6-mm bumps were used for detection of incident neutrons in the x- and y-directions, respectively.

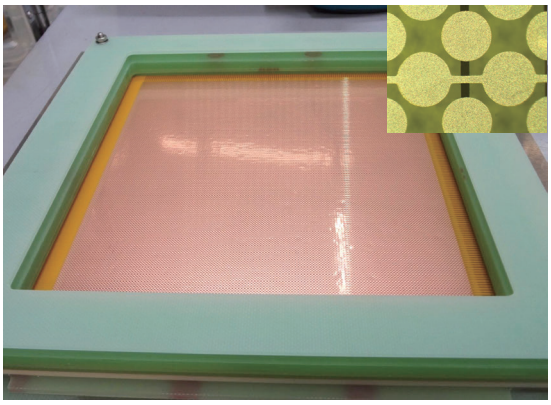

Figure 1. Entire and partially magnified photograph of a developed bump cathode element.

The sensitive area is 128 mm × 128 mm with a pitch of 1 mm in both directions. For use in the detector system, the bump element was placed on the base plate made from an alumina ceramic with thickness of 1.5 mm.

Irradiation experiments for the bump cathode element were performed using a neutron detection system consisting of a pressure vessel, amplifier-shaper-discriminator boards, optical signal transmission devices, position encoders with field-programmable gate arrays, and a data acquisition device. The element was arranged on the base plate with anode wires in the pressure vessel with a 20 mm conversion gap. The base plate had multichannel connectors (X: 128 ch, Y: 128 ch) for signal transmission from a detector element to signal processing electronics mounted outside of the pressure vessel. A schematic sectional view in the pressure vessel is shown in Fig. 2. Gold-plated tungsten wires with diameter of 20 μm were used as anode wires, and a total of 128 wires were arranged with 1 mm pitch. Gaseous amplification around each anode wire was induced by the strong electric field between the electrodes. The conversion gap, distance from drift plane to anode wires, for nuclear reaction between neutrons and ^{3}He is 20 mm, and the distance from the anode wires to the cathode bumps was 1.0 mm.

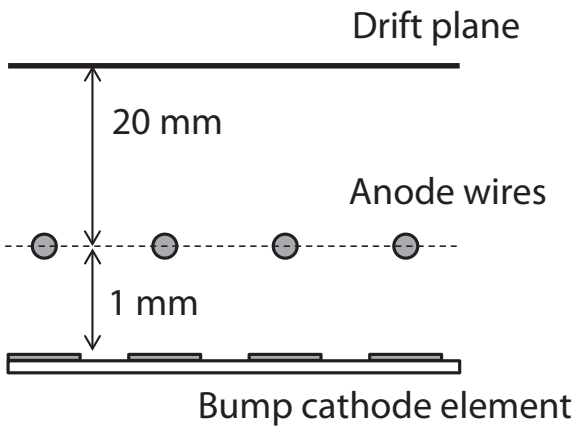

Figure 2. Schematic sectional view in the pressure vessel.

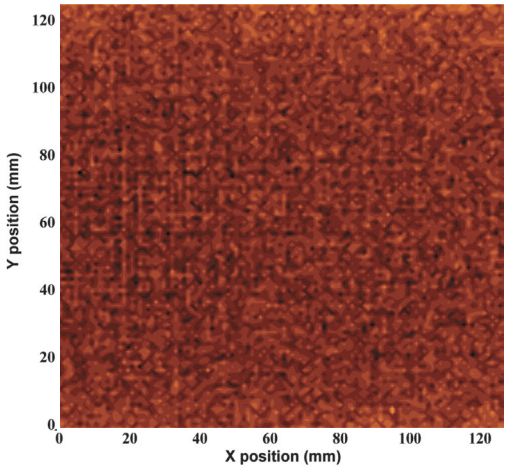

Figure 3. Flat-field image under Cf-252 neutron irradiation.

3. Experimental results

Preliminary neutron irradiation experiments were performed using the developed bump cathode element with a fill gas of composition He/(15%)CF_4 at 0.7 MPa. Neutron irradiation to the element was performed by embedding a Cf-252 neutron source. Figures 3 and 4 show the flat-field image measured by the detector, which confirmed the spatial homogeneity of the detector element, and the histogram of the pixel counts of the flat-field image, respectively. The histogram of all pixel counts was evaluated by a Gaussian fit and showed good homogeneity. The average pixel count was 134 with a standard deviation of σ = 13.5, which corresponded to an average count fluctuation of 10.1%. The intrinsic spatial resolution can be calculated from the obtained flat-field image in our detector system [2]. The average intrinsic spatial resolution in the sensitive region was 1.89 mm FWHM calculated by taking into account the track lengths of the secondary particles with He/(15%)CF_4 at a pressure of 0.7 MPa.

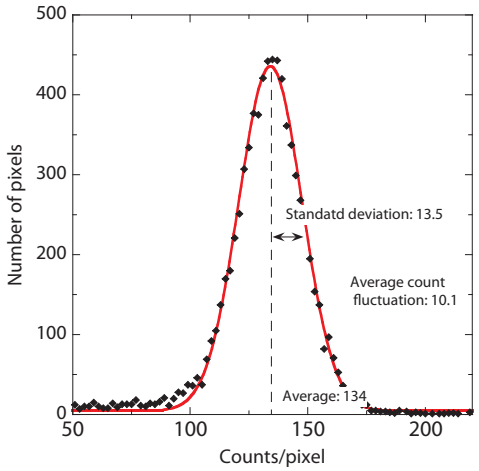

Figure 4. Histogram of the count distribution of the flat-field image.

References

[1] K. Toh et. al., Nuclear Inst. and Meth. Phys. Res., A726 (2013) 169.

[2] K. Toh et. al., J. Phys. Conf. Ser. 528 (2014) 012045.

K. Toh[1], T. Nakamura[1], K. Sakasai[1], and H. Yamagishi[2]

[1]Neutron Instrumentation Section, Materials and Life Science Division, J-PARC center; [2]Nippon Advanced Technology

Muon Science

Status of J-PARC MUSE

1. D-line

The D-line, which is a superconducting decay/surface channel with a modest-acceptance (about 40 mSr) pion injector, was originally constructed with a re-used superconducting magnet, which had been used at KEK-MSL for more than 30 years, having a cold bore (inner bore radius of ϕ12), and therefore beam windows at the inlet and outlet.

Through the beam commissioning, we achieved a beam with much more narrowed momentum bite. The beam has been realized by slit slicing of the laterally dispersed beam after bending magnet of beam transport optics. In that condition, we used two slits for limiting the beam passing. In the first slit, located next to DQ6, the slit opening was laterally 30 mm and vertically 20 mm. Then, in the second slit, located next to Septum, the slit opening was also laterally 30 mm and vertically 240 mm. (the full opening is 240 mm in the both slits). As a result, the beam condition yields a minimum momentum bite, where $\Delta p/p$ is 1.7% as σ of Gaussian function and the beam divergence is laterally 24 mm and vertically 60 mm within full width (6 σ) of 2D Gaussian, as shown in Fig. 1.

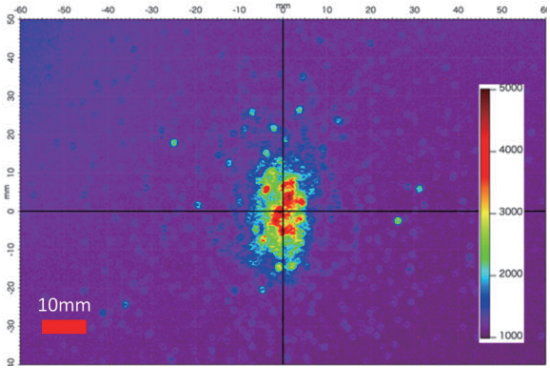

Figure 1. Beam pattern image obtained by profile monitor.

At the D2 area, a beam collimator was designed with conically tapered hole along the beam focusing envelope: the 250-mm diameter at the beam port is focused up to 50-mm diameter at the beam extraction port, as shown in Fig. 2(a) and (b). At the extraction port, 50 μm-thick Kapton window is divided between vacuum and air. The distance from the gate bulb to the extraction is 600 mm. The distance allows enough room to place Ge detectors for measuring the muonic X-rays emitted from the front side (beam upstream side) of the target.

(a)

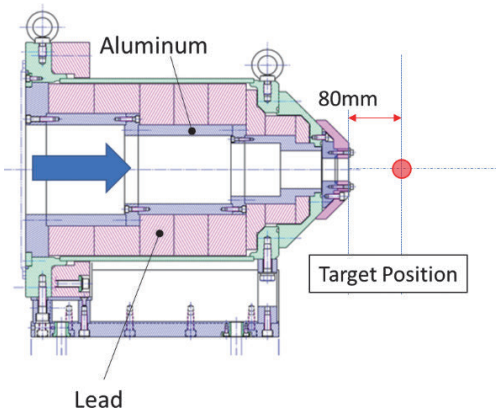

(b)

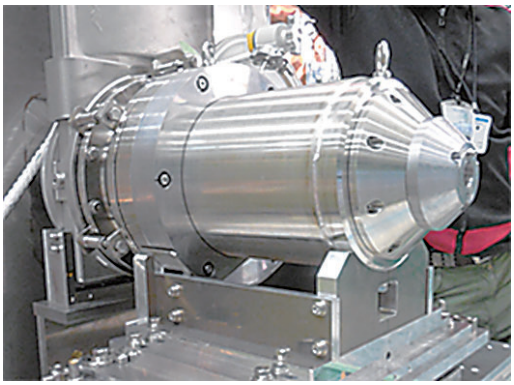

Figure 2. Beam collimator: (a) design (b) its picture patteimage obtained by profile monitor.

2. S-line

The S-line was open for users in FY2017. As of the end of 2017, 43 researchers from 25 research institutes around the world, including 10 students and 5 researchers from overseas, have carried out 17 experiment proposals, as shown in Fig. 3. Thanks to the intense proton

Figure 3. Users from Toyota CRDL and KTH Sweden are preparing the sample mounted in a cryo-furnace.

beam power of 400 kW, they were able to take muSR measurements at a rate as high as 200 million events per hour at the S1 area. Besides, the stable operation of the user program is enhancing the sample environments in order to meet various users' demands. For example, the newly-installed cryo-furnace in the S1 area made it possible to change seamlessly the sample temperature from 1.5 K to 500 K.

3. U-line

At the U-line, we conducted ultra-slow muon spin rotation experiments using a silver plate sample. In February 2018, we observed for the first time rotation spectrum using ultra-slow muon in U-line at J-PARC MLF, as shown in Fig. 4. We will continue to perform beam commissioning and upgrade of the apparatus of the beamline components for further optimization of the beam profile, confirmation of time resolution of the ultra-slow muon beam, and deceleration test for the depth profile experiment.

4. H-line

During the summer shutdown in 2017, we started the construction of a new power sub-station (~5 MW) designed to operate the H-line. The construction site is located in the northeast side of the MLF. A new hatch for electric transmission lines on the MLF wall was completed during the summer shutdown. Subsequently, the building of the bedding of the sub-station was started, as shown in Fig. 5, and the earth retaining work was finished successfully during FY2017.

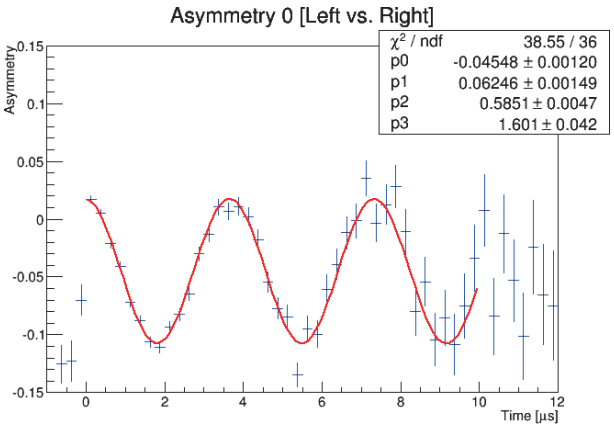

Figure 4. The first ultra-slow muon rotation spectrum obtained in the silver plate with 20 G transverse field in J-PARC MLF.

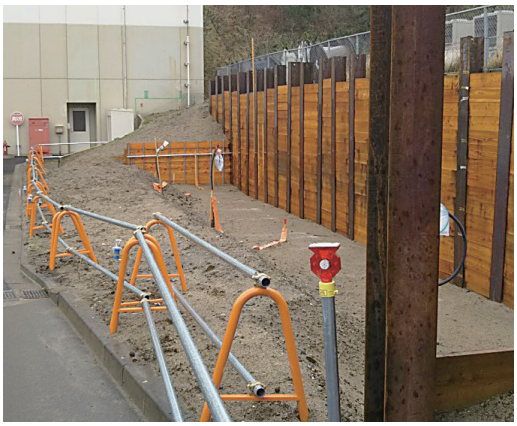

Figure 5. Current status of the construction of the electric power sub-station.

Y. Miyake[1,2], N. Kawamura[1,2], K. Shimomura[1,2] , P. Strasser[1,2], A. Koda[1,2], Y. Ikedo[1,2], H. Fujimori[1,2], S. Makimura[1,2], Y. Kobayashi[1,2], J. Nakamura[1,2], Y. Oishi[1,2], T. Adachi[1,2], K.M. Kojima[1,2], T. Yamazaki[1,2], S. Takeshita[1,2] , M. Tampo[1,2], W. Higemoto[2,3], and T.U. Ito[2,3]

[1]Institute of Materials Structure Science, KEK; [2]Muon Science Section, Materials and Life Science Division, J-PARC Center; [3]Advanced Science Research Center, Japan Atomic Energy Agency (JAEA-ASRC)

Present Status of the M2 Tunnel, the Central Part of MUSE

The muon production target and the front-end part of all muon beamlines, the D, U, S and H lines, are located in the proton beamline tunnel. The proton beam line from the muon target to the neutron target, named M2 tunnel, is in a high radiation field due to the beam loss at the muon target, so all the devices there, *i.e.* the beamline magnets, the vacuum components and so forth, were fabricated according to the design strategy [1], that was created with the effect of radiation in mind. The muon section is in charge of the operation of all devices in the M2 tunnel shown in Fig. 1.

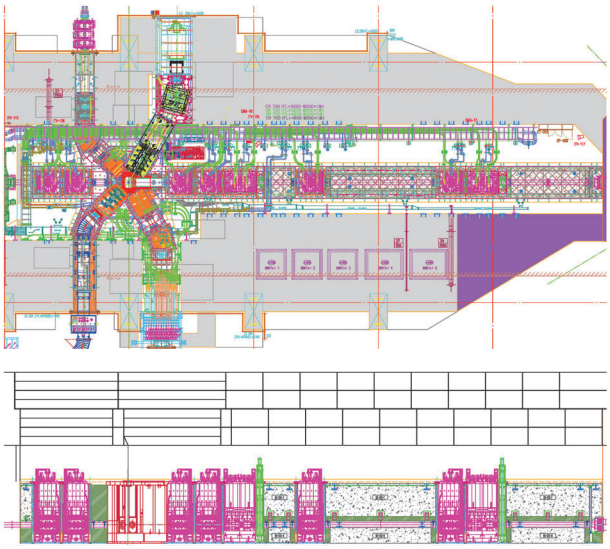

Figure 1. The horizontal (upper) and the vertical sectional view (lower) of the M2 tunnel. The proton beam is transported from the left to the right side of the neutron target through it.

In the M2 tunnel, eight magnets were installed to transport the proton beam: six quadrupole magnets and two pairs of horizontal and vertical steering magnets. All of them were fabricated under the design framework shown in Fig. 2. The materials adopted in these magnets were selected according to the simulated result of the absorbed dose shown in Fig. 3. As of the insulator of the coil, there were two options: use of mineral insulation cable (MIC) or polyimide impregnated (PI) coil [2]. A MIC has a MgO insulation layer and an outer copper sheath in addition to a central conductor part. The radiation hardness of MgO is much higher than that of an organic insulator like polyimide resin. However, MgO is fragile, so the MgO layer must be surrounded by the copper sheath. Many MIC magnets were adopted in J-PARC.

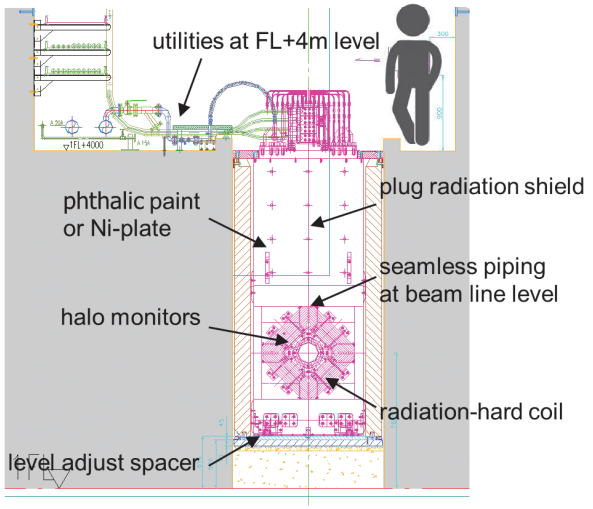

Figure 2. The cross-sectional view of the conceptual design framework of a magnet placed in the M2 tunnel.

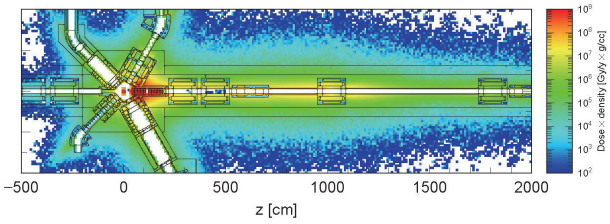

Figure 3. A typical simulated result of the distribution of the absorbed dose in the M2 tunnel for a 1-MW 40-year operation.

Due to the difference in the ampacity between a MIC and a PI coil, different power supplier and cable to the magnet are used in each case. Their initial costs were also different. Thus, either MIC or PI was carefully selected according to the experience in KEK-PS. If the absorbed dose around the coil was expected to exceed 400 MGy for a 1-MW 40-year operation, MIC was selected, as shown in Table 1. It was possible to adopt PI in the magnets of the upstream of the muon target, QM1 and QM2, and in most of the downstream, QN4 and XY23.

Just after the Great East Japan Earthquake in 2011, while checking the soundness of the devices, unexpected high activation was accidentally found in most of the downstream of the M2 tunnel around M23, which is the profile monitor located just beside XY23. The dose from the residual activity was much higher than expected. This was explained by beam loss higher than its design value due to two reasons: (1) enlarging the beam profile to suppress the pitting damage on the wall of the neutron target vessel, and (2) an underestimation of the

Table 1. The accumulated dose in some magnets for a 1-MW 40-year operation. They were averaged over the volume of each part, and the practical selection of either MIC or PI was done by referencing the detailed distribution.

MGy/40y	yoke	coil	pole/duct	insulator
QM2	0.1	0.7	10.1	PI
QN2	21.3	65.7	2574.9	MIC
X22	202.5	414.7	349.3	MIC
X23	4.4	15.1	19.5	PI
SQ1	75.8	207.8	114.2	MIC
DQ1	271.1	900.4	559.8	MIC
DB1	0.4	2.2	2.0	PI

small-angle scattering of protons by the muon target in the simulation code. In response to this, an ad-hoc review meeting was called to discuss the possibility of the insulation breakdown in the downstream PI magnets and to plan appropriate countermeasures.

The beam loss around M23 was estimated to be about 0.08 W/m, which was deduced from the observed dose rate of 70 mSv/h at a distance of 1 cm from the surface, applying the empirical formula [3,4]: $D = 3.4 \times 10^{-4} P \log_{10}((T + t)/t)$, where D is the dose rate at 40 cm, P is the beam loss rate in a unit of W/m, $T =$ 1 week and $t = 4$ hours are the operation and cooling times, respectively. Assuming that a loss rate of about 0.1 W/m is kept for 40 years (5000 hour op./year), the absorbed dose will be below 1 MGy, applying the empirical proportionality of the absorbed dose; $D_a = 12 \times 10^{-3} P$ [3]. The estimated value is much lower than the allowable limit of PI, 400 MGy. This low loss rate was achieved by introducing octupole magnets in the upstream of the M2 tunnel, by which the outer side of the beam envelope is folded to the inner side. The octupole magnets were introduced to reduce the heat generation in the outer edge of the neutron target vessel, but they were also useful to suppress the beam loss in the M2 tunnel. The octupole magnets were put into use before May 2013, and by November 2015, the loss rate was reduced to 0.02 W/m. The beam loss rate is determined by the observed dose rate, and thus the loss rate involves the operation history. While the proton beam intensity increased from 300 kW in May 2013 to 500 kW in November 2015, the loss was successfully suppressed and controlled. The beam loss is monitored by the loss monitor, a wire chamber, mounted on M23. In addition, dosimetry is regularly performed on the accelerator maintenance day by inserting a budge through a gap between magnets to the beamline level, 2.4 m downwards from the utility service floor of the M2 tunnel, to measure the dose from the magnet body. The result shown in Fig. 4 proves that the beam loss is well controlled. With the upcoming increase of the proton beam intensity, the regular check becomes more important to keep the beam loss low.

Figure 4. The result of the regular dosimetry for the devices in the downstream of the M2 tunnel.

At present, the possibility of a serious problem in a PI magnet and the necessity of replacement is quite small. Thus, it is thought that the preparation of a standby PI magnet is not urgent. A standby MIC magnet was fabricated in 2013JFY. This one can be replaced with QN4, but not with QM1 and 2 due to the difference in the power supplier. Also, a steering magnet does not have any standby. In the future, a standby magnet should be prepared sequentially.

References

[1] N. Kawamura *et al.* 2009 *Nucl. Inst. and Meth. A* **600** 114.
[2] K.H. Tanaka *et al.* 2008 *IEEE Transactions on Applied Superconductivity* **18** 244.
[3] CERN PS 87-3, "Kaon Factories seen from the CERN PS"
[4] OHO 97, "固定損失の評価"

N. Kawamura[1,2], S. Meigo[3], S. Makimura[1,2], and S. Matoba[1,2]
[1]*Muon Science Section, Materials and Life Science Division, J-PARC Center;* [2]*Institute of Materials Structure Science, KEK;* [3]*Neutron Source Section, Materials and Life Science Division, J-PARC Center*

Current Status of μSR Set Up at D1

At the D-line, muons are kicked out by using the magnetic kicker and delivered to the D1 and/or the D2 area. Here we report the current status of the D1 area.

At the D1-area, a μSR spectrometer is installed as the key instrument. Since high-momentum muons, up to 100 MeV/c, surface muons, and negatively charged muons can be delivered at D1, it is possible to perform any type of μSR measurement, except for ultra-slow μSR. For example, μSR under high pressure can be carried out only at D1.

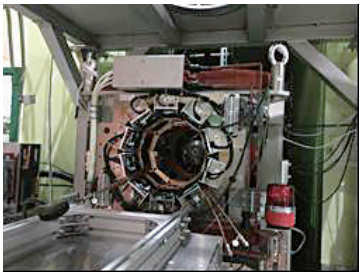

Figure 1. μSR spectrometer at D1.

• Beam profile

Figure 2 shows one example of the profile of surface muon beam at the sample position, which was measured in the air. For most of the μSR, this beam tuning is used.

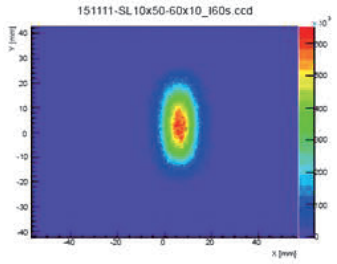

Figure 2. Example of the profile of the surface muon beam.

• Cryogenics and furnace

Temperature control is an important factor for μSR measurements, so several kinds of refrigerators are available to maintain it. The lowest temperature (~80 mK), is obtained by using the top-loading dilution refrigerator. In our top-loading DR, a sample can be changed by unloading or loading just the sample holder. This feature is quite useful for the μSR experiment. Furthermore, the cooling system of the DR is based on a pulse-tube type refrigerator and liquid Helium is not required at all to cool down the system.

Recently, we have been developing a low background sample holder for small sample in DR. An example is shown in Fig. 3. The holder is 10-mm pure silver and the muons, which do not hit the sample holder, fly away.

"Minicryo" is a useful cryostat to cool down quickly to ~4 K within an hour. In most of measurements, a "fly-past chamber" is used to obtain a better S/N ratio. For example, by using a thin-foil sample holder (Ag10-20 μm) and fly-past chamber, 15-20% of asymmetry can be achieved in a 5×5 mm^2 sample.

For high-temperature measurements, up to 800 K, an infrared furnace is available.

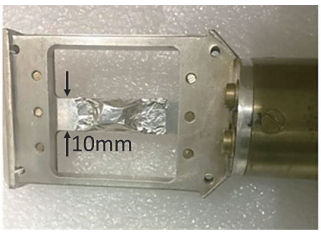

Figure 3. Example of a low background DR holder (10 mm).

• Magnets

Magnetic fields of 3.8 kG and 120 G, respectively, can be applied along the beam direction and perpendicularly to it. A micro transverse coil ("μTC"), designed for the S1 spectrometer and able to apply up to 250 G, is also available for TF μSR measurement.

For precise zero-field measurements, an active zero-field correction system is being applied now. In this system, the magnetic fields are monitored not at the sample position, but near the center of the spectrometer and a feedback system is used.

• Detector and DAQ

"Iroha", developed at MLF, is used as a slow control system,. All μSR systems, including DAQ, can be controlled through it. Auto run sequence is also available from Iroha.

"Kalliope" is now stably used for electron/positron detectors.

The μSR system is still developing to obtain better beam and sample environment. Any contribution is welcome.

W. Higemoto[1,2,3] and A. Koda[2,4]

[1]Advanced Science Research Center, Japan Atomic Energy Agency; [2]Muon Science Section, Materials and Life Science Division, J-PARC Center; [3]Department of Physics, Tokyo Institute of Technology; [4]Institute of Materials Structure Science, KEK

Status of the D Line (D2 Area) Commissioning

During the summer shutdown period in FY2015, a new solenoid was installed into an existing beam line. This solenoid is a warm-bore type and requires no foils for protection from thermal radiation. The inner radius of the coils was increased from 12 to 20 cm. Thus, a drastic improvement of the muon intensity is expected. In FY2016, two new experimental tools were prepared to determine this low-energy decay muon: a new type of beam profile monitor and an automatic optimization program for beam line components, such as magnetic bends and quadrupoles (named FORTUNE).

In FY2017, the momentum narrowing was achieved by slit slicing a horizontally dispersed beam after passing through bending magnets of beam transport optics. For this purpose, we used two slits for limiting beam passing. In the first slit, which is next to DQ6, the final size of the slit opening was 240 mm horizontally and 240 mm vertically. Then, in the second slit, located next to Septum, the slit opening was 30 mm horizontally and 240 mm vertically (the full opening is 240 mm in both slits). As a result, the beam condition yields that a minimum momentum bite, $\Delta p/p$ is 1.7% as σ of Gaussian function and beam divergence with laterally 30 mm and vertically 60 mm within full width (6 σ) of 2D Gaussian, as shown in Fig. 1 at the D2 area. The muon intensity that was obtained was more than 100 times larger than with the previous solenoid setup at 5 MeV/c momentum (~120 keV in energy). Therefore, the expected intensity of the negative muon is ~3×10^3 muon/s @1 MW.

The success of beam transport with narrow momentum bites and beam divergence enabled us to install a new collimator with lead radiation shield with aluminum cover after the gate valve. The drawing and snapshot are shown in Figs. 2 and 3. The collimator has conically tapered shape along with the beam focusing envelope. The diameter of an exit-hole is 50 mm, and a Kapton foil of 50-μm thickness separates vacuum from the air. By using this apparatus, the distance of the focusing point from the gate valve was decreased to 600 mm (200 mm shorter than in the previous setup). Also, this distance provides the opportunity to place Ge detectors for measuring muonic X-rays emitted from the upstream side of target.

After these developments, we constructed a new muonic X-rays measurement chamber, which can be filled with helium gas surrounding the sample without evacuation. Therefore, now many new types of samples, such as archeological materials, art objects and so on are coming into our research scope.

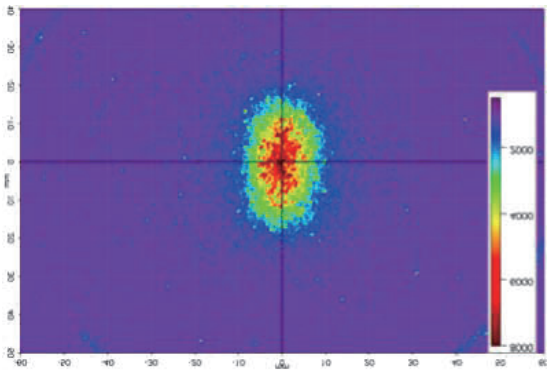

Figure 1. Beam profile at the D2 area focusing point.

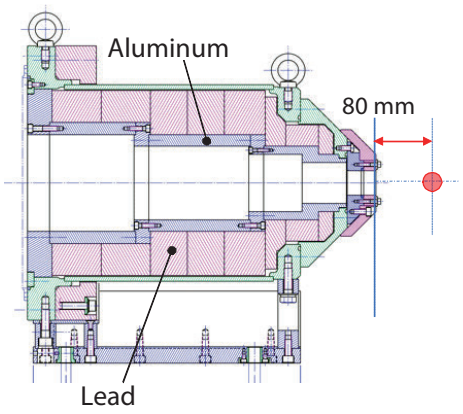

Figure 2. Drawing of the collimator.

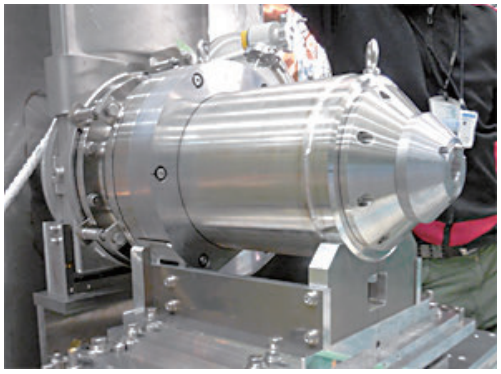

Figure 3. Snapshot of the collimator.

M. Tampo[1], K. Hamada[1,2], S. Doiuchi[1,2], S. Takeshita[1,2], K. Shimomura[1,2], and Y. Miyake[1,2]
[1]*Institute of Materials Structure Science, KEK;* [2]*Muon Science Section, Materials and Life Science Division, J-PARC Center*

Ultra-Slow Muon Beam Commissioning

We observed muon spin rotation spectrum for a silver plate sample, by using an ultra-slow muon beam in J-PARC. In 2016, we confirmed for the first time the generation of an ultra-slow muon in J-PARC. Since then, the beam commissioning of the ultra-slow muon continued in order to obtain high intensity and small size ultra-slow muon beam. Figure 1 shows an ultra-slow muon setup in the Material and Life Science Experimental Facility (MLF), J-PARC. Ultra-slow muons generated in the vicinity of the tungsten (W) target are accelerated by electrostatic lenses and transported to the μSR spectrometer using a series of electrostatic quadrupole lenses, bends and a magnetic bend. The generation method of ultra-slow muon is described in detail elsewhere [1].

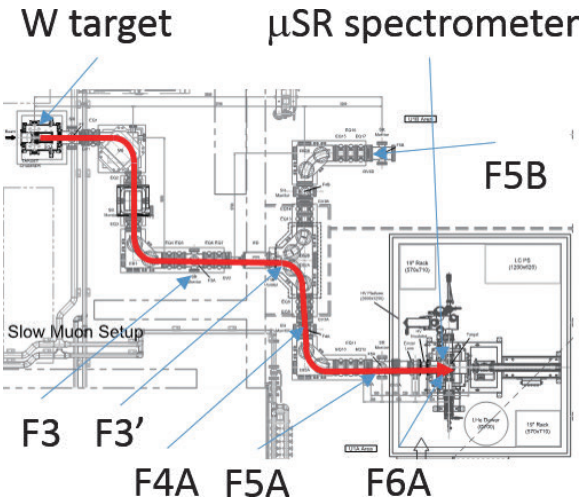

Figure 1. Ultra-slow muon setup in MLF, J-PARC. Multichannel plate detectors for counting the number of ultra-slow muons are placed at F3, F3', F4A, F5A, F5B and F6A. The μSR spectrometer can detect decayed positrons from ultra-slow muons stopped in the sample.

The progress of the rate of ultra-slow muons at several focusing points for the period of two years, is shown in Fig. 2. The rate of the ultra-slow muon at F3 reached 73 μ^+/s and the event rate of decayed positrons from the ultra-slow muon was 42 /*s* in February 2018. Figure 3 shows the first observed transverse field μSR spectrum using a 30-keV ultra-slow muon. The sample was a silver plate with diameter of 20 mm and the transverse magnetic field was 20 Gauss. It took about three days to accumulate one million events for the spectra.

At present, we continue to perform μSR experiments varying the incident energy of the ultra-slow muon beam from 50 eV to 30 keV, using as a sample a silver layer with thickness of 50 nm on silicon dioxide, in order to confirm the validity of the ultra-slow muon beam in J-PARC.

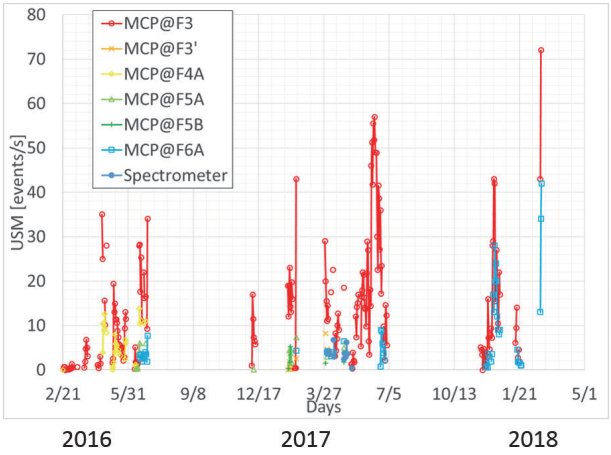

Figure 2. Progress of the event rate at the various focusing points for a period of two years.

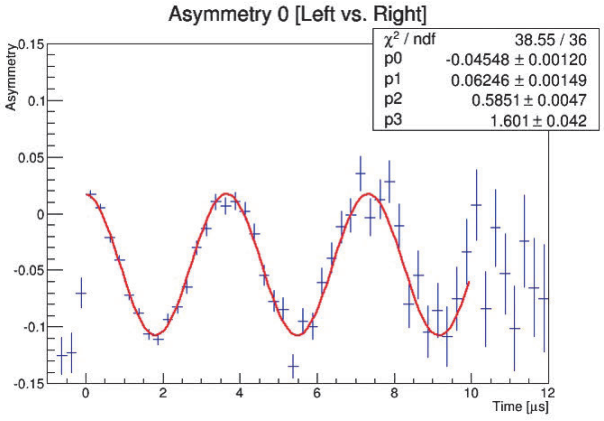

Figure 3. A μSR spectrum of the silver sample with 20-Gauss transverse field using an ultra-slow muon beam.

Reference

[1] A. D. Pant *et al.*, JPS Conf. Proc. **21** (2018) 011060.

T. Adachi[1,2], A.D. Pant[1,2], and Y. Ikedo[1,2]

[1]*Muon Science Section, Materials and Life Science Division, J-PARC Center;* [2]*Institute of Materials Structure Science, KEK*

Completion of ARTEMIS spectrometer at S1 experimental area

1. Introduction

S1 experimental area, located in experimental hall No. 1 of MLF, delivers the conventional 30 MeV/c momentum muon beam, called the surface muon. With funds from the external budget of Element Strategy of Tokyo Institute of Technology, we have built a general-purpose spectrometer named ARTEMIS, (Advanced Research Targeted Experimental Muon Instruments at S-line) that has been described in the preceding MLF annual reports and elsewhere [1-3]. The quality of the spectrometer generally depends not only on the physical design parameters and reliability, but also on the ease of operations performed by the external users who may not have knowledge about hardware. The first goal of the spectrometer construction is to set up a system, which can be operated by such users; ARTEMIS has reached that level in fiscal year 2017.

Another factor to be considered in spectrometer construction is the continuous increase of the beam power. Starting in January 2018, the beam power reached 400 kW, almost half of the design maximum intensity of MLF. The corresponding count rate of positron events became over 400 Mevents/hour (if all the slits are wide open), yielding more than three positron counts per channel per frame (400 Mevents/h = 400 M /1280/3600/25 events/ch/frame = 3.47 events/ch/frame) within the muon life time. The transient properties of the electronics have to be well-behaving to handle this high rate without signal distortion.

As the accelerator power increases, the proton beam tends to be double pulsed, separated by 600 nano seconds, in order to operate the machine without too much heat load or radiation damages. To avoid the overlap of muons from the double pulse structure, an electric kicker is installed in the S-line, so that the second muon pulse originating from the second proton pulse is kicked out of the beamline or sent to other branches of the beamline. In FY2017, the kicker system was in operational to the user experiments, if required, because of the double pulse operation of the accelerator. The result of the operation is explained later in more detail.

2. IROHA2 façades for ARTEMIS and D1

IROHA2, the framework system controlling all the sample environment devices and data acquisition (DAQ) software, has a sequence server, which is the interface between the experimentalist and the IROHA2 system to run automatically a sequence of measurements. The experimentalist chooses a façade (a preset procedure to perform a certain function in Python script) from the list on the IROHA sequence web browser to construct the sequence of measurements. The original IROHA2 system developed by the MLF computer environment team has very basic façades, such as starting/stopping DAQ or setting the target temperature and other parameters on the standard temperature controller (Lakeshore 350) used in MLF.

Table 1. muon version of IROHA2 façades.

Façade	Function
START	Start the run, wait for the preset statistics, and stop the run if achieved*.
STOP	Wait for the preset statistics and stop the run if achieved*.
SET_Temperature	Set the target temperatures and wait for the time and tolerance used in the WAIT_Temperature command.
WAIT_Temperature	Wait until the tolerance is satisfied for the preset wait time.
SET_HeaterRange	Set the heater range of Lakeshore 350 temperature controller.
SET_PID	Set the PID parameter of Lakeshore 350 temperature controller.
SET_Flow	Set the helium flow rate controlled by MKS RP4000B.
SET_Magnet	Set the magnetic field at the sample position.
SET_vectorH	Set the magnetic field at the sample position in vector field mode.
SET_ZFFB	Set on/off the active zero-field feedback system.
SET_Rod	Set position and angle of the sample rod.
TITLE_x	Set the field x of the run title.
DEFVAR_x	Set the variable in x (=integer, float and string) format for looping.

* In the background, automatic histogram generation and database registration is performed.

Before moving to the IROHA2 framework system, which is the standard of MLF, the muon spin relaxation (μSR) spectrometers at MLF (ARTEMIS and D1 spectrometer) had been controlled by a LabVIEW macro (RODEM), which works as the autorun controller. For this hand-made system, we developed a reporting system of accumulated statistics from DAQ and an automatic histogram generator from the list-mode data, as well as a database registration system of run titles and experimental conditions. In order to incorporate it with the existing automated systems, we developed a series of muon extension of IROHA2 façades. In Table 1, I summarized the new commands in the IROHA2 sequence.

3. Experimental monitor and histogram viewer with user login access control

Monitoring the ongoing experiments from public internet outside of the facility is one of the key features, with which the user facilities must be equipped. The life quality of the visiting experimentalists improves and the supervision of the experiments by the collaborating local staff becomes easier with the external monitoring system installed. At the same time, the protection of the privacy of the experiment from the general public has to be guaranteed. The solution is a user login to the monitoring website: the login id is distributed to each experimental number so that only the related experimental data may be visible. We completed the external monitoring system and histogram viewer with user login access controls. The entire system (detector, DAQ, monitoring system, automatic histogram converter and database registration system) has been used in the course of beam power increase and performed successfully up to the 400-kW operation.

4. Muon Kicker performance

The S-Line kicker is an electric beam kicker, consisting of bi-polar power supplies generating pulsed high-voltage of ±54 kV by using MOS-FET to switch charging/discharging of the high-voltage circuits. If the users want to utilize both of the double-pulsed muon beams, a switch yard magnet, which is a static component equipped with the S-Line kicker chamber, is used to deliver the muon beam to the S1 area. Since resuming the beam operation in 2017 running the primary proton beam power of 150 kW, the served beam was single-bunched. Therefore, the S-Line kicker was in a stand-by state. However, the accelerator team decided to operate in double-bunched mode for one week in March 2018 to reduce the radiation loss problem. It was the first time to turn on the kicker in the user beamtime.

Unfortunately, the kicker failed after running for only 3 days due to a malfunction of the high-voltage circuit. The recovery from the failure was relatively easy, because all the MOS-FET units are designed equivalent regardless of the polarity; the bipolar high-voltage, which drives the kicker, is generated by connecting the high-voltage taps of the pulsed transformers by the MOS-FET of the same design. To recover from the failure, only one of the high-voltage units was to be replaced. Since we do not have the S2 area yet, we replaced the faulty unit for S1 with the one used in the S2 area with opposite polarity of the high-voltage. Since the power supply is placed in the beamline, we had to wait for the maintenance day in order to remove the concrete shields. The replacement of the power supplies was completed in one hour. Thus, the half-day maintenance was enough to fix the failure.

Another issue, raised during the operational running of the kicker system, was the positron contamination. We found out that positrons have a kicked trajectory with a much smaller angle than that for muons of the same momentum. Since most of the beamline components select momentum, the beamline is tuned to the momentum p. The corresponding kinetic energy $E \sim p^2/2m$ or velocity $v \sim p/m$ becomes much larger for the positrons because of the 1/200 times lighter mass. Since the electrostatic kicker is the device to kick the particle traveling along the electrode during its travel time, the kicking of positrons may be more difficult than that of muons. Although most of the positrons are discriminated by the Wien filter, the so-called DC separator, remnant positrons with a momentum of the beamline can reach the experimental area.

We have found that the prompt positrons are seen in the spectrum, even if the beam kicker is triggered,

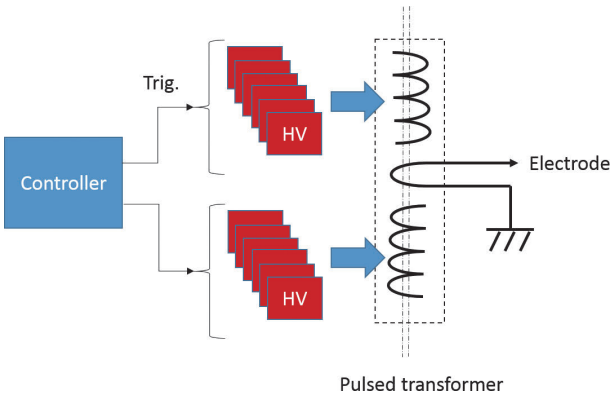

Figure1. Schematic drawing of the S-line electric kicker system. HV represents a high-voltage power supply.

suggesting that the beam profile of the positrons is considerably spread at the inlet of the septum magnet. This may cause a serious problem when utilizing the first muon pulse; the prompt positron of the second pulse may appear at around 600 ns after the muon timing of the first pulse. Since we do not have the S2 area, the second muon pulse is currently used for the S1 experiment, if the single-pulsed muon beam is required. However, we may need to improve the positron contamination before we utilize the beam branch at the other side, S2. We plan to increase the high voltage of the DC separator, in order to eliminate the positrons more effectively.

References

[1] *MLF annual report* 2014, p.136-137; 2015, p. 132-133; 2016, p.143-144.

[2] K.M. Kojima, *et al., JPS Conf. Proc.,* **21**, 011062 (1–6), (2018).

[3] K. M. Kojima, *et al., J. Phys: Conf. Ser.,* **551**, 012063, (2014).

K.M. Kojima[1,2], A. Koda[1,2], M. Hiraishi[1,2], H. Okabe[1,2], S. Takeshita[1,2], H. Lee[1,2], P. Strasser[1,2], Y. Irie[1,2], and R. Kadono[1,2]

[1]*Muon Science Section, Materials and Life Science Division, J-PARC Center;* [2]*Institute of Materials Structure Science, KEK*

H-Line Construction – Recent Progress

A new beam line, named H-line [1], is being constructed in the east #1 experimental hall of the MLF. The H-line is planned to be used for various experiments, which need high statistics, *i.e.* high-intensity beams and long beamtime. These characteristics enable precise measurements, such as muon *g-2*/EDM experiment [2] and high-precision measurement of the hyperfine splitting of the ground state of muonium (MuSEUM experiment [3]), and is also best suited for rare decay search, like the DeeMe experiment [4], which searches for charged lepton flavor violation (cLFV) using muonic atoms.

In order to deliver a high-intensity beam to experimental areas, the H-line has a large capture solenoid (HS1). It is located 600 mm from the muon production target and its acceptance is 108 mSr. Coils of HS1 are wound with radiation-resistant mineral insulation cables (MIC) [5]. Because MIC is a normal conducting wire, HS1 needs powerful electricity (~ 1 MW). Other beamline components, such as bending magnets (HB1, HB2), transportation solenoids (HS2, HS3), and focusing quadrupole triplet (HQ1-3) also have large aperture for efficient muon transportation. Figure 1 is a layout drawing of the H-line (1st phase).

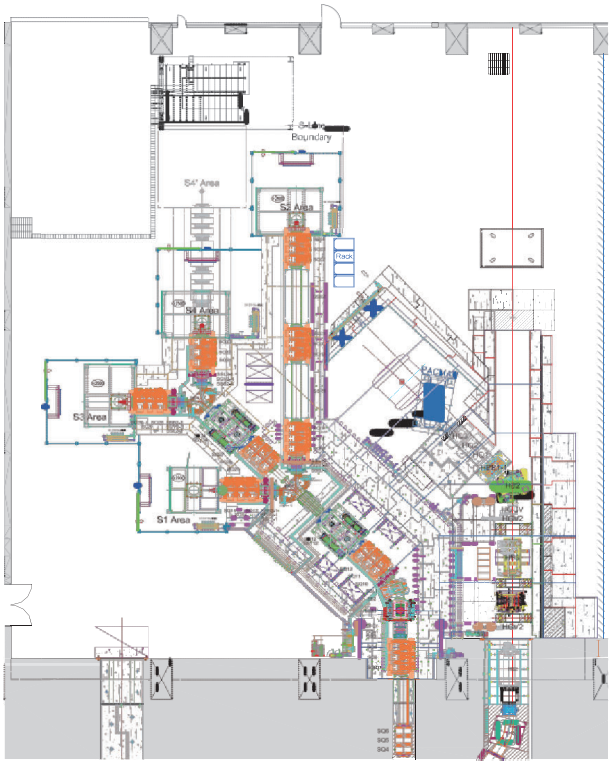

Figure 1. A layout plan of experimental hall #1 in the first phase of the H-line construction.

The frontend apparatuses of the H-line (HS1, HB1, HGV1) were installed during the summer shutdown in 2012 and 2014. In 2016, all radiation shields until the first branch of the H-line, H1 area, were placed. A beam blocker (HBB1) was also installed. With the beam blocker inserted, the dose rate inside the H1 area is expected to be about 10 μSv/h, even when the beam is on.

The construction of a new electric power sub-station for the H-line is one of the most significant recent advancements. The capacity of the electric sub-station is about 5 MW, which is necessary to operate the H-line. The construction site is located in the northeast side of the MLF, as shown in Fig. 2.

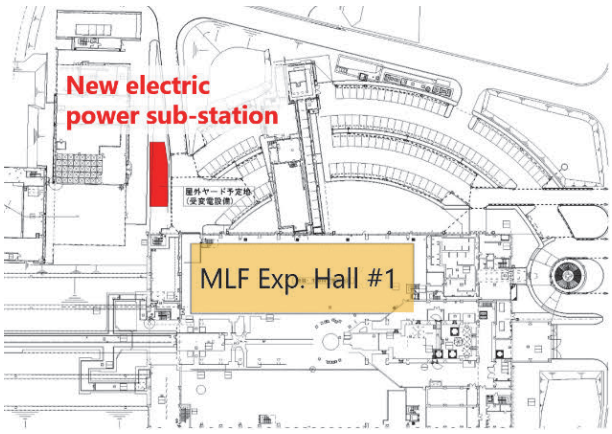

Figure 2. Construction site of a new electric power sub-station. It is located outside the MLF building.

The construction started in FY2017 and still continues. During the summer shutdown in 2017, a new hatch for electric transmission lines was completed on the MLF wall. The size of the aperture is 2 m × 1 m . Figure 3 is its picture taken during its construction period. The cabling work is scheduled after the electric sub-station is completed.

After the hatch construction, we have started building the bedding of the electric sub-station. Earth retaining work was finished successfully in FY2017. Pictures taken before and after the construction work in FY2017 are shown in Fig. 4.

The platform of the new electric sub-station will be completed in 2018. In addition, the cabling work of the high-voltage lines is also scheduled for 2018.

Figure 3. Aperture for electric transmission lines. It is located above the carry-in entrance of the east #1 experimental hall of the MLF.

Figure 4. Recent progress of the construction of the electric power sub-station.

References

[1] N. Kawamura, *et al.*, J. Phys.: Conf. Ser. **408**, 012072 (2013).
[2] T. Mibe, *et al.*, Chin. Phys. C **34**, 745 (2010).
[3] K. Shimomura, AIP conf. proc. **1382**, 245 (2011).
[4] H. Natori, *et al.*, Nucl. Phys. B (Proc. Suppl.) **248-250**, 52 (2014).
[5] H. Fujimori, *et al.*, Nucl. Instrum. Methods Phys. Res. Sect. A **600**, 114 (2009).

T. Yamazaki[1,2] and N. Kawamura[1,2]
[1]Muon Science Section, Materials and Life Science Division, J-PARC Center; [2]Muon Science Laboratory, High-Energy Accelerator Research Organization (KEK-IMSS)

MLF Safety

Research Safety

1. Radiation safety

(Operation of the "Low-surface contamination area" at the MLF Experimental halls)

The low-surface contamination area has been adopted at the MLF Experimental halls from November 2016. The purpose is to avoid surface-contamination problems caused by a sample, an environmental atmosphere and so on, and to expand the flexibility of the experiments conducted at MLF. Consequently, many experiments using gaseous and liquid samples were conducted at the MLF experimental halls. During the operation of the low-surface contamination area, there was no critical problem. However, the monitor for take-out articles, installed in 2016, sometimes had troubles due to damage of the light shielding sheets. One monitor for large-size take-out articles was additionally installed in order to increase the usability for users. During the summer maintenance period in 2017, a temporary classification change from the low-surface contamination area to second class radiation-controlled area at the MLF Experimental halls was carried out for the first time to make the maintenance work on the instruments easier.

(Radiological License Upgrade)

The application for radiological license up-grades in FY2017 was approved on February 26, 2018.

The following items were updated on February 26, 2018:

(1) Addition of usage purposes of the radiation generator licensing

Materials science, neutrino experiment, elementary physics, particle physics and nuclear physics were added to the usage purpose.

(2) Addition of RAM building

The RAM building (Radio-Activated Materials building) has a storage area for radio-activated materials produced by the radiation generator and supplements the storage area in the MLF building. The storage area for radio-activated materials in the RAM building has 5 large underground pits and can be operated as a first class radiation-controlled area.

2. Chemical safety

As usual, routine chemical safety checks of user-brought chemical materials, such as specimen and reagents, were performed by the chemical-safety team to evaluate their toxicity and the stability of their actual physical state-powder, solid, liquid or gas. After checking, the individual beamline staffs confirmed or rejected the usability of the actual materials. As a result, the experiments were performed without serious troubles. Figure 1 shows a trend for the number of chemical materials subjected to safety check. As of the form of the sample, solid was used most frequently, then powder, liquid, and gas. From the viewpoint of organic or in-organic matter, inorganic matter was used more frequently. In 2017, the total number of chemical materials to go through chemical safety check was increased, and, as a result, 8045 chemical materials were brought to MLF, which was a 25% increase compared with the last year.

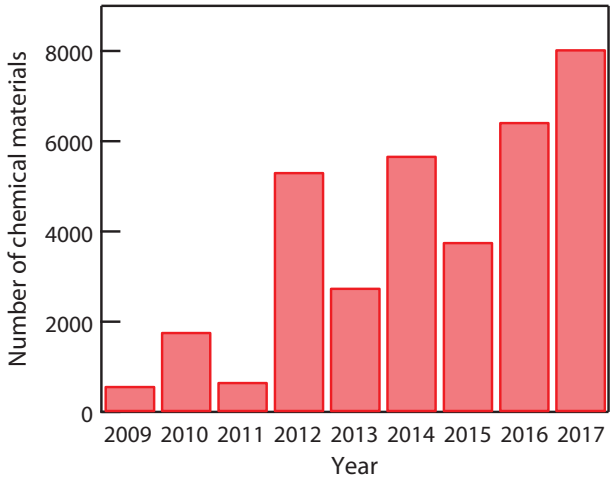

Figure 1. Trend of chemical materials undergoing chemical safety check.

3. Unattended operation of the cryo-furnace

When conducting high-temperature experiments, the users have the obligation to monitor the status of the furnace at the beamline. To reduce that workload, the sample environment team and the instrument safety team considered introducing an unattended operation. As a result, the unattended operation of the high-temperature experiment was first applied to the cryo-furnace, if the following conditions were met:

1) Passed safety check by the instrument safety team.
2) Maximum temperature is less than 800 K.
3) Heater output is less than 400 W.
4) Interlock system in case of temperature abnormality is available.
   Heater stops automatically when the maximum temperature is exceeded, without automatic return.
5) No fire spreading by the multiple holder into which heater is placed.

Table 1. List of unattended operation cryo-furnace.

BL	Type	Temperature range (K)	Heater output (W)	Sensor
BL01	Top loading	4 ~ 600	100, 150	Rhodium iron
BL02	Top loading	15 ~ 680	50	platinum
BL09	Top loading	10 ~ 800	100	K type thermocouple
BL14	Top loading	5 ~ 550	100	platinum
BL20	Bottom loading	4 ~ 600	70	Platinum, N type thermocouple
BL20	Auto sample changer	4 ~ 800	150	platinum
BL21	Auto sample changer	20 ~ 500	75, 130	platinum
BL21	Top loading	5 ~ 500	75	platinum
SE	Top loading	5 ~ 700	240, 50	Platinum, silicon

6) Monitoring of the signal light of the alarm indication system in the monitoring room.

Table 1 show the list of cryo-furnace which is achieved unattended operation now.

4. Crane safety

Three cranes were used safely in experimental hall No.1 and experimental hall No.2, which has an ex-tension building. These cranes are used mostly to change the experimental setup during beam time and to perform summer maintenance by the technical staffs. They were also used in construction works to install new devices after August. Figure 2 shows the statistics of the total crane usage in both experimental halls as a function of every month. The cranes were used 207 times in total. The total use slightly decreased compared with the last year.

The statistics for 2017 indicated high use in October due to the summer maintenance completion.

As usual, the crane safety team checked monthly the mechanical sling, lifting sling, etc. and replaced the old ones with new ones when necessary. Furthermore, a crane operator, who wants to use the cranes in the experimental halls, needs to attend hands-on training by the crane safety team staff before the actual operation. As a result, there were no serious troubles with the crane operations.

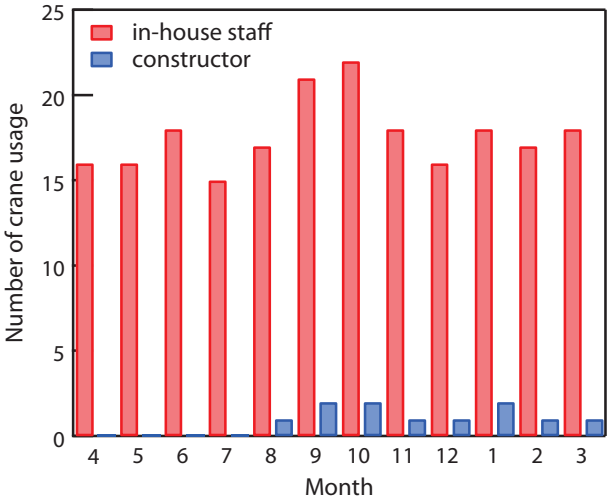

Figure 2. Trend of the total crane usage in one year.

M. Harada[1], M. Ooi[1], M. Sekijima[1], K. Kawakami[2], K. Aizawa[2], A. Hori[2], H. Tanaka[2], W. Kambara[2], M. Sawabe[2], K. Suzuya[3], N. Kawamura[4], Y. Sakaguchi[5], R. Takahashi[2], Y. Yamaguchi[5], and K. Soyama[6]

[1]Neutron Source Section, Materials and Life Science Division, J-PARC Center; [2]Technology Development Section, Materials and Life Science Division, J-PARC Center; [3]Neutron Science Section, Materials and Life Science Division, J-PARC Center; [4]Muon Science Section, Materials and Life Science Division, J-PARC Center; [5]Neutron Science and Technology Center, CROSS; [6]Materials and Life Science Division

MLF Operations in 2017

Beam Operation Status at MLF

In Japanese Fiscal Year (JFY) 2017, the beam operation at the MLF started on April 1, 2017, with a beam power of 150 kW and ended on April 2, 2018. Table 1 shows the scheduled time and availability in JFY 2017. In the schedule, 2017A switched to 2017B on November 16. Since Target #2, which was replaced in the summer of 2016, did not have the helium bubbler to mitigate cavitation erosion at the target vessel, the beam power had to be lower than 200 kW. In JFY 2017, the beam power had been maintained as low as 150 kW from April 1 to the end of June. After the target was replaced by Target #8 with helium bubbler in the summer of 2017, the beam power was gradually increased from 300 kW to 400 kW. The beam operation with a single-bunch beam continued up to 400-kW beam operation. Due to the RF condition in the RCS, the beam is delivered to the target in two bunches with separation time of about 600 ns for beam power larger than 500 kW, which will start in the next fiscal year.

Since no significant failures occurred in JFY 2017, the achieved average availability was as high as 92%. In the past, a relatively long beam shutdown period was required to complete the purification of the cryogenic system for the neutron moderator. In the summer of 2016, the impurities in the loop of the cryogenic system had been removed entirely; after that, the periodical purification is not required. Thus, a long uninterrupted work period of 4,179 h was attained in JFY 2017.

The beam operation was stopped on several occasions due to minor failures described below. Malfunctions related to the Personnel Protection System (PPS) at BL04 occurred on May 15. The pump or the helium bubbler in the mercury loop failed on December 1. On January 16, the beam operation was stopped due to flow decrease of the cooling water for the LINAC.

Table 1. Run cycle, scheduled time and availability.

Run	Duration	Scheduled time (h)	Beam time (h)	Availability (%)
74	Apr 1 – Apr 19	403	385.3	95.6
75	Apr 26 – Jun 29	1224	1135.1	92.7
76	Oct 2 – Nov 15	504	454.5	90.2
77	Nov 16 – Dec 23	765	698.0	91.2
78	Jan 10 – Apr 2	1642	1506.5	91.8
2017A	Apr 1 – Nov 15	2131	1974.9	92.7
2017B	Nov 16 – Apr 2	2493	2287.6	91.8
Overall		4538	4179.4	92.1

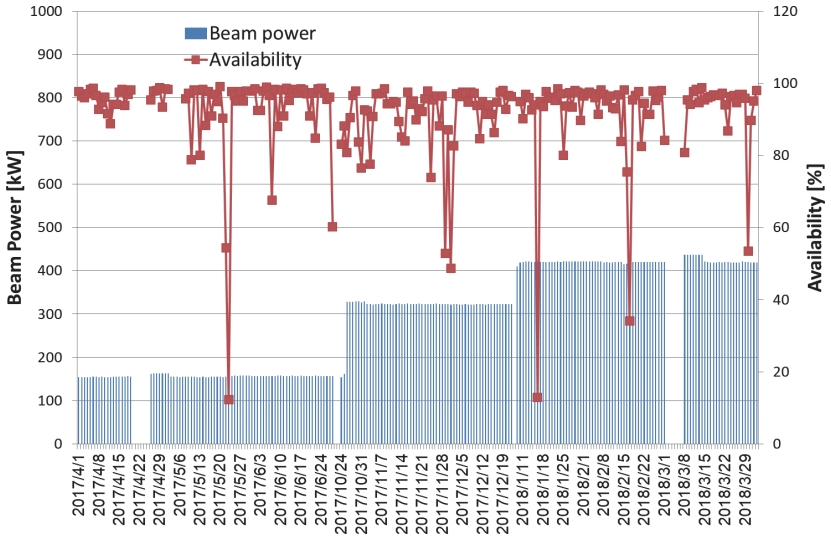

Figure 1. Beam power trend (blue line) at the MLF and availability per day (red line).

Users at the MLF

In fiscal year (FY) 2017, the initial beam power of 150 kW was increased to 300 kW after the summer maintenance period, and again to 400 kW from January 2018. Due to the high beam power and stable operation throughout the year, the number of users grew to the highest number to date. In particular, the number of foreign users of the neutron and muon experimental facilities in FY 2017 was almost twice that of FY 2016.

The trend for the number of users at the MLF since the start of the operations in FY 2008 is summarized in Table 1 and Fig. 1.

Table 1. The number of domestic and foreign users by fiscal year.

	FY2008		FY2009		FY2010		FY2011		FY2012		FY2013	
	Domestic Users	Foreign Users	Domestic Users	Foreign Users	Domestic Users	Foreign Users	Domestic Users	Foreign Users	Domestic Users	Foreign Users	Domestic Users	Foreign Users
Neutron	107		317		476		259		708		449	
	95	12	303	14	432	44	238	21	628	80	399	50
Muon	18		40		50		23		56		61	
	18	0	38	2	42	8	21	2	46	10	50	11

	FY2014		FY2015		FY2016		FY2017	
	Domestic Users	Foreign Users	Domestic Users	Foreign Users	Domestic Users	Foreign Users	Domestic Users	Foreign Users
Neutron	824		559		852		927	
	711	113	476	83	744	108	742	185
Muon	91		69		99		179	
	78	13	59	10	83	16	149	30

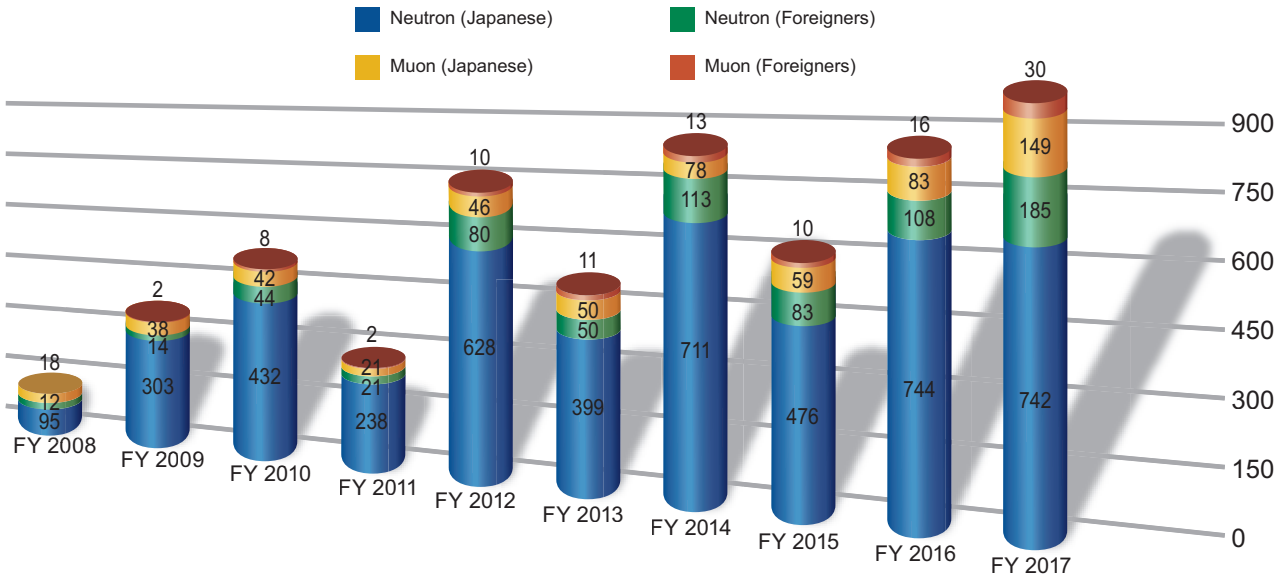

Figure 1. The number of domestic and foreign users by fiscal year.

MLF Proposals Summary – FY2017

Table 1. Breakdown of Proposals Numbers for the 2017 Rounds.

Beam-line	Instrument		2017A		2017B		Full Year					
			Submitted	Approved	Submitted	Approved	Submitted			Approved		
			GU	GU	GU	GU	PU/S	IU	ES	PU/S	IU	ES
BL01	4D-Space Access Neutron Spectrometer - ***4SEASONS***		18(0)	9(0)	19(1)	11(1)	0	1	1	0	1	1
BL02	Biomolecular Dynamics Spectrometer - ***DNA***		16(1)	13(1)	18(1)	13(1)	0	1	0	0	1	0
BL03	Ibaraki Biological Crystal Diffractometer - ***iBIX***	(100–β)‡	8	1	6	0	0	0	0	0	0	0
		(β)†	2	0	0	0	19	0	0	10	0	0
BL04	Accurate Neutron-Nucleus Reaction Measurement Instrument - ***ANNRI***		9	7	12	3	0	1	0	0	1	0
BL05	Neutron Optics and Physics - ***NOP***		6	3	2	2	0	0	0	0	0	0
BL06	Neutron Resonance Spin Echo Spectrometers - ***VIN ROSE***		0	0	0	0	0	0	0	0	0	0
BL08	Super High Resolution Powder Diffractometer - ***S-HRPD***		11	8	12	8(0)	0	0	0	0	0	0
BL09	Special Environment Neutron Power Diffractometer - ***SPICA***		0	3	0	0	0	0	0	0	0	0
BL10	Neutron Beamline for Observation and Research Use - ***NOBORU***		11	6	8	7	0	1	0	0	1	0
BL11	High-Pressure Neutron Diffractometer - ***PLANET***		8(0)	6(0)	15(0)	8	0	1	0	0	1	0
BL12	High Resolution Chopper Spectrometer - ***HRC***		12	7	9	3	1	0	0	1	0	0
BL14	Cold-neutron Disk-chopper Spectrometer - ***AMATERAS***		28	10	22	6	0	1	0	0	1	0
BL15	Small and Wide Angle Neutron Scattering Instrument - ***TAIKAN***		18(2)	17(2)	26(0)	11(0)	0	3	1	0	3	1
BL16	High-Performance Neutron Reflectometer with a horizontal Sample Geometry - ***SOFIA***		19	9	7	7	0	0	0	0	0	0
BL17	Polarized Neutron Reflectometer - ***SHARAKU***		9(1)	10(1)	20(1)	15(1)	0	1	1	0	1	1
BL18	Extreme Environment Single Crystal Neutron Diffractometer - ***SENJU***		16(0)	11(0)	22(0)	5(0)	0	2	1	0	2	1
BL19	Engineering Diffractometer - ***TAKUMI***		23	13	25	11(0)	0	1	2	0	1	2
BL20	Ibaraki Materials Design Diffractometer - ***iMATERIA***	(100–β)‡	13	6	19	4	0	0	0	0	0	0
		(β)†	44	24	20	20	18	0	0	18	0	0
BL21	High Intensity Total Diffractometer - ***NOVA***		19	17	17	7	0	0	0	0	0	0
BL22	Energy Resolved Neutron Imaging System - ***RADEN***		13(1)	11(1)	16(2)	8(2)	0	3	0	0	3	0
BL23	Polarization Analysis Neutron Spectrometer - ***POLANO***		0	0	0	0	0	0	0	0	0	0
D1	Muon Spectrometer for Materials and Life Science Experiments - ***D1***		15(1)	4(0)	15(1)	9(0)	0	1	0	0	1	0
D2	Muon Spectrometer for Basic Science Experiments - ***D2***		12(0)	7(0)	13(0)	9(0)	0	1	0	0	1	0
S1	General purpose μSR spectrometer - ***ARTEMIS***		12(1)	9(1)	14(1)	9(1)	0	1	0	0	1	0
UA	Muon U		0	0	0	0	0	1	0	0	1	0
Total			**290**	**211**	**360**	**233**	**38**	**20**	**6**	**29**	**20**	**6**

GU : General Use **PU :** Project Use or Ibaraki Pref. Project Use **S :** S-type Proposals
IU : Instrument Group Use **ES :** Element Strategy
† : Ibaraki Pref. Exclusive Use Beamtime (β = 80% in FY2017)
‡ : J-PARC Center General Use Beamtime (100–β = 20% in FY2017)
( ) : Proposal Numbers under Neu User Promotion or P-type proposals (D1,D2) in GU

Table 2. Proposals Numbers of Long Term Proposal for the 2017 Rounds.

Application FY	1st Year		2nd Year		3rd year	
	Submitted	Approved	Submitted	Approved	Submitted	Approved
2017	24	8	-	-	-	-

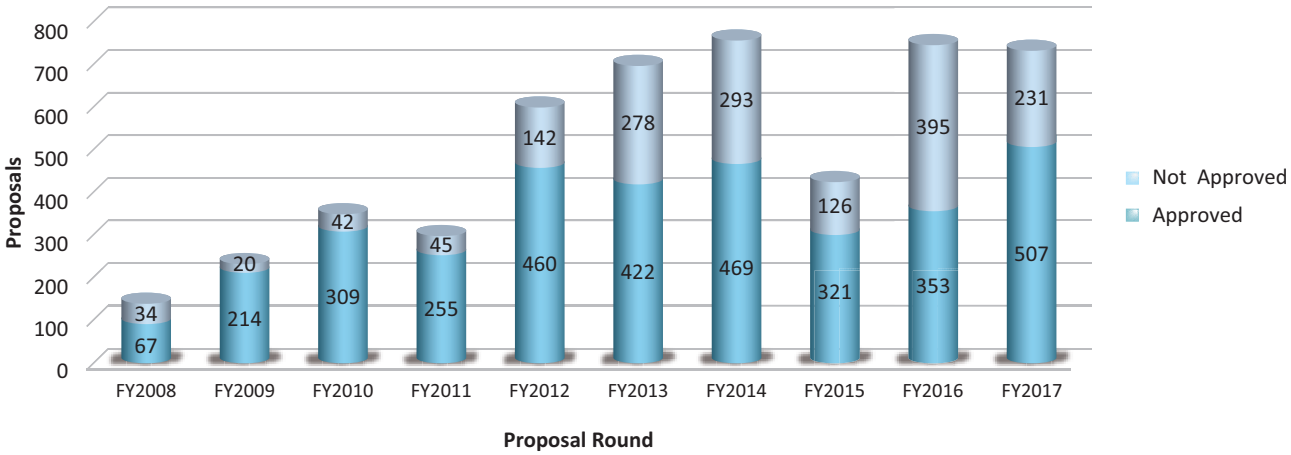

Figure 1. MLF Proposal Numbers over Time.

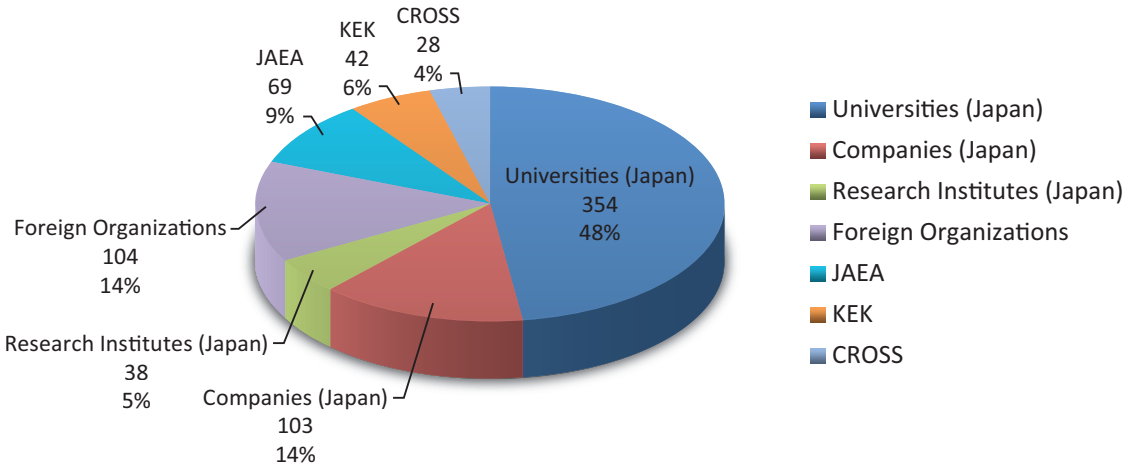

Figure 2. Origin of Submitted Proposals by affiliation - FY2017.

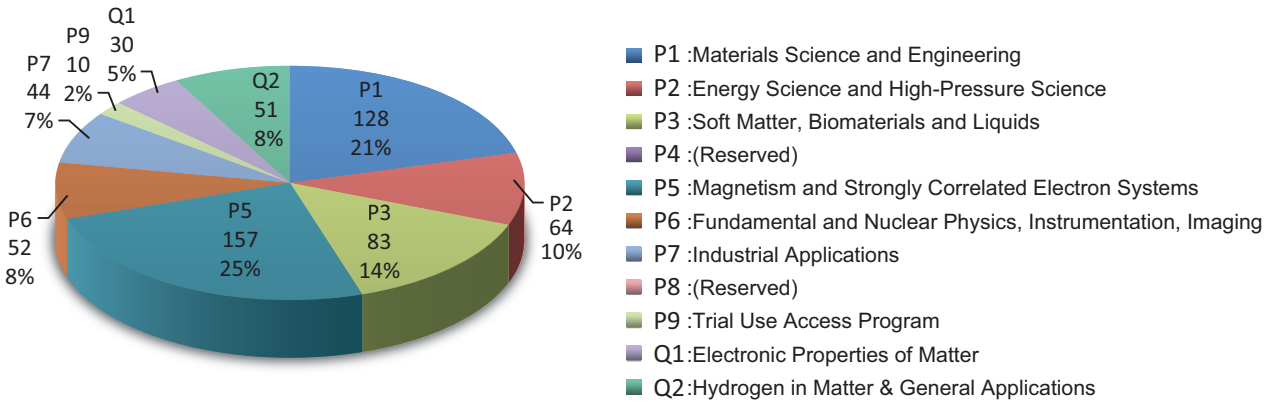

Figure 3. Submitted Proposals by Sub-committee/Expert Panel - FY2017.

MLF Division Staff 2017

Toshiji Kanaya (Head)
Hideki Seto (Deputy Head)
Kazuhiko Soyama (Deputy Head)
Izumi Kuwahara

Neutron Source Section

*: additional duties

<JAEA>

Hiroshi Takada (Leader)
Katsuhiro Haga (Sub-Leader)
Katsuhiro Aoyagi
Tomokazu Aso
Shinpei Fukuda
Wenhai Guan
Kouhei Hanano
Masahide Harada
Shoichi Hasegawa *
Miyuki Hoshino
Hidemitsu Hosokawa
Masato Ida
Tetsuya Kai *
Yoshinori Kikuchi
Hidetaka Kinoshita *
Hiroyuki Kogawa
Shin-ichiro Meigo *
Hideki Muto
Masakazu Nakamura
Takashi Naoe
Norio Narui
Masaaki Nishikawa
Motoki Ooi
Kenichi Oikawa *
Kenji Sakai
Masakazu Seki
Mitsuaki Sekijima
Motonori Takagi
Makoto Teshigawara
Hiroyuki Uehara *
Eiichi Wakai
Takashi Wakui
Akihiko Watanabe
Yoshinori Yanagida
Shizuka Yoshinari

Neutron Science Section

*: additional duties

<JAEA>

Kenji Nakajima (Leader)
Yukinobu Kawakita (Sub-Leader)
Kazuya Aizawa *
Hiroyuki Aoki
Kazuhiro Aoyama
Hideo Harada *
Masahide Harada *
Takeshi Harada
Stefanus Harjo
Takanori Hattori
Yuu Hirano *
Kousuke Hiroi
Miho Igarashi
Yasuhiro Inamura
Hirotaku Ishikawa
Hideaki Isozaki
Tetsuya Kai
Ryoichi Kajimoto
Wataru Kambara *
Kouji Kaneko *
Chiho Katagiri
Seiko Kawamura
Takuro Kawasaki
Tatsuya Kikuchi
Atsushi Kimura *
Ryoji Kiyanagi
Maiko Kofu
Kazuo Kurihara *
Bing Li
Satoshi Morooka *
Naoki Murai
Hiroshi Nakagawa *
Shoji Nakamura *
Mitsutaka Nakamura
Takashi Ohhara
Mariko Ohtake
Kenichi Oikawa
Asami Sano
Mariko Segawa *
Yoshichika Seki
Kaoru Shibata
Naoko Shimizu
Takenao Shinohara
Yuhua Su
Hiroshi Suzuki *

Kentaro Suzuya
Shinichi Takata
Tarou Tamada *
Itaru Tamura *
Katsuaki Tomoyori *
Yosuke Toh *
Wakana Ueno
Masao Watanabe *
Dai Yamazaki *

<KEK>

Shinichi Ito (Sub-Leader)
Hideki Seto
Hitoshi Endo
Takashi Honda
Kazutaka Ikeda
Takashi Ino
Takashi Kamiyama
Naokatsu Kaneko
Kenji Mishima
Fumiya Nemoto
Hidetoshi Oshita
Toshiya Otomo
Kaoru Taketani
Shuki Torii
Norifumi Yamada
Testuya Yokoo
Masao Yonemura
Masato Hagihara
Takafumi Hawai
Seiji Sugai

Technology Development Section

*: additional duties

<JAEA>

Kazuya Aizawa (Leader)
Takayuki Oku (Sub-Leader)
Takeshi Nakatani
Masao Watanabe
Chikako Doda
Wu Gong
Wataru Kambara
Kazuhiro kawakami
Masaki Sawabe
Shigekazu Inayoshi
Ryuta Takahashi
Akihiro Hori
Hiromichi Tanaka
Tomokazu Aso *
Seiko Kawamura *
Masahide Harada *
Yasuhiro Inamura *
Tetsuya Kai *
Hiroyuki Kogawa *
Mitsutaka Nakamura *
Tatsuya Nakamura *
Motoki Ooi *
Kenji Sakai *
Kaoru Sakasai *
Kentaro Suzuya *
Shinichi Takata *
Motoyasu Adachi *
Tarou Tamada *
Satoru Fujiwara *
Yu Hirano *
Tatsuhito Matsuo *
Rumi Shimizu *
Fumiaki Kono *

<KEK>

Masataka Sakaguchi
Hiroshi Fujimori *
Takashi Ino *
Naokatsu Kaneko *
Naritoshi Kawamura *
Kenji Kojima *
Shunsuke Makimura *
Setsuo Sato
Tomohiro Seya
Kaoru Taketani *
Shuki Torii *
Testuya Yokoo *

Neutron Instrumentation Section

*: additional duties

<JAEA>

Kaoru Sakasai (Leader)
Noriko Amezawa
Masumi Ebine *
Ryuji Maruyama
Tatsuya Nakamura
Kentaro Toh
Noriaki Tsutsui
Dai Yamazaki

Muon Science Section

*: additional duties

<KEK>

Ryosuke Kadono (Leader)
Naritoshi Kawamura (Sub-Leader)
Taihei Adachi
Pant Amba Datt
Hiroshi Fujimori
Koji Hamada
Masatoshi Hiraishi
Hua Li
Yutaka Ikedo
Yasuo Kobayashi
Akihiro Koda
Kenji Kojima
Shunsuke Makimura
Shiro Matoba
Yasuhiro Miyake
Junpei Nakamura
Yu Oishi
Hirotaka Okabe
Koichiro Shimomura
Patrick Strasser
Masato Tabe
Soshi Takeshita
Motonobu Tanpo
Shogo Doiuchi
Tatsuhiko Tachibana
Takayuki Yamazaki

<JAEA>

Wataru Higemoto *
Takashi Ito *

CROSS Staff 2017

Director **Hideaki Yokomizo**

Science Coordinators

Kazuhisa Kakurai
Mikio Kataoka
Makoto Hayashi
Yoshiaki Fukushima

Research & Development Division

*: additional duties

Jun-ichi Suzuki (Head)
Kenichi Funakoshi (Deputy Head)
Tsukasa Miyazaki *(Deputy Head)
Sayaka Suzuki

<BL01 Group>
Kazuya Kamazawa (Leader)
Kazuhiko Ikeuchi
Kazuki Iida

<BL02 Group>
Masato Matsuura (Leader)
Takeshi Yamada
Taiki Tominaga

<BL11 Group>
Kenichi Funakoshi *(Leader)
Jun Abe
Shinichi Machida

<BL15 Group>
Kazuki Ohishi (Leader)
Jun-ichi Suzuki *
Hiroki Iwase

<BL17 Group>
Jun-ichi Suzuki *(Leader)
Noboru Miyata (Sub-Leader)
Kazuhiro Akutsu
Takayasu Hanashima

<BL18 Group>
Akiko Nakao (Leader)
Koji Munakata
Taketo Moyoshi

<BL22 Group>
Hirotoshi Hayashida (Leader)
Joseph Don Parker
Yoshihiro Matsumoto
Shuoyuan Zhang

<Technical Support Group>
Koji Kiriyama (Leader)
Takayoshi Ito (Sub-Leader)
Yoshifumi Sakaguchi
Yukihiko Kawamura
Hiroshi Kira
Motoyuki Ishikado
Nobuo Okazaki
Makoto Kobayashi
Satoshi Kasai
Toshiaki Morikawa
Hideyuki Hiramatsu
Yutaka Ebara
Kentaro Moriyama
Keiichi Ohuchi
Masae Sahara

Health and Safety Division

*: additional duties

Yasuhiro Yamaguchi (Head)
Koji Kiriyama *
Rei Ohuchi *

Utilization Promotion Division

*: additional duties

Junichi Sato (Head)
Tsukasa Miyazaki (Deputy Head)
Kenichi Funakoshi *(Deputy Head)
Junko Ohta
Tazuko Mizusawa
Toshiki Asai
Atsuko Irie
Megumi Kawakami
Taeko Ishikawa
Miho Kawato

Administration and Finance Division

Michihiko Murasawa (Head)
Yoshitaka Yasu
Takashi Hikita
Rei Ohuchi
Mika Gunji
Mutsumi Shiraishi
Sayaka Suzuki

Proposals Review System, Committees and Meetings

Proposal Review System

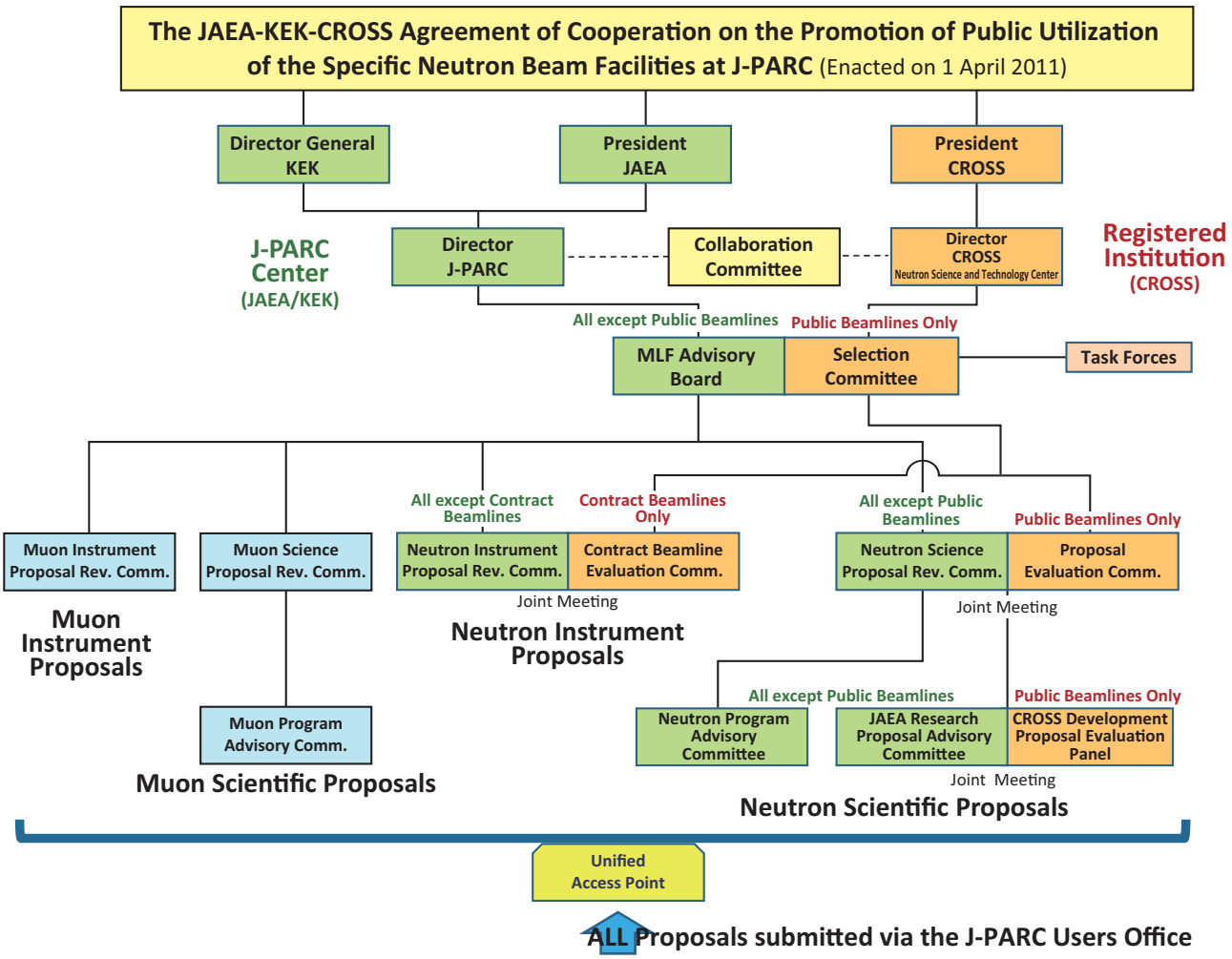

Figure 1. Proposals Review System Framework.

Materials and Life Science Facility Advisory Board

Jun Akimitsu	Okayama University
Taka-hisa Arima	The University of Tokyo
Yoshiaki Kiyanagi	Nagoya University
Mitsuhiro Shibayama	The University of Tokyo
Jun Sugiyama	Toyota Central R&D Labs., Inc.
Masaaki Sugiyama	Kyoto University
Masaki Takata	Tohoku University
Atsushi Takahara	Kyushu Universitu
Michihiro Furusaka	Hokkaido University
Toshio Yamaguchi	Fukuoka University
Hiroshi Amitsuka	Hokkaido University
Kenya Kubo	International Christian University
Toshiji Kanaya	High Energy Accelerator Research Organization
Hideki Seto	High Energy Accelerator Research Organization
Takashi Kamiyama	High Energy Accelerator Research Organization
Toshiya Otomo	High Energy Accelerator Research Organization
Yasuhiro Miyake	High Energy Accelerator Research Organization
Ryosuke Kadono	High Energy Accelerator Research Organization
Masatoshi Futakawa	Japan Atomic Energy Agency
Kazuya Aizawa	Japan Atomic Energy Agency
Masayasu Takeda	Japan Atomic Energy Agency
Kazuhiko Soyama	Japan Atomic Energy Agency
Kenji Nakajima	Japan Atomic Energy Agency
Yukinobu Kawakita	Japan Atomic Energy Agency
Jun-ichi Suzuki	Comprehensive Research Organization for Science and Society

Selection Committee

Jun Akimitsu	Okayama University
Taka-hisa Arima	The University of Tokyo
Yoshiaki Kiyanagi	Nagoya University
Mitsuhiro Shibayama	The University of Tokyo
Jun Sugiyama	Toyota Central R&D Labs., Inc.
Masaaki Sugiyama	Kyoto University
Masaki Takata	Tohoku University
Atsushi Takahara	Kyushu University
Michihiro Furusaka	Hokkaido University
Toshio Yamaguchi	Fukuoka University
Yasuhiro Iye	Japan Society for Promotion of Science
Naoki Kishimoto	Research Center for Strategic Materials
Hiroyuki Kishimoto	Sumitomo Rubber Industries, LTD.
Shinji Tsuneyuki	The University of Tokyo

Neutron Advisory Committee (NAC)

NAC convened 26-27 February, 2018 at the J-PARC Research Building, Tokai

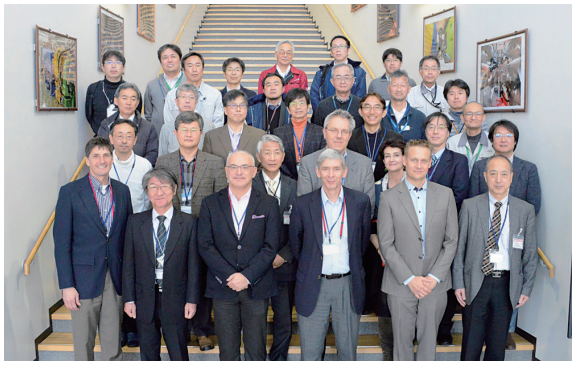

Group photo of NAC

Neutron Advisory Committee (26-27 Feb. 2018)

Robert McGreevy (chair)	Rutherford Appleton Laboratory
Bertrand Blau	Paul Scherrer Institut (PSI)
Mark Wendel	Oak Ridge National Laboratory
Yoshiaki Kiyanagi	Nagoya University
Christiane Alba-Simionesco	The Laboratoire Leon Brilloin (LLB) Sacley
Jamie Schulz	Australian Nuclear Science and Technology Organization (ANSTO)
Dimitri Argyriou	Ames Laboratory
Chang Hee Lee	Korea Atomic Energy Research Institute
Mitsuhiro Shibayama	Institute for Solid State Physics, Tokyo University
Masaaki Sugiyama	Research Reactor Institute, Kyoto University

Muon Advisory Committee (MAC)

MAC convened 28 February – 1 March, 2018 at the KEK Tokai Campus, Tokai

Group photo of MAC

Muon Advisory Committee (28 Feb-1 Mar. 2018)

Francis Pratt (chair)	Rutherford Appleton Laboratory
Prokscha Thomas	The Paul Scherrer Institute
Andrew MacFarlane	The University of British Columbia
Klaus Jungmann	University of Groningen
Kenya Kubo	International Christian University
Toshiyuki Azuma	RIKEN Advanced Science Institute
Yasuo Nozue	Osaka University
Jun Sugiyama	Toyota Centaral R & D Labs., Inc.

Workshops, Conferences, Seminars and Schools in 2017

International Symposiums held by J-PARC MLF and CROSS

International Conference on Neutron Optics (NOP2017)
5-8 July 2017, Nara Kasugano International Forum IRAKA, Nara

International Conference on Neutron Scattering 2017 (ICNS2017)
9-13 July 2017, Daejeon Convention Center, Daejeon, South Korea

Conferences held jointly by J-PARC MLF and CROSS

2017 Meeting on J-PARC MLF Industrial Use
20-21 July 2017, Akihabara Convention Hall, Tokyo


Photo of the 2017 Meeting on J-PARC MLF Industrial Use (photo courtesy of M. Hayashi)

The 20th CROSSroads Workshop "Hybrid Ribosomes – Toward New Cancer Treatments"
28-29 Aug. 2017, IBARAKI Quantum Beam Research Center and KEK Tokai Campus, Ibaraki

Group photo of CROSSroads 20 (photo courtesy of J-PARC Center)

Mini Symposium: The Cutting Edge of Protein Dynamics Research
5 Sep. 2017, IBARAKI Quantum Beam Research Center, Ibaraki

The 5th Workshop on Pulsed Neutron Imaging
26-27 Sep. 2017, Winc Aichi, Nagoya

User Group Meeting on MLF Spectrometers DIRECTION 2017
16-17 Oct. 2017, IBARAKI Quantum Beam Research Center, Ibaraki


Group photo of the User Group Meeting on MLF Spectrometers DIRECTION 2017 (photo courtesy of CROSS)

J-PARC Workshop: Deuterated Materials Enhancing Neutron Science for Structure Function Applications
19-20 Oct. 2017, IBARAKI Quantum Beam Research Center, Ibaraki

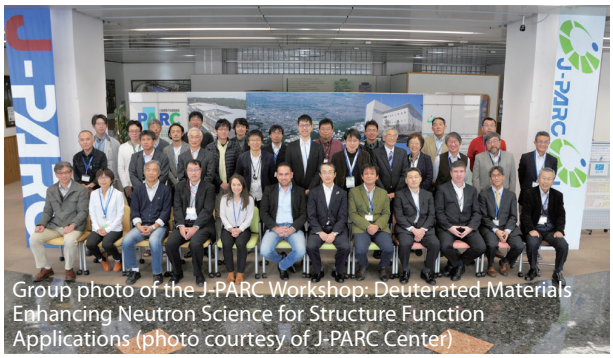

Group photo of the J-PARC Workshop: Deuterated Materials Enhancing Neutron Science for Structure Function Applications (photo courtesy of J-PARC Center)

2017 Z-Code Intermediate Level Training Course
2 Nov. 2017, LMJ Tokyo, Tokyo

2nd Workshop on the Collaborative Use of Large Research Institutions and the KEI Super Computer 2017
10 Jan. 2018, IBARAKI Quantum Beam Research Center, Ibaraki

2017 Z-Code Beginner Level Training Course
22-23 Feb. 2018, LMJ Tokyo, Tokyo

2017 Quantum Beam Science Festival (The 9th MLF Symposium and The 35th PF Symposium)
2-4 Mar. 2018, Ibaraki Prefectural Culture Center, Mito

Group photo of the 2017 Quantum Beam Science Festival

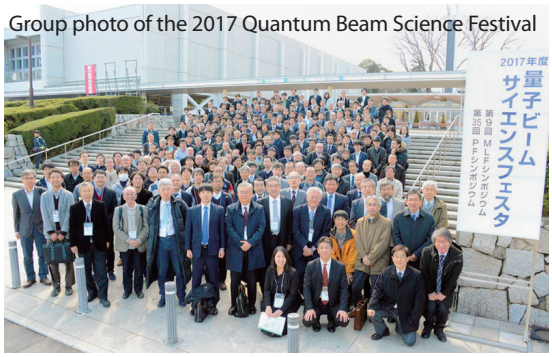

Workshops held by KEK

Advanced Nano-Structure Analysis for Soft Interfaces using Neutron Reflectometry (BL16)
10 Sep. 2017, TKP, Tokyo

Fundamental Physics with Pulsed Cold Neutrons (BL05)
20 Oct. 2017, Nagoya University, Nagoya

Construction of the VIN ROSE (BL06)
6 Nov. 2017, KEK Tokai Campus, Ibaraki

High-Resolution Neutron Powder Diffraction Method using SuperHRPD (BL08)
29 Nov. 2017, KEK Tsukuba Campus, Ibaraki

Analysis of Ordered/Disordered Structure in Hydrides with a Total Scattering Technique (BL21)
19 Dec. 2017, KEK Tokai Campus, Ibaraki

Workshops and Seminars held by CROSS and other organizations

4th Symposium on the Collaborative Use of Large Research Institutions and the KEI Super Computer 2017
8 Sep. 2017, Akihabara UDX, Tokyo

Photo of the 4th Symposium on the Collaborative Use of Large Research Institutions and the KEI Super Computer 2017 (photo courtesy of J-PARC Center)

2017 1st Workshop on Structural Biology
11 Sep. 2017, KENKYUSHA EIGO Center, Tokyo

2017 Workshop on Magnetic Materials
12 Oct. 2017, Essam Kanda Hall, Tokyo

2017 Workshop on Materials Science
20 Oct. 2017, FUKURACIA Yaesu, Tokyo

2017 1st Workshop on Residual Stress and Strain
26 Oct. 2017, KENKYUSHA EIGO Center, Tokyo

2017 Workshop on Non-destructive Visualization and Analysis Methods
8 Nov. 2017, KENKYUSHA EIGO Center, Tokyo

Ibaraki Society for the Promotion of the Use of Neutrons
"2017 Meeting on Magnetic Materials"
20 Nov. 2017, Essam Kanda Hall, Tokyo

2017 Workshop on Metallographic Structure
24 Nov. 2017, Essam Kanda Hall, Tokyo

2017 Workshop on Soft Matter Neutron Scattering
27 Nov. 2017, Essam Kanda Hall, Tokyo

2017 Workshop on Neutron Science
28 Nov. 2017, Essam Kanda Hall, Tokyo

2017 Workshop on Analytical Methods in Small Angle Scattering
8 Dec. 2017, Essam Kanda Hall, Tokyo

2017 Workshop on Battery Materials
22 Jan. 2018, KENKYUSHA EIGO Center, Tokyo

2017 Workshop on Surfaces and Interfaces
30 Jan. 2018, KENKYUSHA EIGO Center, Tokyo

2017 Workshop on Liquids and Amorphous Materials
1 Mar. 2018, Ibaraki Prefectural Culture Center, Mito

2017 2nd Workshop on Residual Stress and Strain
26 Mar. 2018, Essam Kanda Hall, Tokyo

2017 2nd Workshop on Structural Biology
29 Mar. 2018, KENKYUSHA EIGO Center, Tokyo

Schools in 2017

Hello Science from J-PARC: Looking at the World with Neutrons
29 Sep. 2017, iVil, Tokai

The 9th AONSA Neutron School/The 2nd Neutron and Muon School
16-20 Nov. 2017, J-PARC Center and IBARAKI Quantum Beam Research Center, Ibaraki

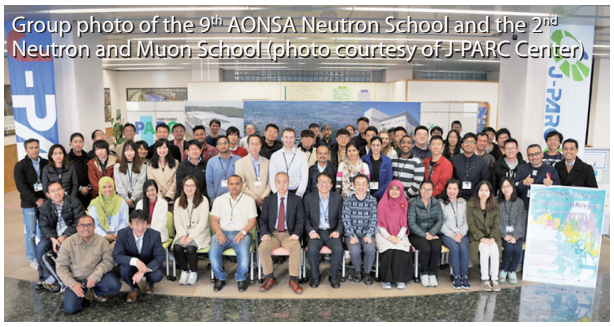
Group photo of the 9th AONSA Neutron School and the 2nd Neutron and Muon School (photo courtesy of J-PARC Center)

Hello Science from J-PARC: Using Muons to Peer into Things Big and Small
22 Dec. 2017, iVil, Tokai

Award List

The University of Tokyo "Graduate School of Engineering Dean Award", "Shoji Tanaka Award (Physics Engineering Excellent Master Thesis Award)", "President's Award"
Versatile topological magnetic phases and emergent transport phenomena in chiral magnets $MnSi_{1-x}Ge_x$
Y. Fujishiro (2018-03)

Quantum Beam Science Festa 2017 Student Award
Study on structure, hydration and stability of proteins in sugar solution using WAXS and SANS
S. Ajito (2018-03-03)

Koshiba Prize (High Energy Accelerator Science Promotion Association)
Development and application of high multiplicity positron detector Kalliope system
K. M. Kojima (2018-02-13)

KEK Technical award
Transport and intensity measurement technique of coherent Lyman alpha light realizing ultra-slow muon generation
J. Nakamura (2017-12-26)

The 15th JSNS Technology Prize
Construction of High Resolution Chopper Spectrometer HRC and implementation of Neutron Brillouin Scattering Method
S. Ito, T. Yokoo, T. Masuda, H. Yoshizawa, Y. Endoh, D. Kawana, R. Sugiura, T. Asami, M. Soda, S. Ibuka, and T. Hawai (2017-12-02)

The 17th JSNS Poster Prize
Dynamics of polyrotaxane glass by neutron quasielastic scattering
M. Taniguchi (2017-12-02)

The 17th JSNS Poster Prize
Pressure-induced quantum phase transition in singlet ground state magnet $CsFeCl_3$
S. Hayashida, M. Hagihala, N. Kurita, H. Tanaka, M. Matsumoto, Y. Uwatoko, S. Itoh, M. Soda, T. Hong, O. Zaharko, and T. Masuda (2017-12-02)

JAEA President Award 2017 [R & D Achievement Prize]
Construction of DNA spectrometer and its leading researches
K. Shibata, Y. Kawakita, H. Nakagawa, S. Kambara, T. Yamada, M. Matsuura, and T. Tominaga (2017-11-06)

66th Symposium on Macromolecules Best poster award
Dynamics of polyrotaxane glass by neutron quasielastic scattering
M. Taniguchi (2017-10-02)

IUMRS-ICAM 2017 Young Scientist Award GOLD AWARD
Ion-Specific Hydration States and Interaction Potentials of Zwitterionic Poly(sulfobetain) Brushes
Y. Higaki (2017-08-30)

ACS Editor's Choice
Effect of Charged Group Spacer Length in Zwitterionic Sulfobetaines for Hydration State of Poly(sulfobetaine) Brushes
Y. Higaki, Y. Inutsuka, T. Sakamaki, Y. Terayama, A. Takenaka, K. Higaki, N. L. Yamada, Y. Ikemoto, and A. Takahara (2017-07-25)

Highlights of 2016 in Measurement Science and Technology
Profile measurement of a bent neutron mirror using an ultrahigh precision non-contact measurement system with an auto focus laser probe
S. Morita, J. Guo, N. L. Yamada, N. Torikai, S. Takeda, M. Furusaka, and Y. Yamagata (2017-05-04)

Commendation for Science and Technology by the Minister of Education, Culture, Sports, Science and Technology, Japan in 2017
Cooperation of SPring-8 / J-PARC / K-computer and Advanced tire developments
H. Kishimoto, T. Shiozawa, F. Kaneko, Y. Shinohara, and Y. Masubuchi (2017-04)

MLF Publication 2017

1 Y. Onuki, A. Hoshikawa, S. Nishino, S. Sato, and T. Ishigaki
Rietveld Texture Analysis for Metals Having Hexagonal Close-Packed Phase by Using Time-of-Flight Neutron Diffraction at iMATERIA
Adv. Eng. Mater. **20** 1700227 (2017)

2 P. Miao, X.H. Lin, A. Koda, S. Lee, Y. Ishikawa, S. Torii, M. Yonemura, T. Mochiku, H. Sagayama, S. Itoh, K. Ikeda, T. Otomo, Y.X. Wang, R. Kadono, and T. Kamiyama
Large Magnetovolume Effect Induced by Embedding Ferromagnetic Clusters into Antiferromagnetic Matrix of Cobaltite Perovskite
Adv. Mater. **29** 1605991 (2017)

3 H. Seto, S. Itoh, T. Yokoo, H. Endo, K. Nakajima, K. Shibata, R. Kajimoto, S. Ohira-Kawamura, M. Nakamura, Y. Kawakita, H. Nakagawa, and T. Yamada
Inelastic and quasi-elastic neutron scattering spectrometers in J-PARC
BBA - General Subjects **1861** 3651-3660 (2017)

4 T. Matsuo, T. Tominaga, F. Kono, K. Shibata, and S. Fujiwara
Modulation of the picosecond dynamics of troponin by the cardiomyopathy-causing mutation K247R of troponin T observed by quasielastic neutron scattering
BBA - Proteins and Proteomics **1865** 1781-1789 (2017)

5 M. Yoshimoto, R. Futamura, A. Hoshikawa, T. Ishigaki, T. Uchida, and T. Iiyama
Unusually Stable Plastic Crystal Phase of CCl_4 Confined in Graphitic Slit-shaped Micropores from Neutron Diffraction
Chem. Lett. **46** 923-925 (2017)

6 T. Yoshimura, Y. Nakatani, K. Matsuoka, K. Akutsu, and H. Iwase
Single-alkyl and multi-alkyl chain-containing amphiphilic oligomers with several sugar side chains: solution properties and nanostructural analysis of aggregates by SANS
Colloid Polym. Sci. **295** 793-802 (2017)

7 T. Adachi, T. Kawamata, and Y. Koike
Novel electronic state and superconductivity in the electron-doped high-Tc T′-superconductors
Condensed Matter. **2** 23 (2017)

8 A.S. Tremsin, D. Perrodin, A.S. Losko, S.C. Vogel, T. Shinohara, K. Oikawa, J.H. Peterson, C. Zhang, J.J. Derby, A.M. Zlokapa, G.A. Bizarri, and E.D. Bourret
In-Situ observation of phase separation during growth of $Cs_2LiLaBr_6$:Ce crystals using energy-resolved neutron imaging
Cryst. Growth Des. **17** 6372-6381 (2017)

9 A. Watanabe, G. Kobayashi, N. Matsui, M. Yonemura, A. Kubota, K. Suzuki, M. Hirayama, and R. Kanno
Ambient pressure synthesis and H-conductivity of $LaSrLiH_2O_2$
Electrochemistry **85** 88-92 (2017)

10 T. Nakao, K. Terada, A. Kimura, S. Nakamura, O. Iwamoto, H. Harada, T. Katabuchi, M. Igashira, and J. Hori
Developments of a new data acquisition system at ANNRI
EPJ Web Conf. **146** 03021 (2017)

11 H. Harada, O. Iwamoto, N. Iwamoto, A. Kimura, K. Terada, T. Nakao, S. Nakamura, K. Mizuyama, and M. Igashira
Research and development for accuracy improvement of neutron nuclear data on minor actinides
EPJ Web Conf. **146** 11001 (2017)

12 K. Kino, H. Hasemi, A. Kimura, and Y. Kiyanagi
Measurement of the neutron capture resonances for platinum using the Ge spectrometer and pulsed neutron beam at the J-PARC/MLF/ANNRI
EPJ Web Conf. **146** 11024 (2017)

13 A. Kimura, H. Harada, S. Nakamura, Y. Toh, M. Igashira, T. Katabuchi, M. Mizumoto, and J. Hori
Neutron capture cross section measurements of 120Sn, 122Sn and 124Sn with the array of Ge spectrometer at the J-PARC/MLF/ANNRI
EPJ Web Conf. **146** 11031 (2017)

14 T. Katabuchi, M. Mizumoto, M. Igashira, K. Terada, A. Kimura, S. Nakamura, T. Nakao, O. Iwamoto, and N. Iwamoto
Measurement of the neutron capture cross section of 99Tc using ANNRI at J-PARC
EPJ Web Conf. **146** 11050 (2017)

15 Y. Mizuguchi, Y. Hijikata, T. Abe, C. Moriyoshi, Y. Kuroiwa, Y. Goto, A. Miura, S. Lee, S. Torii, T. Kamiyama, C.H. Lee, M. Ochi, and K. Kuroki
Crystal structure, site selectivity, and electronic structure of layered chalcogenide $LaOBiPbS_3$
EPL **119** 26002 (2017)

16 Y. Ueno, M. Aoki, Y. Fukao, Y. Higashi, T. Higuchi, H. Iinuma, Y. Ikedo, K. Ishida, T.U. Ito, M. Iwasaki, R. Kadono, O. Kamigaito, S. Kanda, D. Kawall, N. Kawamura, A. Koda, K.M. Kojima, M.K. Kubo, Y. Matsuda, T. Mibe, Y. Miyake, T. Mizutani, K. Nagamine, K. Nishiyama, T. Ogitsu, R. Okubo, N. Saito, K. Sasaki, K. Shimomura, P. Strasser, M. Sugano, M. Tajima, K.S. Tanaka, D. Tomono, H.A. Torii, E. Torikai, A. Toyoda, K. Ueno, A. Yamamoto, and M. Yoshida
New precise measurement of muonium hyperfine structure interval at J-PARC
Hyperfine Interactions **238** 14 (2017)

17 T. Hemmi, S. Harjo, H. Kajitani, T. Suwa, T. Saito, K. Aizawa, and K. Osamura
Evaluation of Bending Strain in Nb3Sn Strands of CIC Conductor Using Neutron Diffraction
IEEE Transactions on Applied Superconductivity **27** 1-5 (2017)

18 S.W. Park, H. Mizoguchi, H. Hiraka, K. Ikeda, T. Otomo, and H. Hosono
Transformation of the Chromium Coordination Environment in LaCrAsO Induced by Hydride Doping: Formation of $La_2Cr_2As_2O_yH_x$
Inorg. Chem. **56** 13642-13645 (2017)

19 S. Iimura, Y. Tomota, S. Matsuishi, R. Masuda, M. Seto, H. Hiraka, K. Ikeda, T. Otomo, and H. Hosono
Ferrimagnetic Cage Framework in $Ca_{12}Fe_{10}Si_4O_{32}Cl_6$
Inorg. Chem. **56** 566-572 (2017)

20 Y. Tomota, N. Sekido, S. Harjo, T. Kawasaki, and W. Gong
In situ observations of transformation behavior upon heating for a 1.5Mn-1.5Si-0.2C steel-comparison between neutron diffraction, XRD, EBSD and dilatometry
ISIJ International **57** 2237-2244 (2017)

21 Y. Onuki, S. Fujieda, S. Suzuki, and H. Fukutomi
Improvement of magnetostrictive properties of Fe-15mol%Ga alloy by texture formation during high temperature uniaxial compression deformation
ISIJ International **57** 755-757 (2017)

22 Y. Oba, S. Morooka, K. Ohishi, J. Suzuki, T. Tsuchiyama, and E.P. Gilbert

Characterization of microstructure using Bragg edge and energy-resolved small-angle neutron scattering
ISSS-2017 151-154 (2017)

23 H. Mizoguchi, S. Park, T. Honda, K. Ikeda, T. Otomo, and H. Hosono
Cubic Fluorite-Type CaH_2 with a Small Bandgap
J. Am. Chem. Soc. **139** 11317-11320 (2017)

24 H. Sato, Y. Shiota, S. Morooka, Y. Todaka, N. Adachi, S. Sadamatsu, K. Oikawa, M. Harada, S.H. Zhang, Y.H. Su, T. Kamiyama, M. Ohnuma, M. Furusaka, T. Shinohara, and Y. Kiyanagi
Inverse pole figure mapping of bulk crystalline grains in a polycrystalline steel plate by pulsed neutron Bragg-dip transmission imaging
J. Appl. Cryst. **50** 1601-1610 (2017)

25 Y. Oba, S. Morooka, K. Ohishi, J. Suzuki, S. Takata, N. Sato, R. Inoue, T. Tsuchiyama, E.P. Gilbert, and M. Sugiyama
Energy-resolved small-angle neutron scattering from steel
J. Appl. Cryst. **50** 334-339 (2017)

26 A. Esmaeili, T. Kamiyama, and R. Oishi-Tomiyasu
New functions and graphical user interface attached to powder indexing software CONOGRAPH
J. Appl. Cryst. **50** 651 (2017)

27 M. Huang, Y. Toh, M. Ebihara, A. Kimura, and S. Nakamura
Development of a correction method for the time-of-flight prompt gamma-ray analysis
J. Appl. Phys. **121** 104901 (2017)

28 T. Hayashi, K. Segawa, K. Sadakane, K. Fukao, and N.L. Yamada
Interfacial interaction and glassy dynamics in stacked thin films of poly(methyl methacrylate)
J. Chem. Phys. **146** 203305 (2017)

29 Y. Kawabata, B. Bradbury, S. Kugizaki, K. Weigandt, Y.B. Melnichenko, K. Sadakane, N.L. Yamada, H. Endo, M. Nagao, and H. Seto
Effect of interlamellar interactions on shear induced multilamellar vesicle formation
J. Chem. Phys. **147** 034905 (2017)

30 Y. Onuki, A. Hoshikawa, S. Sato, T. Ishigaki, and T. Tomida
Quantitative phase fraction analysis of steel combined with texture analysis using time-of-flight neutron diffraction
J. Mater. Sci. **52** 11643-11658 (2017)

31 T. Matsukawa
Evaluation of Hydrogen-Bonding Distance in Organic Nonlinear Optical Crystals for High-Output Terahertz-Wave Generation
J. Mol. Struc. **1134** 835-839 (2017)

32 M. Hino, T. Oda, N.L. Yamada, H. Endo, H. Seto, M. Kitaguchi, M. Harada, and Y. Kawabata
Supermirror neutron guide system for Neutron Resonance Spin Echo spectrometers at a pulsed neutron source
J. Nucl. Sci. Technol. **54** 1223-1232 (2017)

33 S. Maeda, Y. Kameda, Y. Amo, T. Usuki, K. Ikeda, T. Otomo, M. Yanagisawa, S. Seki, N. Arai, H. Watanabe, and Y. Umebayashi
Local Structure of Li(+) in Concentrated Ethylene Carbonate Solutions Studied by Low-Frequency Raman Scattering and Neutron Diffraction with (6)Li/(7)Li Isotopic Substitution Methods
J. Phys. Chem. B **121** 10979-10987 (2017)

34 T. Yamaguchi, K. Yoshida, T. Yamaguchi, Y. Kameda, K. Ikeda, and T. Otomo
Analysis of Prepeak Structure of Concentrated Organic Lithium Electrolyte by Means of Neutron Diffraction with Isotopic Substitution and Molecular Dynamics Simulation
J. Phys. Chem. B **121** 5355-5362 (2017)

35 T. Yamada, T. Takahashi, T. Tominaga, S. Takata, and H. Seto
Dynamical Behavior of Hydration Water Molecules between Phospholipid Membranes
J. Phys. Chem. B **121** 8322-8329 (2017)

36 D.L. Price, O. Borodin, M.A. González, M. Kofu, K. Shibata, T. Yamada, O. Yamamuro, and M.L. Saboungi
Relaxation in a Prototype Ionic Liquid: Influence of Water on the Dynamics
J. Phys. Chem. Lett. **8** 715-719 (2017)

37 K. Iida, R. Kajimoto, Y. Mizuno, K. Kamazawa, Y. Inamura, A. Hoshikawa, Y. Yoshida, T. Matsukawa, T. Ishigaki, Y. Kawamura, S. Ibuka, T. Yokoo, S. Itoh, and T. Katsufuji
Time-of-Flight Elastic and Inelastic Neutron Scattering Studies on the Localized 4d Electron Layered Perovskite $La_5Mo_4O_{16}$
J. Phys. Soc. Jpn. **86** 064803 (2017)

38 K. Iida, M. Ishikado, Y. Nagai, H. Yoshida, A.D. Christianson, N. Murai, K. Kawashima, Y. Yoshida, H. Eisaki, and A. Iyo
Spin Resonance in the New-Structure-Type Iron-Based Superconductor $CaKFe_4As_4$
J. Phys. Soc. Jpn. **86** 093703 (2017)

39 K. Tomiyasu, M. Sato, S. Koyama, T. Nojima, R. Kajimoto, S. Ji, and K. Iwasa
Magnetic Properties of Electron-Doped $LaCoO_3$
J. Phys. Soc. Jpn. **86** 094706 (2017)

40 K. Kodama, K. Ikeda, S.-I. Shamoto, and T. Otomo
Alternative Equation on Magnetic Pair Distribution Function for Quantitative Analysis
J. Phys. Soc. Jpn. **86** 124708 (2017)

41 Y. Doi, M. Wakeshima, K. Tezuka, Y. Shan, K. Ohoyama, S. Lee, S. Torii, T. Kamiyama, and Y. Hinatsu
Crystal structures, magnetic properties, and DFT calculation of B-site defected 12L-perovskites $Ba_2La_2MW_2O_{12}$ (M = Mn, Co, Ni, Zn)
J. Phys.: Condens. Matter **29** 365802 (2017)

42 S. Asano, K. Tsutsumi, K. Sato, and M. Fujita
Ce-substitution effects on the spin excitation spectra in $Pr_{1.4-x}La_{0.6}Ce_xCuO_{4+\delta}$
J. Phys.: Conf. Ser. **807** 52009 (2017)

43 K. Kamazawa and T. Moyhoshi
Possible low spin state of Fe ions in $HoBaFe_4O_7$
J. Phys.: Conf. Ser. **828** 012012 (2017)

44 T. Haku, M. Soda, M. Sera, K. Kimura, J. Taylor, S. Itoh, T. Yokoo, Y. Matsumoto, D. Yu, R.A. Mole, T. Takeuchi, S. Nakatsuji, Y. Kono, T. Sakakibara, L.J. Chang, and T. Masuda
Neutron Scattering Study in Breathing Pyrochlore Antiferromagnet $Ba_3Yb_2Zn_5O_{11}$
J. Phys.: Conf. Ser. **828** 012018 (2017)

45 K. Hiroi, T. Shinohara, H. Hayashida, J.D. Parker, K. Oikawa, M. Harada, Y.H. Su, and T. Kai
Magnetic field imaging of a model electric motor using polarized pulsed neutrons at J-PARC/MLF
J. Phys.: Conf. Ser. **862** 012008 (2017)

46 T. Ino, M. Ohkawara, K. Ohoyama, T. Yokoo, S. Itoh, Y. Nambu, M. Fujita, H. Kira, H. Hayashida, K. Hiroi, K. Sakai, T. Oku, and K. Kakurai
Development of a Polarized 3He Neutron Spin Filter for POLANO at J-PARC
J. Phys.: Conf. Ser. **862** 012011 (2017)

47 R. Maruyama, T. Bigault, A.R. Wildes, C.D. Dewhurst, T. Saerbeck, D. Honecker, D. Yamazaki, K. Soyama, and P Courtois
Accessible length scale of the in-plane structure in polarized

neutron off-specular and grazing-incidence small-angle scattering measurements
J. Phys.: Conf. Ser. **862** 012017 (2017)

48 T. Shinohara, K. Hiroi, Y.H. Su, T. Kai, T. Nakatani, K. Oikawa, M. Segawa, H. Hayashida, J.D. Parker, Y. Matsumoto, S.Y. Zhang, and Y. Kiyanagi
Polarization analysis for magnetic field imaging at RADEN in J-PARC/MLF
J. Phys.: Conf. Ser. **862** 012025 (2017)

49 S. Ibuka, T. Yokoo, S. Itoh, K. Kamazawa, M. Nakamura, and M. Imai
Spin wave dispersion just above the magnetic order-order transition in the metallic antiferromagnet Mn_3Pt
J. Phys.: Conf. Ser. **868** 012017 (2017)

50 M. Abe, H. Iba, K. Suzuki, H. Minamishima, M. Hirayama, K. Tamura, J. Mizuki, T. Saito, Y. Ikuhara, and R. Kanno
Study on the deterioration mechanism of layered rock-salt electrodes using epitaxial thin films – Li(Ni, Co, Mn)O_2 and their Zr-O surface modified electrodes
J. Power Sources **345** 108-119 (2017)

51 Y. Narita, Y. Takahashi, M. Harada, K. Oikawa, D. Kobayashi, K. Hirose, H. Sato, S. Ikeda, T. Endoh, and H. Ohno
Fast neutron tolerance of the perpendicular-anisotropy CoFeB–MgO magnetic tunnel junctions with junction diameters between 46 and 64 nm
Japanese Journal of Applied Physics **56** 0802B3 (2017)

52 S. Hosokawa, K. Kimura, M. Yamasaki, Y. Kawamura, K. Yoshida, M. Inui, S. Tsutsui, A.Q.R. Baron, Y. Kawakita, and S. Itoh
Impurity effects in the microscopic elastic properties of polycrystalline Mg-Zn-Y alloys with a synchronized long-period stacking ordered phase
Journal of Alloys and Compounds **695** 426-432 (2017)

53 Y. Sakaguchi, H. Asaoka, and M. Mitkova
Silver photodiffusion into Ge-rich amorphous germanium sulfide - Neutron reflectivity study
Journal of Applied Physics **122** 235105 (2017)

54 T. Nyuui, G. Matsuba , S. Sato, K. Nagai, and A. Fujimori
Correlation between gas transport properties and the morphology/dynamics of crystalline fluorinated copolymer membranes
Journal of Applied Polymer Science **135** 45665 (2017)

55 K. Toh, T. Nakamura, K. Sakasai, and H. Yamagishi
Development of a bump cathode element for two-dimensional neutron detection
Journal of Instrumentation **12** C12011 (2017)

56 T. Nakamura, K. Toh, N. Tsutsui, M. Ebine, A. Birumachi, and K. Sakasai
Development of a position-sensitive scintillation neutron detector for a new protein single-crystal diffractometer at J-PARC MLF
Journal of Instrumentation **12** C12025 (2017)

57 Y. Idemoto, T. Sekine, N. Ishida, and N. Kitamura
Change of local structures for $0.5Li_2MnO_3$–$0.5LiMn_{1/3}Ni_{1/3}Co_{1/3}O_2$ in first charge process of different rates
Journal of Materials Science **52** 8630-8649 (2017)

58 S. Ohira-Kawamura, T. Oku, M. Watanabe, R. Takahashi, K. Munakata, S. Takata, Y. Sakaguchi, M. Ishikado, K. Ohuchi, T. Hattori, H. Kira, K. Sakai, T. Aso, Y. Yamauchi, and S. Isomae
Sample environment at the J-PARC MLF
Journal of Neutron Research **19** 15-22 (2017)

59 T. Kai, T. Kamiyama, F. Hiraga, M. Ooi, K. Hirota, and Y. Kiyanagi
Measurements of neutronic characteristics of rectangular and cylindrical coupled hydrogen moderators
Journal of Nuclear Science and Technology **55** 283-289 (2017)

60 S. Fujiwara, T. Chatake, T. Matsuo, F. Kono, T. Tominaga, K. Shibata, A. Sato-Tomita, and N. Shibayama
Ligation-Dependent Picosecond Dynamics in Human Hemoglobin as Revealed by Quasielastic Neutron Scattering
Journal of Physical Chemistry B **121** 8069-8077 (2017)

61 F. Fujisaki, K. Mori, M. Yonemura, Y. Ishikawa, T. Kamiyama, T. Otomo, E. Matsubara, and T. Fukunag
Mechanical synthesis and structural properties of the fast fluoride-ion conductor $PbSnF_4$
Journal of Solid State Chemistry **253** 287-293 (2017)

62 Y. Sakai, J.Y. Yang, R. Yu, H. Hojo, I. Yamada, P Miao, S. Lee, S. Torii, T. Kamiyama, M. Ležaić, G. Bihlmayer, M. Mizumaki, J. Komiyama, T. Mizokawa, H. Yamamoto, T. Nishikubo, Y. Hattori, K. Oka, Y.Y. Yin, J.H. Dai, W.M. Li, S. Ueda, A. Aimi, D. Mori, Y. Inaguma, Z.W. Hu, T. Uozumi, C.Q. Jin, Y.W. Long, and M. Azuma
A Site and B Site Charge Orderings in an s–d Level Controlled Perovskite Oxide $PbCoO_3$
Journal of the American Chemical Society **139** 4574-4581 (2017)

63 Y. Seki, T. Shinohara, J.D. Parker, W. Yashiro, A. Momose, K. Kato, H. Kato, M. Sadeghilaridjani, Y. Otake, and Y. Kiyanagi
Development of multi-colored neutron talbot–lau interferometer with absorption grating fabricated by imprinting method of metallic glasswith absorption grating fabricated by imprinting method of metallic glass
Journal of the Physical Society of Japan **86** 44001 (2017)

64 H. Tanoue, N.L. Yamada, K. Ito, and H. Yokoyama
Quantitative Analysis of Polymer Brush Formation Kinetics using Quartz Crystal Microbalance: Viscoelasticity of Polymer Brush
Langmuir **33** 5166-5172 (2017)

65 Y. Higaki, Y. Inutsuka, T. Sakamaki, Y. Terayama, A. Takenaka, K. Higaki, N.L. Yamada, Y. Ikemoto, and A. Takahara
Effect of Charged Group Spacer Length on Hydration State in Zwitterionic Poly (sulfobetaine) Brushes
Langmuir **33** 8404-8412 (2017)

66 K. Hori, N.L. Yamada, Y. Fujii, T. Masui, H. Kishimoto, and H. Seto
Structure and Mechanical Properties of Polybutadiene Thin Films Bound to Surface-Modified Carbon Interface
Langmuir **33** 8883-8890 (2017)

67 H. Tanoue, M. Inutsuka, N.L. Yamada, K. Ito, and H. Yokoyama
Kinetics of Dynamic Polymer Brush Formation
Macromolecules **50** 5549-5555 (2017)

68 P.G. Xu, Y, Tomota, Y. Arakaki, S. Harjo, and H. Sueyoshi
Evaluation of austenite volume fraction in TRIP steel sheets using neutron diffraction
Materials Characterization **127** 104-110 (2017)

69 N. Tsuchida, N. Nagahisa, and S. Harjo
Room-temperature creep tests under constant load on a TRIP-aided multi-microstructure steel
Materials Science and Engineering: A **700** 631-636 (2017)

70 Y. Tomota, S. Sato, M. Uchida, P.G. Xu, S. Harjo, W. Gong, and T. Kawasaki
Quantitative Evaluation of Texture and Dislocations during Annealing after Hot Deformation in Austenitic Steel Using Neutron Diffraction
Materials Science Forum **905** 25-30 (2017)

71 S. Harjo, T. Kawasaki, Y. Tomota, and W. Gong
Unusual Plastic Deformation Behavior in Lath Martensitic Steel Containing High Dislocation Density

Materials Science Forum **905** 46-51 (2017)

72 T. Ungár, S. Harjo, T. Kawasaki, Y. Tomota, G. Ribárik, and Z.M. Shi
Composite behavior of lath martensite steels induced by plastic strain, a new paradigm for the elastic-plastic response of martensitic steels
Metallurgical and Materials Transactions A **48** 159-167 (2017)

73 S. Harjo, T. Kawasaki, Y. Tomota, W. Gong, K. Aizawa, G. Tichy, Z.M. Shi, and T. Ungár
Work Hardening, Dislocation Structure, and Load Partitioning in Lath Martensite Determined by In Situ Neutron Diffraction Line Profile Analysis
Metallurgical and Materials Transactions A **48** 4080-4092 (2017)

74 S. Ohisa, Y.J. Pu, N.L. Yamada, G. Matsuba, and J. Kido
Influence of solution- and thermal-annealing processes on the sub-nanometer-ordered organic–organic interface structure of organic light-emitting devices
Nanoscale **9** 25-30 (2017)

75 M. Igarashi, T. Matsumoto, F. Yagihashi, H. Yamashita, T. Ohhara, T. Hanashima, A. Nakao, T. Moyoshi, K. Sato, and S. Shimada
Non-aqueous selective synthesis of orthosilicic acid and its oligomers
Nature Communications **8** 140 (2017)

76 R. Iizuka, T. Yagi, H. Gotou. T. Okuchi, T. Hattori, and A. Sano-Furukawa
Hydrogenation of iron in the early stage of Earth's evolution
Nature Communications **8** 14096 (2017)

77 B. Li, Y. Kawakita, Y.C. Liu, M.C. Wang, M. Matsuura, K. Shibata, S. Kawamura, T. Yamada, S.C. Lin, K. Nakajima, and S. Frank Liu
Polar rotor scattering as atomic-level origin of low mobility and thermal conductivity of perovskite $CH_3NH_3PbI_3$
Nature Communications **8** 16086 (2017)

78 S. Ito, N. Kurita, H. Tanaka, S. Ohira-Kawamura, K. Nakajima, S. Itoh, K. Kuwahara, and K. Kakurai
Structure of the magnetic excitations in the spin-1/2 triangular-lattice Heisenberg antiferromagnet $Ba_3CoSb_2O_9$
Nature Communications **8** 235 (2017)

79 S. Miyajima, H. Shishido, Y. Narukami, N. Yoshioka, A. Fujimaki, M. Hidaka, K. Oikawa, M. Harada, T.i Oku, M. Arai, and T. Ishida
Neutron flux spectrum revealed by Nb-based current-biased kinetic inductance detector with a 10B conversion layer
Nucl. Instrum. Meth. A, **842**, 71-75 (2017)

80 T. Hosobata, N.L. Yamada, M. Hino, Y. Yamagata, T. Kawai, H. Yoshinaga, K. Hori, M. Takeda, S. Takeda, and S. Morita
Development of precision elliptic neutron-focusing supermirror
Opt. Express **25** 20012-20024 (2017)

81 N. Naganawa, S. Awano, M. Hino, M. Hirose, K. Hirota, H. Kawahara, M. Kitaguchi, K. Mishima, T. Nagae, H.M. Shimizu, S. Tada, S. Tasaki, and A. Umemoto
Development of high spatial resolution cold/ultra- cold neutron detector using fine-grained nuclear emulsion
Pcodeedings of Science PoS (KMI2017) 77 (2017)

82 T.U. Ito, A. Koda, K. Shimomura, W. Higemoto, T. Matsuzaki, Y. Kobayashi, and H. Kageyama
Excited configurations of hydrogen in the $BaTiO_{3-x}H_x$ perovskite lattice associated with hydrogen exchange and transport
Phys. Rev. B **95** 020301(R) (2017)

83 X.L. Xu, D.D. Meng, X.G. Zheng, I. Yamauchi, I. Watanabe, and Q.X. Guo
Critical slowing of quantum atomic deuterium/hydrogen with features of multiferroicity in the geometrically frustrated system $Co_2(OD)_3Cl/Co_2(OH)_3Cl$
Phys. Rev. B **95** 024111 (2017)

84 M. Matsuura, S. Kawamura, M. Fujita, R. Kajimoto, and K. Yamada
Development of spin-wave-like dispersive excitations below the pseudogap temperature in the high-temperature superconductor $La_{2-x}Sr_xCuO_4$
Phys. Rev. B **95** 024504 (2017)

85 K. Kamazawa, M. Ishikado, S. Ohira-Kawamura, Y. Kawakita, K. Kakurai, K. Nakajima, and M. Sato
Interaction of spin-orbital-lattice degrees of freedom: Vibronic state of the corner-sharing-tetrahedral frustrated spin system $HoBaFe_4O_7$ by dynamical Jahn-Teller effect
Phys. Rev. B. **95** 104413 (2017)

86 P. Miao, X.H. Lin, S. Lee, Y. Ishikawa, S. Torii, M. Yonemura, T. Ueno, N. Inami, K. Ono, Y.X. Wang, and T. Kamiyama
Hole-doping-induced melting of spin-state ordering in $PrBaCo_2O_{5.5+x}$
Phys. Rev. B **95** 125123 (2017)

87 H. Ishibashi, S. Shimono, K. Tomiyasu, S. Lee, S. Kawaguchi, H. Iwane, H. Nakao, S. Torii, T. Kamiyama, and Y. Kubota
Small crystal distortion and long-range antiferro-orbital ordering in the spinel oxide CoV_2O_4
Phys. Rev. B. **95** 144424 (2017)

88 S. Klotz, K. Komatsu, H. Kagi, K. Kunc, A. Sano-Furukawa, S. Machida, and T. Hattori
Bulk moduli and equations of state of ice VII and ice VIII
Phys. Rev. B **95** 174111 (2017)

89 K. Iwasa, Y. Otomo, K. Suyama, K. Tomiyasu, S. Ohira-Kawamura, K. Nakajima, and J.M. Mignot
Crystalline-electric-field excitations and spin dynamics in $Ce_3Co_4Sn_{13}$ semimetallic chiral-lattice phase
Phys. Rev. B **95** 195156 (2017)

90 S. Ibuka, S. Itoh, T. Yokoo, and Y. Endoh
Damped spin-wave excitations in the itinerant antiferromagnet γ -$Fe_{0.7}Mn_{0.3}$
Phys. Rev. B. **95** 224406 (2017)

91 P. Babkevich, N.E. Shaik, D. Lançon, A. Kikkawa, M. Enderle, R.A. Ewings, H.C. Walker, D.T. Adroja, P. Manuel, D.D. Khalyavin, Y. Taguchi, Y. Tokura, M. Soda, T. Masuda, and H.M. Rønnow
Magnetic excitations from two-dimensional interpenetrating Cu framework in $Ba_2Cu_3O_4Cl_2$
Phys. Rev. B **96** 014410 (2017)

92 M. Kofu, N. Hashimoto, H. Akiba, H. Kobayashi, H. Kitagawa, K. Iida, M. Nakamura, and O. Yamamuro
Vibrational states of atomic hydrogen in bulk and nanocrystalline palladium studied by neutron spectroscopy
Phys. Rev. B **96** 054304 (2017)

93 C. Wang, D.W. Yu, X.Q. Liu, R.Y. Chen, X.Y. Du, B.Y. Hu, L.C. Wang, K. Iida, K. Kamazawa, S. Wakimoto, J. Feng, N.L. Wang, and Y. Li
Observation of magnetoelastic effects in a quasi-one-dimensional spiral magnet
Phys. Rev. B **96** 085111 (2017)

94 K. Matsuura, H. Sagayama, A. Uehara, Y. Nii, R. Kajimoto, K. Kamazawa, K. Ikeuchi, S. Ji, N. Abe, and T. Arima
Spin-Orbital Correlated Dynamics in the Spinel-Type Vanadium Oxide MnV_2O_4
Phys. Rev. Lett. **119** 017201 (2017)

95 T. Matsumoto, T. Ohhara, H. Sugimoto, S.M. Bennington, and S. Ikeda
Quantum twin spectra in nanocrystalline silicon
Phys. Rev. Materials **1** 051601 (2017)

96 J.N. Hendriks, A.W.T. Gregg, C.M. Wensrich, A.S. Tremsin, T. Shinohara, M. Meylan, E.H. Kisi, V. Luzin, and O. Kirsten
Bragg-edge elastic strain tomography for in situ systems from energy-resolved neutron transmission imaging
Phys. Rev. Materials **1** 053802 (2017)

97 Y. Kousaka, T. Koyama, K. Ohishi, K. Kakurai, V. Hutanu, H. Ohsumi, T. Arima, A. Tokuda, M. Suzuki, N. Kawamura, A. Nakao, T. Hanashima, J. Suzuki, J. Campo, Y. Miyamoto, A. Sera, K. Inoue, and J. Akimitsu
Monochiral helimagnetism in homochiral crystals of $CsCuCl_3$
Phys. Rev. Materials **1** 071402 (2017)

98 D.A. Pushin, D. Sarenac, D.S. Hussey, H. Miao, M. Arif, D.G. Cory, M.G. Huber, D.L. Jacobson, J.M. LaManna, J.D. Parker, T. Shinohara, W. Ueno, and H. Wen
Far-field interference of a neutron white beam and the applications to noninvasive phase-contrast imaging
Physical Review A **95** 043637 (2017)

99 Y. Matsumoto, M. Segawa, T. Kai, T. Shinohara, T. Nakatani, K. Oikawa, K. Hiroi, Y.H. Su, H. Hayashida, J.D. Parker, S. Zhang, and Y. Kiyanagi
Recent progress of radiography and tomography at the energy-resolved neutron imaging system RADEN
Physics Procedia **88** 162-166 (2017)

100 Y. Seki, T. Shinohara, W. Ueno, J.D. Parker, T. Samoto, W. Yashiro, A. Momose
Experimental evaluation of neutron absorption grating fabricated by oblique evaporation of gadolinium for phase imaging
Physics Procedia **88** 217-223 (2017)

101 N. Naganawa, S. Awano, M. Hino, M. Hirose, K. Hirota, H. Kawahara, M. Kitaguchi, K. Mishima, T. Nagae, H.M. Shimizu, S. Tasaki, and A. Umemoto
A neutron detector with submicron spatial resolution using fine-grained nuclear emulsion
Physics Procedia **88** 224-230 (2017)

102 H. Hayashida, K. Hiroi, T. Oku, H. Kira, K. Sakai, T. Shinohara, T. Kai, J.D. Parker, Y. Matsumoto, S. Zhang, T. Ino, M. Ohkawara, and K. Kakurai
Development of an in-situ SEOP 3He neutron spin filter for magnetic imaging techniques
Physics Procedia **88** 231-236 (2017)

103 T. Kai, K. Hiroi, Y.H. Su, T. Shinohara, J.D. Parker, Y. Matsumoto, H. Hayashida, M. Segawa, T. Nakatani, K. Oikawa, S. Zhang, and Y. Kiyanagi
Reliability estimation of neutron resonance thermometry using tantalum and tungsten
Physics Procedia **88** 306-313 (2017)

104 K. Oikawa, Y.H. Su, Y. Tomota, T. Kawasaki, T. Shinohara, T. Kai, K. Hiroi, S.Y. Zhang, J.D. Parker, H. Sato, and Y. Kiyanagi
A comparative study of the crystallite size and the dislocation density of bent steel plates using Bragg-edge transmission imaging, TOF neutron diffraction and EBSD
Physics Procedia **88** 34-41 (2017)

105 Y.H. Su, K. Oikawa, T. Shinohara, T. Kai, K. Hiroi, S. Harjo, T. Kawasaki, W. Gong, S.Y. Zhang, J.D. Parker, H. Hayashida, H. Sato, Y. Kiyanagi, and Y. Tomota
Time-of-flight Neutron Transmission Imaging of Martensite Transformation in Bent Plates of a Fe-25Ni-0.4C Alloy
Physics Procedia **88** 42-49 (2017)

106 T. Kamiyama, K. Iwase, H. Sato, S. Harjo, T. Ito, S. Takata, and K. Aizawa
Microstructural Information Mapping of a Plastic-deformed α-iron Plate during Tensile Tests using Pulsed Neutron Transmission
Physics Procedia **88** 50-57 (2017)

107 D. Ito, Y. Saito, H. Sato, and T. Shinohara
Visualization of solidification process in lead-bismuth eutectic
Physics Procedia **88** 58-63 (2017)

108 T. Kanaya, M. Murakami, T. Maede, H. Ogawa, R. Inoue, K. Nishida, G. Matsuba, N. Ohta, S. Takata, T. Tominaga, J. Suzuki, Y. Han, and T. Kim
Role of molecular weight in shish-kebab formation during drawing by small-angle neutron and X-ray scattering
Polymer J. **49** 831-837 (2017)

109 Y. Sato on behalf of the E34 collaboration
Muon g-2/EDM experiment at J-PARC
PoS (INPC2016) 006 (2017)

110 H.M. Shimizu, W.M. Snow, V.P. Gudkov, J.D. Bowman, J. Curole, B.M. Goodson, H. Harada, P. Hautle, M. Hino, K. Hirota, G. Ichikawa, T. Ino, S. Ishimoto, T. Iwata, A. Kimura, M. Kitaguchi, Y. Kiyanagi, J. Koga, K. Mishima, Y. Miyachi, T. Momose, T. Morishima, K. Nagamoto, A. Okada, T. Okudaira, S. Penttila, B. Plaster, K. Sakai, D. Schaper, S. Takada, K. Taketani, X. Tong, A.S. Tremsin, Y. Yamagata, T. Yamamoto, N. Yamanaka, M. Yokohashi, and T. Yoshioka
Discrete Symmetry Tests in Neutron-induced Compound States
PoS (INPC2016) INPC2016 187 (2017)

111 N. Oi, H.M. Shimizu, K. Hirota, M. Kitaguchi, C.C. Haddock, W.M. Snow, T. Yoshioka, S. Matsumoto, K. Mishima, T. Ino, and T. Shima
Measurement of Neutron Scattering from Noble Gas to Search for Short-range Unknown Force
PoS (INPC2016) INPC2016 188 (2017)

112 T. Okudaira, H.M. Shimizu, M. Kitaguchi, K. Hirota, S. Takada, T. Yamamoto, A. Okada, T. Yoshioka, T. Ino, K. Sakai, K. Asahi, T. Momose, T. Iwata, M. Hino, T. Shima, and Y. Yamagata
Measurement of Angular Correlations in the (n,γ) Reaction for T-violation Search
PoS (INPC2016) INPC2016 188 (2017)

113 T. Yamamoto, H.M. Shimizu, M. Kitaguchi, K. Hirota, T. Okudaira, S. Takada, A. Okada, T. Yoshioka, T. Ino, K. Sakai, K. Asahi, T. Momose, T. Iwata, M. Hino, T. Shima, and Y. Yamagata
Measurement of Angular Correlation of (n,gamma) Reaction with Polarized Neutrons
PoS (KMI2017) KMI2017 049 (2017)

114 N. Naganawa, S. Awano, M. Hino, M. Hirose, H. Kawahara, M. Kitaguchi, K. Mishima, T. Nagae, H.M. Shimizu, S. Tada, S. Tasaki, and A. Umemoto
Development of High Spatial Resolution Cold/Ultracold Neutron Detector using Fine-grained Nuclear Emulsion
PoS (KMI2017) KMI2017 077 (2017)

115 S. Iimura, H. Okanishi, S. Matsuishi, H. Hiraka, T. Honda, K. Ikeda, T.C. Hansen, T. Otomo, and H. Hosono
Large-moment antiferromagnetic order in overdoped high-Tc superconductor $^{154}SmFeAsO_{1-x}D_x$
Proc. Natl. Acad. Sci. U. S. A. **114** E4354-E4359 (2017)

116 K. Hagiwara, T. Tanaka, P.K. Das, T. Yano, Y. Yamada, I. Ou, T. Mori, T. Kayano, M.S. Reen, R. Dhir, Y. Koshio, M. Sakuda, A. Kimura, S. Nakamura, N. Iwamoto, and H. Harada
Comparison of g production data from thermal neutron capture on gadolinium with the Monte Carlo simulation
Proceedings of Science **294** KMI1017-035 (2017)

117 N. OI, H.M. Shimizu, K. Hirota, M. Kitaguchi, C.C. Haddock, W.M. Snow, T. Yoshioka, S. Matsumoto, K. Mishima, T. Ino, and T. Shima
Measurement of neutron scattering from noble gas to search for a short-range unknown force
Proceedings of the 26th International Nuclear Physics

Conference, 11-16 September, 2016, Adelaide, Australia, Proceedings of Science KMI2017 050 (2017)

118 H. Natori, N. Teshima, M. Aoki, H. Nishiguchi, T.D. Nguyen, Y. Takezaki, Y. Furuya, S. Ito, S. Mihara, D. Nagao, Y. Nakatsugawa, T.M. Nguyen, Y. Seiya, K. Shimizu, and K. Yamamoto
A fast high-voltage switching multiwire proportional chamber
Prog. Theor. Exp. Phys. **2** 023C01 (2017)

119 W. Higemoto, R. Kadono, N. Kawamura, A. Koda, K.M. Kojima, S. Makimura, S. Matoba, Y. Miyake, K. Shimomura, and P. Strasser
Materials and Life Science Experimental Facility at the Japan Proton Accelerator Research Complex IV: The Muon Facility
Quantum Beam Sci. **1** 11(1-24) (2017)

120 M. Inutsuka, H. Tanoue, N.L. Yamada, K. Ito, and H. Yokoyama
Dynamic contact angle on a reconstructive polymer surface by segregation
RSC Adv. **7** 17202-17207 (2017)

121 H. Mamiya, Y. Oba, N. Terada, N. Watanabe, K. Hiroi, T. Shinohara, and K. Oikawa
Magnetic Bragg dip and Bragg edge in neutron transmission spectra of typical spin superstructures
Scientific Reports **7** 15516 (2017)

122 A.S. Tremsin, J. Rakovan, T. Shinohara, W. Kockelmann, A.S. Losko, and S.C. Vogel
Non-destructive sudy of bulk crystallinity and elemental composition of natural gold single crystal samples by energy-resolved neutron imaging
Scientific Reports **7** 40759 (2017)

123 S. Takagi, Y. Iijima, T. Sato, H. Saitoh, K. Ikeda, T. Otomo, K. Miwa, T. Ikeshoji, and S.I. Orimo
Formation of novel transition metal hydride complexes with ninefold hydrogen coordination
Scientific Reports **7** 44253 (2017)

124 S. Harjo, N. Tsuchida, J. Abe, and W. Gong
Martensite phase stress and the strengthening mechanism in TRIP steel by neutron diffraction
Scientific Reports **7** 15149 (2017)

125 M. Fujihala, H. Koorikawa, S. Mitsuda, K. Morita, T. Tohyama, A. Koda, H. Okabe, K. Tomiyasu, S. Itoh, T. Yokoo, S. Ibuka, M. Tadokoro, M. Itoh, H. Sagayama, R. Kumai, Y. Murakami, D. Nakamura, and S. Takeyama
Possible Tomonaga-Luttinger spin liquid state in the spin-1/2 inequilateral diamond-chain compound $K_3Cu_3AlO_2(SO_4)_4$
Scientific Reports **7** 16785 (2017)

126 A. Cereser, M. Strobl, S.A. Hall, A. Steuwer, R. Kiyanagi, A.S. Tremsin, E.B. Knudsen, T. Shinohara, P.K. Willendrup, A.B.S. Fanta, S. Iyengar, P.M. Larsen, T. Hanashima, T. Moyoshi, P.M. Kadletz, P. Krooß, T. Niendorf, M. Sales, W.W. Schmahl, and S. Schmidt
Time-of-Flight Three Dimensional Neutron Diffraction in Transmission Mode for Mapping Crystal Grain Structures
Scientific Reports **7** 9561 (2017)

127 Y. Tomota, W. Gong, S Harjo, and T. Shinozaki
Reverse austenite transformation behavior in a tempered martensite low-alloy steel studied using in situ neutron diffraction
Scripta Materialia **133** 79-82 (2017)

128 Y.X. Wang, T. Ohnuki, Y. Tomota, S. Harjo, and T. Ohmura
Multi-scaled heterogeneous deformation behavior of pearlite steel studied by in situ neutron diffraction
Scripta Materialia **140** 45-49 (2017)

129 R. Mashita, R. Inoue, T. Tominaga, K. Shibata, H. Kishimoto, and T. Kanaya
Quasielastic Neutron Scattering Study of Microscopic Dynamics in Polybutadiene Reinforced with an Unsaturated Carboxylate
Soft Matter **13** 7862-7869 (2017)

130 V.K. Sharma, P. Mandal, S.K. Ghosh, T. Yamada, K. Shibata, S. Mitra, and R. Mukhopadhyay
Effects of Ionic Liquids on the Nanoscopic Dynamics and Phase Behaviour of a Phosphatidylcholine Membrane
Soft Matter **13** 8969-8979 (2017)

131 K. Mori, T. Kasai, K. Iwase, F. Fujisaki, Y. Onodera, and T. Fukunaga
Structural origin of massive improvement in Li-ion conductivity on transition from $(Li_2S)_5(GeS_2)(P_2S_5)$ glass to $Li_{10}GeP_2S_{12}$ crystal
Solid State Ionics **301** 163-169 (2017)

132 H. Shishido
Neutron detection using the superconducting Nb-based current-biased kinetic inductance detector
Superconductor Science & Technology **30** 094003 (2017)

133 M.W. Hsu, Y.H. Tsai, Y. Chen, and K.S. Lin
Multifunctional nanocarrier combined with micro-RNA as a gene therapy tool
The 6th International Conference on Bio-based Polymers 269-270 (2017)

134 N.V. Mdlovu, T.W. Chang, Y.H. Tsai, Y. Chen, and K.S. Lin
Iron oxide-pluronic F127 polymer nanocomposites as carriers for doxorubicin drug delivery system
The 6th International Conference on Bio-based Polymers 273-274 (2017)

Editorial Board - MLF Annual Report 2017

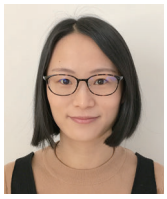

Chief Editor
Yuhua Su
Technology Development Section

Yukinori Nagatani
Muon Science Section

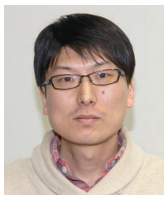

Jun Abe
CROSS

Takashi Naoe
Neutron Source Section

Akinori Hoshikawa
Ibaraki University

Kenichi Oikawa
Neutron Science Section

Kenji Mishima
Neutron Science Section

Joseph Parker
CROSS

Tazuko Mizusawa
CROSS

Kaoru Sakasai
Neutron Instrumentation Section

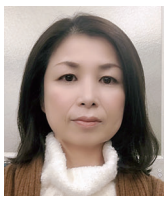

Yukiko Nagai
Technology Development Section

J-PARC

JAPAN PROTON ACCELERATOR RESEARCH COMPLEX

High Energy Accelerator Research Organization (KEK)
Japan Atomic Energy Agency (JAEA)

http://j-parc.jp/

Materials and Life Science Division
J-PARC Center

http://j-parc.jp/MatLife/

CROSS

Comprehensive Research Organization for Science and Society

http://www.cross-tokai.jp/

J-PARC 18-04